GAS ADSORPTION ON Cu-BTC AND Cr-BDC METAL ORGANIC FRAMEWORKS (MOFs)

submitted in partial fulfilment of the requirements

for the degree of

DOCTOR OF PHILOSOPHY

by

Pradip Chowdhury

DEPARTMENT OF CHEMICAL ENGINEERING

INDIAN INSTITUTE OF TECHNOLOGY GUWAHATI

December, 2009

CERTIFICATE

It is certified that the work contained in the thesis entitled **"Gas Adsorption On Cu-BTC and Cr-BDC Metal Organic Frameworks (MOFs)"** by **Pradip Chowdhury**, has been carried out under my supervision and that this work has not been submitted elsewhere for a degree.

Sasidhar

Date: 07 May, 2010

Signature of the Supervisor

Name: Sasidhar Gumma

Designation: Assistant Professor

Department: Chemical Engineering

Dedicated To

My Respected Parents

&

Babla

Acknowledgements

First and the foremost, I would like to offer my sincere gratitude to my thesis supervisor, **Dr. Sasidhar Gumma** for his immense interest and enthusiasm on the project. His technical prowess and vast knowledge on diverse fields left quite an impression on me. He was always accessible and worked for hours with me 'day in and day out'. Although the journey was beset with complexities but I always found his helping hand when it mattered most. He has been a constant source of encouragement for me.

I would also like to profoundly acknowledge **Prof. Aloke Kr. Ghoshal**, Ex. HOD (Department of Chemical Engineering) and Chairman of the doctoral committee for his advice during the course of my studies. His constant visits to the research lab and queries on research updates always kept me on my toes. The voluntary suggestions helped me immensely. His friendliness gave me certain degree of comfort and confidence in many ways.

I would also like to thank **Prof. Arun Chattopadhyay**, Head, Department of Chemistry and **Dr. Anil Verma** (Department of Chemical Engineering), members of my doctoral committee for their invaluable suggestions during my progress review seminars. Their advice proved to be instrumental in shaping my thesis to logical conclusion.

My heartiest respect goes to **Dr. Prabirkumar Saha**, Head, Department of Chemical Engineering and **Dr. Vijay S. Moholkar**, DPPC Chairman for their suggestions on administrative proceedings during the course of time.

I am still in awe of my meetings with **Prof. Jubaraj Bikash Baruah**, Ex. HOD, Department of Chemistry. His suggestions were instrumental in propping me up. I revere his persona and vast knowledge in the field of Inorganic Chemistry.

Central Instruments Facility (CIF), Centre for Nanotechnology, Mechanical Workshop and Material Science Lab (Department of Mechanical Engineering) provided me with all the facilities to carry my research work whenever I approached them.

My special thanks go to **Mr. Balen Chandra Mahanta** (Junior Technician) of our department for his helping hand in matters related to my experimental setup. His in hand experience in various fields made things easier. I would also like to acknowledge **Mr. Subodh Purohit** (Ex. Scientific Officer) for helping me to acquaint with different analytical instruments. I will long cherish my interactions with other technical and non-technical staffs of our department especially, **Bhagya Boro** and **Bipul Deka**.

I am really fortunate to have so many good friends and seniors in our department. Some of my seniors mainly, **Dr. Biswanath Saha** (Bise Da), **Mr. Debasis Ghosh** (Deba Da), **Dr. Subham Paul** provided me with all the basic "know-how" of our department. My special thanks go to my colleagues and batch mates. I passed so many wonderful days along with my friends, be in the department or in hostel. Whenever needed, I found their helping hands. **Mehabub** was always calm under all circumstances and gave me valuable suggestions. **Barun's** information on subjects related to academics proved vital. **Monash** helped me with various logistical supports. Never ending queries from **Somen Jana** pushed me to dig deep into different subject matters. Along with them I will cherish the quality times that I spent in our Research Lab along with Girivasu, Gaurishankar, Mannava Ashok, Subrata, Samuel and Durgesh. I am indebted to **Swarup Laha** for nursing me when I was very sick in the hostel. **Dr. Bittagopal Mondal** (Bitta Da) helped me a lot in getting hold on some research papers that I couldn't access from our college.

One name that will always remain close to my heart is **Chaitanya Bikkina**. His diligence and punctuality was inspiring. Both of us gelled together nicely in our research work. The brain-storming sessions on different subjects helped me to improve my research aptitude.

Last but not the least, I gratefully acknowledge M/S Rubotherm (Germany) for their financial support in carrying the project work.

Date: 07-05-2010

Place: IIT Guwahati

Pradip Chowdhury

(Pradip Chowdhury)

ABSTRACT

Metal organic frameworks have gained considerable attention in recent years. Due to their high surface area and pore volume they are being widely evaluated for potential applications in several areas including adsorptive separations, gas storage and catalysis. Early adsorption studies on MOFs concentrated on hydrogen storage; this was followed by evaluation of their potential for CO_2 and methane adsorption. Only recently adsorption of other gases is being investigated for their potential applications in adsorptive separations.

The aim of this work is two-fold; apart from systematic measurement and analysis of these frameworks for adsorption of several carefully gases with industrial potential, this work also aims to correlate the adsorptive behaviour of the gases to their physical properties. In order to achieve this objective, adsorbate gases themselves, experimental temperature and pressure were carefully chosen for these measurements.

Two different frameworks *viz.* Cu-BTC (HKUST-1) and Cr-BDC (MIL-101) were studied. Gravimetric experiments for measurement of pure gas adsorption were systematically carried out using a magnetic suspension balance (Rubotherm). Gases like N_2, O_2, Ar, CO, CO_2, CH_4, C_3H_8 and SF_6 with varying physical properties (e.g. molecular diameter, polarizability, dipole-quadrupole moments) were chosen as probes for studying adsorption properties of these MOFs concerned. These studies were carried out at selected temperatures between 283 to 353 K and pressures ranging between 0-100 bar.

It was observed in literature, synthesis of MOFs under different reaction conditions (i.e. temperature) and post synthesis treatments yield samples with different specific surface areas and pore-volume. This difference affects the overall adsorption properties of the framework. Under these circumstances it has often been a practice to use a "scaling-factor" to match

isotherms obtained in different laboratories or comparing experimental data with simulation results. The results obtained in this work showed that such scaling factor may not be unique; it changes with loading, but rather independent of temperature, pressure or the adsorbate. At the zero pressure limit it would be equal to the ratio of Henry constants.

The isotherms on Cu-BTC could be well described by Langmuir, Virial or Virial-Langmuir type models; however that on Cr-BDC required a Dual Site Langmuir type model. Cr-BDC is known to have heterogeneity to adsorption with active metal centers and sites inside the pores of super tetrahedra being the two major locations for adsorption. The enthalpy of adsorption at low loading was directly related to polarizability of the adsorbates as in case of zeolites; CO and CO_2 however were exceptions due to their polarity. For all gases considered, the enthalpies of adsorption were found to be lower than those on purely siliceous zeolite like silicalite, suggesting that only moderate interaction exists between the gas and the frameworks.

Comparative adsorption study of three different gases viz. CO, CO_2 and CH_4 on Cu-BTC and Cr-BDC frameworks up to high pressures indicates that the polarity of the gas molecules plays an important role in determining their adsorption behaviour. In the low loading region the difference between enthalpies of adsorption for all three gases are modest for Cu-BTC whereas they are more pronounced in case of Cr-BDC. This behaviour is attributed to availability of accessible open metal centers for electrostatic interactions. Due to these electrostatic interactions, CO which has dipole moment initially adsorbs more than a non-polar molecule like CH_4. However, as the open metal centers needed for electrostatic interactions are occupied the effect of these interactions decreases and methane (which has slightly higher polarizability than CO) starts to adsorb more after this region. Due to large pore volume of Cr-BDC, the loading for gases at our highest experimental pressure does not

seem to approach saturation as in case of Cu-BTC. The adsorption behaviour for these gases can be well correlated to the temperature, pressure and polarity.

CO_2+CH_4 binary adsorption was studied on Cu-BTC at at 305 K and for pressures up to 10 bar using an infinite dilution gas chromatographic method; appropriate thermodynamic analysis using Virial-Langmuir model was performed on these experimental results. Based on this analysis, cross virial coefficients for adsorption were estimated. The results indicate that that within 10 bar the adsorption of CO_2+CH_4 mixture on Cu-BTC follows Ideal Adsorbed Solution Theory closely. The selectivity value lies between 5.7 and 7.2.

The results presented in this work indicate that MOF materials have high capacity (or at least comparable to those on zeolites) for a variety of gases; on the other hand they only have modest enthalpies of loading unlike in case of polar zeolites. Both these properties make them attractive candidates for applications in adsorptive separations.

CONTENTS

PAGE NO.

Acknowledgements iv

Abstract vii

List of Tables xvi

List of Figures xviii

List of Symbols xxii

CHAPTER 1: Introduction 1

1.1 Review on Adsorption 1

1.2 Adsorbents of Industrial Importance 5

- 1.2.1 Zeolites 7
- 1.2.2 Major Considerations on Sorbent Selection 11
- 1.2.3 Equilibrium Adsorption isotherms 12

1.3 Pressure Swing Adsorption (PSA) Process 14

1.4 Novel Adsorbents 16

1.5 Background of Present Research Work 17

1.6 Research Objectives 18

CHAPTER 2: Literature Survey 22

2.1 Metal Organic Frameworks (MOFs) 22

PAGE NO.

2.1.1 Introduction 22

2.1.2 Strategies for Construction of MOF Structures 25

2.1.3 Potential Research Areas 30

2.1.3.1 Adsorptive Separation/Purification 32

2.1.3.2 Gas Storage 34

2.1.3.3 Catalysis 40

2.2 Cu-BTC or HKUST-1 Framework 40

2.3 Cr-BDC or MIL-101 Framework 41

2.4 Review of Adsorption of the Gases of our Interest 43

CHAPTER 3: Theory 55

3.1 Phase Rule 55

3.2 Fundamental Property Relations 56

3.3 Phase Equilibrium Relations 57

3.4 Gibbs' Adsorption Isotherm 59

3.5 Spreading Pressure 60

3.6 Ideal Adsorbed Solution Theory (IAST) 61

3.7 Models for Pure Gas Isotherms 62

3.7.1 Langmuir Isotherm 62

3.7.2 Dual Site Langmuir (DSL) Isotherm 63

3.7.3 Virial Isotherm 64

PAGE NO.

3.7.4 Virial-Langmuir (V-L) Isotherm 65

3.7.5 Enthalpy of Adsorption 66

3.7.6 Equation of State (EoS) Approach 67

3.7.7 Models Using EoS Approach 69

3.7.7.1 Henry's Law Region 69

3.7.7.2 Virial Formalism 69

3.7.7.3 Virial-Langmuir Formalism 71

CHAPTER 4: Experimental 73

4.1 Synthesis 73

4.1.1 Synthesis of Cu-BTC Framework or HKUST-1 73

4.1.1.1 Materials 73

4.1.1.2 Procedure 74

4.1.2 Synthesis of Cr-BDC Framework or MIL-101 75

4.1.2.1 Materials 75

4.1.2.2 Procedure 75

4.2 Characterization 76

4.2.1 Scanning Electron Microscopy (SEM) and Optical Microscopy Imaging 76

4.2.2 Powder X-ray Diffraction (PXRD) 76

4.2.3 Laser Particle Size Analysis 77

4.2.4 Thermogravimetric Analysis 77

4.2.5 Surface Area Analysis 77

4.3 Pure Gas Adsorption Measurements Using Gravimetry 78

PAGE NO.

4.3.1 Overview of Gravimetric Measurements 78

4.3.2 Experimental Setup 80

4.3.2.1 System Description 81

4.3.2.2 Experimental Protocol 85

4.3.2.3 Experimental Conditions 91

4.3.3 Data Handling 94

4.3.3.1 Bulk Gas Properties 94

4.3.3.2 Buoyancy Volume 96

4.3.3.3 Calculation of Excess Amount Adsorbed 97

4.4 Binary Adsorption Measurements Using Gas Chromatography 98

4.4.1 Review of GC Technique for Characterization of Adsorption Equilibria 98

4.4.2 Slope of Isotherms Using GC Method 98

4.4.3 Experimental Setup 100

4.4.3.1 System Description 101

4.4.3.2 Experimental Protocol 102

4.4.3.3 Data Handling 104

4.5 Details of Gases Used 106

CHAPTER 5: Results and Discussion 107

5.1 Introduction 107

5.2 Correlation between Adsorption Characteristics and Surface Area of Cu-BTC Framework 108

5.2.1 Characterization 108

5.2.1.1 Morphology of Cu-BTC 108

5.2.1.2 Powder X-ray Diffraction Analysis 111

PAGE NO.

5.2.1.3 Thermogravimetric Analysis 111

5.2.1.4 Surface Area and Pore Volume Analysis 113

5.2.1.5 Particle Size and Packing Density Measurements 117

5.2.2 Analysis of Gas Adsorption on Cu-BTC Samples 118

5.2.2.1 Adsorption Isotherm Measurements and Modeling 118

5.2.2.2 Correlation of Surface Area and Adsorption Characteristics 127

5.2.2.3 Enthalpy of Adsorption on Cu-BTC (sample **B**) 132

5.3 Gas Adsorption Properties of Cr-BDC Framework (or MIL-101) 134

5.3.1 Characterization 134

5.3.1.1 Thermogravimetric Analysis 134

5.3.1.2 BET Surface Area Analysis 135

5.3.1.3 SEM and Powder XRD Analysis 139

5.3.2 Measurement of Adsorption Isotherms on Cr-BDC 140

5.3.3 Modeling 146

5.3.4 Calculation of Adsorption Enthalpies 150

5.3.5 Variation of Adsorption Enthalpy with Loading 151

5.3.6 Enthalpy at Zero Coverage 152

5.4 Comparative Study of CH_4, CO_2 and CO Adsorption on Cu-BTC and Cr-BDC Metal Organic Frameworks 155

5.4.1 Isotherms 156

5.4.2 Modeling 164

5.4.3 Enthalpy of adsorption 168

5.4.4 Effect of Adsorbate Polarity on Adsorption Characteristics 171

5.5 Binary Adsorption of CO_2+CH_4 Mixture on Cu-BTC Using Gas Chromatography 181

5.5.1 Measurement of Slopes of Partial Isotherms at Infinite Dilution 181

5.5.2 Modeling of Infinite Dilution GC Results 184

PAGE NO.

5.5.3 Estimation of Adsorption Isotherms of CO_2+CH_4 Binary Mixture 187

CHAPTER 6: Conclusions and Future Scope 191

6.1 Conclusions 191

6.2 Future Scope 197

REFERENCES 198

APPENDIX 213

RESEARCH PUBLICATIONS 258

LIST OF TABLES

TABLE	TABLE CAPTION	PAGE NO.
1.1	Chronology of major events in the field of zeolite synthesis and application	10
1.2	Chronology of major events in PSA process development	15
2.1	Details of adsorptive separation studies on MOFs carried out by various researchers	33
2.2	Literature review of adsorption on MOFs (**A**) CH_4 and CO_2 adsorption (**B**) Hydrogen adsorption	37
2.3	Literature review of Ar adsorption on various adsorbents	44
2.4	Literature review of N_2 adsorption on various adsorbents	45
2.5	Literature review of O_2 adsorption on various adsorbents	47
2.6	Literature review of CO_2 adsorption on various adsorbents	48
2.7	Literature review of CH_4 adsorption on various adsorbents	50
2.8	Literature review of C_3H_8 adsorption on various adsorbents	53
2.9	Literature review of CO adsorption on various adsorbents	53
2.10	Literature review of SF_6 adsorption on various adsorbents	54
3.1	Enthalpy of adsorption for different isotherm models	67
4.1	List of major hardware used along with their specifications and operating ranges	84
4.2 (A)	Details of experimental conditions for gravimetric measurements	91

PAGE NO.

4.2 (B) Experimental conditions for gas chromatographic Measurements 92

4.3 Physical properties of various gases 93

4.4 Second virial coefficients for different gases 95

4.5 List of major hardware used in the GC experiments 101

4.6 Details of experimental conditions for GC measurements 102

4.7 Details of gas purity 106

5.1 Physical properties of Cu-BTC 114

5.2 Comparison of surface area and pore volumes for different Cu-BTC samples 116

5.3 Virial isotherm parameters for adsorption of N_2, O_2, Ar and CO_2 on Cu-BTC 123

5.4 Langmuir parameters for adsorption of SF_6 and C_3H_8 on Cu-BTC 127

5.5 Surface area and pore volume results of different Cr-BDC samples 136

5.6 Dual Site Langmuir isotherm parameters for adsorption on Cr-BDC 149

5.7 Virial-Langmuir model fit parameters for CO, CO_2 and CH_4 adsorption on Cu-BTC 165

5.8 Dual Site Langmuir model fit parameters for CO, CO_2 and CH_4 on Cr-BDC 167

5.9 GC measurements 182

5.10 Cross virial coefficients for CO_2+CH_4 adsorption on Cu-BTC 186

LIST OF FIGURES

FIGURE	FIGURE CAPTION	PAGE NO.
1.1	Schematic diagrams depicting framework structures of two common zeolites, (A) Zeolite **A** (B) Zeolite **X** or **Y**	9
1.2	IUPAC classifications of adsorption isotherms	13
2.1	MOF-5 structure and topology	24
2.2	Assembly of Metal Organic Frameworks	27
2.3	Schematic for $Cu_3(BTC)_2(H_2O)_3$ (BTC= 1,3,5-benzenetricarboxylate) metal organic framework	41
2.4	Schematic for Cr-BDC or MIL-101 Framework	42
4.1	Typical gravimetric experimental setup	78
4.2	Schematic of gravimetric experimental setup used in the work	80
4.3	Schematic of experimental Gas Chromatography setup used in the work	100
5.1	Optical microscopy images: (I) Sample **A** (top) (II) Sample **B** (bottom)	109
5.2	SEM micrographs of Cu-BTC products: (I) Sample **A** (top) (II) Sample **B** (bottom)	110
5.3	Powder XRD pattern of synthesized Cu-BTC samples	112
5.4	Thermogravimetric analysis of Cu-BTC samples	113
5.5	N_2 physisorption on Cu-BTC at 77 K	115
5.6	Particle size distribution of Cu-BTC	117

PAGE NO.

5.7 Adsorption isotherms for N_2, Ar and O_2 on Cu-BTC 120

5.8 Adsorption isotherms for CO_2 on Cu-BTC 122

5.9 Adsorption isotherms for SF_6 on Cu-BTC 125

5.10 Adsorption isotherms for C_3H_8 on Cu-BTC 126

5.11 Variation of scaling factor with loading for N_2 adsorption on Cu-BTC 129

5.12 Comparison of adsorption capacities of samples **A** and **B** for various gases in low loading region 130

5.13 Comparison of adsorption capacities of samples **A** and **B** for various gases in high loading region 131

5.14 Enthalpy at zero loading vs. polarizability on Cu-BTC (sample **B**) 133

5.15 Thermogravimetric analysis of Cr-BDC 135

5.16 N_2 physisorption on Cr-BDC sample at 77 K 137

5.17 Pore size distribution of Cr-BDC from N_2 physisorption at 77 K 138

5.18 Scanning electron microscopy images of Cr-BDC 139

5.19 Powder XRD pattern of Cr-BDC 139

5.20 Adsorption isotherms of Argon on Cr-BDC 141

5.21 Adsorption isotherms of CH_4 on Cr-BDC 142

5.22 Adsorption isotherms of CO_2 on Cr-BDC 143

5.23 Adsorption isotherms of C_3H_8 on Cr-BDC 144

5.24 Adsorption isotherm of SF_6 on Cr-BDC 145

5.25 Virial domain plot of SF_6 on Cr-BDC 147

PAGE NO.

5.26 Enthalpy of adsorption for various gases on Cr-BDC 152

5.27 Variation of enthalpy at zero coverage with polarizability of adsorbate 153

5.28 Variation of Henry's law constant at 319 K with polarizability of the adsorbate 154

5.29 Adsorption isotherms for CH_4 on Cu-BTC 157

5.30 High pressure adsorption isotherms for CO_2 on Cu-BTC 158

5.31 High pressure adsorption isotherms for CO on Cu-BTC 159

5.32 Adsorption isotherms for CH_4 on Cr-BDC 160

5.33 High pressure adsorption isotherms for CO_2 on Cr-BDC 161

5.34 High pressure adsorption isotherms for CO on Cr-BDC 162

5.35 Comparison of adsorption of CO and CH_4 on Cu-BTC with reported GCMC simulation 164

5.36 Comparison of enthalpy of adsorption of CH_4, CO_2 and CO on Cu-BTC (sample **C**) and Cr-BDC in low loading 169

5.37 Variation of enthalpy of adsorption with loading on Cu-BTC (sample **C**) at 295 K 170

5.38 Variation of enthalpy of adsorption with loading on Cr-BDC at 295 K 171

5.39 Variation of Henry constant with temperature for CO, CO_2 and CH_4 on Cu-BTC and Cr-BDC 172

5.40 CH_4 adsorption on Cu-BTC and Cr-BDC at 295 K 174

5.41 CO adsorption on Cu-BTC and Cr-BDC at 295 K in the low pressure region 175

PAGE NO.

5.42 CO adsorption on Cu-BTC and Cr-BDC at 295 K in the high pressure region 176

5.43 CO_2 adsorption on Cu-BTC and Cr-BDC at 295 K 176

5.44 Comparison of adsorption isotherms of CO_2, CO and CH_4 on Cu-BTC framework at 295 K (virial domain plot) 178

5.45 Comparison of adsorption isotherms of CO_2, CO and CH_4 on Cu-BTC framework at 353 K (virial domain plot) 178

5.46 Comparison of adsorption isotherms of CO_2, CO and CH_4 on Cr-BDC framework at 295 K (virial domain plot) 179

5.47 Comparison of adsorption isotherms of CO_2, CO and CH_4 on Cr-BDC framework at 353 K (virial domain plot) 180

5.48 Variation of retention time of inert (helium) with bulk gas density 183

5.49 Variation of slope of partial isotherms at infinite dilution with fugacity for CO_2+CH_4 mixture on Cu-BTC at 305 K 186

5.50 Variation of amount adsorbed from CO_2+CH_4 mixture at 305 K, $yCH_4 = 0.1$ 188

5.51 Variation of amount adsorbed from CO_2+CH_4 mixture at 305 K, $yCH_4 = 0.9$ 188

5.52 Variation of amount adsorbed from CO_2+CH_4 mixture at 305 K, $P = 1$ bar 189

5.53 Variation of amount adsorbed from CO_2+CH_4 mixture at 305 K, $P = 10$ bar 189

5.54 Variation of selectivity of CO_2+CH_4 mixture with pressure at 305 K 190

5.55 Variation of selectivity of CO_2+CH_4 mixture with mole fraction at 305 K 190

LIST OF SYMBOLS

A	Specific surface area of the adsorbent, $m^2\ g^{-1}$
a	Specific area of adsorbent per mole of adsorbate, $m^2\ mol^{-1}$
b	Second virial coefficient in adsorbed phase, $mmol^{-1}\ g$
$\delta^{(i)}$	Affinity parameters for sites of type i
b_{ij}	Cross virial coefficients (when $i = j$), $mmol^{-1}\ g$
b_{mix}	Second virial coefficient for the mixture in the adsorbed phase, $mmol^{-1}\ g$
B^{gas}	Second virial coefficients in gas phase, $m^3\ kmol^{-1}$
c	Third virial coefficient in adsorbed phase, $mmol^{-2}\ g^2$
c_{ijk}	Cross virial coefficients (when $i = j = k$)
c_{mix}	Third virial coefficient for the mixture in the adsorbed phase, $mmol^{-2}\ g^2$
C	Number of chemical species
f_i	Fugacity of species i in the adsorbate mixture, bar
f_i^g	Fugacity of species i in the bulk gas-phase mixture, bar
F	Number of degrees of freedom
g	Molar Gibbs' free energy, $J\ mol^{-1}$
h	Molar enthalpy, $kJ\ mol^{-1}$
Δh_{ads}	Enthalpy of adsorption, $kJ\ mol^{-1}$
$\Delta h_{ads,0}$	Enthalpy of adsorption at zero loading, $kJ\ mol^{-1}$
β	Henry constant, $mmol\ g^{-1}\ bar^{-1}$
β_i	Henry constant for species i in the adsorbed phase, $mmol\ g^{-1}\ bar^{-1}$
k	$-\ln \beta$, where β is Henry constant (units as appropriate)
k	Scaling factor

m	Mass of solid adsorbent, g
M_t	Observed mass in gravimetric experiment, g
$M_{t,0}$	True adsorbent mass with the bucket measured in vacuum, g
M_{ex}	Excess amount adsorbed, g
M_w	Molecular weight of the gas
n_i	Molar flow rate of species i, mmol sec^{-1}
N	Excess amount adsorbed, mmol g^{-1}
M	Maximum loading corresponding to monolayer coverage, mmol g^{-1}
$M^{(i)}$	Saturation capacity of species i
M_{mix}	Saturation loading for the mixture at given T, P and y_i, mmol g^{-1}
N_i^0	Pure component loading of species i at column condition, mmol g^{-1}
P	Pressure, bar
P_{amb}	Ambient pressure, bar
P_i	Partial pressure of a component i in the bulk gas phase, bar
P_i^0	Pressure at the standard state, bar
q	Volumetric flow rate of the carrier gas, cm^3 min^{-1}
R	Universal gas constant, 8.314 J mol^{-1} K^{-1}
s	Molar entropy of the adsorbed phase, kJ mol^{-1} K^{-1}
T	Temperature, K
T_{amb}	Ambient temperature, K
t_i	Retention time for species i, second
t_{inert}	Retention time of inert, second
t	t -statistics
u	Molar internal energy of the adsorbed phase, kJ mol^{-1}

x_i	Adsorbed phase mole fraction of species i
y_i	Gas phase mole fraction of species i
V_{bucket}	Bucket volume, cm^3
V_s	Impenetrable solid volume, cm^3
$V_{buoyancy}$	Buoyancy volume, cm^3
V_N	Net retention volume in GC experiment, cm^3
V_R	Retention volume of an adsorbing species in GC experiment, cm^3
Z	Compressibility factor for the adsorbed phase

GREEK LETTERS

α_{ij}	Separation factor between species i and j
α	Polarizability
μ_i	Chemical potential of species i in adsorbed phase, kJ mol^{-1}
μ_i^g	Chemical potential of species i in gas phase, kJ mol^{-1}
χ	Number of phase
π	Spreading pressure, N m^{-1}
ψ	Reduced spreading pressure, mmol g^{-1}
η_i	Net retention of species i, mmol
ϕ_i^{gas}	Fugacity coefficient of bulk gas
γ_i	Activity coefficient in adsorbed phase

CHAPTER 1

Introduction

Metal organic frameworks have gained a large attention in the research community over last decade. They are highly porous materials with large surface areas and have potential applications in several areas. Adsorptive separation and high pressure hydrogen / gas storage are also being investigated on these frameworks.

The forces acting on the surface of a solid are unsaturated and hence when the solid is exposed to a gas, the gas molecules associate with the surface through van der Waal's and/or chemical bonds with the solid surface. This phenomenon is known as adsorption **[1]**. Adsorption can be broadly classified into two categories: physical adsorption or physisorption and chemical adsorption or chemisorption. Physical adsorption involve only relatively weak intermolecular forces (i.e. van der Waals forces) and the physisorbed molecule undergoes no significant change in electronic structure whereas chemisorption involves, essentially, the formation of a chemical bond between the sorbate molecule and the surface of the adsorbent i.e. the molecule's electronic structure is significantly perturbed upon adsorption.

1.1 Review on Adsorption

The concept of adsorption was conceived as early as eighteenth century by Scheele and Fontana when they observed porous solids to reversibly adsorb vapors but the practical applications of this property largely remain unexplored. A few familiar practical examples that were practised in earlier times include removal of moisture from gas streams using suitable hydrophilic agents in driers, removal of impurities such as H_2S and mercaptans from natural gas, removal of harmful organic pollutants from water etc. **[2]**. The above processes are very much still in vogue and are classified as purification processes. Major advances in the field of adsorption took place in the later half of the twentieth century with the advent of new adsorbents mainly *zeolites* and development of efficient process cycles.

Although first synthetic zeolite was synthesized by Milton at the Union Carbide Corporation but the history of this class of adsorbent goes dates back. It all started with the discovery of a mineral called "*stilbite*" by a Swedish mineralogist Crönsted. The said mineral showed intumescence when heated in a flame and this new family of material was named "*zeolite*". The etymology of the word "zeolite" explains its origin from Greek words "zeo" and "lithos" meaning "to boil" and "stone". Since then for most of the times natural zeolite crystals were making their presence felt in "museums" to the amusement of the visitors till the advent of first man-made synthetic zeolites **[3]**. Simultaneously new and efficient process cycles were developed and adsorption established itself as one of the major unit operations in process industries.

All adsorption separation processes involve two principal steps. They are: (a) *adsorption*, when one component is being preferentially adsorbed onto the solid from its mixture and (b) *desorption* or *regeneration*, during which the adsorbent bed is cleaned to be used for the next cycle. Adsorptive separation processes can be categorized on certain principles. They are summarized as **[1]**:

(1) *Based on mechanism of separation*: Adsorptive separation is achieved by one of the following three mechanisms: steric, kinetic and equilibrium. Steric effect is also known as size-selective sieving. Here the microporous adsorbent allows only the smaller molecule (diameter of the molecule is comparable with the dimension

of the micropore) to pass through whereas larger size molecules are totally excluded. Adsorbents e.g. zeolites having uniform pore size distribution shows steric effect. A common example is separation of linear from branched and cyclic hydrocarbons on 5A zeolite. Kinetic separation is achieved due to the differences in diffusion rates of different molecules. It is achieved with adsorbents of varying pore size distribution. A classic example is the separation of N_2 from Air using molecular sieve carbon. Equilibrium separation on the other hand depends on the differences between relative affinities of the adsorbent towards various adsorbates. Majority of the adsorption processes operate through equilibrium mechanism.

(II) *Based on feed composition*: The separation processes may also be divided in the line of feed concentration. Based on feed concentration the separation process may be divided into bulk separation and purification. As had been defined by Keller [1], bulk separation is the point when 10 wt% or more of the mixture is adsorbed. Purification processes are generally separation processes when the components adsorbed are generally present in low concentration, have little economic value and are not recovered.

(III) *Based on method of adsorbent regeneration*: Adsorbents can be regenerated by several mechanisms. Widely used ones include temperature swing adsorption (TSA) cycles, pressure swing adsorption (PSA) cycles, purge gas stripping and displacement desorption. TSA cycles are run on heating-cooling mechanism whereas PSA process involves steps like: pressurization-adsorption-countercurrent blowdown and countercurrent purge. PSA processes are fast whereas each heating-cooling cycle in a TSA process requires a lot of time and used exclusively for processes, in which the amount of adsorptive gases being processed are small.

Apart from TSA and PSA, other regeneration processes include purge gas stripping and displacement desorption. In inert purge gas stripping cycle, the adsorbent is regenerated by passing a non-adsorbing and weakly adsorbing gas through the adsorber without changing the temperature or pressure. The void in the bed is filled with the inert gas upon completion of regeneration. However, in a displacement desorption a gas or vapour that adsorbs about as strongly as the adsorbate is used; regeneration is thus facilitated both by adsorbate partial-pressure reduction and by competitive adsorption of the displacement medium [1]. Displacement desorption process requires more complex scheme of operation and is used only in situations where rest of the processes fail. Some important examples of displacement desorption technique are MOLEX and PAREX processes. The MOLEX process uses the Sorbex simulated moving bed technique (developed by UOP) to recover high purity n-paraffins by continuous adsorptive separation. This technique is similar in concept to liquid chromatography, but carried out on a large commercial scale. UOP's PAREX process is used for the recovery of *para*-xylene from mixed xylenes that offers high product purity, high product recovery, high efficiency and extended adsorbent life. "Mixed xylenes" is a mixture of C_8 aromatic isomers that includes ethyl benzene, *para*-xylene, *meta*-xylene, and *ortho*-xylene. They boil so closely together that separation by distillation is not practical. PAREX process provides an efficient means of recovering *para*-xylene using a zeolitic adsorbent [1-2]

The importance of adsorption based processes can be gauged from situations when other conventional separation processes don't perform efficiently. A few typical cases are given below [1]:

(I) Although process simplicity and scalability is the reason behind popularity of distillation over other unit operations, however when the relative volatility between the key components to be separated is less than 1.2 to 1.5 or even lesser, distillation becomes highly energy intensive and fails when relative volatility is unity. In such cases, alternate separation mechanisms like adsorption yield better result. Adsorption based separation techniques can be highly efficient because of high separation factors achievable between the key components by pragmatic selection of a suitable zeolite. Separation of isomers e.g. n-paraffin from iso-paraffin using 5A molecular sieve, separation of iso-paraffins, iso-olefins from di-n-butylamine using 10X molecular sieve are the examples where adsorptive separation are more effective than distillation [**1, 2**].

(II) When the component of our interest is present in low concentration and bulk of the feed is of low-value, adsorption is preferred to distillation.

(III) When the two groups of components to be separated are having overlapping boiling ranges, adsorption based separation is effective if they contain chemically or geometrically dissimilar molecules.

1.2 Adsorbents of Industrial Importance

The success and failure of any adsorption based system largely depends on the selection of a proper adsorbent for a particular application. Although literature is crowded with examples of various adsorbents but only a few could last over the ages of technological advances. Some well known adsorbents are: silica gel, activated alumina, activated carbon, carbon molecular sieves and zeolites. Each of these adsorbents has certain specific features that have been exploited in various applications ranging from adsorptive separation/purification, ion-exchange and catalysis.

The primary classification between the adsorbents shows two distinct types of surfaces: 'hydrophilic' and 'hydrophobic'. Such type of behavior can be attributed to the surface polarity (as a result of presence of ions in the structure) of the adsorbents. Polar adsorbents *viz.* zeolites, activated alumina, silica gel etc. show a tremendous affinity towards polar molecules whereas non-polar activated carbon shows little or no affinity towards polar adsorbates. Zeolites owe their hydrophilic nature to the polarity of the heterogeneous surface whereas presence of hydroxyl groups on the surface of silica gel or activated alumina is largely responsible for their 'hydrophilicity' by hydrogen bond formation. These features are particularly important for consideration during equilibrium based separation processes. The fundamental physical properties of the targeted adsorbate molecule like polarizability, permanent dipole moment, quadupole moment, magnetic susceptibility in comparison with the other molecules present in the mixture needs to be examined in detail at first before sorbent design or selection.

The most important feature of any adsorbent material is their porosity. Basically, a highly porous material possess high specific surface area and total pore volume. Pore size distribution is also an important consideration during physical characterization of a porous material. Parameters like bulk density, crush strength and erosion resistance are also important considerations while characterizing any solid adsorbent before practical applications. International Union of Pure and Applied Chemistry (IUPAC) categorized porous materials into three different categories by size: microporous (<2 nm), mesoporous (2-50 nm) and macroporous (>50 nm). Within the microporous regime, there exists a fundamental difference between different adsorbents. For adsorbents like silica gel, activated carbon or activated alumina there is a distribution of micropore size whereas in a zeolitic adsorbent since the micropore size is controlled by the crystal structure there is virtually no distribution of pore size. This unique feature of zeolites leads to significant results in adsorption properties and set them apart from other conventional adsorbents.

1.2.1 Zeolites

Zeolites are crystalline aluminosilicates of alkai or alkali earth elements, such as sodium, potassium and calcium. The chemical composition of zeolites can be represented by the following stoichiometry:

$$M_{x/n}[(AlO_2)_x(SiO_2)_y].zH_2O$$

Where x and y are integers with y/x equal to or greater than 1, n is the valance of cation M, and z is the number of water molecules in each unit cell **[1]**. The zeolite framework basically consists of an assemblage of SiO_4 and AlO_4 terahedra, joined together in various regular arrangements through shared oxygen atoms, to form an open crystal lattice containing pores of molecular dimensions. Since the crystal lattice determines the micropore structure, it results into pores of uniform size with no distribution, a feature very unique amongst adsorbents.

In the zeolite framework each aluminium atom introduces one net negative charge and must be balanced by an exchangeable cation. Replacing the cation by means of ion exchange imparts exciting adsorptive properties into the structure and had been widely exploited. The water molecules present within the framework can be removed easily by simple heating or evacuation which leaves almost an unaltered skeleton with a void fraction varying between 0.2-0.5. The Si/Al ratio is very important in a zeolite framework. Generally the ratio is never less than one but there is no upper limit to it. The adsorption properties show a systematic shift as ratio changes from Aluminium rich to Silicon rich. Aluminium rich zeolitic frameworks are hydrophilic and have very high affinities for water and other polar molecules whereas microporous silicas (Si rich) *viz.* silicalite are hydrophobic. The transition from hydrophilic to hydrophobic character generally occurs at a Si/Al ratio ranging from 8 to10. Thus the adsorptive properties of zeolites vary considerably with Si/Al ratio and cationic form of the framework **[1, 2]**.

There are different types of zeolitic frameworks cited in literature **[2]**. A few examples are given below:

(A) Sodalite (the channels are constricted by six-membered oxygen rings with free diameter of about 2.8 Å).

(B) "Small-pore" zeolites such as Type A, Chabazite, and Erionite (access is through eight-membered oxygen rings with free diameter of 3.0-4.5 Å).

(C) "Medium-pore" pentasil zeolites include names such as ZSM-5, ZSM-11, and Silialite (characterized by ten-membered oxygen rings and intermediate channel with free diameter of 4.5-6.0 Å).

(D) "Large-pore" zeolites such as Type X, Type Y, and Mordenite (access is through twelve-membered oxygen rings with free diameter of 7.0-7.4 Å).

The schematic representation of two zeolite framework structures is given below:

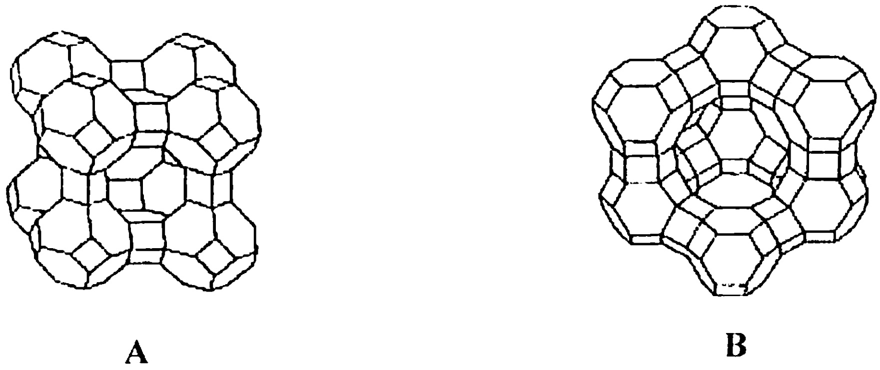

Figure 1.1: Schematic diagrams depicting framework structures of two common zeolites. (**A**) Zeolite A (**B**) Zeolite X or Y **[1, 2]**.

The structural unit in both Type A zeolite and Types X and Y, is the truncated octahedron as shown in Fig. 1.1. The unit is also known as sodalite cage or beta cage. The four member rings of the sodalite units are linked through four member prisms, which assemble into Type A framework. The free diameter in the central cavity is 11.4 Å, which is entered through six eight member oxygen-ring apertures with a minimum diameter of 4.4 Å. In case of Type X and Y zeolite frameworks the sodalite units are linked through six member prisms and the aperture is formed by the 12 member oxygen rings with a free diameter of approximately 7.4 Å.

Although 'Zeolite' was discovered in the eighteenth century, it took approximately another century before practical applications of this class of material was realized e.g. reversible adsorption-desorption of water, ion-exchange etc. By the advent of the 20th century its potential in various other fields materialized e.g. adsorption of organic and smaller molecules etc. Soon the shape-selective nature was noted and in 1932 McBain coined the term 'molecular sieve' to the zeolite minerals **[4]**. With the advent of X-ray crystallography detailed information on structural configuration was possible and it opened a new door to the understanding of the zeolite frameworks. Table 1.1 gives detail information on zeolite synthesis, invention and applications ever since the report of first man-made synthetic zeolite till date.

Table 1.1: Chronology of major events in the field of zeolite synthesis and application [3]

Year	Inventor/Industry	Synthesis & Applications
1949-1954	Milton-Breck	Synthesis of zeolites A,X,Y
1954-1962	Union Carbide Corporation & Mobil	Commercialization of zeolites A,X,Y leading to applications in: Drying, n-iso alkane separation Catalysis: isomerization on Y, cracking on X and Y
1967-1981	Mobil, Henkel	Synthesis of high silica zeolites MFI & BEA used for shape selective processes, dewaxing and Xylene isomerization and production Ion exchange: detergents, A zeolites instead of phosphates.
1982-1986	Union Carbide Corporation, Chevron, UOP-Norsk Hydro	Synthesis of aluminophosphates, SAPO, MeAPO and their major applications were in Isodewaxing, methanol to olefins.
1983	Enichem	Synthesis of titanium silicalites TS 1 and its major use was in phenol hydroxylation
1992	Mobil	MCM-41, mesoporous molecular sieves
1994-1998	Corma	Nanocrystalline zeolites

1.2.2 Major Considerations on Sorbent Selection

The key role that an adsorbent plays in any application is providing with the surface area required for selective sorption of the preferentially adsorbed species. The selection of a proper sorbent for a particular application is complex and requires prior knowledge on certain aspects. The most important scientific basis for sorbent selection is the equilibrium isotherm. The equilibrium isotherms of all the constituents of the gas mixture need to be determined in different operating conditions of pressure and temperature. Different theories have been proposed to model adsorption of gas mixtures from pure component data. Based on equilibrium isotherm data, following factors are found to be very important in choosing a proper adsorbent **[1, 5]**:

(A) *Selectivity*: A high selectivity is desirable to realize any adsorptive separation process. The parameter, separation factor can be defined as

$$\alpha_{ij} = \frac{x_i / y_i}{x_j / y_j} \tag{1.1}$$

Where x_i and y_i are the equilibrium mole fractions of the component '*i*' in adsorbed and gas phases respectively. Ideally a high separation factor means a better selectivity for the adsorbent.

(B) *Capacity*: Sorbent capacity in the operating temperature and pressure range is very important information. A high capacity is desirable since the capacity determines the size and therefore the cost of the adsorbent beds.

(C) *Sorbent regeneration*: The method of sorbent regeneration *viz*. PSA or TSA and the magnitude of the required swing is a major consideration on sorbent selection.

(D) *Product purities*: Product purity is a key factor in deciding the effectiveness and overall economy of the process.

(E) Length of unused bed (LUB): A short LUB or a sharp concentration front is desirable since it results in high sorbent productivity as well as high product purity.

Apart from the aforementioned factors there are certain other factors like stability and cost which are equally important for consideration during selecting a sorbent. Sorbent deactivation during catalysis primarily by coke deposition is an important consideration in the processing of crude petroleum. The total void space in an adsorbent bed generally varies with the sorbents. A low void space is desirable for effective product recoveries. The gas mixture remaining within the voids of a saturated bed remain unrecovered and hence reduce the efficiency of the process.

1.2.3 Equilibrium Adsorption Isotherms

Adsorption of a pure component of gas on a solid at equilibrium can be represented by the following function:

$$N = f(P,T) \tag{1.2}$$

N is the amount adsorbed in cc STP per gm, P is the pressure and T is temperature.

At constant temperature, the amount of gas adsorbed onto a solid surface is only a function of P and is known as adsorption isotherm **[1]**.

The IUPAC classification **[2, 6]** of adsorption isotherms is shown in Fig. 1.2. Type I isotherm is characteristic of a microporous adsorbent where molecular diameter of the adsorbate molecule matches exactly with the pore diameter of the adsorbent. There is a definite saturation limit to such type of an adsorbent which corresponds to the complete filling of the micropores. Types II, III and VI corresponds to non-porous or macroporous adsorbents whereas types IV and V characterizes mesoporous adsorbents. Isotherms of types II and IV are associated with stronger gas-solid interactions whereas types III and V associated with weaker gas-solid interactions. An isotherm of type IV suggests the formation of multilayer either on a plane surface or on the walls of pores much larger than the molecular diameter of the adsorbate molecule. Isotherms of types II and III characterizes adsorbents with wide range of pore sizes. For such type of adsorbents as the pressure increases adsorption occurs from monolayer to multilayer followed by capillary condensation.

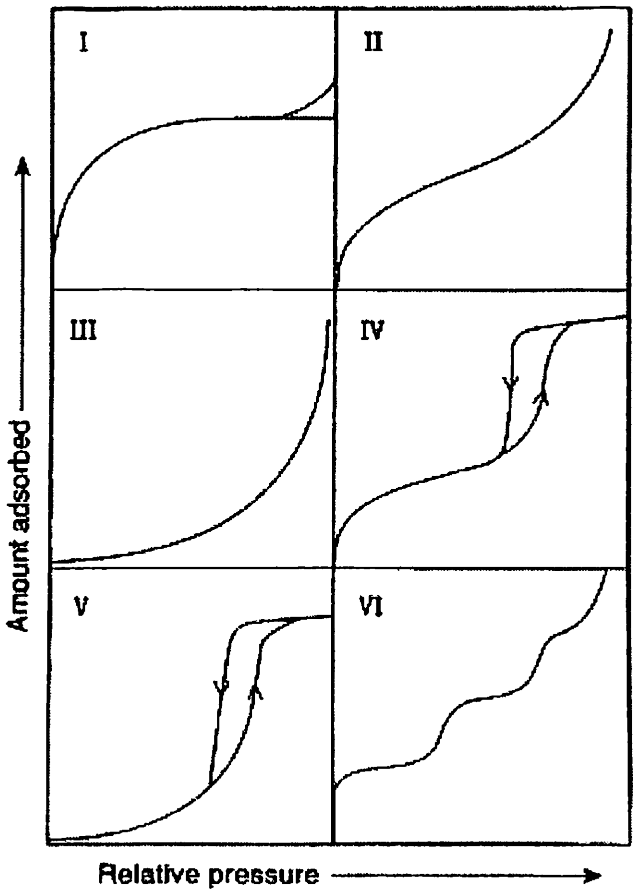

Figure 1.2: IUPAC classifications of adsorption isotherms [6].

1.3 Pressure Swing Adsorption (PSA) Process

Invention of Pressure Swing Adsorption or PSA process was a major breakthrough in adsorption based applications. The credit for inventing PSA process went jointly to Skarstrom and Guerin de Montgareuil and Domine in 1957-1958. PSA process involves steps like: pressurization-adsorption-countercurrent blowdown and countercurrent purge. Technically there was a fundamental difference between either of the processes developed by the above researchers. The Esso process developed by Skarstrom used a low pressure purge to clean the adsorbent bed following the blowdown step whereas the Air Liquede process developed by Guerin de Montgareuil and Domine, utilized a vacuum swing **[1, 7]**.

The salient feature of a PSA process lies in the fact that pressure can be changed much more rapidly, thus making it possible to operate a PSA process on a faster cycle, thereby increasing the throughput per unit of adsorbent bed volume. There are also a few drawbacks of the process such as PSA processes are restricted to components that are not too strongly adsorbed. If the preferentially adsorbed species is very strongly adsorbed, a high vacuum is required to effectively remove the adsorbed product during the regeneration step.

The chronology of events leading to the development of PSA process is given in the following tabular form (Table 1.2):

Table 1.2: Chronology of major events in PSA process development [7, 8]

Year	Developments
1930-1933	First PSA patent filed and issued to Finlayson and sharp
1953-1954	In this paper H. Kahle outlined the principles of PSA process
1955-1956	Synthetic zeolite produced commercially
1957-1958	C.W. Skarstrom and P. Guerin de Montgareuil and D. Domine patented their findings on PSA
1960-1965	Development of 'Heatless Drier' for small scale air-drying and 'Isosiv' process for separation of linear hydrocarbons
1965-1970	Development and commercialization of PSA hydrogen purification
1970-1973	Development of large-scale O_2 PSA process and O_2 selective carbon sieves produced commercially
1976-1980	Development of PSA nitrogen process using CMS adsorbent and small scale medical oxygen unit
1982	Large scale vacuum swing process for air separation
1988	Development of second generation zeolite adsorbents for air separation by vacuum swing
1992-1993	High selectivity LiX for air separation
1993	Praxair patents on VSA air separation

1.4 Novel Adsorbents

New materials usher new technologies. Synthesizing novel materials has long been cherished as a stepping stone in technological advancement. It is not long back when zeolites and activated carbon, known to be the most versatile, used primarily in wide ranging industrial applications. But as the need grows for more efficient, economical and highly specific functions, conventional adsorbents were not found effective enough to deal with such problems. Although, improved synthesis and different post-treatment procedures of zeolites and activated carbon resulted into some of their derivatives but the need of the hour was to design and synthesize materials that could be more effective.

In the quest for designing novel adsorbents, attention has been paid to develop hybrid structures involving both inorganic and organic components by employing novel synthetic routes. The general concept was to take advantage of both the metal coordination and functionalities of the organic components. The concept of reticular synthesis which can be described as the process of assembling judiciously designed rigid molecular building blocks into predetermined ordered structures or networks, held together by strong bonding is found to be the key to the true design of novel solid-state materials. Researchers have envisioned that to fully realize the benefits of designing crystalline solid state frameworks the structural integrity and rigidity of the molecular building blocks must remain unaltered throughout the construction process: key feature of reticular synthesis [9]. The said mechanism plays a pivotal role in producing robust porous materials by connecting rigid rod-like organic moieties with inflexible inorganic clusters acting as joints. The length and functionalities of the organic units determine the size and chemical environment of the resulting void spaces. Accordingly, the concept of 'tailor-made' materials finally realized. Appropriate selection of starting materials can give rise to myriad of different structures. Within a short period of time a large variety of extended structures have been successfully prepared and the collection of compounds has been given various names e.g. 'co-ordination polymers', 'hybrid organic-inorganic materials', 'organic zeolite analogues' or 'metal organic frameworks'. Although each terminology signifies certain aspects of the materials it encompasses but for a solid to be truly called a 'Metal Organic Framework' or MOF, it must possess robustness implying strong bonding, assembling units are available for modification by organic synthesis and geometrically a well-defined structure **[10]**.

1.5 Background of Present Research Work

Metal Organic Frameworks (MOFs) represent a new family of novel adsorbents. They generally consist of inorganic and organic building blocks. They have high surface area (~1000 to 5000 $m^2 g^{-1}$), large pore volume (0.7-1.5 $cm^3 g^{-1}$) and low to moderate heat of adsorption (~12 to 30 kJ mol^{-1} at moderate coverage). All these features make this class of adsorbents very attractive from an application point of view. However, certain challenges remain before these materials can be exploited for adsorption. It has often been found that the materials synthesized in different laboratories (or even in different batches from the same lab) have different adsorption characteristics and it is often difficult to reproduce experimental results with accuracy. This variation is usually attributed to the difference in degree of purity of the adsorbent as well as residual solvent used during synthesis which is left inside the pores. Moreover, some of these materials are known to have low thermal stability and decompose on exposure to moisture for long periods of time.

1.6 Research Objectives

Limited adsorption data is available on MOFs. The adsorption isotherm data even on a widely studied MOF like Cu-BTC is limited to gases like CO_2 and CH_4 with a few exceptions; data on other gases is usually limited to low pressures. A thorough analysis and interpretation of adsorption properties for gases with varying physical properties is not available till date on any MOF; on the other hand such analysis will be highly useful in understanding the behavior of the materials and will enable chemists towards tailor make materials targeted for specific applications. The work aims at developing a better understanding of the adsorption properties of metal organic frameworks.

Out of numerous metal organic frameworks synthesized, IRMOF (Isoreticular Metal Organic Framework) series along with Cu-BTC and MIL (Matérial Institut Lavoisier) series are the most widely known and studied. As part of our research objective on adsorption study we chose two members representative of two different families. The adsorbents of our interest are:

(I) Cu-BTC or HKUST-1 (Hong Kong University of Science and Technology)

(II) Cr-BDC or MIL-101 (Matérial Institut Lavoisier)

The main objectives are:

(I) To study the affect of surface area on the adsorption properties of Cu-BTC

(II) To measure adsorption characteristics for variety of gases with different physical properties. The results are analyzed to:

(A) Correlate the adsorption characteristics with properties of gas

(B) Compare adsorption properties of Cu-BTC and Cr-BDC framework

(III) To develop a new technique combined with appropriate thermodynamic formulation for fast characterization of binary adsorption equilibria.

A detailed study of available literature on MOFs' indicate that specific surface area of same MOF synthesized and reported from different laboratories varies widely. This difference which is due to synthesis and post treatment procedures, greatly affects the adsorption properties of these materials. One of the goals of this study was to validate the use of a "scaling-factor" (ratio of amounts adsorbed on different samples) to match isotherms obtained in different laboratories or comparing experimental data with simulation results. Cu-BTC was chosen for this study since it is one of the widely studied MOF with reported values of surface areas varying between ca. 700 to 1500 $m^2 g^{-1}$.

Cu-BTC is widely studied due to its simple synthesis procedure, high loading for CO_2 at moderate pressure (10 bar) and high selectivity for CO_2/CH_4 separation. However, it is thermally unstable above 250°C; it also has poor stability in humid environment. Cr-BDC on the other hand is a MOF first reported by Férey and co-workers in the year 2005. It is stable until 350°C and possesses one of the highest known unit cell volume (ca. 702, 000 $Å^3$) reported till date. It is also known to adsorb exceptionally large amounts of CO_2 at high pressures (> 40 bar). Hence, Cr-BDC was chosen as another representative material for present investigation.

Adsorption of gases *viz.* N_2, O_2, Ar, CO, CO_2, CH_4, SF_6 and C_3H_8 was investigated on these MOFs. As outlined earlier, the choice of gases was based on their differences in physical properties like molecular size, polarizability and electric moments apart from their potential use for industrial applications. Experiments were performed up to pressures of about 10 bar for these gases on both the materials.

In addition, adsorption isotherms up to 100 bar were also measured for three gases *viz.* CO, CO_2 and CH_4 which have almost same kinetic diameter, but varying degrees of electric moments (CH_4 is non-polar, CO_2 has a quadrupole and CO has a dipole moment). It would be interesting to observe their adsorption behaviour over a wide temperature and pressure range on these two frameworks, which are known to have open metal centers that facilitate electrostatic interactions. Moreover, these gases are also important from industrial perspective. Additionally, as will be discussed later, it is necessary to have high pressure pure gas adsorption data for lighter species to be able to model binary adsorption equilibria. As an example, in order to calculate adsorption of a binary mixture of (CO_2+CH_4) on Cu-BTC using IAST (Ideal Adsorbed Solution Theory) at 10 bar , reliable values of pure gas adsorption data for CH_4 are needed to about 90 bar.

Finally, any realistic process development requires estimate / prediction of mixed gas adsorption. While IAST is often used as a tool to achieve this objective, its validity still needs to be tested. Conventional measurement techniques for mixed gas adsorption are time-consuming; in this work we have developed an infinite dilution gas chromatographic technique along with a Virial-Langmuir isotherm model, to obtain binary interaction parameters. The binary parameters obtained can be readily used to make predictions for mixed gas adsorption. The CO_2+CH_4 mixture was chosen for this study because of its importance in various industrial applications.

This thesis is arranged as follows. **Chapter 2** presents a literature review on synthesis and adsorption on metal organic frameworks, adsorption data for several gases of our interest on various adsorbent materials. **Chapter 3** includes theory on adsorption thermodynamics and models for pure and mixed gas adsorption equilibrium. **Chapter 4** presents various physical characterization methods used for characterizing the adsorbents, along with a detailed description and protocol for adsorption equilibrium measurement (gravimetric and gas chromatographic) methods. This chapter also includes a data handling section that describes conversion of experimental measurements to desired results. **Chapter 5** presents discussion on experimental results including adsorption of various gases Cu-BTC, Cr-BDC, comparison of adsorption characteristics of CO, CO_2 and CH_4 on both these frameworks for pressures up to 100 bar followed by infinite dilution gas chromatographic method for binary adsorption equilibria of CO_2+CH_4 on Cu-BTC framework. **Chapter 6** presents conclusions and scope for future research.

CHAPTER 2

Literature Survey

2.1 Metal Organic Frameworks (MOFs)

2.1.1 Introduction

"Metal Organic Frameworks" or MOFs represent a class of novel materials that has caught the attention of researchers owing to their great diversity in structures resulting from co-ordination between inorganic metal atoms/ions and organic ligands as linkers. Proper selection of metal atoms/ions and organic linkers leads to innumerable possibilities in the co-ordination geometry with wide variation in structural architecture. A few very attractive motifs include honeycomb, brickwall, bilayer, ladder, herringbone, diamondoid, rectangular grid, and octahedral geometries **[9-16]**. The inorganic part in a MOF topology invariably (with a few exceptions) consists of first-row transition metals whereas organic links such as cyanide, glutamate, formate, triazole, oxalate, carboxylate, and squarates are well known **[9, 11-23]**. MOFs are crystalline porous solids composed of a 3-D network of metal ions held in place by multidentate organic molecules where the spatial organization of these structural units results to a system of channel and cavities in the nanometer length scale. The 'tunable matrices' or so-called 'tailor made' structures of MOFs has made it possible to design and synthesize materials meeting specific applications.

Although references cited in some review articles highlighted the concept of novel solids was introduced as early as sixties however history of these materials goes dates back (early examples are Hofmann type clathrates, Prussian-Blue type structures, and Werner complexes) but the true interest in this field of synthesizing MOFs generated decades later **[24-25]**. MOF-

5 was reported [26] and published in 1999. The inability of these solids to maintain permanent porosity and avoid structural rearrangements upon guest removal or guest exchange, leading to complete collapse of the framework has an obvious shortcoming initially. MOFs exhibiting permanent porosity have been reported later. In the following paragraphs structural configuration of MOF-5 is been discussed. MOF-5 consists of Zn^{2+} and 1,4-benzenetricarboxylate. Fig. 2.1 shows the structure and topology of MOF-5.

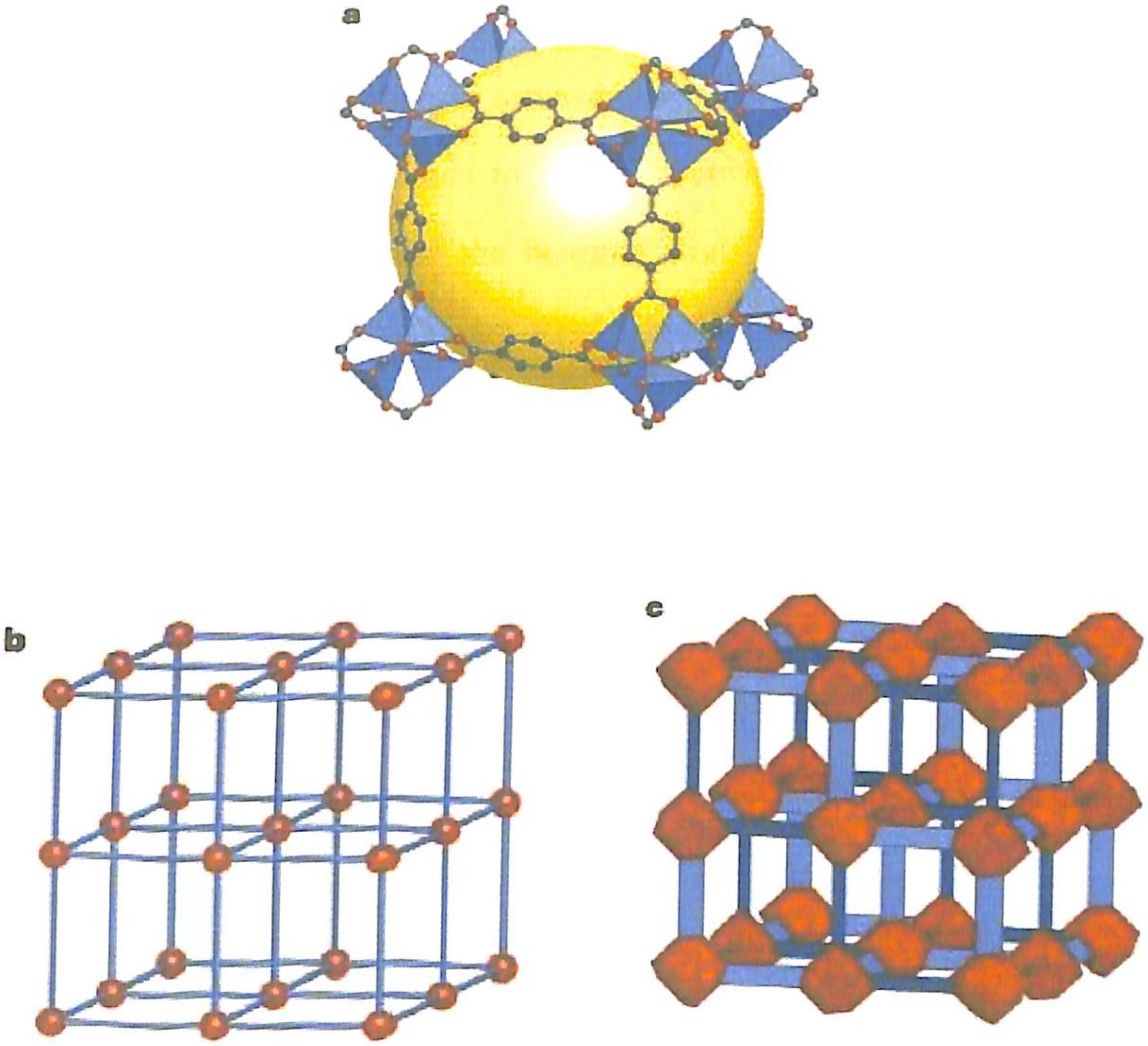

Figure 2.1: MOF-5 structure and topology. (a) The MOF-5 structure shown as ZnO_4 tetrahedra (blue polyhedral) (b) The topology of the structure shown as a ball-and-stick model (c) The structure shown as the envelopes of the (OZn4)O12 cluster (red truncated tetrahedron) and benzene dicarboxylate (BDC) ion (blue slat) **[9]**.

In MOF-5, $Zn_4O(CO_2)_6$ units containing four ZnO_4 tetrahedra with a common vertex and six carboxylate carbon atoms that define an octahedral secondary building unit (SBU) are joined together by benzene links. This leads to a cubic network in which the vertices are the octahedral SBUs and the edges are the benzene struts. In practice, this compound was prepared from Zn(II) and BDC acid under pre-determined conditions to effect the octahedral SBU in situ. Since the SBU and the benzene links are relatively large and rigid entities, the structure produced has exceptional porosity and large micropore volume (larger than any known zeolite). The stability of the said framework is also very high. The exceptional stability of MOF-5 can be understood by comparing its basic network, composed of single atom vertices (Fig. 2.1(b)) with the actual structure of MOF-5 (Fig. 2.1(a)) which has cationic clusters at the vertices. The basic network has no resistance to shear if the links are considered to be universal joints. However, in actual MOF-5 structure, the cationic cluster has a truncated tetrahedral envelop (Fig. 2.1(c)), and the rigidly planar $O_2C\text{-}C_6H_4\text{-}CO_2$ linkers have a planar slat envelop. The linkage of these two groups produces an inherently rigid structure held together by mutually perpendicular hinges.

2.1.2 Strategies for Construction of MOF Structures

The key to successfully designing metal organic frameworks lies in the use of linkers meant to achieve desired network topologies by connecting transition-metal centers or polynuclear clusters serving as nodes of the network. Myriad of different possibilities are there depending on our choice of metal atoms/ions and organic linkers. Flexibility or the rigidity of the frameworks is greatly affected by the choice of organic linker in the structure. To illustrate the complete behavior let us consider the following example **[27]**.

In Fig: 2.2 (A), we have the assembly of a tetrahedrally co-ordinated metal center and a linear organic linker like 4,4′-bipyridine. It results in a structure with an expanded diamond topology. Each bond of the diamond network is replaced by a sequence of bonds that expands the networks and yields void space proportional to the length of the linker. In Fig. 2.2 (B) the organic linker is 1,4-benzene dicarboxylate. It allows for the formation of an aggregate of metal ions into M-O-C clusters that generally referred as secondary building units (SBUs) which finally extends into a cube. A few inferences can be drawn from these observations.

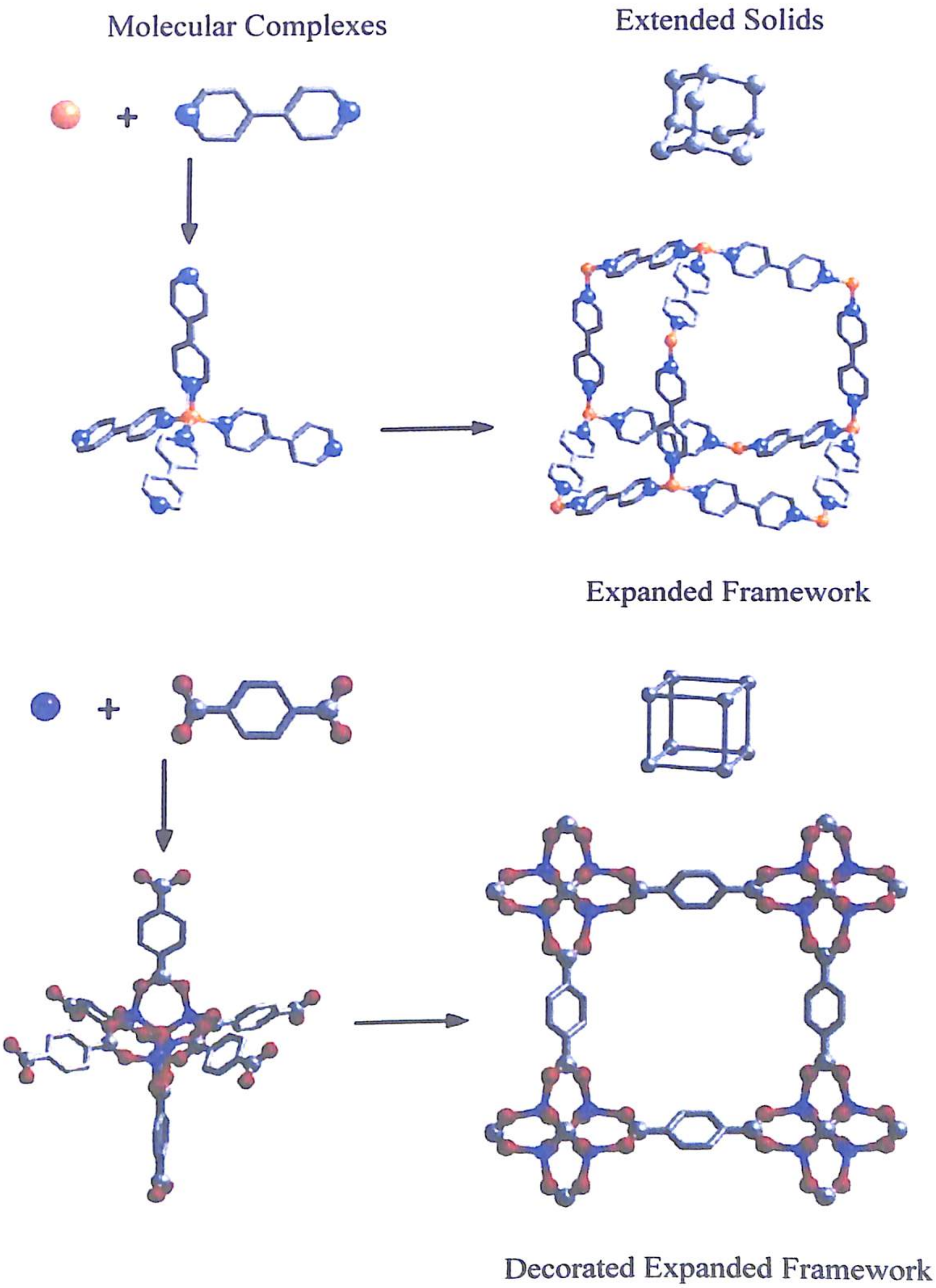

Figure 2.2: Assembly of Metal Organic Frameworks. (A) Flexible metal-bipyridine structures with expanded diamond topology (Metal-orange, Carbon-gray, Nitrogen-blue) (B) Rigid metal-carboxylate clusters expanding into a cube (Metal-purple, Carbon-gray, Oxygen-red). For the sake of clarity all hydrogen atoms are not shown [27].

(A) Aggregated metal ions or clusters in case **B** allow for the formation of a more rigid structure or frameworks since metal ions are locked into their positions by carboxylates whereas in case **A** the framework is having one metal ion at a network vertex. Thus the SBUs serve as large rigid vertices that can be joined by rigid organic links to produce extended frameworks of high structural stability.

(B) The use of long links in case **A** increase the spacing between the vertices yielding a void space proportional to the length of the linker. Although in principle such expanded structures provide large pores but often in practice they are subject to high interpenetration or interweaving leading to low porosity whereas replacement of a vertex by a group of vertices results in open structures without a tendency of interpenetration and optimal pore volume may be achieved.

So, successful synthesis of MOFs depends on the assembling of rigid molecular building blocks into ordered structures held together by strong bonds also known as “Reticular Synthesis”.

Reticular meaning “net-like”, concerns the linking of molecular building blocks into predetermined structures in which such units are repeated and held together by strong bonds. The structural integrity and rigidity of the building blocks remain unaltered throughout the construction process. The chemistry boasts of conceiving of a structure first and then making it in a laboratory. The Cambridge Structure Database (CSD) documents structures of more than 11,000 extended metal organic compounds in which a metal ion or cluster has been linked by an organic moiety where the linking functionality is a cyanide, pyridyl, phosphate or carboxylate. Among them, approximately 3,000 compounds have known to have 3-D structures and about twice that number have 2-D structures. The formation of a particular framework topology is of critical importance since there could be various possibilities for each geometrical shape. As an example, more than 100 different topologies are possible for linking tetrahedral building blocks together into structures with just one kind of vertex and it purely depends on the designer's discretion to select a particular combination. In reticular synthesis, it is essential to establish the exact chemical conditions that will yield specific metal containing (cationic) secondary building unit (SBU) in situ, whereas organic (anionic) SBUs are pre-assembled using organic synthetic methods. For a given cationic SBU, the geometry of the organic unit plays an important role in giving direction to the structure. For example structures of different dimensionality are possible in a combination as explained above viz. a truncated cuboctahedron (0-D), a linear rod (1-D), the square grid (2-D) and network (3-D) [9]

Although variation and robustness of zeolite structures too attracted researchers to expand their range of composition beyond aluminosilicates which finally resulted into synthesizing new framework topologies and in eighties and early nineties saw the introduction of aluminophosphates, metal aluminophosphate zeotypes and many more. But the complexity in synthesis conditions where starting precursors undergo transformations (a subject not yet fully understood) together with significant trial-and-error make the complete process complicated.

Strong bonding is very essential for achieving permanent porosity in metal organic frameworks. If the bonding is weak, inter-network van der Waals interactions play a major role and only non-porous interpenetrated materials result. Thus the major challenge that needs to overcome in MOF synthesis is to ensure minimizing interpenetration sufficiently that will help to open up pores and channels and finally to prevent the collapse of the resulting structures upon pore evacuation. However, it is also been noted that the reduction of pore size by interpenetration of frameworks could also be beneficial in specific cases such as H_2 storage [**28**].Increasing surface areas, access to open metal centres or sites are known key strategies to improve H_2 loading by physisorption on porous MOFs. Catenation (intergrowth of two or more identical frameworks), has been an interesting topic in MOF research and is being explored for increasing H_2 storage capacity on MOFs. It is used as an alternative way to reduce pore sizes in porous MOFs. There were evidences in published articles about the improvement in H_2 loading in catenated structures [**28**]. Catenation actually can take multiple forms *viz.* interpenetration (maximum displacement between frameworks) or interweaving (minimum displacement between frameworks). Interpenetration leads to maximizing the exposed surfaces of catenated frameworks whereas interweaving leads to reinforcement of individual frameworks resulting into improving rigidity and framework stability with an increase in thickening of walls.

Ma et al. [**28**] explained that catenation can increase the overlap of the attractive potential of opposite walls thus enhancing the interaction between hydrogen molecules and the frameworks and the boosted energy fields of the pore walls also increase the number of effective hydrogen binding sites.

2.1.3 Potential Research Areas

Ever since the first successful synthesis of a metal organic framework (MOF-5) there has been a continuous surge in research activities in this field. The concept of reticular design enables 'tailoring' a MOF structure with regular porosity at the nanometer scale. "Tunability' coupled with very high 'surface area' and 'pore volume' made metal organic frameworks a very interesting proposition for research in various fields. MOFs are highly crystalline with very low crystalline framework densities and interestingly most of the pores fall under IUPAC microporous regime i.e. < 2 nm and can be synthesized in very pure form. The salient features and beneficial traits shown by MOFs attracted researchers across the globe to exploit its potentials.

Buoyed by the success of MOF-5, a major focus of the researchers turned onto synthesizing novel materials or frameworks that involves a simple and pragmatic choice of metal atoms and organic linkers as building blocks. Their intriguing features raised enough speculations in different quarters and till date more than 2,000 MOF structures with compositional and architectural diversity have been synthesized, unparalleled by any other class of materials. The most widely studied MOF series since its inception can be grouped as follows:

(I) The Isoreticular Metal Organic Framework or IRMOF series (MOF-5 being also known as IRMOF-1).

(II) Cu-BTC or HKUST-1.

(III) Matérial Institut Lavoisier or MIL series

Although the number speaks volumes about their variation in structural configuration but not all them are stable. Thermal and chemical stability, along with high surface area is what researchers look for in a good material to be effective at the industrial level. Structural aspects of these adsorbents mainly improved synthesis procedures and better activation methods along with gas adsorption studies primarily focusing on H_2 storage had been carried out and cited in different articles. Interesting results on CO_2 and CH_4 adsorptions were reported in various articles. Molecular simulations explaining "host-guest" interactions were explained in detail by various research groups. A thorough review of various research articles identifies the following areas where major research activities are going on:

(I) Adsorptive separation/purification [29-41]

(II) Gas storage [42-56]

(III) Heterogeneous catalysis [57-67]

Apart from these aspects, the potential of MOF materials are also being investigated in areas like non-linear optics, microelectronics and healthcare [68-72].

2.1.3.1 Adsorptive Separation/Purification

Many MOF materials, owing to their tunable structures and uniform pore size distributions have been investigated for studying their effectiveness in adsorptive separation applications. The research works primarily focused on two certain aspects: theoretical and experimental. Experimental studies on pure gas adsorption of various gases on different MOFs have been studied using mechanisms like gravimetric, volumetric and/or gas chromatography at widely different conditions of pressure and temperature. Equilibrium adsorption isotherms from pure component study give valuable information on adsorbate-adsorbent interaction and hence on separation factor. Binary or mixed adsorption experimental data on MOFs are very scarce and most of the data reported in articles till date concentrates on Ideal Adsorption Solution Theory or IAST model to predict binary adsorption behavior for a particular gas mixture from their pure component study. Extensive theoretical investigations have been carried out on adsorption and diffusion of gases or gas mixtures in MOFs using quantum chemical calculations or molecular simulations. Molecular Dynamics (MD) simulations, Grand Canonical Monte Carlo (GCMC) simulations are well known molecular simulation techniques to study adsorption behavior. Table 2.1 gives an illustrative documentation of some works done or undertaken in adsorptive separation applications on MOFs.

Table 2.1: Details of adsorptive separation studies on MOFs carried out by various researchers

MOF	Researcher	Work done (Theoretical/ Experimental)	Ref
IRMOF	Sarkisov et al.	Used molecular dynamics (MD) to examine the self diffusion of methane, n-pentane, n-hexane, cyclohexane, n-heptane in MOF-5 or IRMOF-1 at low loadings	[29]
	Skoulidas et al.	Molecular dynamics approach to probe self diffusion and transport diffusion of small gas species in several MOFs as a function of pore loading at room temperature	[30]
	Dürren et al.	Investigated the adsorption of methane in a series of isoreticular MOFs or IRMOFs synthesized by Yaghi et al. and compared them with other porous materials *viz.* zeolites, carbon nanotubes using GCMC simulations	[31]
	Kawakami et al.	Studied adsorption of N_2, CO_2, Ar, H_2 and O_2 on Zn(BDC) using GCMC and compared simulation results with experimental data generated by Li et al.	[32]
	Eddaoudi et al.	Reported adsorption isotherms for Ar, N_2, CCl_4, $CHCl_3$, C_6H_6 and cyclohexane in IRMOF-1	[33]
	Huang et al.	Studied separation between p-xylene and o-xylene in a variant of IRMOF-1	[34]
	Liu et al.	Carried out comparative molecular simulation study of CO_2/N_2 and CH_4/N_2 separation in zeolites and MOFs	[35]
	Keskin et al.	Studied membrane based CH_4/CO_2 separation	[36]

MOF	Researcher	Work done (Theoretical/ Experimental)	Ref
Cu-BTC	Krungleviciute et al.	Provided experimental evidence that Ar enters the octahedral cages of Cu-BTC but not CCl_4	[37]
	Vishnyakov et al.	Reported first molecular structural model and described the preferential adsorption sites for Ar at low temperature using GCMC simulation	[38]
	Wang et al.	Improved the already existing process for large scale production of Cu-BTC and carried out adsorptive separation experiments of some common gases *viz.* N_2, O_2, CO, CO_2, CH_4, N_2O, C_2H_4 and C_2H_6.	[39]
	Wang et al.	Systematic simulation study on adsorption separation of gas mixtures *viz.* CO_2/CO, C_2H_4/CO_2 and C_2H_4/C_2H_6	[40]
	Yang et al.	Studied $CO_2/N_2/O_2$ mixture adsorption in MOFs using molecular simulation	[41]

2.1.3.2 Gas Storage

Storage of gases in porous adsorbents is new traits that are gaining grounds in the field of adsorption study for various applications. It is a long time since scientists and researchers have been looking for an alternate source energy that can replace fossil fuels since their reserve is decreasing at an alarming rate. Molecular H_2 is targeted to a more viable option. Automobile sector is a major consumer of energy and with the advancement of fuel cell technology, direct on-board use of hydrogen in vehicular transportation is a real possibility. The difficulty lies in the storage of H_2, which would be safe and economical. Conventional storage mechanisms like high pressure (compression) storage, cryogenic storage or even storage in metal hydrides are found lacking in certain aspects, be in terms of cost, safety or kinetics. Storage of H_2 in porous adsorbents is a subject that is gaining importance in the recent past. Ever since the development of highly porous metal organic frameworks (MOFs) a major focus is shifted towards its ability to store hydrogen. An outstanding property of MOFs that has prompted their study as hydrogen storage candidate is their large apparent surface area and pore volume. Although literature is crowded with research articles on H_2 storage on MOFs but the results are far from encouraging (with a few exceptions) and a disparity between results are conspicuous. The H_2 adsorption capacity on MOFs is falling short of U.S. Department of Energy (DOE) targets. The 2010 energy density targets for hydrogen storage system (including container and necessary components) are 7.2 MJ kg^{-1} and 5.4 MJ L^{-1}, which translates as 6.0 wt% and 45 kg H_2 per m^3 **[73]**.

Methane is the major component of natural gas with a high heat of combustion. It is abundant compared to conventional fossil fuels and emits least amount of CO_2 per unit of heat produced. Methane, mostly in vehicular transportation is used as compressed natural gas (CNG) and in few cases as liquefied natural gas (LNG). Liquefied natural gas or LNG offers a comparable energy density to that of petrol or diesel but its storage, requiring expensive cryogenic tanks together with boil-off losses has prevented its widespread commercial applications. CNG mode of storage on the other hand requires pressure as high as 200 bar in pressure vessels. The whole process is costly since it requires expensive multistage compression. The concept of adsorbed natural gas (ANG) where the gas is stored as an adsorbed phase in a porous solid can be a viable alternative to CNG. To promote the vehicular application of methane, the U.S. Department of Energy (DOE) has set target for methane storage at 180 v(STP)/v(standard temperature and pressure equivalent volume of methane per volume of the adsorbed material) under 35 bar, near ambient temperature, with the energy density of ANG being comparable to that of CNG used in current practice **[45]**.

MOFs owing to their extraordinary surface area and pore volume are fast becoming a material to reckon with in this field.

The importance of CO_2 capture is by far the most important subject concerning the environment and need no introduction when it comes to the matter of pollution and global warming. Separation of CO_2 from its mixture coming out of various sources is a major consideration at the industrial level. Aqueous amine solutions are used most widely to absorb and capture CO_2. Problems arising out of corrosion and solvent regeneration are two major hurdles to overcome in a conventional "amine-based" process. On the other hand pressure swing adsorption (PSA) technology using porous adsorbents as a tool is a very good alternative. Many research efforts are going on to identify and develop suitable materials having high affinity towards CO_2 showing good capacity and selectivity as well.

Based on many research and review articles published, we tried to summarize some of the works, mostly experimental in a tabular form (Table 2.2). The contents of the table focus on and show how fast MOFs are becoming a major research area in gas storage applications.

Table 2.2: Literature Review of Adsorption on MOFs **(A)** CH_4 and CO_2 adsorption **(B)** Hydrogen adsorption

(A)

Researcher	**Material**	**Gas**	**Work done (Theoretical/ Experimental)**	**Ref**
Eddaoudi et al.	MOF-5, IRMOF-6	CH_4	Showed good capacity at room temperature.	[42]
Bourrelly et al.	MIL-53, 47	CH_4, CO_2	Explained differences in adsorption mechanism where CO_2 adsorption on MIL-53 shows "breathing-effect".	[43]
Millward et al.	MOF-2, MOF-505, MOF-74, HKUST-1, IRMOF-1,3,6,11, MOF-174	CO_2	Provided ample data to show MOFs to the most effective adsorbent to capture CO_2 than any known conventional adsorbents	[44]
Senkovska et al.	HKUST-1, MIL-101, $Zn_2(bdc)_2dabco$	CH_4	Studied high pressure adsorption and concluded HKUST-1 to be the most promising adsorbent	[45]
Llewellyn et al.	MIL-100, 101	CH_4, CO_2	Reported highest uptake for CO_2 on MIL-101 (better activated sample) so far with significant for CH_4 as well.	[46]

(B)

Researcher	Material	Work done (Theoretical/ Experimental)	Ref
Rosi et al.	MOF-5	Adsorbed H_2 up to 4.5 wt% at 78 K and 1% at room temperature and pressure of 20 bar.	[47]
Rowsell et al.	IRMOF-1,8,11,18 & MOF-177	All the measurements were carried out at 77 K and up to atmospheric pressure and H_2 uptake were found to be 13.2, 15.0, 16.2, 8.9 and 12.5 mg g^{-1} respectively.	[48]
Wong-Foy et al.	IRMOF-1,6,11,20 MOF-177,74 HKUST-1	The measurements were carried out at 77 K and pressure up to 90 bar. The saturation capacity varied widely for each MOF.	[49]
Pan et al.	MMOM	Adsorbed up to 1wt% at room temperature and pressure approximately 48 atm.	[50]
Férey et al.	MIL-53	3.2 wt% (Cr^{3+} based) and 3.8 wt% (Al^{3+} based) at 77 K and pressure under 1.6 MPa.	[51]
Latroche et al.	MIL-100, 101	At room temperature capacity was 0.15 wt% with pressure below 7.33 MPa, but at 77 K it goes up to 3.28 wt% at pressure below 2.65 MPa (for MIL-100) whereas for MIL-101 the capacity was as high as 6.1 wt% at 77 K.	[52]

Contd…

Researcher	**Material**	**Work done (Theoretical/ Experimental)**	**Ref**
Li et al.	MOF-5, IRMOF-8	Demonstrated the concept of dissociation/spillover in hydrogen storage which enhanced the capacity significantly	[53, 54]
Li et al.	HKUST-1, MIL-101	Showed at 77 K and at low pressure HKUST is more effective whereas at room temperature and high pressure MIL-101 is having more capacity.	[55]
Panella et al.	HKUST-1, MOF-5	Compared the adsorption capacity between these two different MOFs. At 77 K and at high pressures MOF-5 stores more H_2 whereas at low pressures Cu-BTC shows more promises	[56]

From the above table, we can summarize that till date MOF-177 is reported to show highest hydrogen adsorption capacity. Wong-Foy et al. **[49]** reported H_2 loading as high as 7.5 wt% on MOF-177 at 77 K and 70 bar pressure. The corresponding Langmuir surface area was measured to be ~4500 m^2 g^{-1}, although a few more research papers published by the same group reported higher Langmuir surface area (~ 5640 m^2 g^{-1}). At ambient condition the reported H_2 uptake decreased quite substantially as reported by another research group **[52]**. They measured a Langmuir surface area of ~ 4300 m^2g^{-1} and the corresponding H_2 loading was 0.62 wt% at 298 K and 100 bar pressure.

2.1.3.3 Catalysis

Unlike adsorptive separation or gas storage like applications, limited work is done on MOFs being used as catalysts. Despite elevated metal content of MOFs, their use in catalysis is largely hampered by the relatively low stability to thermal treatments, varying chemical environments and moisture. The organic linker of the structure is generally gets affected first. Additionally, organic linkers tend to block the coordination sphere of the metal ions making it non-accessible to the reactants. However, with the publication of MOFs with accessible metal sites by various research groups have opened their possibility to be used in several catalytic applications. The research in this area is growing fast as is evidenced from number of publications **[57-67]**.

2.2 Cu-BTC or HKUST-1 Framework

Cu-BTC [$Cu_3(BTC)_2$, BTC = 1,3,5-benzenetricarboxylate] also known as HKUST-1 is a widely studied MOF. It was first reported by Chui et al. **[74]** in 1999. In this framework, two octahedrally co-ordinated Cu atoms are connected to eight oxygen atoms of tetracarboxylate units to form a dimeric Cu paddle wheel. Each BTC ligand holds three dimeric Cu paddle wheels to form a microporous open framework with face-centered cubic symmetry.

Cu-BTC has a 3-D channel structure connecting a system of tetrahedral-shaped cages accessible through small windows (ca. 3.5 Å in diameter). The large cavities are connected through square-shaped windows with a diameter of ca. 9 Å. Fig. 2.3 shows the structure schematically.

The importance of Cu-BTC can be gauged from the fact that ever since Chui and his colleagues reported this co-ordination polymer, there was a growing interest generated in the following years leading to the improvisation of the synthesis methods and better activation procedures resulting into more stable and highly porous solids. Research in various areas *viz.* gas separation, storage and catalysis has been going on presently. It won't be an exaggeration to mention that Cu-BTC turns out to be one of the most sought after adsorbent at the research level.

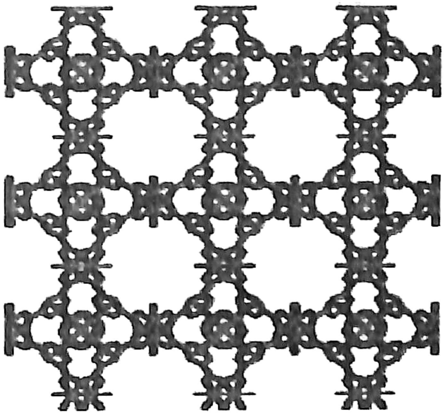

Figure 2.3: Schematic for $Cu_3(BTC)_2(H_2O)_3$ (BTC= 1,3,5-benzenetricarboxylate) metal organic framework. In this figure Cu-Green, O-Red, C-Gray). For the sake of clarity all hydrogen atoms are not shown [37, 74].

2.3 Cr-BDC or MIL-101 Framework

Cr-BDC [BDC = 1,4-benzenedicarboxylate] framework or MIL-101 (an acronym for Matérial Institut Lavoisier) is a recent addition to the ever increasing list of metal organic frameworks. Férey et al. [75] first synthesized and reported this chromium-terephthalate based solid. The synthesized product showed a very high specific surface area and pore volume. They reported MIL-101 to be very stable for months under ambient atmosphere. The structure remains stable at high temperature (up to 473 K) and in presence of different organic solvents. These properties make MIL-101 an attractive candidate for adsorption study of various gases.

MIL-101, the hybrid solid is synthesized from carboxylate moieties (benzene-1,4-dicarboxylate or bdc) and trimeric chromium(III) octahedral clusters having removable terminal water molecules and therefore provide potential unsaturated metal sites in the structure. The resulting zeotype architecture as shown in Fig. 2.4 are built by the connection of large hybrid supertetrahedra which further assemble to form very large mesopores. The cell volume for MIL-101 is ca. 702, 000 Å^3. Removal of guests results into an accessible diameter of size ~29 Å and 34 Å.

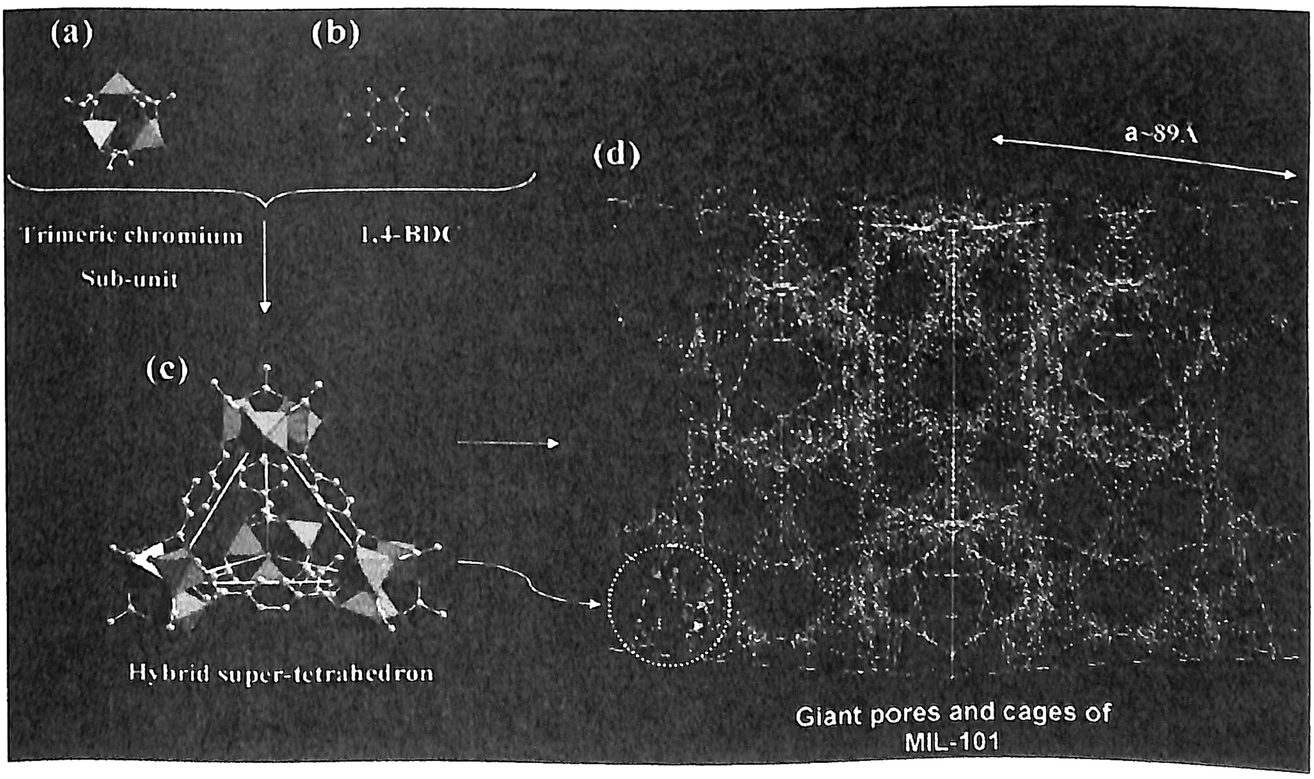

Figure 2.4: Schematic for Cr-BDC or MIL-101 Framework (a) Inorganic trimer (b) Benzene-1,4-dicarboxylic acid (bdc) (c) Supertetrahedra made from the linkage of inorganic trimers and bdc (d) Schematic view of MIL-101 structure [75-76].

2.4 Review of Adsorption of the Gases of our Interest

In the preceding paragraph, H_2 together with CO_2 and CH_4 are found to be the major thrust areas when it comes to the gas adsorption study on various MOF surfaces. But to effectively study the nature of gas adsorption and to finding out the adsorption parameters, it is always pragmatic to widen the scope of the study to various other gas molecules (which can be used as probes) depending on their physical properties.

The choice of various gases for our experimental study includes Ar, N_2, O_2, CO_2, CH_4, CO, C_3H_8 and SF_6. A detailed literature review on adsorption study of each of these gases on different adsorbent surfaces by various researchers is given below in Tables 2.3 through 2.10. Judiciously interpolation was done wherever necessary for sake of easier comparison.

Table 2.3: Literature review of Ar adsorption on various adsorbents

Adsorbent	Pressure	Temperature	Loading	Isosteric Heat	$-\Delta h_{ads,0}$ (kJ mol^{-1})	Henry constant / β (mmol g^{-1} bar^{-1})	Ref
	P / (bar)	T / K	N / mmol g^{-1}	$-\Delta h_{ads}$ / (kJ mol^{-1})			
13X	25, 50, 100	298	1.5, 2.12, 2.5				[77]
	12.5, 100	288	0.9, 2.5	11-8	10.94		[78]
4A	70	298	1.86				[77]
5A	84	298	2.46				[77]
AC (AS)	5, 12.5	288	0.85, 1.8	11.9-9.2	11.8		[78]
AC (BPL)	1.4, 6.06, 37.3	303	0.39, 1.16, 3.6				[79]
AC (Centaur)	1.72, 5.38, 37.4	303	0.39, 0.94, 3.3				[79]
AC (WS42)	1.41, 6.33, 37.2	303	0.34, 1.21, 4.0				[79]
CMS1	1.74, 5.52, 37.5	303	0.37, 0.84, 2.1				[79]
Cu-BTC	5, 10	298	1.25, 2.13				[80]
NaETS-4	1.07	288	0.12	20			[81]
NaX	0.97	304	0.2		12.7		[82]
		304.12			12.7		[83]
Na-ZSM-5	1.09	296.2	0.25	18-16	18		[82]
Silicalite	1.20, 4.14, 7.3	305.75	0.19, 0.57, 0.9			0.17	[84]
	0.8	305.75	0.14		15.8		[85]
ZSM-5		305.75			15.8		[83]

Table 2.4: Literature review of N_2 adsorption on various adsorbents

Adsorbent	Pressure	Temperature	Loading	Isosteric Heat	$-\Delta h_{ads,0}$ (kJ mol^{-1})	Henry constant / β (mmol g^{-1} bar^{-1})	Ref
	P / (bar)	T / K	N / mmol g^{-1}	$-\Delta h_{ads}$ / (kJ mol^{-1})			
13X	66	298	2.95				[77]
	12, 100	288	1.2, 2.5	14-9.1	13.91		[78]
	4, 12	298	0.8, 2				[86]
4A	100	298	2.24			0.7	[77]
5A	1, 4.7	293	0.58, 1.58				[87]
	1.21, 6.4, 17.4	296	0.7, 1.71, 2.4				[88]
	96	298	2.58				[77]
AC	3.9, 10.2, 95	303	0.82, 1.59, 3.3				[89]
AC (AS)	5, 12.5	288	0.85, 1.3	12-9.2	11.95		[78]
AC(BPL)	1.59, 5.14, 37.5	303	0.41, 0.96, 3.0				[79]
AC (Centaur)	1.36, 5.86, 37.3	303	0.35, 0.98, 3.0				[79]
AC (Norit R1)	1.11, 4.99, 59.8	298	0.39, 1.27, 4.1			0.4	[90]
AC (WS42)	1.37, 5.82, 37.4	303	0.43, 1.28, 3.8				[79]
CaA	1.12	308	0.67	30-20			[91]
Cu-BTC	5, 10	298	1.61, 2.32				[80]
	1	295	0.31				[92]
	4, 12	298	1, 1.8				[86]
		300		4.5			[93]
	1	295	0.25			0.31	[39]

Adsorbent	Pressure	Temperature	Loading	Isosteric Heat	$-\Delta h_{ads,0}$ (kJ mol^{-1})	Henry constant / β (mmol g^{-1} bar^{-1})	Ref
	P / (bar)	T / K	N / mmol g^{-1}	$-\Delta h_{ads}$ / (kJ mol^{-1})			
IRMOF-1		300			6.8		[93]
IRMOF-3		300			5.8		[93]
MOF-177	1.01	298	0.1				[94]
MS (CMS1)	1.35, 5.9, 37.4	303	0.34, 0.82, 1.9				[79]
NaETS-4	1.07	288	0.25	21.3			[81]
NaX	1.11	305.5	0.4	20-18	19.9		[82]
		305.62			19.9		[83]
Na-ZSM-5	1.13	294.9	0.4	24-19.5	24.1		[82]
Silicalite	1.19, 4.09, 7.1	304.9	0.2, 0.56, 0.8	15.07		0.18	[84]
	1, 4.7	313	0.25, 0.7				[95]
	0.93	295.95	0.2	17.5-18	17.6		[85]
	1.01, 4.56	313	0.2, 0.72				[96]
H-ZSM-5	1.07	294.3	0.25	20.7-16.5	20.7		[82]

Table 2.5: Literature review of O_2 adsorption on various adsorbents

Adsorbent	Pressure	Temperature	Loading	Isosteric Heat	$-\Delta h_{ads,0}$ (kJ mol^{-1})	Henry constant / β (mmol g^{-1} bar^{-1})	Ref
	P / (bar)	T / K	N / mmol g^{-1}	$-\Delta h_{ads}$ / (kJ mol^{-1})			
5A	1, 4.4	293	0.17, 0.69			0.18	[87]
	0.96, 5.34, 17.7	296	0.18, 0.83, 1.8				[88]
AC (BPL)	1.6, 5.05, 37.4	303	0.42, 0.99, 3.4				[79]
AC (Centaur)	1.81, 6.67, 37.2	303	0.43, 1.16, 3.2				[79]
AC (WS42)	1.84, 6.21, 37.4	303	0.44, 1.29, 4.3				[79]
CaA	1.06	308	0.22	19-16			[91]
Cu-BTC	1	295	0.25				[91]
	1, 2	298	0.5, 0.85				[86]
	1	295	0.2			0.21	[39]
MOF-178	1.01	298	0.17				[94]
MS (CMS1)	1.67, 5.03, 37.4	303	0.37, 0.81, 2.2				[79]
NaETS-4	1.07	288	0.16	24.5			[81]
NaX	1	306.1	0.2		15		[82]
Silicalite	1	305.3	0.15		16.3		[85]

Table 2.6: Literature review of CO_2 adsorption on various adsorbents

Adsorbent	Pressure	Temperature	Loading	Isosteric Heat	$-\Delta h_{ads,0}$ (kJ mol^{-1})	Henry constant / β (mmol g^{-1} bar^{-1})	Ref
	P / (bar)	T / K	N / mmol g^{-1}	$-\Delta h_{ads}$ / (kJ mol^{-1})			
13X	4, 12	298	6.0, 7.0				[86]
5A	1.2, 5.2, 10	303	3.07, 3.5, 3.6	19.64			[97]
AC (Norit R1)	0.99, 4.97, 49.9	298	2.23, 5.65, 10			4.74	[90]
AC (Norit)	38	313	0.24				[98]
MIL-53 (Al)	5, 10, 25	304	3.3, 8.2, 10.4	35-17			[43]
MIL-53 (Cr)	5, 10, 25	304	3.3, 8.0, 10	35-17			[43]
Cu-BTC	4, 12	298	10, 12.5				[86]
	0.97	313	1.6		14.5		[93]
Cu-BTC (sample b)	0.9	295	4.7			6.24	[39]
Cu-BTC (sample c)	10, 17.5	298	7.4, 8.0				[39]
H-Mordenite	1.01, 1.39	303	2.2, 2.38				[99]
H-ZSM-5	1.03	296.9	1.9	38-27	38		[82]
IRMOF-1		300			14.5		[93]
	0.8	298	0.57				[100]
IRMOF-3	1.03	313	1.25		19.5		[93]
	1	298	0.91				[100]
MIL-100	10, 60	303	9, 18.5	63-20	62		[46]
MIL-101 (Sample a)	10, 34	303	9, 25	32-18			[46]

Adsorbent	Pressure	Temperature	Loading	Isosteric Heat	$-\Delta h_{ads,0}$ (kJ mol^{-1})	Henry constant / β (mmol g^{-1} bar^{-1})	Ref
	P / (bar)	T / K	N / mmol g^{-1}	$-\Delta h_{ads}$ / (kJ mol^{-1})			
MIL-101 (sample b)	10, 60	303	12, 32	32-18			[46]
MIL-101 (sample c)	10, 40	303	14.5, 34.8	45-25	44		[46]
MIL-47	5, 10, 20	304	6.3, 8.8, 11.4	25-20			[43]
	1	298	1.59				[100]
MOF-177	1	298	0.68				[100]
MOF-5	1.01	296	2.1				[101]
NaETS-4	1.07	288	3.26	67			[81]
NaX	0.29	304.4	4.6	49-36	49.1		[82]
	0.69	305.8	5.4				[82]
	1.19	312	4.64	50-31			[91]
	1	293	6	47-35	47		[102]
		293.15			48		[83]
Na-ZSM-5	0.72	297.1	1.9	50-29	50		[82]
Silicalite	0.79, 8.63, 17	304.4	1.31, 2.8, 3	24.065		3.85	[84]
	1.04, 5.17, 20.4	307.8	1.45, 2.5, 3	28			[103]
	1, 4.5	313	1.45, 2.4				[95]
	0.8	303.6	1.5	27-28	27.2		[85]
ZIF-8	0.9	298	0.8				[100]

Table 2.7: Literature review of CH_4 adsorption on various adsorbents

Adsorbent	Pressure	Temperature	Loading	Isosteric Heat	$-\Delta h_{ads,0}$ (kJ mol^{-1})	Henry constant / β (mmol g^{-1} bar^{-1})	Ref
	P / (bar)	T / K	N / mmol g^{-1}	$-\Delta h_{a,k}$ / (kJ mol^{-1})			
13X	25, 50, 89	298	2.84, 3.1, 3.1				[77]
	5, 25, 50	288	1.9, 3, 3.2	17-7	17.53		[78]
	4, 12	298	1.6, 3.6				[86]
4A	92	298	1.56				[77]
5A	84	298	2.91				[77]
5A	1.2, 5.2, 10	303	0.77, 1.46, 1.8	12.97			[97]
AC	5.4, 10.8, 89.7	303	2.4, 3.36, 5				[89]
AC (AS)	5	288	1.6	14.4-7.8	14.35		[78]
AC (BPL)	2.99, 6.52, 37.4	303	1.75, 2.63, 5.1				[79]
AC (Centaur)	2.9, 6.32, 37.3	303	1.75, 2.63, 5.1				[79]
AC (Norit R1)	1.01, 5.04, 57.5	298	1.08, 2.89, 6.4			1.72	[90]
AC (WS42)	2.85, 6.14, 37.3	303	1.82, 2.87, 6.2				[79]
MIL-53 (Al)	5, 10, 25	304	2.2, 3.7, 6.0	17			[43]
BaY	1.07, 5.53, 56	298	0.65, 1.83, 3.9				[104]
CaY	0.96, 6.28, 52.9	298	0.57, 1.95, 4.6				[104]
MIL-53 (Cr)	5, 10, 25	304	2, 3.7, 5.8				[43]
Cu-BTC	6.25, 50, 100	303	5.63, 9.38, 9.5				[45]
	0.94	295	0.92				[105]
	1	295	0.6				[92]
	10, 50	298	5.35, 9.59				[106]

Adsorbent	Pressure	Temperature	Loading	Isosteric Heat	$-\Delta h_{ads,0}$ (kJ mol^{-1})	Henry constant / β (mmol g^{-1} bar^{-1})	Ref
	P / (bar)	T / K	N / mmol g^{-1}	$-\Delta h_{ads}$ / (kJ mol^{-1})			
Cu-BTC	4, 12	298	2.3, 4				[86]
		300			12.5		[93]
Cu-BTC (sample b)	0.9	295	0.8			1.14	[39]
IRMOF-1		300			9.5		[93]
IRMOF-14	10, 50	298	3.57, 12.72				[106]
IRMOF-3		300			12.5		[93]
MCM-41	5, 10, 30	303.15	0.5, 0.95, 2.3				[107]
MgY	0.96, 5.47, 59	298	0.4, 1.69, 4.5				[104]
MIL-100	10, 60	303	3, 9.5	20-9	19	480	[46]
MIL-101	6.25, 50, 100	303	2.5, 7.19, 8.6				[45]
MIL-101 (Sample a)	10, 34, 80	303	3.7, 10, 14.5	18-10			[46]
MIL-101 (Sample b)	10	303	3.7	18-10			[46]
MIL-101 (Sample c)	10	303	3.7	18-10	18	580	[46]
MS (CMS1)	3.09, 4.94, 37.5	303	1.26, 1.52, 2.5				[79]
NaETS-4	1.07	288	0.54	29.3			[81]
NaX	0.93	304.3	0.60	19.2-19.8	19.2		[82]
		304.41			19.2		[83]
NaY	1.24, 6.14, 60.4	298	0.31, 1.59, 4.1				[104]

Adsorbent	Pressure	Temperature	Loading	Isosteric Heat	$-\Delta h_{ads,0}$ (kJ mol^{-1})	Henry constant / β (mmol g^{-1} bar^{-1})	Ref
	P / (bar)	T / K	N / mmol g^{-1}	$-\Delta h_{ads}$ / (kJ mol^{-1})			
Na-ZSM-5	0.83	296.3	0.7	26.5-22.5	26.5		[82]
Silicalite	1.04, 4.14, 7.4	304	0.59, 1.37, 1.7	18.649		0.71	[84]
	1.17, 7.4	342.6	0.31, 1.2				[84]
	1.39, 5.19, 20.6	307.8	0.69, 1.49, 2.3		20		[103]
	0.93	296.07	0.65	21-21.5	20.9		[85]
	1	297	0.70	21	21		[102]
	1.01, 4.86	313	0.55, 1.5				[96]
SrY	1.1, 4.86, 53.2	298	0.6, 1.66, 4.2				[104]
Zn-dabco	6.25, 50, 100	303	3.75, 8.44, 8.8				[45]
ZSM-22		309			27.2		[83]
ZSM-5		297.15			21.0		[83]

Table 2.8: Literature review of C_3H_8 adsorption on various adsorbents

Adsorbent	Pressure	Temperature	Loading	Isosteric Heat	$-\Delta h_{ads,0}$ (kJ mol^{-1})	Henry constant / β (mmol g^{-1} bar^{-1})	Ref
	P / (bar)	T / K	N / mmol g^{-1}	$-\Delta h_{ads}$ / (kJ mol^{-1})			
Activated carbon	1.81, 5.73, 9.8	303	4.78, 5.42, 6.0				[89]
Cu-BTC	1	283	6.2				[92]
	1	318	3.0				[92]
H-Mordenite	1.16, 2.07	303	1.14, 1.24				[99]
NaX	1	293	3.4				[102]
		293.15			34.4		[83]
Silicalite	1.08, 5.56	307.8	1.95, 2.03		40.0		[103]
ZSM-5		309.45			41.0		[83]

Table 2.9: Literature review of CO adsorption on various adsorbents

Adsorbent	Pressure	Temperature	Loading	Isosteric Heat	$-\Delta h_{ads,0}$ (kJ mol^{-1})	Henry constant / β (mmol g^{-1} bar^{-1})	Ref
	P / (bar)	T / K	N / mmol g^{-1}	$-\Delta h_{ads}$ / (kJ mol^{-1})			
5A	1.2, 5.2, 10	303	1.03, 1.81, 2.1	13.18			[97]
Cu-BTC (sample b)	1	295	0.8			1.27	[39]
Silicalite	1.18, 4.1, 7.3	305.3	0.27, 0.72, 1.0	16.656		0.26	[84]
	1.23, 4.07, 7.4	341.4	0.14, 0.41, 0.7				[84]

Table 2.10: Literature review of SF_6 adsorption on various adsorbents

Adsorbent	Pressure	Temperature	Loading	Isosteric Heat	$-\Delta h_{ads,0}$ (kJ mol^{-1})	Henry constant / β (mmol g^{-1} bar^{-1})	Ref
	P / (bar)	T / K	N / mmol g^{-1}	$-\Delta h_{ads}$ / (kJ mol^{-1})			
Alumina	1.01	305	0.2	20.93		0.17	[108]
BPL Carbon	0.81	305	2.25	8.5-7		17.76	[108]
H-ZSM-5	0.19	294.7	1.4	35-38	35.2		[82]
NaX	0.67	304.6	2.2	28-38	28.2		[82]
	0.51	305	1.55	29.302		14.01	[108]
	0.65	295	2.5	28-40	28		[102]
		295.45			28.4		[83]
Na-ZSM-5	0.33	295.2	1.65	42-40	42		[82]
PCB Carbon	0.51	305	2.5	9.5-8		45.4	[108]
Silicalite	1.22	305	1.35	39.348		17.27	[108]
	1.38, 5.49	307.8	1.88, 1.99		35.0		[103]
	0.13	304.79	1.3	34.5-34	34.4		[85]
	1	298	1.9	36-40	36		[102]
ZSM-5		298.15			35.9		[83]

CHAPTER 3

Theory

3.1 Phase Rule

The two phases in equilibrium are the bulk gas and the adsorbed phase with their own sets of intensive properties. By definition equilibrium means equality of

[a] Thermal potential (or temperature)

[b] Mechanical potential (or pressure)

[c] Mass potential (or chemical potential)

The equality of thermal potential is obvious as in that both phases must be at the same temperature, otherwise, heat exchange would occur and the system will no longer be in equilibrium. Equality of chemical potentials of each species in the two phases at equilibrium assures no net mass transfer.

The problem arises when we try to equate the mechanical potentials. Thermodynamically the adsorbed phase is two-dimensional and pressure as an intensive variable is meaningless. Pressure and its corresponding extensive variable volume are not appropriate coordinates for the work term in two-dimensional adsorbed phase **[109]**. An intensive variable called spreading pressure is defined for the adsorbed phase to fix its state **[110]**. Its units are N m^{-1} i.e. same as that of surface tension. The corresponding extensive variable is the molar area, a, which is the area of the solid per mole of adsorbed gas. The mechanical work term for the adsorbed phase per mole of solid is thus ($\pi . a$), analogous to ($P.V$) in the bulk phase.

Since it is customary to express the amount adsorbed N, based on unit mass of the adsorbent, the area is also expressed on the same basis as specific area $A = N.a$ and has the units of $m^2\ kg^{-1}$.

Due to the extra intensive variable caused by lack of mechanical equilibrium, the phase rule **[111]** for adsorption becomes

$$F = C - \chi + 3 \tag{3.1}$$

Where, F = number of degrees of freedom

C = number of chemical species and

χ = number of phases

Thus, there is one extra degree of freedom in the surface phase equilibria compared to the bulk-phase equilibria.

3.2 Fundamental Property Relations

The following fundamental properties are written for the adsorbed phase. In this treatment the solid is considered neither a component nor a phase. The fundamental property relation for adsorbed phase is **[112-113]**

$$d(N.u) = T.d(N.s) - \pi.d(N.a) + \sum \mu_i.dN_i \tag{3.2}$$

Or, $$du = T.ds - \pi.da + \sum \mu_i.dx_i \tag{3.3}$$

where, N is the total number of moles adsorbed per unit mass of the adsorbent, u is the molar internal energy, T is the temperature, s is the molar entropy, π is the spreading pressure, a is the area of adsorbent per unit mass per number of moles adsorbed (N), μ_i is the chemical potential of a component i and N_i is the number of moles of component i adsorbed per unit mass of the adsorbent. In Eq. (3.3) x_i is the mole fraction of the component of i in the adsorbed phase. It is obvious from this equation the thermodynamic variable π (spreading pressure) is defined by the equation

$$\pi = -\left(\frac{\partial u}{\partial a}\right)_{s,x_i} \tag{3.4}$$

The molar enthalpy h for the adsorbed phase is given by,

$$h = u + \pi.a \tag{3.5}$$

Resulting in the following equation from Eq. (3.3)

$$dh = T.ds + a.d\pi + \sum \mu_i.dx_i \tag{3.6}$$

Using the usual Legendre transformations, the molar Gibbs free energy g of the adsorbed phase can be written as

$$dg = -s.dT + a.d\pi + \sum \mu_i.dx_i \tag{3.7}$$

3.3 Phase Equilibrium Relations

In the following equations, the super-script g denotes the bulk gas phase and all other variables refer to the adsorbed phase. The variables x_i and y_i denote the adsorbed phase and the gas phase compositions, respectively. The phase equilibrium relation given by the equality of chemical potentials in both phases is

$$\mu_i^g = \mu_i \qquad \text{Or} \qquad d\mu_i^g = d\mu_i \tag{3.8}$$

Where, μ_i^g and μ_i are the chemical potentials of a component i in the bulk gas phase and adsorbed phase respectively. The gas phase chemical potential under isothermal conditions can be written as

$$d\mu_i^g = RTd\ln \hat{f}_i^g \qquad \text{(constant } T \text{)} \tag{3.9}$$

Where, f_i^g is the fugacity of species i in the bulk gas phase mixture. Similarly, the adsorbed phase chemical potential μ_i is related to its fugacity $\hat{f}_i$ under isothermal conditions through

$$d\mu_i = RTd\ln\left(\hat{f}_i\right) \qquad \text{(constant } T \text{)} \tag{3.10}$$

Combining Eq. (3.8), (3.9) and (3.10) gives,

$$d\ln\left(\hat{f}_i\right) = d\ln\left(\hat{f}_i^g\right) \tag{3.11}$$

Performing the integration on Eq. (3.11), from a pure component at low spreading pressure π^* to π in the mixture for the adsorbed phase and from a low pressure P^* to P in the mixture for the bulk gas phase,

$$\hat{f}_i\{\pi\} = \hat{f}_i\{\pi^*\}.\frac{\hat{f}_i^g\{P\}}{\hat{f}_i^g\{P^*\}} \tag{3.12}$$

The fugacities in both the phases as the limits π^* and P^* approach zero can be approximated as

$$\underset{\pi^*\to 0}{Lt}\ \hat{f}_i\{\pi^*\} = \pi^* \text{ and } \underset{P^*\to 0}{Lt}\ \hat{f}_i^g\{P^*\} = P^* \tag{3.13}$$

Eq. (3.13) then becomes

$$f_i\{\pi\} = \frac{\pi^*}{P^*} \cdot f_i^g\{P\} \qquad (3.14)$$

The ideal gas-like behavior can also be assumed at these low spreading pressures.

$$\pi^* A = N_i^* . RT = H_i . P_i^* . RT \qquad (3.15)$$

Where H_i is the Henry constant for the adsorbed phase. Combining Eqs. (3.14) and (3.15) **[109, 114]**

$$\hat{f}_i\{\pi\} = \frac{H_i . RT}{A} \cdot \hat{f}_i^g\{P\} \qquad (3.16)$$

3.4 Gibbs' Adsorption Isotherm

For the sake of clarity ideal bulk gas phase is used in the following equations. However, without any loss of generality, pressure can be replaced by the fugacity of a real gas mixture at any stage. From Eq. (3.8) the chemical potential in the surface phase given in terms of the bulk gas phase properties is,

$$d\mu_i = RTd\ln(y_i P) \qquad \text{(constant } T\text{)} \qquad (3.17)$$

From the fundamental property relations, any molar property M for the adsorbed phase can be written as,

$$N.M = M\{T, \pi, N_1, N_2, \ldots\} \qquad (3.18)$$

The total differential is

$$d(N.M)=\left[\frac{\partial(N.M)}{\partial\pi}\right]_{T,N_i}d\pi+\left[\frac{\partial(N.M)}{\partial T}\right]_{\pi,N_i}dT+\sum_i\left[\frac{\partial(N.M)}{\partial n_i}\right]_{\pi,T,N_{j\neq i}}dN_i \qquad (3.19)$$

Gibbs-Duhem relation follows Eq. 3.19 and is given as

$$\left[\frac{\partial M}{\partial\pi}\right]_{T,x}d\pi+\left[\frac{\partial M}{\partial T}\right]_{\pi,x}dT-\sum_i x_i d\left[\frac{\partial(N.M)}{\partial n_i}\right]_{\pi,T,N_{j\neq i}}=0 \qquad (3.20)$$

Using g for the property M in Eq. (3.20) together with Eq. (3.17), the Gibbs' adsorption isotherm is given by

$$-a.d\pi+RT\sum x_i d\ln(y_i P)=0 \qquad \text{(constant } T\text{)} \qquad (3.21)$$

Substituting $a=A/N$,

$$-A.d\pi+RT\sum N_i d\ln(y_i P)=0 \qquad \text{(constant } T\text{)} \qquad (3.22)$$

For a single component system the equation simplifies to

$$-A.d\pi+RT.N.d\ln P=0 \qquad \text{(constant } T\text{)} \qquad (3.23)$$

This is called as the Gibbs' adsorption isotherm in adsorption literature **[115]**.

3.5 Spreading Pressure

Integrating Eq. (3.22) from zero pressure to a pressure P,

$$\psi=\frac{\pi.A}{RT}=\int_0^P\frac{N}{P}.dP \qquad (3.24)$$

The quantity ψ has the units of moles per unit mass of adsorbent. It is called reduced spreading pressure and is often used synonymously with π. At $P = 0$, there is no adsorption and the spreading pressure is zero.

The spreading pressure is not an experimentally measurable quantity. Thus, relations like Eq. (3.24) are used to calculate its value for a pure gas adsorption. A detail procedure for calculation of spreading pressure using various isotherm models is given in Appendix A and more cumbersome exercise is necessary to find its value for multi component mixtures **[99]**.

3.6 Ideal Adsorbed Solution Theory (IAST)

A solution thermodynamic approach yields the following phase equilibrium relation for equality of fugacities in bulk and adsorbed phases.

$$y_i P \hat{\phi}_i^{gas} = x_i \gamma_i P_i^0 \tag{3.25}$$

Where, y_i is bulk gas mole fraction, P is the pressure, $\hat{\phi}_i^{gas}$ is fugacity coefficient of bulk gas to account for non-ideality, x_i is adsorbed phase mole fraction, γ_i is activity coefficient in adsorbed phase (to account for non-ideal adsorbate mixture) and P_i^0 is pressure at the standard state.

A convenient standard state is pure gas at same temperature and spreading pressure as that of the mixture. If the adsorbate mixture is ideal (IAST) and neglecting gas phase non-ideality Eq. 3.25 simplifies to

$$y_i P_i^{gas} = x_i P_i^0 \tag{3.26}$$

With this phase equilibrium relations along with an equation for total amount adsorbed (N), one can predict binary gas adsorption equilibria (i.e. finding partial amount adsorbed N_i for a given gas mixture of mole fraction y_i at T and P . For example in case of binary equilibrium, the following eight equations need to be solved.

$$x_1 P_1^0 = y_1 P \tag{3.27}$$

$$x_2 P_2^0 = y_2 P \tag{3.28}$$

$$f_1\{N_1^0, P_1^0\} = 0 \tag{3.29}$$

$$f_2\{N_2^0, P_2^0\} = 0 \tag{3.30}$$

$$f_3\{N_1^0, P_1^0, \psi\} = 0 \tag{3.31}$$

$$f_4\{N_2^0, P_2^0, \psi\} = 0 \tag{3.32}$$

$$x_1 + x_2 = 1 \tag{3.33}$$

$$\frac{1}{N} = \frac{x_1}{N_1^0} + \frac{x_2}{N_2^0} \tag{3.34}$$

f_1 and f_2 are isotherms for pure gas 1 and pure gas 2 respectively. f_3 and f_4 are relations for spreading pressure ψ obtained via Eq. (3.24) **[112]**.

3.7 Models for Pure Gas Isotherms

In this section we present a review of various isotherm models used in this work

3.7.1 Langmuir Isotherm

The Langmuir model is based on the following assumptions:

[a] Fixed number of well defined localized sites

[b] Each site can hold one molecule

[c] All sites are energetically homogeneous

[d] No lateral adsorbate-adsorbate interactions

Based on these assumptions, the Langmuir equation can be represented by any one of the following forms

$$\begin{aligned} \frac{N}{M} &= \frac{(\beta / M)P}{1+(\beta / M)P} \\ N &= \frac{M\beta P}{M+\beta P} \\ P &= \frac{\beta NM}{M-N} \end{aligned} \tag{3.35}$$

Where, P is the pressure, M is the maximum loading corresponding to monolayer coverage and β is Henry constant.

In the above equation, M is assumed to be independent of temperature (T), while β is dependent on T and is given by Vant Hoffs' equation of the form

$$\beta = \beta_{(0)}\, e^{-\beta_{(1)}/T} \tag{3.36}$$

3.7.2 Dual Site Langmuir (DSL) Isotherm

The Dual Site Langmuir (DSL) model is a four-parameter isotherm, distinguishing two categories of different active sorption sites in the adsorbent, each one following a Langmuir adsorption behavior. The DSL model is represented by **[116]**

$$N = \frac{M^{(1)}\delta^{(1)}P}{1+\delta^{(1)}P} + \frac{M^{(2)}\delta^{(2)}P}{1+\delta^{(2)}P} \tag{3.37}$$

Where, $M^{(i)}$ and $\delta^{(i)}$ denotes saturation capacity and affinity parameters for sites of type 'i' respectively.

The temperature dependency is included through affinity parameters via

$$\delta^{(i)} = \delta^{(i)}_{(0)} \exp\left(\frac{-\Delta h^{(i)}_{ads}}{R} \left[\frac{1}{T} - \frac{1}{T_0} \right] \right) \tag{3.38}$$

Where, $\delta^{(i)}$ is the affinity at reference at T_0 and $-\Delta h^{(i)}_{ads}$ is the enthalpy of adsorption on site i with respect to temperature T_0.

The Henry's constant in this case is given by

$$\beta = M^{(1)}\delta^{(1)} + M^{(2)}\delta^{(2)} \tag{3.39}$$

3.7.3 Virial Isotherm

Based on two dimensional virial equation of state of the form

$$\frac{\pi a}{RT} = 1 + \frac{b}{a} + \frac{c}{a^2} \tag{3.40}$$

The surface phase virial isotherm model can be derived and is represented by (Appendix A)

$$\ln(P/N) = k + bN + cN^2 \tag{3.41}$$

e^{k} is the Henry constant and is related to the gas-solid interactions only. The other higher coefficients *viz.* b, c etc. are called as second and third virial coefficients respectively.

The following temperature dependency is usually used for the virial coefficients

$$k = \ln \beta_{(0)} + \frac{\beta_{(1)}}{T} \tag{3.42}$$

$$b = b_{(0)} + \frac{b_{(1)}}{T} \tag{3.43}$$

$$c = c_{(0)} + \frac{c_{(1)}}{T} \tag{3.44}$$

The physical interpretations of the virial coefficients are strictly valid only for homogeneous adsorbents at low coverages. Since virial equation is open ended, there is no limit on the amount adsorbed as the pressure is increased. But, this can lead to erroneous results if the virial equation is extrapolated beyond the range of data. However, within the temperature and pressure limits of the data, virial equation is flexible and thermodynamically consistent. The virial equation is also reliable to calculate Henry's law constants with good accuracy. In fact in a virial domain plot [$\ln(P/N)$ vs N] or [$\ln(f/N)$ vs N] the intercept is k and is directly related to Henry constant. Henry's constant β is given by

$$\beta = e^{-k} \tag{3.45}$$

3.7.4 Virial-Langmuir (V-L) Isotherm

The Langmuir equation usually assumes energetic homogeneous surface, rarely possible in realistic situation. On the other hand, virial equation is flexible, thermodynamically correct and describes the heterogeneity of the surface. However, the virial model does not explain the saturation at high pressure, a phenomena usually observed in many cases.

To overcome this limitation, virial model is modified with an additional term to introduce saturation behavior at high pressure. Eq. (3.41) is modified to give Virial-Langmuir isotherm written as

$$P = \frac{N}{\beta}\left[\frac{M}{M-N}\right]\exp[bN + cN^2] \qquad (N < M) \tag{3.46}$$

Here, β is Henry constant; b , c are virial coefficients; M is the saturation capacity **[102]**.

If the virial coefficients in the Eq. (3.46) are zero, the above expression reduces to the well known Langmuir equation.

The temperature dependency of the parameters β , b and c in this case is given by expressions similar to those in Eqs. 3.36, 3.43 and 3.44. Saturation capacity M is also expressed with similar functionality.

$$M = M_{(0)} + \frac{M_{(1)}}{T} \tag{3.47}$$

3.7.5 Enthalpy of Adsorption

The enthalpy of adsorption, $-\Delta h_{ads}$ is usually obtained from experiments or model parameters using the following equation **[102]**

$$\Delta h_{ads} = -R\frac{\partial \ln f}{\partial(1/T)} \tag{3.48}$$

Table 3.1 presents equations for enthalpy of adsorption for various models obtained using the above equation. A detailed derivation is given in Appendix B.

Table 3.1: Enthalpy of adsorption for different isotherm models

Isotherm Models	**Enthalpy of Adsorption Equations**	**Eq. No.**
Langmuir	$\Delta h_{ads} = -R\dfrac{\partial \ln(P)}{\partial(1/T)} = \beta_{(1)}R$	3.49
Virial	$\dfrac{\Delta h_{ads}}{R} = -\left(\beta_{(1)} + b_{(1)}N + c_{(1)}N^2\right)$	3.50
Dual Site Langmuir	$\dfrac{\Delta h_{ads}}{R} = -\dfrac{\Delta h_{ads}^{(1)}M^{(1)}\delta^{(1)}\left(1+\delta^{(2)}P\right)^2 + \Delta h_{ads}^{(2)}M^{(2)}\delta^{(2)}\left(1+\delta^{(1)}P\right)^2}{M^{(1)}\delta^{(1)}\left(1+\delta^{(2)}P\right)^2 + M^{(2)}\delta^{(2)}\left(1+\delta^{(1)}P\right)^2}$	3.51
Virial-Langmuir	$\dfrac{\Delta h_{ads}}{R} = -\left(\beta_1 + b_1N + c_1N^2 + \dfrac{M_{(1)}}{M} - \dfrac{M_{(1)}}{M-N}\right)$	3.52

3.7.6 Equation of State (EoS) Approach

The adsorbed phase can also be described using an equation of state instead of solution thermodynamics which uses a standard state **[114, 117-118]**. EoS approach is sometimes convenient to handle mixture equilibria. In particular, an EoS approach is used in this work to describe binary adsorption equilibria.

The adsorbed phase fugacity is still be related to bulk-gas phase fugacity by the Eq. (3.16). Instead of following the solution thermodynamics approach to denote an ideal standard state and account for non-ideality using the activity coefficient, the adsorbed phase fugacity is directly given by an exact thermodynamic equation **[114]**, analogous to a bulk phase.

$$\ln \hat{f_i} = \frac{1}{RT} \cdot \int_A^{\infty} \left(\left. \frac{\partial \pi}{\partial N_i} \right|_{T,A,N_j} \quad \frac{RT}{A} \right) dA \quad RT.\ln \frac{A}{N_i.RT} = \int_A^{\infty} \left(\left. \frac{\partial (N.Z)}{\partial n_i} \right|_{T,A,N_{j \neq i}} - 1 \right) \frac{dA}{A} - \ln \frac{A}{N_i.RT} \qquad (3.53)$$

Where N is the total amount adsorbed, N_i is amount adsorbed for species i and A is total surface per unit adsorbed mass. In order to evaluate the integrals, a two-dimensional equation of state is needed relating the spreading pressure, molar area and temperature. The fugacity of adsorbed phase can more readily be replaced with more useful fugacity of bulk phase via Eq. 3.16.

$$\ln \hat{f}_i^{g} \frac{\beta_i RT}{A} = \int_A^{\infty} \left(\left. \frac{\partial (N.Z)}{\partial N_i} \right|_{T,A,N_j} - 1 \right) \frac{dA}{A} + \ln \frac{N_i RT}{A}$$

$$\Rightarrow \ln \frac{\hat{f}_i^{g} \beta_i}{N_i} = \int_A^{\infty} \left(\frac{\partial NZ}{\partial N_i} - 1 \right) \frac{dA}{A} \qquad (3.54)$$

Eq. (3.54) can then be applied to pure component isotherms and the required parameters for an EoS can be estimated. Using appropriate mixing rules, the EoS parameters for the mixture can be calculated, which in turn can be used in Eq. (3.54) to calculate the fugacity of the adsorbed phase for the mixture.

The simplicity of this approach lies in the fact that the surface phase fugacity can be directly calculated from the pure component isotherms using mixing rules or fitting the multi-component experimental data to obtain the cross coefficients for the EoS. No other additional functionality or models are required as in the case of solution thermodynamic approach (where a model for activity coefficient dependent on spreading pressure is needed).

3.7.7 Models Using EoS Approach

A brief description on various models used using EoS approach is outlined in the following paragraphs. Detail derivation is given in Appendix C.

3.7.7.1 Henry's Law Region

The simplest EoS for the two dimensional adsorbed phase is an ideal gas-like EoS which is given by

$$Z = \frac{\pi . a}{RT} = \frac{\pi . A}{N.R.T} = 1 \qquad (3.55)$$

Where, Z is the compressibility factor for the adsorbed phase.

Combining Eq. (3.54) and (3.55) we get

$$\frac{\beta_i .R.T}{A} .(P.\varphi_i^{g}) = \frac{N_i .R.T}{A} \qquad (3.56)$$

$$\Rightarrow N_i = \beta_i .P.\varphi_i^{g}$$

3.7.7.2 Virial Formalism

The ideal EoS is limited only to very low pressures (spreading pressures). A simple yet versatile extension can be obtained by virial EoS (with three parameters) written as **[119-121]**

$$Z = \frac{\pi a}{R T} = 1 + \frac{b_{mix}}{a} + \frac{c_{mix}}{a^2} \qquad (3.57)$$

The mixture parameters are given by the mixing rules analogous to those in the gas phase **[109]**.

$$b_{mix} = \sum_i \sum_j x_i.x_j.b_{ij}$$
$$c_{mix} = \sum_i \sum_j \sum_k x_i.x_j.x_k.c_{ijk} \qquad (3.58)$$

For the case of binary mixture Eq. (3.56) can be written as

$$N.Z = N + \frac{N^2}{A}.\left(x_1^2.b_1 + 2.x_1.x_2.b_{12} + x_2^2.b_2\right) + \frac{N^3}{A^2}.\left(x_1^3.c_1 + 3.x_1^2.x_2.c_{112} + 3.x_1.x_2^2.c_{122} + x_2^3.c_2\right) \qquad (3.59)$$

Where N is amount adsorbed from the mixture. Using Eq. (3.59) along with Eq. (3.53), the fugacity of a component i in the adsorbed phase of a binary mixture is

$$\ln \hat{f}_i = \ln\left(\frac{N.x_i.R.T}{A}\right) + N.\sum_j x_j.b_{ij} + N^2.\sum_j \sum_k x_j.x_k.c_{ijk} \qquad (3.60)$$

The constants b_{ij} and c_{ijk} are modified to include the factors $2/A$ and $3/2A^2$ respectively.

Equating the fugacities in the gas and adsorbed phases via Eq. (3.16), we get

$$ln\,\hat{f}_i^{\,g} = ln\left(y_i.P.\hat{\phi}_i^{\,g}\right) = ln\left(\frac{N.x_i.R.T}{A}\right) + N.\sum_j x_j.b_{ij} + N^2.\sum_j \sum_k x_j.x_k.c_{ijk} - ln\left(\frac{\beta_i.R.T}{A}\right)$$

$$\Rightarrow \quad ln\left(y_i.P.\hat{\phi}_i^{\,g}\right) = ln\left(\frac{N.x_i}{\beta_i}\right) + N.\sum_j x_j.b_{ij} + N^2.\sum_j \sum_k x_j.x_k.c_{ijk}$$

(3.61)

Although this model is simple, the challenge in using this approach lies in obtaining the cross coefficients like b_{ij} ($i \neq j$) and c_{ijk}

Following Eq. (3.61), the pure component isotherm simply reduces to virial model as in Eq. 3.41.

3.7.7.3 Virial-Langmuir Formalism

The following formalism was developed in this work to enable use of Virial-Langmuir model for prediction of binary adsorption equilibria.

The compressibility factor Z in this case is given by expression similar to Eq. (3.57) with a Langmurian term added to account for saturation.

$$Z = \frac{\pi a}{RT} = M_{mix} a \ln\left(\frac{M_{mix} a}{(M_{mix} a) - 1}\right) + \frac{b_{mix}}{a} + \frac{c_{mix}}{a^2} \qquad (3.62)$$

The mixing rules similar to Eq. 3.58 are used for b_{mix} and c_{mix}. In addition, the expression for saturation capacity of the binary mixture is given by the mixing rule [101]

$$\frac{1}{M_{mix} A} = \sum_i \frac{x_1}{M_{mix,i} A} \qquad (3.63)$$

Where $M_{mix,i}$ refers to saturation capacity of species i. With these mixing rules, suitable mathematical manipulation of Eq. (3.53) and equating fugacities of bulk and adsorbed phases yields

$$\ln\frac{\hat{f}_i^{g}}{N_i} = -\ln\beta_i + 1 - \frac{M_{mix}}{M_{mix,i}} + \ln\left(\frac{M_{mix}}{M_{mix} - N}\right)\left(1 - \frac{M_{mix}}{N} + \frac{M_{mix}^2}{N.M_{mix,i}}\right) + \sum_i N_i \frac{b_{ij}}{A} + \sum_i \sum_k N_i N_k c_{ijk} \qquad (3.64)$$

The constants b_{ij} c_{ijk} and M_{mix} are modified to include the factors $2/A$ and $3/2A^2$ and A respectively.

For a pure gas the above expression reduces to the expression in Eq. (3.64) and for case of a perfect gas in the bulk gas (fugacity replaced with pressure).

4.1.1.2 Procedure:

High temperature synthesis (sample **A***)*

This method was taken from the work of Wang et al. **[39]**; they have optimized the original synthesis procedure reported by Chui et al. **[74]** and Yaghi et al. **[122]**. Benzene-1,3,5-tricarboxylic acid (1.9664 g, 0.009 mol) was added to ethanol (20 ml) and mixed thoroughly, until it was completely dissolved. Cupric nitrate trihydrate ($Cu(NO_3)_2.3H_2O$; 4.48 g, 0.018 mol) was dissolved into deionized water (10 ml) in another flask. The two solutions were then mixed and stirred at room temperature for 16 hours. The resulting viscous mixture was transferred into a teflon lined stainless steel autoclave. The autoclave was heated inside a hot air oven at 413 K for 48 hours. The reaction vessel was then cooled naturally to room temperature. Blue crystals of Cu-BTC were recovered by filtration and washed thoroughly with deionized water. This product was dried at 358 K overnight. We call the MOF synthesized using this procedure as sample **A**.

Low temperature synthesis (sample ***B****)*

This method was reported by Liu et al. **[80]** and was a modification of previous works by Rowsell and Yaghi **[123]**. 1, 3, 5-benzenetricarboxylic acid (1.0 g) was dissolved in 30 ml of a 1:1 mixture (volume ratio) of ethanol and *N*,*N*-dimethylformamide (DMF). In another flask, 2.077 g of Copper (II) nitrate trihydrate was dissolved in 15 ml of water. The two solutions were then mixed and stirred for 10 minutes. They were then transferred into teflon-lined stainless steel autoclave and heated at 373 K for 10 hours. The reaction vessel was cooled to room temperature normally. The resulting blue crystals were isolated by filtration and extracted with methanol overnight using a Soxhlet extractor to remove solvated DMF. The product was then dried at room temperature. We call this product as sample **B**.

A different batch of sample **B** was prepared for carrying out high pressure adsorption and GC analysis. The batch was labelled as sample **C** in the main text. The reported surface area of this batch of sample was found slightly higher than the first batch.

4.1.2 Synthesis of Cr-BDC Framework or MIL-101

4.1.2.1 Materials

Chromium (III) nitrate nonahydrate [$Cr(NO_3)_3.9H_2O$, Loba Chemie], 1,4-benzene dicarboxylic acid [$C_8H_6O_4$, Loba Chemie], Hydrofluoric acid [HF , Merck] were used as obtained from vendors without further purification.

4.1.2.2 Procedure

The original synthesis procedure was already reported elsewhere **[75]**. $Cr(NO_3)_3.9H_2O$ (4.00 gm, 0.206 mol) was added and dissolved in de-ionized water (48 ml). To this solution 1.64 gm of 1,4-benzene dicarboxylic acid (0.206 mol) was added; 0.5 ml of hydrofluoric acid was added drop wise and the mixture was stirred for approximately 15 minutes. The solution was then transferred to a teflon lined stainless steel reactor and sealed. The reactor was placed inside a hot air oven at 493 K and held for 8 hours. The reactor was cooled to room temperature afterwards. A fine green colored powder was obtained as the major product; significant amounts of terephthalic acid (H_2BDC) were still present in the form of needle shaped colorless crystals along with the product. To remove this impurity, contents were completely transferred into a conical flask and *N*, *N*-dimethylformamide was added incrementally with continuous shaking to dissolve H_2BDC. The solution was then filtered to recover the product. The product was dried at 423 K overnight. However, still significant amount of free terephthalic acid within the pores of MIL-101 were reported to be present **[46]**. An additional ethanol rinse was performed to remove this extra terephthalic acid from the pores. In this step about 200 mg of the dried product was mixed with 15 ml of ethanol and placed in an autoclave at 373 K for 20 hours. After cooling, the resulting product was filtered and washed with ethanol. The product was dried finally at 423 K overnight. This sample is similar to MIL-101^b indicated in the work of Llewellyn et al. **[46]**.

4.2 Characterization

4.2.1Scanning Electron Microscopy (SEM) and Optical Microscopy Imaging

The morphologies of the synthesized Cu-BTC and Cr-BDC products were characterized using a scanning electron microscope (SEM, LEO 1430 VP) equipped with an energy dispersive X-ray spectrometer (EDX).

The different batches of synthesized Cu-BTC samples were analyzed by comparing the images taken in an optical microscope (Axiotech).

4.2.2 Powder X-ray Diffraction Analysis (PXRD)

The synthesized samples were subjected to X-ray diffraction by a diffractometer (XRD, Bruker AXS D8 Advance) equipped with the graphite monochromatized CuKα radiation

(λ=1.5406Å) in 2θ angles ranging from 5^o to 85^o with a step size of 0.05 degree and scanning rate 1 sec.

4.2.3 Laser Particle Size Analysis

The particle size distributions of Cu-BTC samples synthesized from different procedures were ascertained by using Laser Particle Size Analyzer (Malvern, Mastersizer 2000). During the complete exercise water was used as the dispersion medium.

4.2.4 Thermogravimetric Analysis

Thermal stability of both Cu-BTC and Cr-BDC samples were carried out in detail in a TGA apparatus, Mettler TOLEDO (Model no: TGA/SDTA 851^e). A 900 μL alumina crucible was used as sample holder throughout all experiments. All experiments were performed under an inert atmosphere (N_2 flow of about 40 cm^3 min^{-1}) with a slow heating rate (between 2 and 5 K min^{-1}).

4.2.5 Surface Area Analysis

The surface area, pore volume and pore size distributions were measured by performing N_2 adsorption study at 77 K. Surface area analysis was carried out independently at Rubotherm GmbH using BELSORP-max, BEL Japan, Inc. surface area analyzer, at IIT Guwahati using Beckman-Coulter SA 3100 analyzer and at BPCL (R&D, Faridabad) using Autosorb-1 surface area analyzer. Prior to measurement of N_2 adsorption isotherms at 77 K during surface area analysis, all samples were out-gassed under vacuum at 403 K for about 3 hours.

The relative pressure (P_s/P_0) range between 0.05-0.2 was used in the BET surface area calculation.

4.3 Pure Gas Adsorption Measurements Using Gravimetry

4.3.1 Overview of Gravimetric Measurements

A typical gravimetric experimental setup is shown in Fig. 4.1.

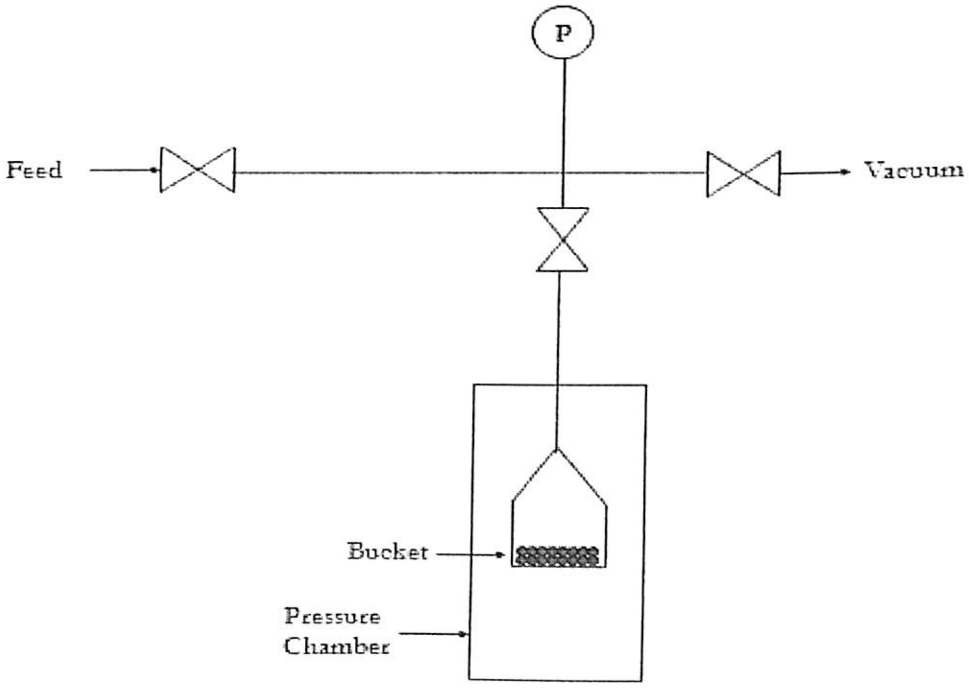

Figure 4.1: Typical gravimetric experimental setup

The adsorbent is loaded in a bucket which is on the other hand suspended from a micro balance. The sample is completely activated by keeping the pressure chamber at a high activation temperature, under vacuum. Sometimes a flow of an inert gas is utilized to facilitate flushing of desorbed components, if the system design allows for such an operation. After activation the pressure chamber is completely vacuumed, isolated and is cooled down to experimental temperature. The true adsorbent mass with the weight of the bucket, $M_{t,0}$ is measured *in vacuo*. The solid is then exposed to the gas of interest at some pressure P. At equilibrium, the observed mass M_t is related to the Gibbs' excess amount adsorbed, M_{ex} by the relation,

$$M_{ex} = M_t - M_{t,0} + V_{buoyancy}\rho^{gas} \tag{4.1}$$

The last term on RHS accounts for the buoyancy correction on the sample and bucket. The density of the gas is usually obtained from an EoS. Some recently developed commercial balances allow simultaneous gas density measurements **[124]**.

The buoyancy volume $V_{buoyancy}$ is typically measured through Eq. (4.1) for measurements conducted using helium, with the assumption that $M_{ex} = 0$ (i.e. helium does not adsorb under experimental conditions). Once calculated from the helium experiments, $V_{buoyancy}$ is then used to calculate the Gibbs' excess amount adsorbed for all other adsorbing gases via Eq. (4.1). The buoyancy volume $V_{buoyancy}$ is the sum of the impenetrable solid volume ($V_s.m$) of an adsorbent of mass m and the difference between the volumes of the balance assembly (buckets, hang downs etc.) between the sample and reference sides. Thus measurement of buoyancy volume fixes the Gibbs' dividing surface.

This method is the simplest in adsorption equilibrium measurements. The operator has control over the final pressure in the system. It is possible to obtain the true mass of the solid after complete desorption in vacuum. Only small amount of solid sample (often less than 1 gm) is needed. By itself this method can be used only for pure component measurements.

4.3.2 Experimental Setup

The schematic of complete experimental setup for measuring pure gas adsorption is shown in Fig. 4.2. For the sake of brevity the auxiliaries are not shown in the main figure.

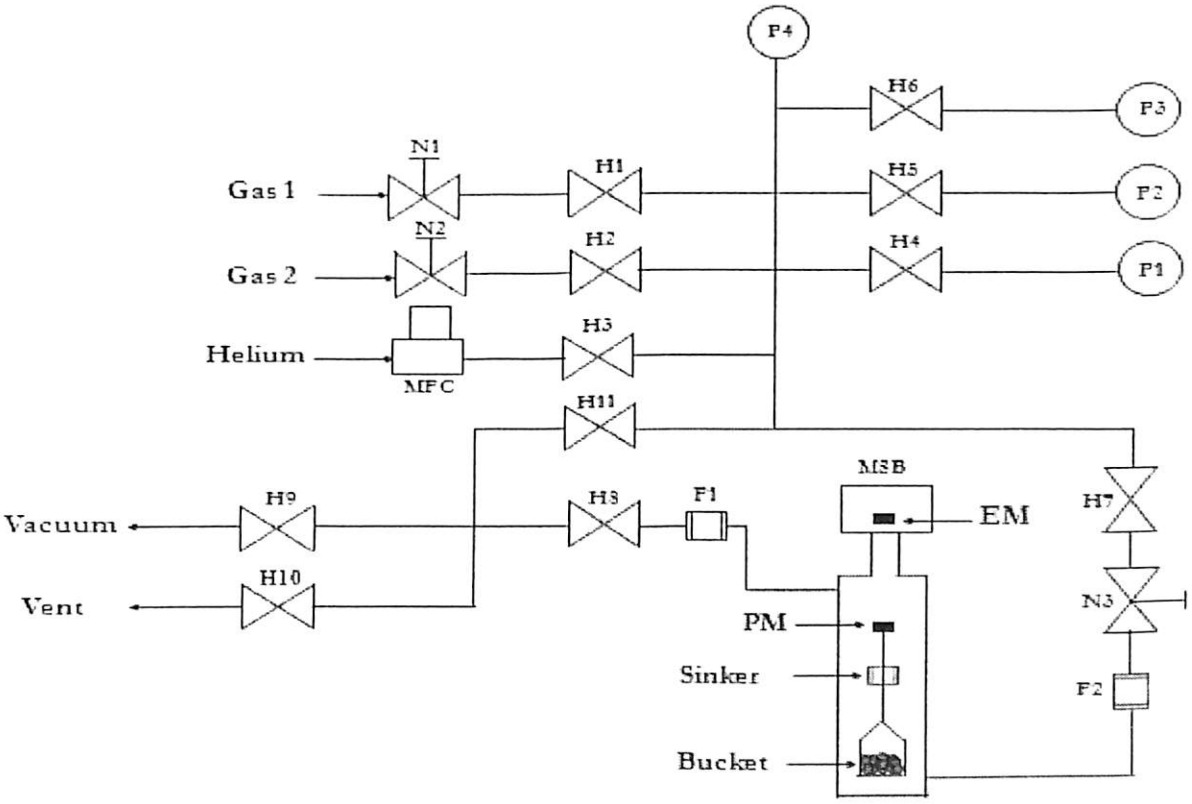

Figure 4.2: Schematic of gravimetric experimental setup used in the work

NOMENCLATURE

MSB # **Magnetic Suspension balance**

H1-H11 # **Pneumatic Valves,** N1, N2, N3 # **Needle Valves**

P1, P2, P3, P4 # **Pressure Transducers**

MFC # **Mass Flow Controller**

F1 & F2 # **Filter** PM# **Permanent Magnet** EM# **Electro Magnet**

4.3.2.1 System Description

The overall experimental setup consists of seven major sections.

1. **Feed section**: The feed section comprises of three pneumatic on-off valves *viz*. H1, H2 and H3, two needle valves (N1 and N2) and one mass flow controller (MFC). The gas of our interest was fed into the system through the assembly of these set of valves. Helium was particularly sent into the system through MFC for a better control of the overall flow during activation and regeneration of the adsorbent bed.

2. **Manifold**: The manifold constitutes the central portion of the setup. It is actually the section lying between the feed section, balance assembly and pressure measurement section. All the pressure transducers are connected to the manifold and it serves as a conduit across the whole setup.

3. **Balance chamber**: Apart from the magnetic suspension balance (MSB), the balance chamber consists of one inlet and one outlet section. In the inlet section we have two on-off valves (H11 and H8) and one filter (F1). The filter prevents any foreign material from contaminating the sample. Additionally, in the outlet section we have one filter (F2), needle valve (N3) and on-off valve (H7) respectively. The purpose of one additional needle valve in the outlet section was to have a better control over flow during evacuating the balance.

The heart of the setup, the magnetic suspension balance (Rubotherm Präzisionsmeßtechnik GmbH) measures the mass following gravimetric principle. The balance is divided into two parts:

[1] The lower pressure chamber containing the bucket and sample

[2] The assembly of all the electronic components lies at the top section

The solid adsorbent sample is placed in a bucket inside the pressure chamber: the bucket is hanged down through a permanent magnet which itself is suspended by an electromagnet. The electromagnet on the other hand is attached to the load cell of a Sartorius microbalance. A PID controller keeps the position of the permanent magnet constant. Since the position of the permanent magnet remains constant, the force transmitted to the microbalance is equal to the weight of the bucket and the sample. Thus, the mass recorded by the microbalance is directly related to the mass of the solid sample. The electromagnet and the balance electronics are completely isolated from the pressure chamber which enables the instrument to be used in a variety of environments.

4. **Vent/Vacuum section**: The complete system was vented from high pressure to atmospheric pressure by operating the pneumatic valve H10 whereas the vacuum line was connected through valve H9 to a vacuum pump. The vacuum pump was capable of maintaining very low sub-atmospheric pressure into the system facilitating complete evacuation of the balance assembly in particular.

5. **Pressure measurement section**: The pressure measurement section comprises of four pressure transducers of different ranges. We had the provision in the system to measure pressures from very low (P1), above atmospheric (P2), high (P3) and very high (P4) with greater accuracy and repeatability. All the pressure transducers were calibrated against high-precision analog gauges.

6. **Temperature measurement section**: Various thermocouples (J/K type) with appropriate temperature indicator were installed into the system for measuring temperature with an accuracy of ± 1°C.

7. **Auxiliary section** (Vacuum pump, air compressor to operate pneumatic valves, Solenoid valves, Refrigerated and heated circulator): Different auxiliary equipments were installed for

smooth functioning of the system. As is already mentioned in the above section, the vacuum pump was used for evacuating the complete system; the air compressor was used for operating the pneumatic valves which on the other hand were operated through a series of solenoid valves being controlled from an electric control panel. Circulating water bath was used for maintaining the experimental temperature inside the balance whereas the heating mantle was used for activating the adsorbent bed and particularly when the required temperature went beyond the boiling point of water.

The major hardware components that were being used along with their specification and operating ranges are given in Table 4.1.

Table 4.1: List of major hardware used along with their specifications and operating ranges

Hardware	**Model**	**Make**	**Range**	**Accuracy**	**Resolution**
Balance	3-position Magnetic suspension balance	Rubotherm	150 bar And 250°C	± 20 μg	10 μg
Pressure transducers	627B11TDCAB	MKS Instruments	0-10 torr	± 0.12% full scale	1 torr
	627B24TBC1B		0-20000 torr		
	PX41C0-050AST-OX	Omegadyne	0-50 psi	±0.5% full scale	
	PX41C0-3500PSIA		0-3500 psi		1 psia
Mass flow controller	GFC-17	Diegler Aalborg	0-200 cc min^{-1}	2% of full scale	1 cc min^{-1}
Vacuum pump	DUO 2.5	Pfeiffer Vacuum	$<6\times10^{-3}$ torr	N/A	N/A
Heated and refrigerated circulator	RW-2025 G	Jeio Tech	-25 to 150°C	±0.05°C at -10°C	0.1°C
Compressor	HS-WP-1	High speed appliances	0-100 psig	N/A	N/A
Thermocouples	J/K Type		0-600°C/0-1200°C	±2% of full scale	1°C
Temperature indicators		Vinit/Masibus			
Heating mantle	N/A	Sigma Instruments	N/A	N/A	N/A

Apart from different types of hardware mentioned in the table 4.1, all connections across the complete system were made with Swagelok fittings and stainless steel tubing (1/8″).

4.3.2.2 Experimental Protocol

The balance can measure the weight of the sample and simultaneously the density of the surrounding gaseous atmosphere in the pressure range from 0-150 bar and temperature up to 523 K. The following is a detail of protocol followed for measurement of equilibria using the balance assembly. The complete protocol may be easily outlined through macros; each macro consists of a pre determined series of valve operations. The necessary valve operations related to a macro would be outlined first and experimental protocol will be explained later based on these macros. The macros are:

[1] Vent Manifold

[2] Vacuum Manifold

[3] Vent Balance Chamber

[4] Vacuum Balance Chamber

[5] Charge Balance

[6] Record equilibrium measurement

Macro: Vent manifold

[a] Open H11 and H10

[b] When P4<350 psi, Open H6

[c] When P3<2500 torr, Open H5

[d] Close H10, H11, H5 and H6

Macro: Vacuum manifold

[a] Ensure vacuum pump is switched on

[b] Vent manifold

[c] Close all valves

[d] Open H11and H9

[e] Wait for approximately 2 minutes

[f] Open H6 and H5

[g] When P2< 10 torr, Open H4. Wait for 5 minutes.

[h] Close H9, H11, H4, H5 and H6 respectively

Macro: Vent balance

[a] Vent manifold

[b] Close all valves

[c] Open H7, H11 and H10 in sequence

[d] When P4<350 psi, Open H6

[e] When P3<2500 torr, Open H5

[f] Wait for about 10 minutes. If $P2 \sim P_{atm}$, Open H8

[g] Close H10, H8, H7, H11, H5 and H6

Macro: Vacuum balance

[a] Ensure vacuum pump is on

[b] Vent manifold

[c] Vent balance

[d] Close all valves

[e] Open H5, H6, H11, H9 and H7 in an order

[f] When P2<10 torr, Open H4 and H8

[g] When P2 is stable for more than 2 minutes, Close H9, H8, H7, H11, H4 and H5

Macro: Charge balance

[a] Choose a particular gas, say Gas 1

[b] Open H1 and close this valve after desired target pressure is achieved inside the balance. The valve should be operated with care, so that pressure inside the balance assembly does not overshoot than the desired value.

[c] If P<10 torr, monitor P1

If P<2500 torr and >10 torr, close H4 and monitor P2

If P<20000 torr and >2500 torr, close H4, H5 and monitor P3

If P>350 psi, close H4, H5, H6 and monitor P4

For the sake of the safety of pressure transducer, H4 is always kept closed during gas injection. Once pressure inside the manifold is <10 torr, then only it is opened for accurate measurement.

[d] Once an incremental amount of gas is injected into the balance (as is shown in the respective transducer reading), let it stabilize.

[e] Step [d] is repeated, keeping in mind all the constraints imposed in step [c] to the final experimental pressure.

Macro: Record equilibrium measurements

[a] Follow step [d] from the "charge balance" section.

[b] Once sample gas is injected into the balance, sufficient time is given for attaining equilibrium value.

This equilibration time varies anywhere between 10 minutes to 120 minutes. Mostly it depends on the solid adsorbent and the particular gas.

If ΔM i.e. changes in sample mass is less than 1 mg for 30 minutes, we assume equilibrium is attained.

[c] Change in sample mass is monitored continuously in the controller section of the balance. Additionally software gives minute details of each step occurring inside the balance chamber.

In the next section detailed experimental protocol is given based on the above macro operation. They are outlined as follows:

Sample loading and initial activation

[1] The solid adsorbent was loaded into the bucket and mounted into the balance.

[2] The balance chamber was sealed and system was ensured to be free from any leaks.

[3] The system was then evacuated by opening valves (**Macro**: vacuum balance)

[4] Activation of the adsorbent was performed to remove any impurities adsorbed on to the solid including water and other solvents from synthesis procedure. The activation temperature was chosen based on thermogravimetric data; as explained later for both Cu-BTC and Cr-BDC samples, this temperature was 403 K. The activation time for the freshly

prepared sample was varied between 8 to 12 hours. However, for subsequent activations (in between two isotherms) of the same sample, only 3-6 hours of activation was enough.

[5] Activation was assumed to be complete when change in sample weight was less than 10 μg (resolution of the balance) for more than 60 minutes. During the activation process, the adsorbent was exposed to the desired temperature under a flow of helium (about 30 cc min^{-1}) under vacuum.

After complete activation, the pressure chamber of the balance containing the sample was thoroughly evacuated and sealed [**Macro**: Vacuum balance]. Heating was then switched off.

Helium buoyancy measurement

[1] Once activation was complete, the balance chamber was brought down to the experimental temperature by flowing water from the circulating bath. Sufficient time was given for temperature inside the balance to reach a steady value.

[2] Helium was introduced into the balance through a mass flow controller [**Macro**: Charge balance].

[3] Data was thoroughly monitored both manually and in the computer [**Macro**: Record equilibrium measurements].

[4] Once sufficient number of data points were generated, the complete system was vented [**Macro**: Vent balance] and then vacuumed [**Macro**: Vacuum balance].

Isotherm measurement

[1] The particular gas of our interest was selected in the feed section.

[2] The gas was injected into the balance incrementally (**Macro**: Charge balance).

[3] Once injected into the balance chamber, sufficient time was given for the system to attain equilibrium. This time varied anywhere between 10 to 120 minutes, depending on the gas-solid interaction. The isotherm data was constantly monitored in the computer as well as manual observation (**Macro**: Record equilibrium measurements).

When change in sample mass was less than 1 mg for 30 minutes, we assumed equilibrium was reached.

[4] Once equilibrium was reached, step [2] was repeated for the next higher pressure.

[5] Once establishing sufficient experimental data, the complete system was vented [**Macro**: Vent balance] and then vacuumed [**Macro**: Vacuum balance].

Sample regeneration

[1] Once measuring an isotherm of a particular gas was over, the adsorbent needed to be regenerated to get rid of all the adsorbed mass from the previous run. This was particularly done by heating the balance chamber to approximately 130°C (Ref: TGA plot), occasionally coupled with a gentle sweep of Helium for about 3 hours.

[2] It was always ensured that the "net sample weight" was reached every time after completion of an adsorption cycle by proper activation i.e. sample regeneration was continued till the initial sample mass (after very first activation once the sample was loaded) was attained.

[3] Once regeneration was done, the sample was brought to the next experimental condition.

[4] Before measuring the next isotherm, the manifold was flushed with the gas of our interest and then evacuated [**Macro**: Vacuum balance].

4.3.2.3 Experimental Conditions

The adsorption equilibria of various gases on Cu-BTC and Cr-BDC metal organic frameworks were measured gravimetrically in a magnetic suspension balance (Rubotherm Präzisionsmeßtechnik GmbH) at widely different conditions of temperature and pressure. An illustrative documentation of different experimental conditions to which each of these adsorbents was exposed to is shown in table 4.2. A detailed description of various physical properties of all gases is given in table 4.3.

Table 4.2 (A): Details of experimental conditions for gravimetric measurements

Adsorbent	**Adsorbate**	**Temperature Range (K)**	**Pressure Range (bar)**
Cu-BTC (Samples **A & B**)	N_2	295, 318	0-10
	O_2	295, 318	0-10
	Ar	295, 318	0-10
	CO_2	295, 318	0-6
	C_3H_8	295, 318	0-10
	SF_6	295, 318	0-10

Adsorbent	**Adsorbate**	**Temperature Range (K)**	**Pressure Range (bar)**
Cu-BTC (Sample **C**)	CO	295, 318, 353	0-70
	CH_4	295, 318, 353	0-100
	CO_2	295, 318, 353	0-60

Adsorbent	**Adsorbate**	**Temperature Range (K)**	**Pressure Range (bar)**
Cr-BDC	Ar	283, 319, 351	0-10
	CH_4	283, 319, 351	0-10
		295, 318, 353	0-100
	CO_2	283, 319, 351	0-6
		295, 318, 353	0-60
	C_3H_8	283, 319, 351	0-10
	SF_6	283, 319, 351	0-10
	CO	295, 318, 353	0-100

Table 4.2 (B): Experimental conditions for gas chromatographic measurements

Adsorbent	**Adsorbate**	**Temperature Range (K)**	**Pressure Range (bar)**
Cu-BTC (Sample **C**)	CH_4+CO_2	305	1-10

Table 4.3: Physical properties of various gases

gas	mol. wt. (g $\mathrm{mol^{-1}}$)	liquid molar volume* ($\mathrm{cm^3\ mol^{-1}}$)	kinetic dia. (Å)	Polarizability ($\times 10^{-25}$ $\mathrm{cm^3}$)	dipole moment ($\times 10^{18}$ esu. cm)	quadrupole moment ($\times 10^{-40}$ C. $\mathrm{m^2}$)	critical properties	
							pressure (bar)	temperature (K)
He	4	32.0	2.58	2.06	0.0	0.0	2.27	5.2
Ar	40	26.3	3.4	16.6	0.0	0.0	48.98	150.9
N_2	28	31.6	3.64	17.6	0.0	1.52	34.0	126.2
O_2	32	28.0	3.5	16.0	0.0	1.3	50.0	154.6
CH_4	16	37.7	3.8	26.0	0.0	0.0	45.99	190.6
SF_6	146	72.7	5.5	44.7	0.0	0.0	35.70	318.6
C_3H_8	44	75.8	4.3	62.9	0.0	4.0	42.48	369.8
CO_2	44	33.3	3.3	26.3	0.0	14.3	73.83	304.2
CO	28	33.0	3.76	19.5	0.112	2.5	34.98	134.4

* At normal boiling point

4.3.3 Data Handling

4.3.3.1 Bulk Gas Properties

Properties of the bulk phase like fugacity and density are obtained from virial equation of state truncated up to second virial coefficient. The density is related to the second virial coefficient. In terms of second virial coefficient, the density can be represented by

$$\rho^{gas} = \frac{2PM_w}{RT(1+\sqrt{\frac{4B^{gas}P}{RT}})} \tag{4.2}$$

Where M_w is molar mass of the gas, P is pressure, T is the temperature, R is gas constant and B^{gas} is the gas phase second virial coefficient. The temperature dependency of the second virial coefficient is given by

$$B^{gas} = B_1 + \frac{B_2}{T} + \frac{B_3}{T^3} + \frac{B_4}{T^8} + \frac{B_5}{T^9} \tag{4.3}$$

Values of B_i for several gases are tabulated in Table 4.4.

Table 4.4: Second virial coefficient for different gases **[125]**

Gas	$B_1 \times 10^2$	$B_2 \times 10^{-1}$	$B_3 \times 10^{-5}$	$B_4 \times 10^{15}$	$B_5 \times 10^{17}$
	(m^3 $kmol^{-1}$)	(m^3 $kmol^{-1}$ K)	(m^3 $kmol^{-1}$ K^3)	(m^3 $kmol^{-1}$ K^8)	(m^3 $kmol^{-1}$ K^9)
N_2	4.670E-02	-1.495E+01	-6.113E+04	8.050E+13	-4.630E+15
O_2	3.900E-02	-1.554E+01	-8.480E+04	1.640E+14	-1.150E+16
Ar	3.805E-02	-1.518E+01	-8.080E+04	1.851E+14	-1.100E+16
CO_2	5.44E-02	-3.64E+01	-1.50E+06	8.59E+16	-1.40E+19
CH_4	5.438E-02	-2.714E+01	-2.135E+05	9.203E+14	-7.850E+16
C_3H_8	1.125E-01	-1.000E+02	-4.314E+06	-1.800E+16	-1.650E+19
SF_6	N/A	N/A	N/A	N/A	N/A
CO	5.122E-02	-1.709E+01	-7.416E+04	4.630E+13	-2.863E+15

N.B. Molar density values for SF_6 were taken from NIST chemistry web book **[126]** for calculating second virial coefficients.

Fugacity of the bulk gas is related to the second virial through

$$\ln\left(\frac{f}{P}\right)=\frac{B^{gas}P}{RT} \tag{4.4}$$

4.3.3.2 Buoyancy volume

Once activation was complete, the pressure chamber of the balance was completely evacuated and then cooled down to the experimental temperature. The signal of the microbalance M_0 is a result of evacuated weight of the sample and that of the bucket.

$$M_0 = M_{bucket,0} + M_{sample,0} \tag{4.5}$$

The solid was then exposed to gas of interest. At equilibrium, the excess amount adsorbed. M_{ex} is related to the microbalance reading M_t and the buoyancy force acting on the bucket and sample by the relationship as is given by Eq. (4.1) in section 4.3.1.

$V_{buoyancy}$ is the buoyancy volume and ρ^{gas} is density of the bulk gas at equilibrium temperature and pressure. In order to calculate excess amount adsorbed from microbalance signal it is necessary to have knowledge of the buoyancy volume, which is sum of the bucket volume and impenetrable solid volume V_s.

$$V_{buoyancy} = V_{bucket} + V_s \tag{4.6}$$

Buoyancy volume is usually obtained by helium pycnometry with non-adsorbing helium assumption. These experiments are performed usually around room temperature. If excess amount adsorbed for helium is zero (non-adsorbing) the Eq. (4.1) reduces to

$$M_t - M_0 = -V_{buoyancy}\rho^{gas} \tag{4.7}$$

Buoyancy volume is thus obtained from slope of the plot of the change in microbalance signal against helium density. Bulk phase helium density can be obtained as explained in section 4.3.3.1.

Throughout this work, the excess amount adsorbed was calculated from the raw measurements by buoyancy volume obtained using helium as a non-adsorbing reference gas at 295 K.

4.3.3.3 Calculation of excess amount adsorbed

An adsorption isotherm measurement involves obtaining the micro balance signal at several bulk gas pressures keeping temperature constant. As explained above the excess amount adsorbed for a gas is given by

$$M_{ex} = M_t - M_0 + V_{buoyancy}\rho^{gas} \tag{4.1}$$

$V_{buoyancy}$ is obtained from helium pycnometry as explained above in section 4.3.3.2. The bulk gas density is calculated from second Virial coefficient as outlined in section 4.3.3.1.

Finally the amount adsorbed in mol kg^{-1}, was calculated using

$$N = \frac{M_{ex}}{M_w} = \frac{M_t - M_0 + V_{buoyancy}\rho^{gas}}{M_w} \tag{4.8}$$

4.4 Binary Adsorption Measurements Using Gas Chromatography

4.4.1 Review of GC Technique for Characterization of Adsorption Equilibria

Gas solid chromatography is a technique in which a gas mixture is separated by a solid adsorbent **[127]**. In a typical elution analysis a small pulse of the solute gas is injected into a column which is already equilibrated with a carrier gas. This pulse travels along the length of the column and eventually exits. The exit stream from the column is sent to a detector and retention time of the pulse is obtained from response of the detector. As explained later, this retention time is related to the slope of the partial adsorption isotherm.

Gas chromatography is the simplest way, at least experimentally, for measuring adsorption equilibrium. It is faster and can be applied over a wide range of pressure and temperature. There are several attempts in literature that apply the method for determination of adsorption equilibrium and kinetics using GC technique **[128-136]**.

4.4.2 Slope of Isotherms Using GC Method

The detailed derivation of the equations relating retention time obtained from the chromatographic experiment to the slope of adsorption isotherm and the assumptions involved therein were widely discussed in literature **[137-139]**. A more simplified version applicable to binary mixture and ideal bulk gas phase has been derived by Van der Vlist et al. **[130]** and is given by

$$\frac{V_N P}{mRT} = \frac{P(V_R - V_G)}{mRT} = P_2 \frac{dN_1}{dP_1} + P_1 \frac{dN_2}{dP_2} \qquad (4.9)$$

Where, V_N = net retention volume **[129, 140]**

V_R = retention volume of the solute

V_G = gas hold up or retention volume of a non-adsorbing species (typically helium)

m = mass of solid adsorbent in the column

P_1, P_2 = partial pressure of components 1 and 2 in the bulk (carrier) gas phase

P = total pressure in the column

$\frac{dN_1}{dP_1}$, $\frac{dN_2}{dP_2}$ = slopes of the partial adsorption isotherms of components 1 and 2 at partial pressures P_1 and P_2 respectively.

Majority of the works were carried out these experiments at constant total pressure; partial pressure variation was obtained by changing the composition of the carrier gas stream. This limits the range of binary data that can be obtained using this technique. Only few works in literature were carried out by an experimental design which allows for variation total column pressure.

A GC technique usually yields only the slopes of the partial isotherms. Major challenge/drawback of GC technique lies in analytical difficulties in mathematical analysis/modeling necessary to obtain the actual isotherms from these slopes **[140]**. In any case, some sort of integration algorithm is necessary to calculate the actual isotherm. Hence, even a small error in the measurement is magnified and accumulated yielding large errors in the isotherm. Moreover, in case of a binary system at finite composition, there are two unknowns (partial isotherm slopes of both components) on RHS of Eq. (4.9) at every data point. A mathematical fitting procedure is necessary to calculate the partial isotherms. Most analysis to date is based on a 3rd degree polynomial fitting method of the slopes **[130, 132, 134, 141]**. Triebe et al. **[135]** and later on Harlick et al. **[142]** used a 5 parameter functional form. Regardless of the technique used, integration of the experimental data introduces substantial uncertainty. Moreover polynomial fitting makes it difficult to attribute any physical significance to the parameters.

4.4.3 Experimental Setup

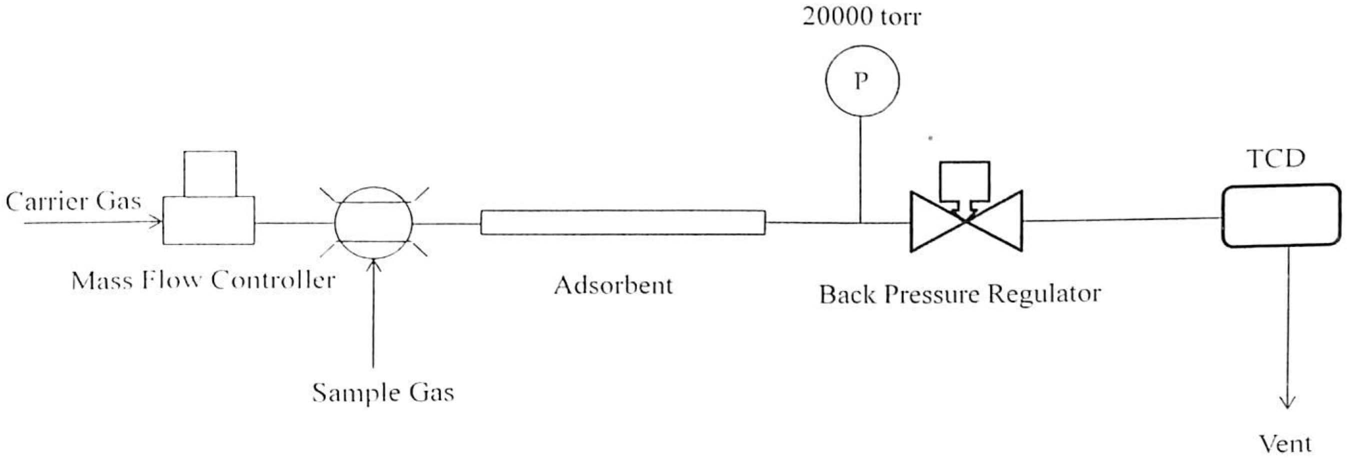

Figure 4.3: Schematic of experimental gas chromatography setup used in the work

NOMENCLATURE

P # **Pressure Transducer**

TCD # **Thermal Conductivity Detector**

4.4.3.1 System Description

A schematic representation of the experimental setup is shown in Fig. 4.3. Table 4.5 lists the major hardware used in the experimental unit.

Table 4.5: List of major hardware used in the GC experiments

Hardware	Model	Make	Range	Accuracy	Resolution
Pressure transducer	627B24TBC1B	MKS Instruments	0-20000 torr	± 0.12% full scale	1 torr
Mass flow controller	GFC-17	Diegler Aalborg	0-200 cc min^{-1}	±2% of full scale	1 cc min^{-1}
Back pressure regulator	KBP1J0A4A5A20000	Swagelok	0-500 psig	N/A	N/A

The complete experimental system can be explained as follows:

The feed section consists of a mass flow control unit through which carrier gas was introduced into the column at a fixed flow rate. Cu-BTC sample was packed into a $1/4''$ stainless copper tube which was used as column. The length of the GC column was $4.5''$ and about 89.4 mg of solid sample was packed into this column (this weight corresponds to value after activation). Both sides of the packed column were sealed with pre-treated glass wool. This column was mounted on a CP 3800 GC supplied by Varian Inc. This GC system was modified and adapted to be used for these measurements. The mounting of the column was done such that injection can be done into the column through an automated gas sampling valve supplied with the GC while the exit of the column was connected to a back pressure regulator and then to thermal conductivity detector of the GC. The solute gas (sample) can be introduced into the column through the GSV while the back pressure regulator was used to control the pressure inside the column.

4.4.3.2 Experimental Protocol

In this work we have performed gas chromatographic experiments to obtain net retention of solute gas (gas 2) at infinite dilution i.e. partial pressure of the solute is essentially zero inside the column; the carrier gas on the other hand is pure species (gas 1). Details of experimental conditions are given in Table 4.6.

Table 4.6: Details of experimental conditions for GC measurements

Solid	Carrier (Gas 1)	Solute (Gas 2)	Inert used to measure gas holdup	Temperature (K)	Pressure (bar)
Cu-BTC (sample **C**)	CH_4	CO_2	He	305	1-10
	CO_2	CH_4	He		

The choice of temperature was due to limitation of the GC oven, which did not have a cryogenic cooling option. Hence, the operation of the GC oven was restricted to temperatures above ambient.

In the following section details experimental protocol of operating the Gas Chromatographic setup for obtaining the "net retention time" of any gas 2 in carrier gas 1 is given below.

[1] **Activation**: Freshly prepared Cu-BTC sample packed inside the column was first activated in the GC oven at about 403 K for more than 8 hours under a flow of about 15 cc min^{-1} of helium. Thereafter the sample was regenerated whenever there was change in carrier gas (from CH_4 to CO_2 or vice-versa) or if the column was left "dry" without any carrier gas flow. This regeneration step consisted of activating the sample for about 2 hours under a flow of helium at 403 K.

[2] **Equilibration of column with carrier gas (Gas 1)**: A pre-determined flow of the carrier gas was first established through the column. In gas chromatography, while choosing a flow rate one needs to ensure that it does not affect the retention of the solute. A few trial runs were initially performed to ensure that choice of flow rate meets these desired criteria. The adsorbent column was equilibrated with this flow of carrier gas at desired temperature and pressure as given in table 4.6. Temperature control in the column was achieved through the GC oven program and column pressure was controlled by using a back pressure regulator. Once desired temperature and pressure were achieved in the column, equilibration time of about 45 minutes to 1 hour was allowed before performing injection.

[3] **Measurement of carrier gas flow**: Although the carrier gas flow rate was controlled through a mass flow controller, in order to increase the accuracy of the retention measurements, the flow rate through the column was measured using soap bubble meter during each run.

[4] **Measurement of retention time of solute**: The sample (Gas 2) was injected into the column through a gas sampling valve. The exit of the column was monitored using thermal conductivity detector of the GC and the run was stopped after ensuring complete elution of the peak. The retention time of the peak (which is its first moment) was obtained using the in-built software provided with the GC. All the runs were repeated until successive runs yielded same retention time value (up to second decimal in minutes).

[5] **Measurement of retention time of inert**: This step was similar to measurement of retention time of solute with helium being injected into the column. The retention obtained in these runs corresponds to gas holdup in the column at column temperature and pressure.

4.4.3.3 Data Handling

The goal of the experiments was to obtain 'net retention' which could be related to the slopes of the partial isotherms. The retention time data from the actual experiments was used along with mass flow controller calibrations to obtain net retention.

Calculation of carrier gas flow rate

Mass flow controllers are typically calibrated to display/control flow rate when used with specified gas at atmospheric pressure. In order to increase the accuracy of flow rate measurements which is very essential in GC measurement technique, the MFC readings were cross checked using a soap bubble meter for each run.

The volumetric flow rate obtained from soap bubble meter was converted into molar flow rate using an ideal gas equation and is given by the relation

$$n = \frac{P_{amb} q}{R T_{amb}} \tag{4.10}$$

Where, P_{amb} and T_{amb} are the ambient temperature and pressure; n and q are the molar and volumetric flow rates respectively.

Calculation of Net Retention

The retention (η) is the product of molar flow rate with that of the retention time (denoted by t).

$$\eta_i = n_i t_i \tag{4.11}$$

The net retention of Gas 2 is the difference between the retention of the Gas 2 and that of the inert (non-adsorbing species like helium). Thus, the net retention is given by

$$\eta_{2,net} = n_2 t_2 - n_{inert} t_{inert} \tag{4.12}$$

Calculation of Slopes of Partial Isotherms at Infinite Dilution

Equation 4.9 can be written in terms of the net retention in moles (instead of volume) as

$$\frac{\eta_{net}}{m} = P_2 \frac{dN_1}{dP_1} + P_1 \frac{dN_2}{dP_2} \tag{4.13}$$

At infinite dilution conditions (under which these experiments were performed) of Gas 2, Eq. (4.13) becomes

$$\underset{y_2 \to 0}{Lt} P_2 = 0; \underset{y_2 \to 0}{Lt} P_1 = P; \Rightarrow \underset{y_2 \to 0}{Lt} \frac{\eta_{2,net}}{Pm} = \underset{y_2 \to 0}{Lt} \frac{dN_2}{dP_2} \tag{4.14}$$

In Eq. (4.14), P and m denote the column pressure and mass of adsorbent in the column respectively. Thus, the quantity on the LHS can be directly obtained from the infinite dilution experiments as outlined above via Eq. (4.12). The quantity on RHS is the slope of the partial isotherm at the prevalent conditions, which was the main thermodynamic information obtained from the GC experiments.

4.5 Details of Gases Used

The minimum percentage purity of different gases used during experiments was more than 99%. Table 4.7 gives a detail of percentage purity of all the gases along with their suppliers.

Table 4.7: Details of gas purity

Gas	**Minimum Percentage Purity (Approx.)**	**Supplier**
Helium	99.995	Assam Air Products
Carbon monoxide	99.95	Vadilal Gases Limited
Methane	99.95	
Propane	99.5	
Sulfur Hexafluoride	99.9	
Nitrogen	99.9	Assam Air Products
Oxygen	99.9	
Carbon dioxide	99.9	
Argon	99.995	BOC India Limited

CHAPTER 5

Results and Discussion

5.1 Introduction

Section 5.2 of this chapter focuses on a systematic study for comparison of adsorption characteristics of Cu-BTC (or, HKUST-1) material prepared using two different synthesis procedures. Adsorption for six gases at two temperatures was measured for this study for pressures up to 10 bar.

Section 5.3 of this chapter discusses the adsorption characteristics of Cr-BDC (or, MIL-101) for five different gases at three widely different temperatures and pressures ranging from 0-10 bar. The modeling results for adsorption isotherms, enthalpy of adsorption and correlation between physical properties of gases and their adsorption characteristics are explained in detail.

Section 5.4 of this chapter discusses the similarities and differences in adsorption properties of industrially relevant gases (viz. CO_2, CO and CH_4) on these two frameworks up to high pressures (50 -100 bar). The effect of physical properties of these gases (CH_4 is non polar, CO_2 has a quadrupole moment and CO has a dipole moment) to their adsorption characteristics are also highlighted.

Section 5.5 of this chapter discusses infinite dilution gas chromatographic measurements for rapid modeling of adsorption of a binary mixture of CH_4+CO_2 on Cu-BTC. The modeling results were compared to Ideal Adsorbed Solution Theory (IAST). It would be shown that a proper thermodynamic model can be conveniently used along with the GC technique for rapid characterization of mixed gas adsorption.

5.2 Correlation between Adsorption Characteristics and Surface Area of Cu-BTC Framework

Two different Cu-BTC samples (**A** and **B**) were prepared as detailed earlier in Section 4.1.1. The synthesis procedure for sample **A** was similar to that of Wang et al. **[39]** and that for sample **B** was similar to that of Liu et al. **[80]**. After drying, the crystals of sample **A** were found to be light blue while that of sample **B** were bright Prussian blue in color. The following sections present the results of their characterization.

5.2.1 Characterization

5.2.1.1 Morphology of Cu-BTC

Images of the two samples were taken by an optical microscope and are shown in Fig. 5.1. These images were taken manually, at 20X magnification using dark-field mode. The crystals of both samples **A** and **B** appear octahedral. The spherical shaped particles (of different color) in sample **A** are impurities formed, viz. Cu_2O. Formation of Cu_2O impurity is not uncommon for high temperature synthesis procedures as was used for sample **A**. **[58, 74]**. The scanning electron microscopy images of the synthesized Cu-BTC products are shown in Fig. 5.2. The images show crystals of contrasting morphologies. Synthesis at low temperature (sample **B**) usually produces crystals of cubic shape with sharp edges, whereas that at higher temperatures yields more spherical shaped particles. Wang et al. **[39]** stated that higher temperature (and pressure) synthesis might result in a 3D polymeric network of Cu-BTC.

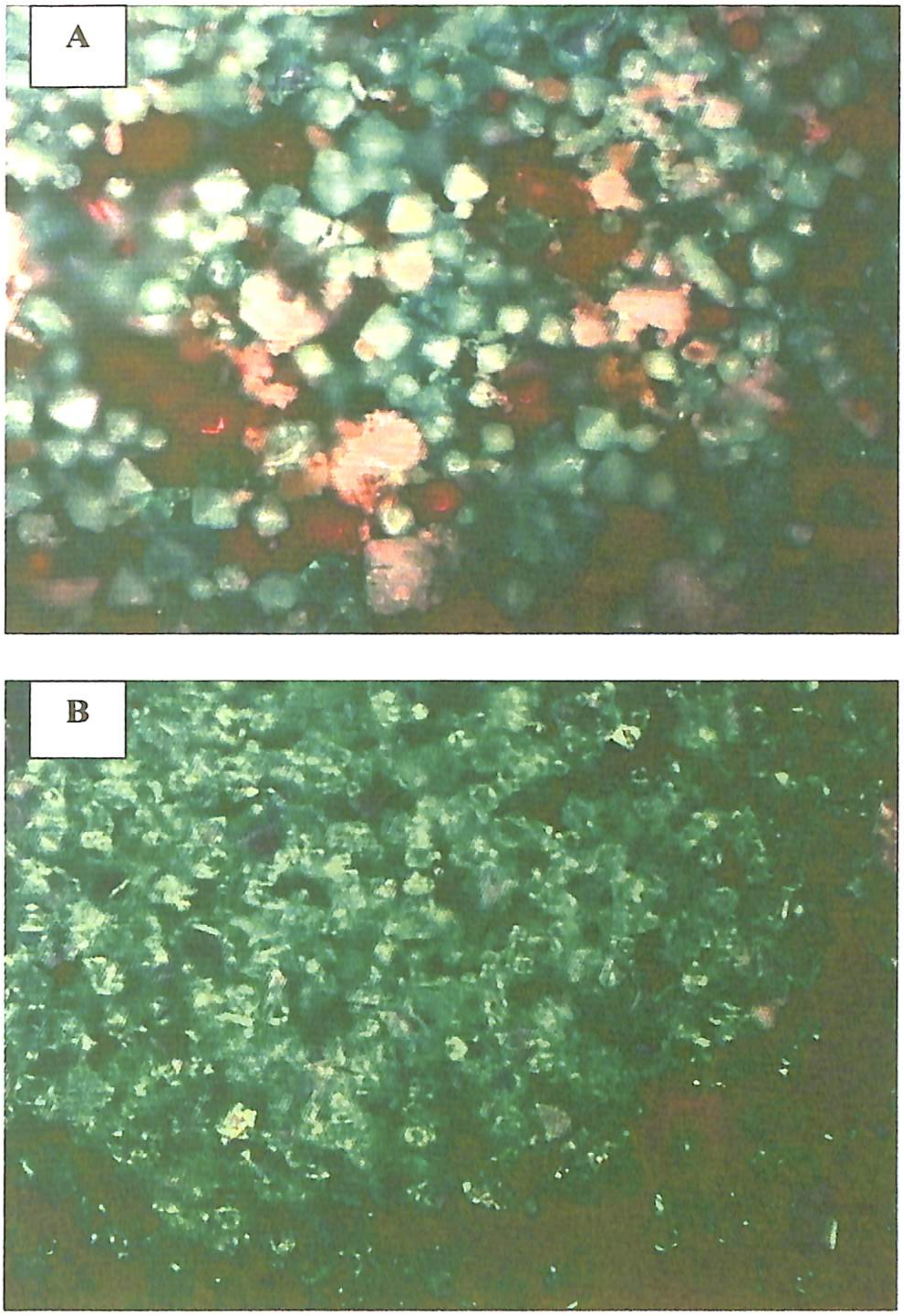

Figure 5.1: Optical microscopy images: (I) Sample A (top) (II) Sample B (bottom).

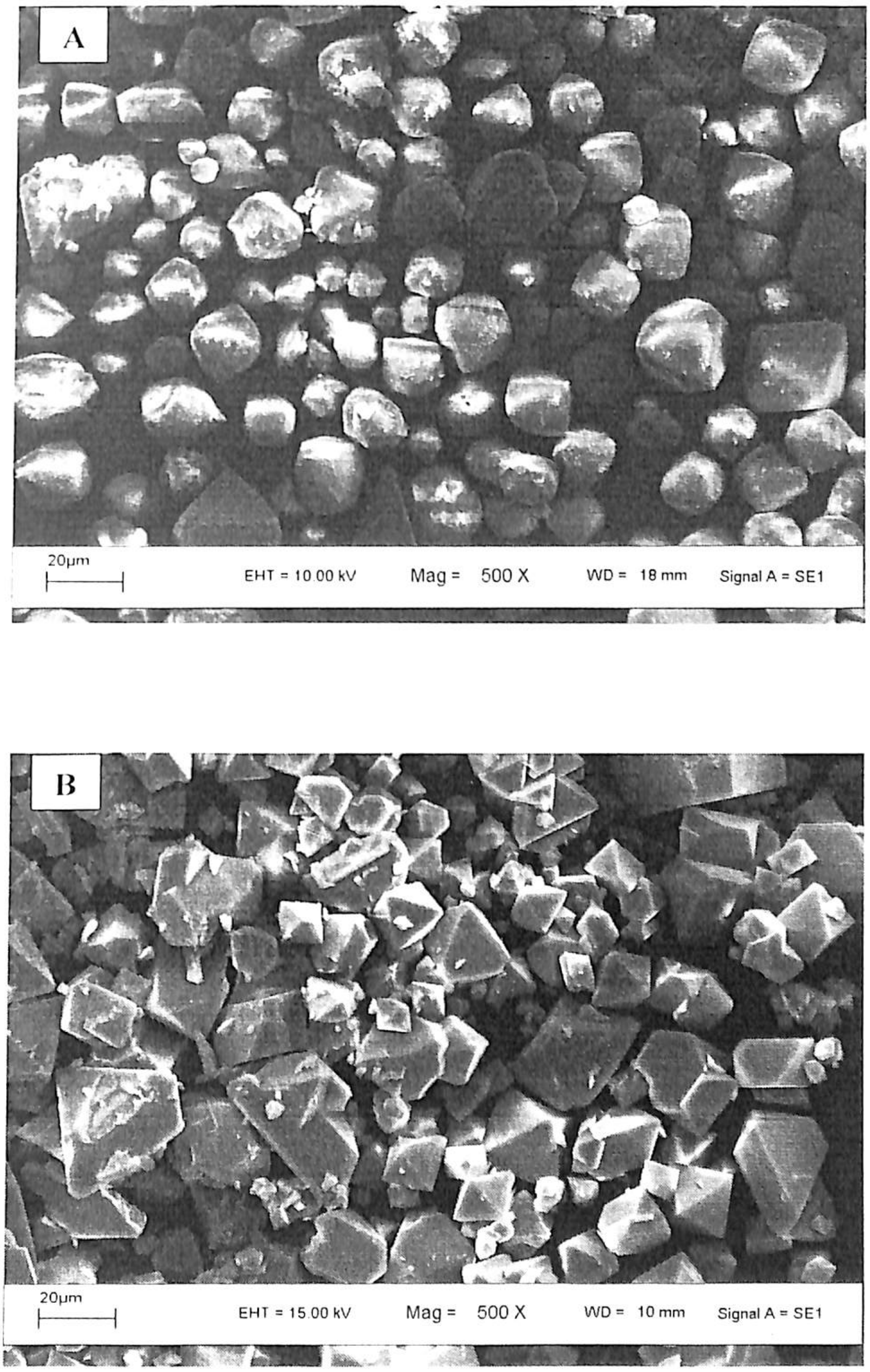

Figure 5.2: SEM micrographs of Cu-BTC products: (I) Sample **A** (top) (II) Sample **B** (bottom).

5.2.1.2 Powder X-ray Diffraction Analysis

The Powder XRD patterns are shown in Fig. 5.3. Both samples showed good crystallinity. The diffraction patterns were in accordance with the published literature data **[55-56, 58]**. The small variations in peak intensities can be due to a difference in degree of hydration **[58, 66]**. Although high temperature synthesis (Sample **A**), leads to the formation of Cu_2O as a by-product (which also appears in optical microscopy) a distinct peak for Cu_2O does not appear in the XRD results; this may be due to low concentration of Cu_2O in sample **A**.

5.2.1.3 Thermogravimetric Analysis

The TGA plots of Cu-BTC samples **A** and **B** are shown in Fig. 5.4. The first weight loss step at around 400 K corresponds to loss of moisture and other volatile solvents. The moisture and other volatile solvent content in both the samples is widely different (30% for sample **A** and 40% for sample **B**). Both samples however show a steady weight between 400 and 550 K. This was considered as the "true" mass of the sample (m_0). The second weight loss step begins at about 550 K representing the degradation of the MOF sample into constituent metallic oxide (CuO in this case). This degradation completes at about 650-700 K. An approximate calculation indicates the resulting weight loss due to decomposition of the tricarboxylate linker to give CuO during the second weight loss step should be about 60.6% of the "true" mass, (m_0) **[80]**. It was observed that only sample **B** yields this expected weight loss. Sample **A** has lower weight loss (about 49.5% of m_0), indicating presence of impurities. An estimate based on difference between observed and expected weight loss, indicates presence of about 15% impurities (which do not decompose during this step) in this sample.

Based on the TGA curve, during the adsorption equilibrium experiments, the sample was activated at about 403 K, corresponding to the sample after the initial weight loss step.

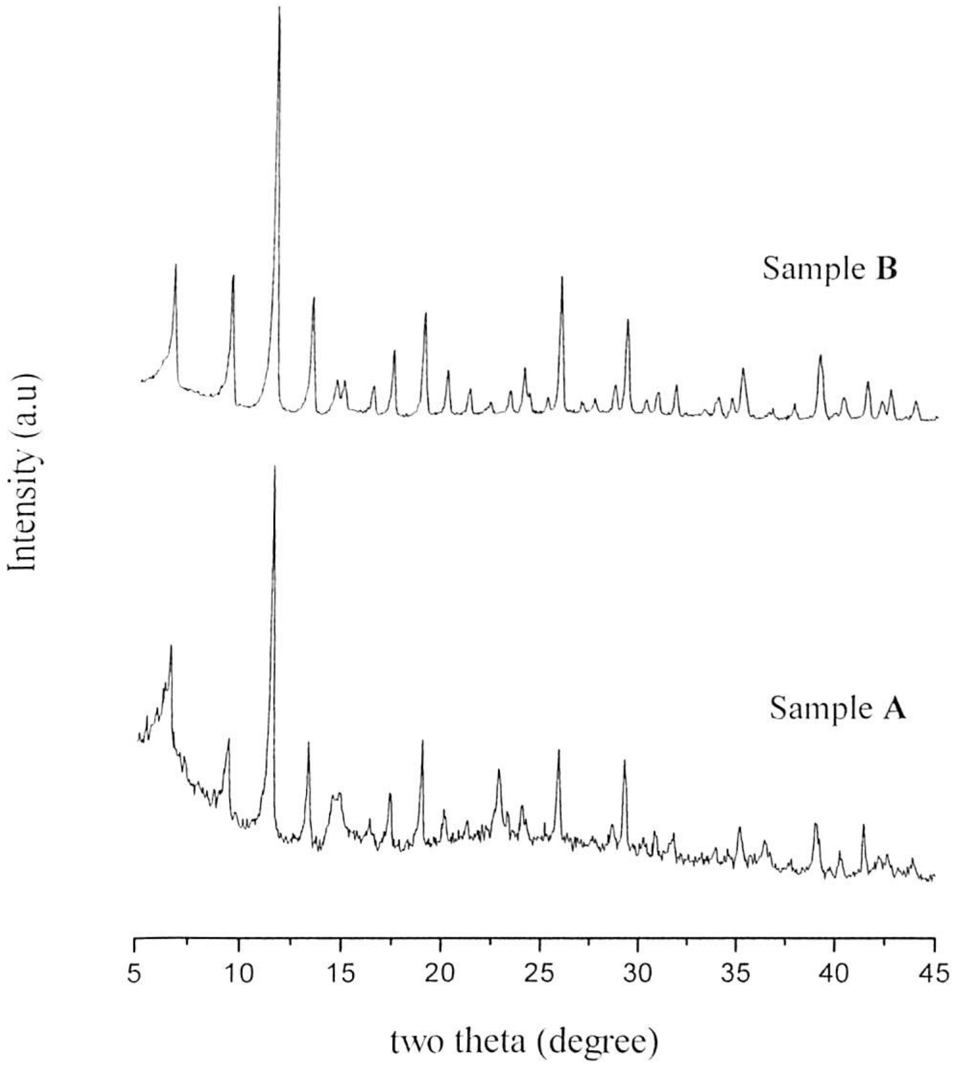

Figure 5.3: Powder XRD pattern of synthesized Cu-BTC samples.

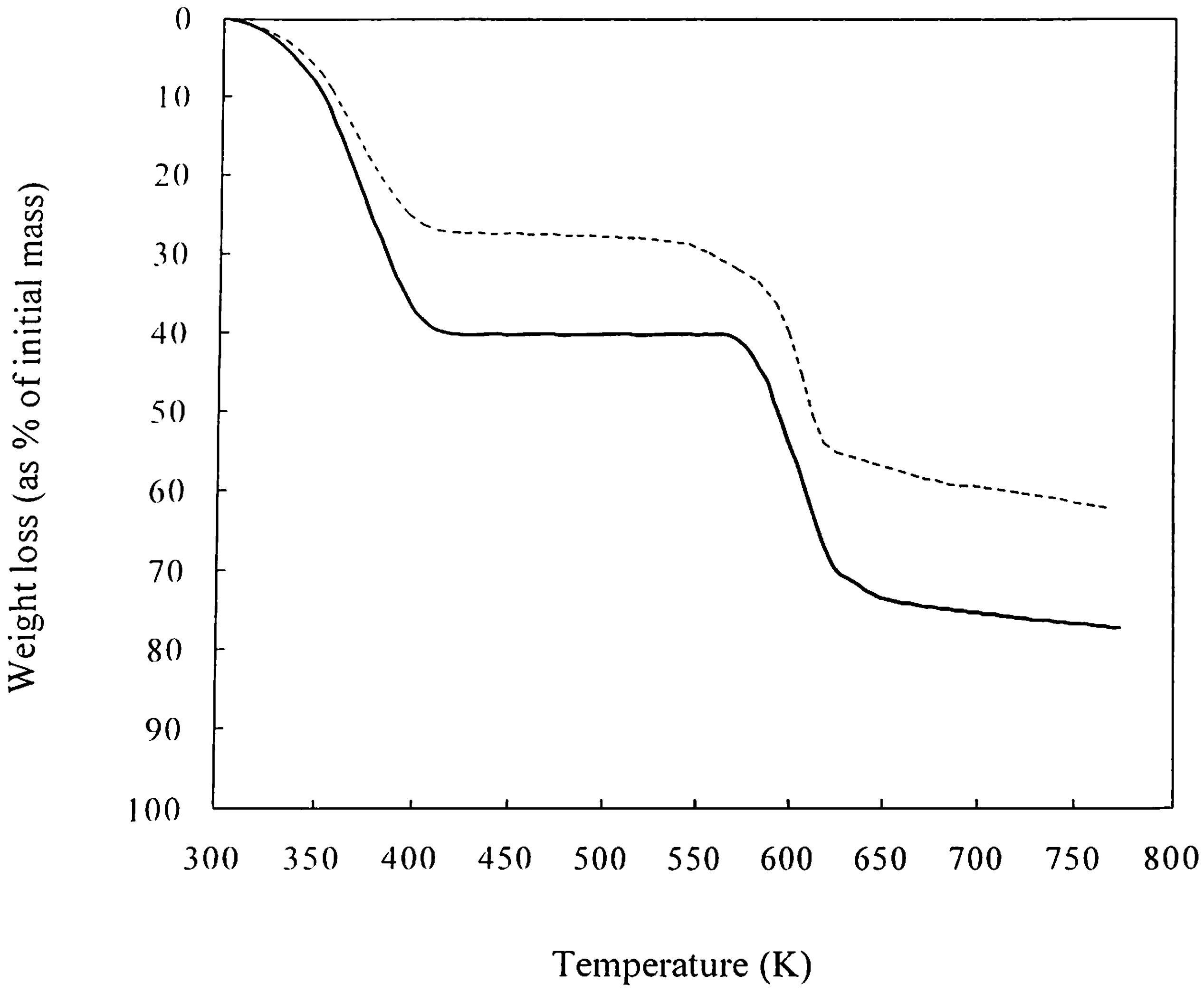

Figure 5.4: Thermogravimetric analysis of Cu-BTC samples obtained from different procedures (Heating rate: 5 K min^{-1} in inert atmosphere). Broken line is for Sample **A** and solid line is for sample **B**.

5.2.1.4 Surface Area and Pore Volume Analysis

The BET surface area and pore volume measurements were obtained from nitrogen physisorption isotherms at 77 K and the results are given in Table 5.1 and Fig. 5.5 respectively. Wang et al. **[39]** (synthesis procedure similar to that of sample **A**) have obtained a sample with BET surface area of approximately 964 m^2 g^{-1}. On the other hand Liu et al. **[80]** (whose synthesis procedure was similar to sample **B**) reported an area of about 1482 m

g^{-1} and a pore volume of 0.828 cm^3 g^{-1}. The results obtained in this work are fairly close to these reported values. Table 5.2 lists the specific surface area and pore volume of various Cu-BTC samples reported in literature.

Table 5.1: Physical properties of Cu-BTC synthesized in this work from different routes

	Sample **A**	Sample **B**	Ratio
Mean particle size, μm	38.4	35.9	
Volume per unit mass of packing, cm^3 g^{-1} (reciprocal of packing density)	1.26	2.02	1.60
BET surface area (from N_2 isotherm at 77 K), m^2 g^{-1}	857	1482	1.73
Total pore volume (from N_2 isotherm at 77 K), cm^3 g^{-1}	0.425	0.753	1.77

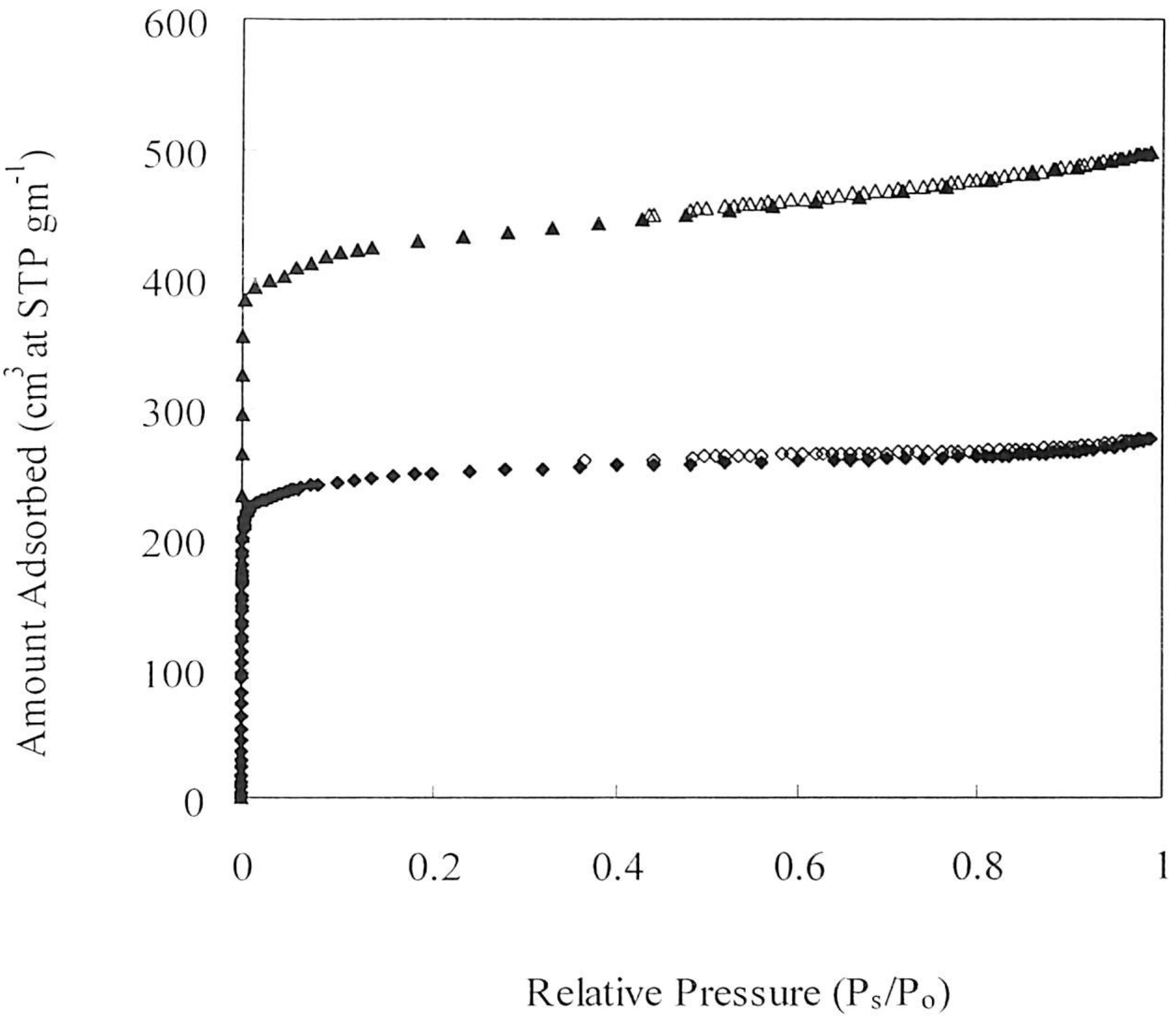

Figure 5.5: N_2 physisorption study at 77 K; Diamonds (curve at the bottom) are for Sample **A** and triangles (curve at the top) are for Sample **B**. Closed symbols are for adsorption branch and open symbols are for desorption branch.

Table 5.2: Comparison of surface area and pore volumes for different Cu-BTC samples cited in literature

References	BET surface area ($m^2 g^{-1}$)	Pore volume ($cm^3 g^{-1}$)
Present work	857, 1482, 1663 (different batches)	0.425, 0.753
[74]	692.2	0.333
[123]	1507	0.75
[39]	964, 1333 (different batches)	0.658
[58]	1502	0.76
[80]	1482	0.828
[55]	1296	0.69
[93]	1540	0.8
[44]	1791	0.701

The differences in the surface areas are mainly due to presence of both free solvent molecules and those that are co-ordinatively bound to open metal atoms. While a thorough activation procedure can in principle remove these solvent molecules, obtaining the correct activation conditions for a given synthesis procedure is often challenging. There are several works in literature that concentrate on developing a "good" activation procedure **[39, 80]**. Although the presence and concentration of impurities is dependent on the synthesis procedure, surface area of Cu-BTC would also be affected by presence of impurities.

5.2.1.5 Particle Size and Packing Density Measurements

The mean particle size and specific volume of Cu-BTC samples made from different routes are listed in Table 5.1. The particle size distribution for the two samples is given in Fig. 5.6 and both samples have particle sizes which are close to one another. However, the packing densities of the two samples are widely different. As earlier, this difference is attributed to presence of solvent molecules, impurities and crystal imperfections **[80, 143]**. The bulk (packing) density of samples **A** and **B** were about 794 and 495 kg m^{-3} indicating the presence of impurities and/or solvent trapped inside the pores.

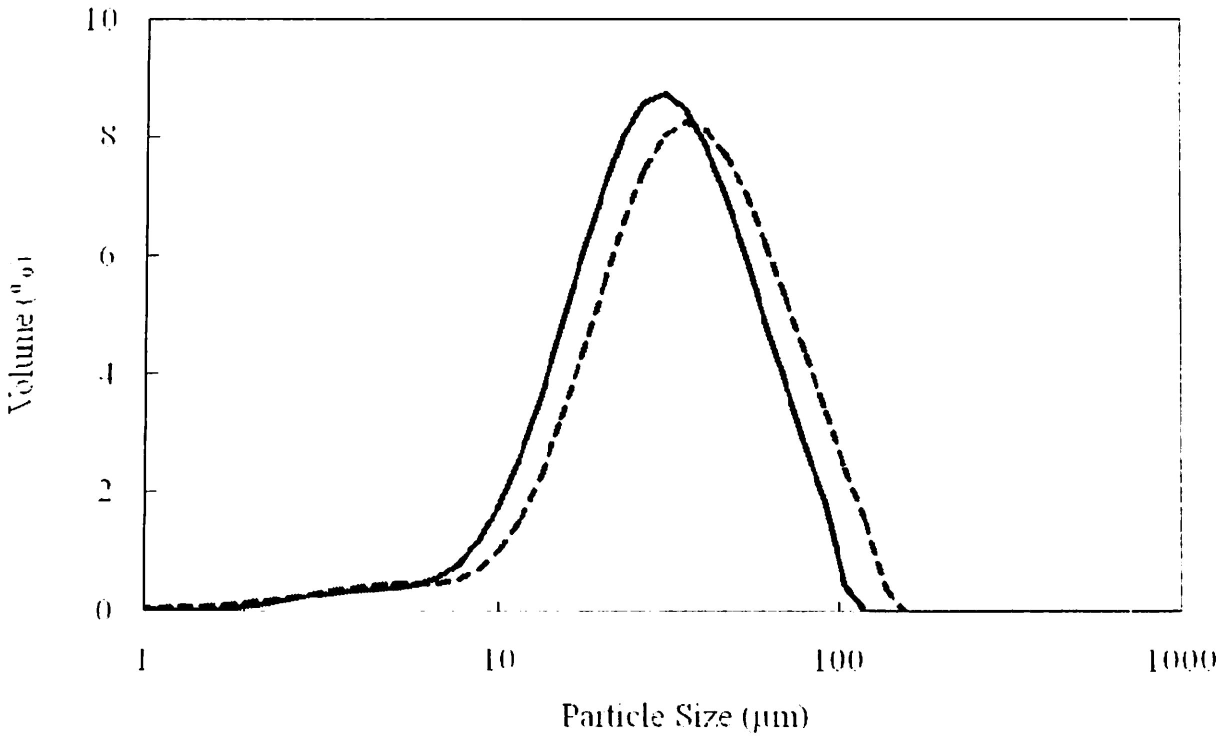

Figure 5.6: Particle size distribution of Cu-BTC samples. Broken line is for Sample **A** and solid line is for sample **B**.

5.2.2 Analysis of Gas Adsorption on Cu-BTC Samples

In order to understand the effect of surface area on adsorption characteristics we have measured adsorption capacities for several gases on these two adsorbent at different conditions, within the pressure range of interest for adsorptive separations. Six different gases viz. N_2, O_2, Ar, CO_2, SF_6 and C_3H_8 with different physical properties were chosen for this purpose and their adsorption capacities at 295 and 318 K were measured on the two samples **A** and **B**

5.2.2.1 Adsorption Isotherm Measurements and Modeling

The adsorption isotherms for N_2, O_2 and Ar on the two adsorbents are given in Fig. 5.7. In line with findings of the earlier works **[39]**, Cu-BTC shows little selectivity between the three gases N_2, O_2 and Ar at 295 and 318 K within the experimental pressure range (0-10 bar). A plateau corresponding to monolayer coverage of a Langmuir type isotherm was not observed within the experimental pressure range. Nitrogen with higher quadrupole moment shows slightly higher loading as compared to O_2 and Ar. Although O_2 has a higher quadrupole moment (Table 4.3) than Ar, their adsorption properties are similar due to slightly higher polarizability of Ar.

As indicated in Table 2.3 this amount adsorbed for Ar on sample **B** at around room temperature is slightly higher than that adsorbed on zeolites like silicalite, Na-ZSM- 5, NaX, Na ETS-4 and 5A under similar conditions; however it is also comparable to adsorption on activated carbon and carbon molecular sieves.

O_2 loading on Cu-BTC is slightly higher than on polar zeolites like 5A and 13X; the gravimetric uptake on Cu-BTC is higher. However, this should not be interpreted to mean than a relatively non-polar molecule like O_2 (with a small quadrupole moment of only) has strong interation with Cu-BTC. The higher gravimetric uptake is only a manifestation of relatively large void volumes of MOF materials, which make these materials lighter compared to zeolites. The strength of interactions of O_2 with the Cu-BTC framework is in fact smaller than with polar zeolites like 5A and 13X as evident from enthalpy at zero loading (- 10.6 kJ mol^{-1} on Cu-BTC as opposed to −15.6 kJ mol^{-1} on zeolite 5A) **[116]**.

The loadings for N_2 on sample **B** also compare well with available literature data **[39, 80, 86]**. The Henry's constant at 295 K for N_2 on Cu-BTC measured in this work is 0.31 mmol g^{-1} bar^{-1}, which is higher than zeolite like silicalite, but lower than that on 5A and activated carbon. In case of N_2, the amounts adsorbed are lower than those on zeolites like 5A, NaX and activated carbon (Norit R1) while it is higher than those on fairly inert zeolites like silicalite and ZSM-5. Polar zeolites enhance adsorption of N_2 (which has a quadrupole moment) in comparison to Ar, while in case of Cu-BTC framework polarity on N_2 is only modest and both N_2 and Ar loadings are comparable. However, this loading was higher than reported values on MOF-177.

The loading of O_2 on Cu-BTC (sample **B**) measured in this work are comparable to those reported in literature **[39, 92]**. However, Liang et al. **[86]** reported a higher value. As in case of Ar, O_2 loading on Cu-BTC is greater than that on zeolites like 5A, NaX and silicalite, while it is comparable to that on activated carbon and carbon molecular sieve. In comparison, MOF-178 also seems to have a slightly lower capacity for O_2 **[94]**.

The behavior of all the three gases was described by virial isotherm equation Eq. 3.41 using only the adsorption second virial coefficient. The parameters of the model for both samples are given in Table 5.3.

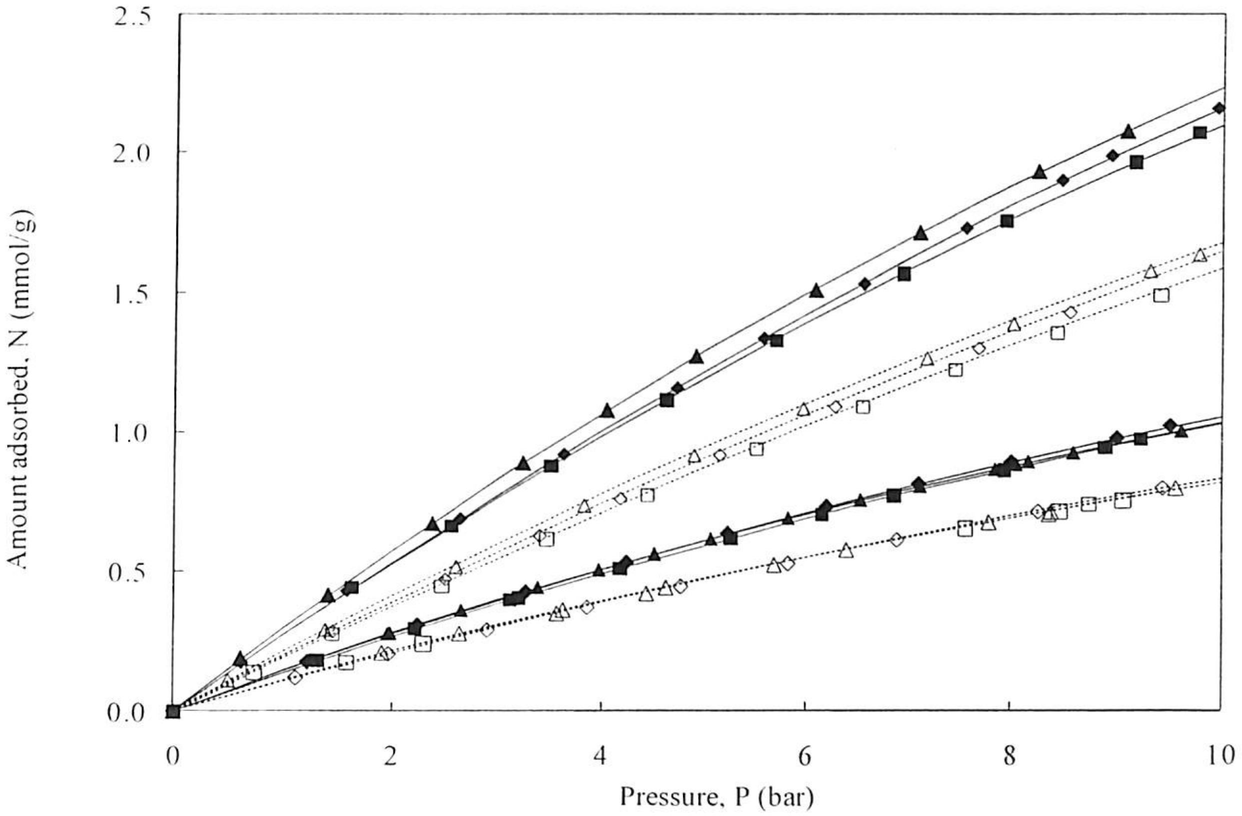

Figure 5.7: Adsorption isotherms for N_2, Ar and O_2 on Cu-BTC. Solid lines / closed symbols: 295 K., Broken lines / open symbols: 318 K Triangles: N_2, Diamonds: Ar, Squares: O_2; Bottom two sets: Sample **A**, Top two sets: Sample **B**. Lines are from virial isotherm model.

The isotherms for CO_2 on both adsorbents (sample **A** and **B**) at 295 and 318 K are given in Fig. 5.8. At about 1 bar and 295 K Wang et al. **[39]** reported a loading of ca. 3.8 mmol g^{-1}, while at 298 K and 1 bar pressure Millward et al. **[44]** reported a loading of ca. 4.07 mmol g^{-1} and Yazaydin et al. **[100]** reported a value of about 5 mmol g^{-1}; these values are comparable to our result of about 3.9 mmol g^{-1} on sample **B**. The value on sample **A** however is lower and only about 1.64 mmol g^{-1}. At around 6.2 bar and 298 K, the loading reported by Millward et al. **[44]** was about 8.8 mmol g^{-1}, while loading on sample **B** in this work was about 10.7 mmol g^{-1} at about 5.8 bar and 298 K. The maximum loading reported by Millward et al. **[44]** was about 10.7 mmol g^{-1} at 30 bar while that by Wang et al. **[39]** (sample **c** in their work) was about 8 mmol g^{-1} at 295 K and 20 bar pressure. Thus, the values of loading obtained in this work for CO_2 adsorption were comparable to those in literature with samples having similar surface area.

This loading for CO_2 on sample **B** is higher than that on benchmark zeolite like 13X; on 13X the amount adsorbed for CO_2 at 298 K and 35 bar is about 7.4 mmol g^{-1} **[44]**. As given in table 2.6 this loading for CO_2 under similar conditions is better than that on zeolites like 13X, 5A, silicalite, H-ZSM-5, Na-ETS-4, H-mordenite, activated carbon, and MOFs like IRMOF-1, IRMOF-3, MOF-5, MOF-177, MIL-47, MIL-100 and ZIF-8. Like the earlier case for N_2, O_2 and Ar, isotherms for CO_2 was modeled using virial model Eq. 3.41. The parameters for the model are given in table 5.3.

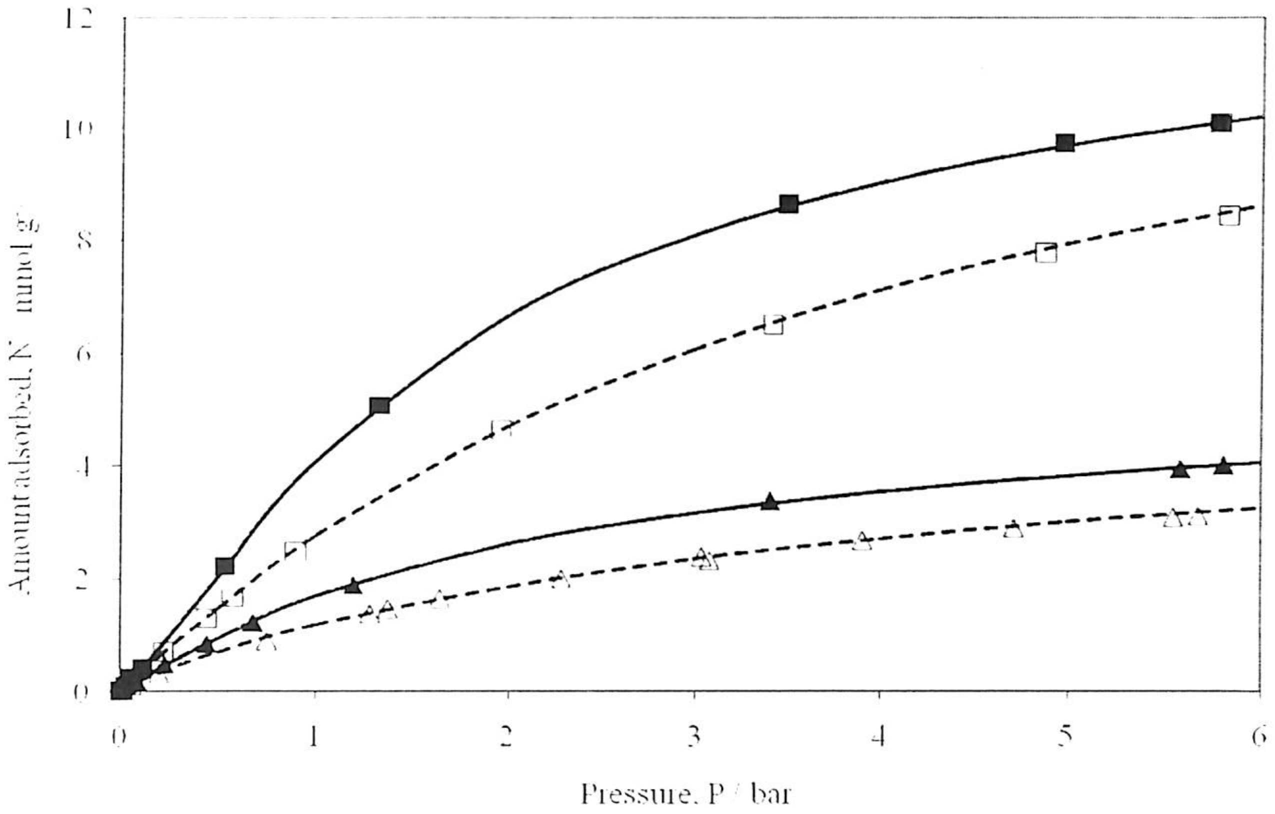

Figure 5.8: Adsorption isotherms for CO_2 on Cu-BTC. Closed symbols: 295 K, Open symbols: 318 K, Squares: Sample **B**, Triangles: Sample **A**. Lines are from virial isotherm model.

Table 5.3: Virial Isotherm Parameters for adsorption of N_2, O_2, Ar and CO_2 on Cu-BTC samples

Adsorbate	Temperature T (K)	β (mmol g^{-1} bar^{-1})		b (mmol^{-1} g)		c (mmol^{-2} g^2)	
		Sample **A**	Sample **B**	Sample **A**	Sample **B**	Sample **A**	Sample **B**
N_2	295	0.15	0.31	0.39	0.16	0	0
	318	0.12	0.22	0.44	0.17	0	0
O_2	295	0.14	0.28	0.32	0.14	0	0
	318	0.12	0.19	0.44	0.13	0	0
Ar	295	0.15	0.28	0.34	0.13	0	0
	318	0.11	0.20	0.35	0.13	0	0
CO_2	295	2.01	3.47	-0.02	-0.11	0.0708	0.0178
	318	1.75	3.14	0.31	0.03	0.0159	0.0076

The isotherms for SF_6 and C_3H_8 on both Cu BTC samples **A** and **B** are given in Figs 5.9 and 5.10 respectively. The isotherms for C_3H_8 are given in separate figures for sake of clarity. The Henry constants for both the gases are substantially higher than the other gases and both gases seem to approach their respective saturation loadings.

Data for SF_6 on Cu-BTC or other MOFs' was not available in literature to the best of our knowledge. However, in comparison to other zeolites like NaX, H-ZSM-5, silicalite and activated carbon the loading of SF_6 on sample **B** is much higher at similar conditions [Table 2.10].

The loading for C_3H_8 reported by Lamia et al. **[144]** at 323 K and 1 bar pressure was about 6.5 mmol g^{-1}; at the same pressure and 318 K, loading on sample **B** measured in this work was about 5.74 mmol g^{-1}. However, the Henry constant value for propane reported by Lamia et al. **[144]** was about 46.4 mmol g^{-1} bar^{-1} at 323 K as compared to a value of about 57 mmol g^{-1} on sample **B**. Although the Henry constant values were comparable or slightly higher for sample used in this work, the saturation capacity for C_3H_8 was lower. On the other hand García-Pérez et al. **[92]**, however reported a lower value of about 3 mmol g^{-1} at 318 K. This loading of C_3H_8 on Cu-BTC is higher in comparison to other adsorbents like H-Mordenite, silicalite, NaX and activated carbon [Table 2.8]. Larger accessible pore volume of the Cu-BTC may be one of the reasons for this extraordinary loading of both C_3H_8 and SF_6 on Cu-BTC in comparison to other adsorbents.

At each temperature, loading of these gases was best described by a Langmuir isotherm Eq. 3.35. The best fit parameters are given in table 5.4.

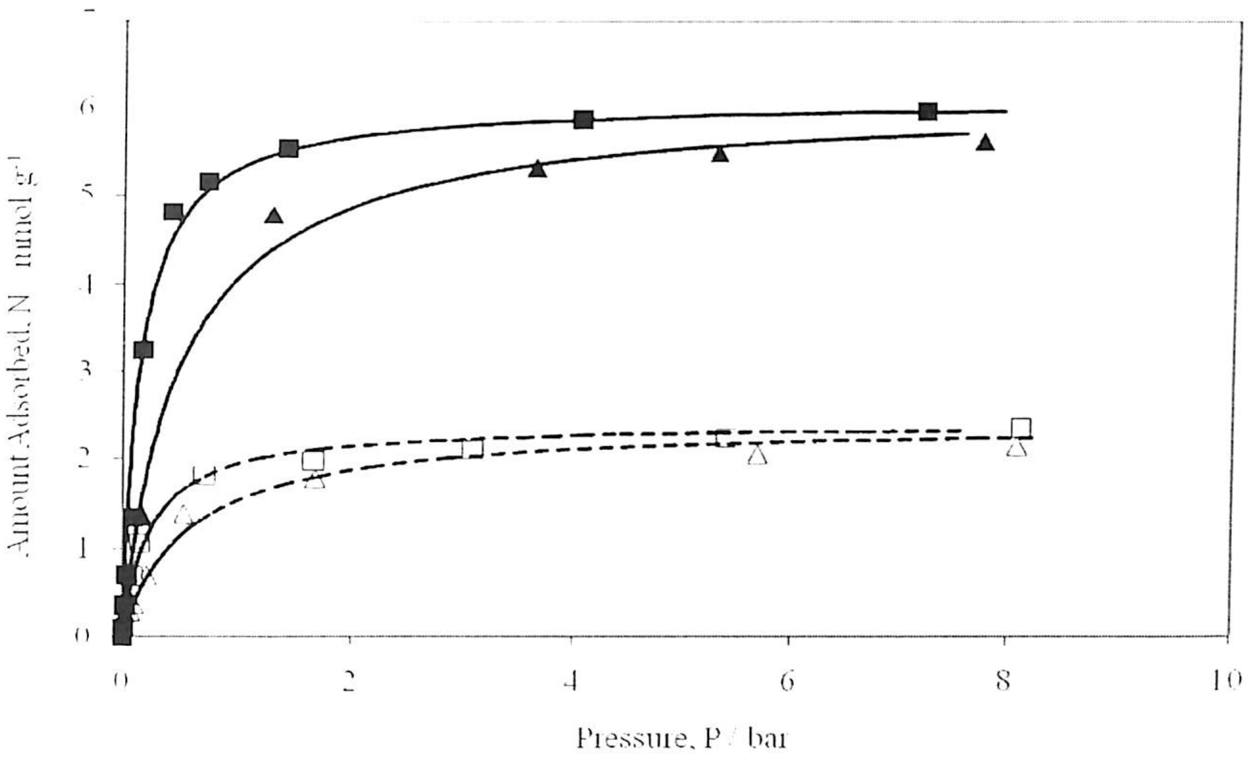

Figure 5.9: Adsorption isotherms for SF_6 on Cu-BTC. Open symbols: 318 K. Closed symbols: 295 K. Squares: Sample **B**. Triangles: Sample **A**. Lines are obtained using Langmuir model.

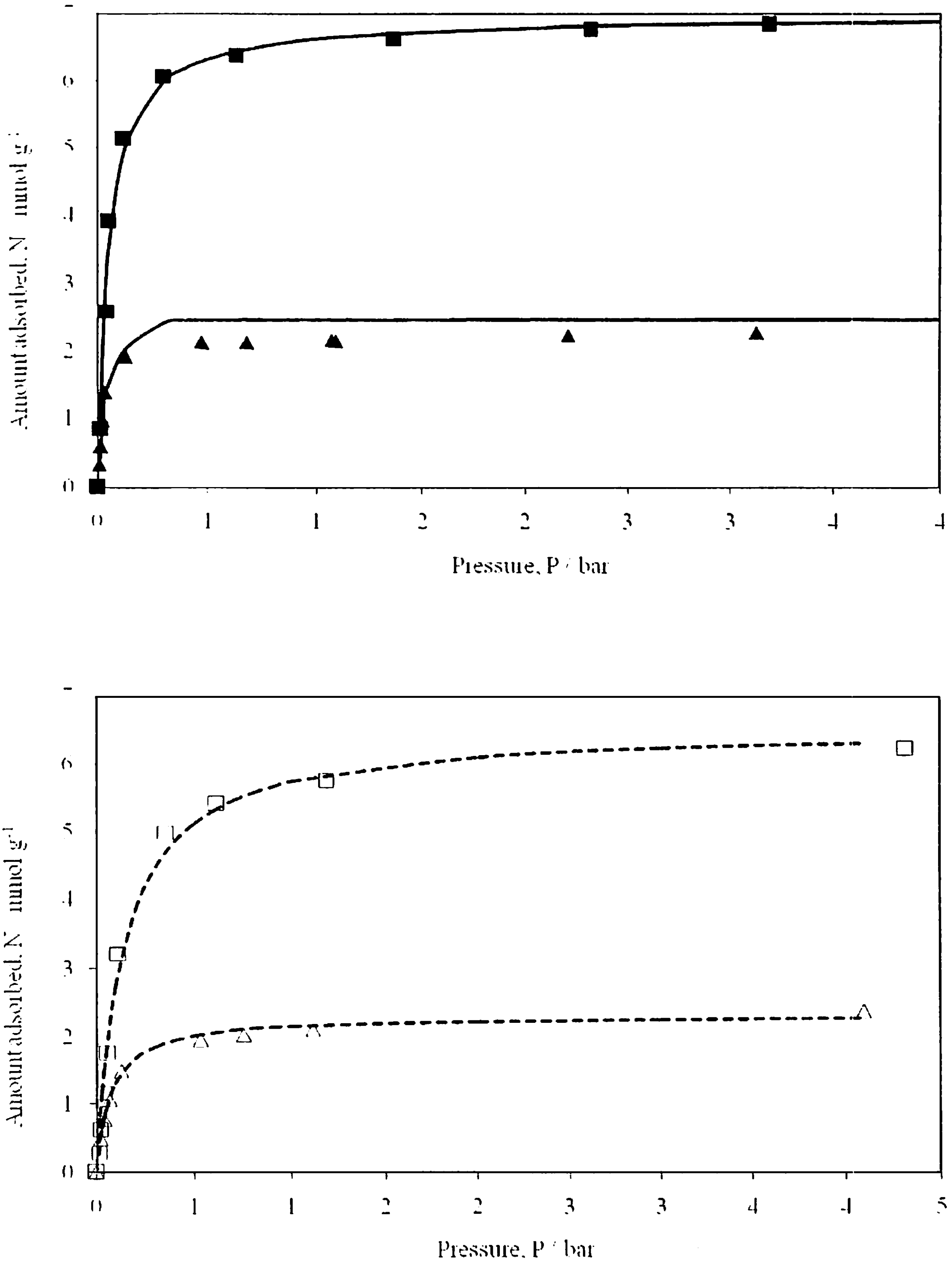

Figure 5.10: Adsorption isotherms for C_3H_8 on Cu-BTC. Closed symbols: 295 K. Open symbols 318 K. Squares: Sample **B**, Triangles: Sample **A**. Lines are obtained using Langmuir model.

Table 5.4: Langmuir parameters for adsorption of SF_6 and C_3H_8 on Cu-BTC

Adsorbate	Temperature T (K)	β (mmol g^{-1} bar^{-1})		M (mmol g^{-1})	
		Sample **A**	Sample **B**	Sample **A**	Sample **B**
C_3H_8	295	57.47	137.47	2.79	6.97
	318	30.49	47.64	2.31	6.52
SF_6	295	11.75	29.0	2.29	6.38
	318	5.14	12.23	2.24	6.08

5.2.2.2 Correlation of Surface Area and Adsorption Characteristics

A thorough review of literature on Cu-BTC **[39, 86, 100, 145]** and as highlighted in the loading results in section 5.2.2.1, there is a large variation in adsorption characteristics of some MOFs like Cu-BTC. In such a scenario it becomes difficult to compare results for adsorption loading obtained from two different samples of the same adsorbent even if they are prepared in the same laboratory but in different batches; this becomes even more confusing when the adsorbent is prepared in different laboratories. The main reason for the difference seem to be the difference in surface area of the MOF (which is dependent on the synthesis recipe used for preparation) and the activation procedure used to remove the solvent molecules coordinated **[80]**. At least six different synthesis routes are available in literature **[39, 58, 123, 145]** for synthesis of Cu-BTC. They result in Langmuir surface areas of 918 to 2257 m^2 g^{-1} **[39, 44, 49, 74, 123, 145]**.

Moreover, simulation models assume "clean" adsorbent free from any guest/solvent molecules and perfect adsorbent crystals free from any defects. When one compares experimental results to simulation, disagreement arises due to "some" unaccounted solvent molecules likely to be present in the sample used in experiments.

To overcome these problems, it is often a common practice in literature to conveniently use a scaling factor, for comparing isotherms between the two MOF samples or for comparison of isotherms between experiments and simulations **[37]**. Thus, the amounts adsorbed (N_i and N_j) for the same gas at similar conditions (T and P) between two different samples or between experiments and simulations are conveniently related through this scaling factor, k_s .

$$N_j = k_s N_i \tag{5.1}$$

Usually this k_s was assumed to be constant and used as a "fit" parameter to match the isotherms between the two samples. One of the aims of this study was to validate the use of such a scaling factor by systematic investigation of adsorption characteristics of a variety of gases on two different MOF (Cu-BTC in this case) samples having widely different surface areas.

While it is desirable to have a unique scaling factor, a look at the model parameters (Tables 5.3 and 5.4) reveals that a single value of scaling factor does not exist. In fact this value continuously changes with loading and is different for each gas. As an example, the scaling factor for N_2 at both temperatures is shown in Fig. 5.11. It was generated using the model parameters from Table 5.3. The variation for other gases also is similar and is dependent on the form of the isotherm(s).

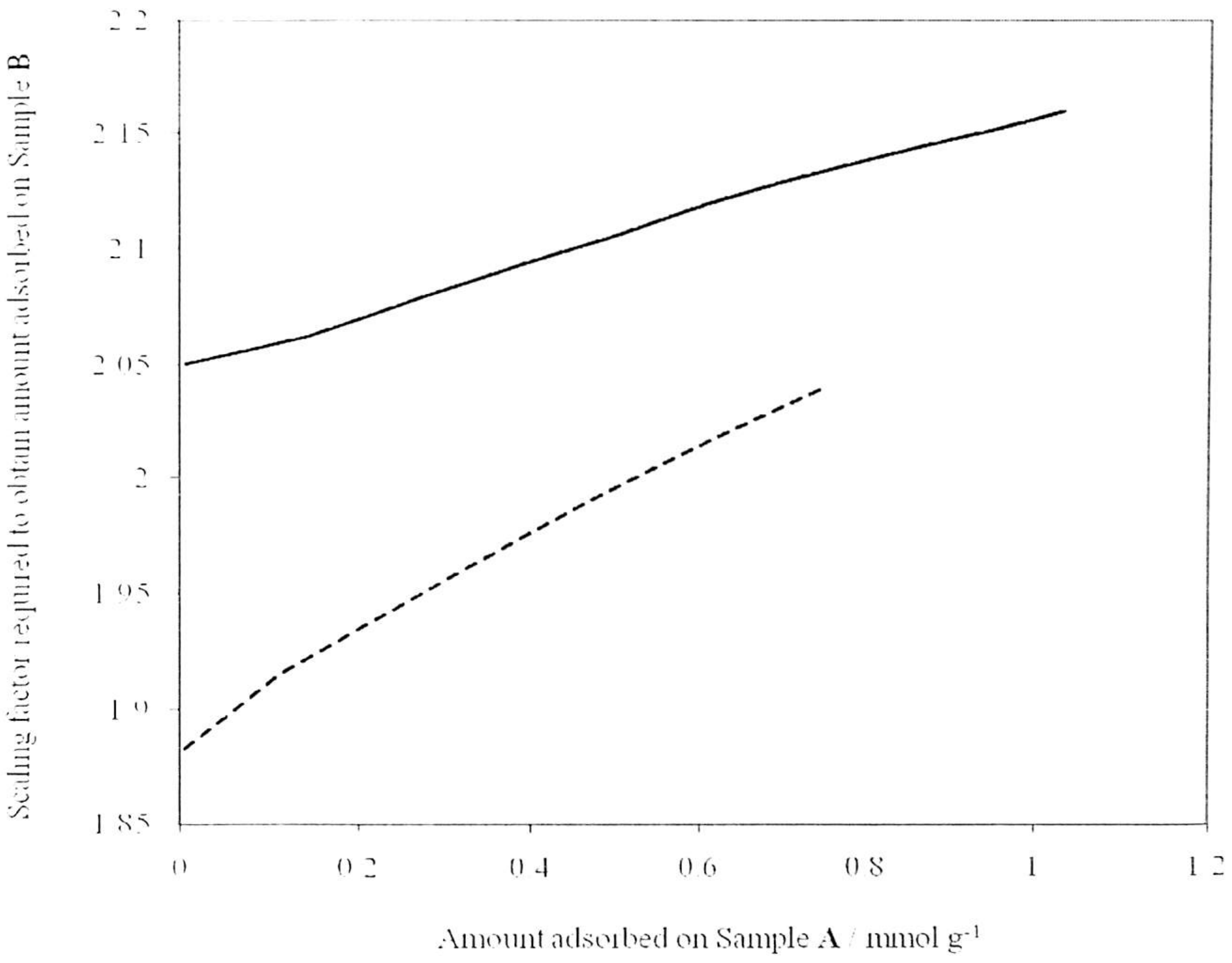

Figure 5.11: Variation of scaling factor with loading for N_2 adsorption on Cu-BTC. Abscissa is calculated amount adsorbed on Sample **A** at a given temperature and pressure. Ordinate is the scaling factor required to obtain adsorption amount on Sample **B** at the same temperature and pressure. Solid line is for adsorption at 295 K and broken line is at 318 K.

Although using the model parameters or experimental data to find the value of scaling factor is a rigorous approach, it is not useful from an application point of view; one needs to measure isotherms on a synthesized sample whenever synthesis route or surface areas are different.

To overcome this trouble, we plot amounts adsorbed on both samples at the same conditions (temperature and pressure) for all the gases studied in this work. These results are presented in Figs. 5.12 and 5.13 respectively. At a chosen temperature (295 or 318 K) and pressure amount adsorbed on samples **A** and **B** was calculated using model parameters. In case the model correlations deviate significantly from experimental results at these conditions (which were the case in certain regions for C_3H_8 and SF_6) an appropriately interpolated value was used from experimental measurements.

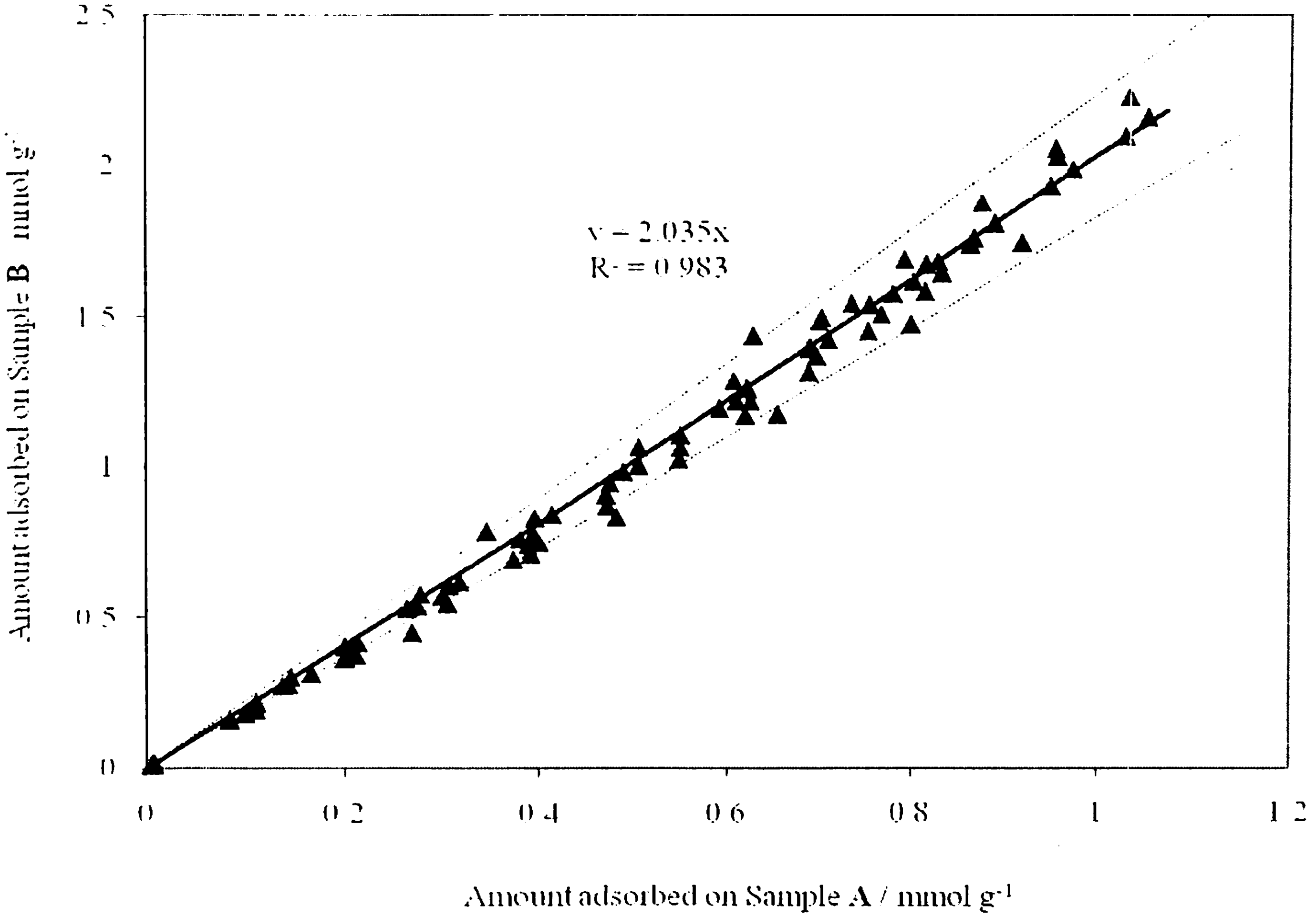

Figure 5.12: Comparison of adsorption capacities of samples **A** and **B** for various gases in low loading region. Abscissa is calculated amount adsorbed on Sample **A** at a given temperature and pressure. Ordinate is for adsorption on Sample **B** at the same temperature and pressure. Solid Line is best fit straight line through origin, with equation as shown; broken lines are 10% envelopes around the best fit line.

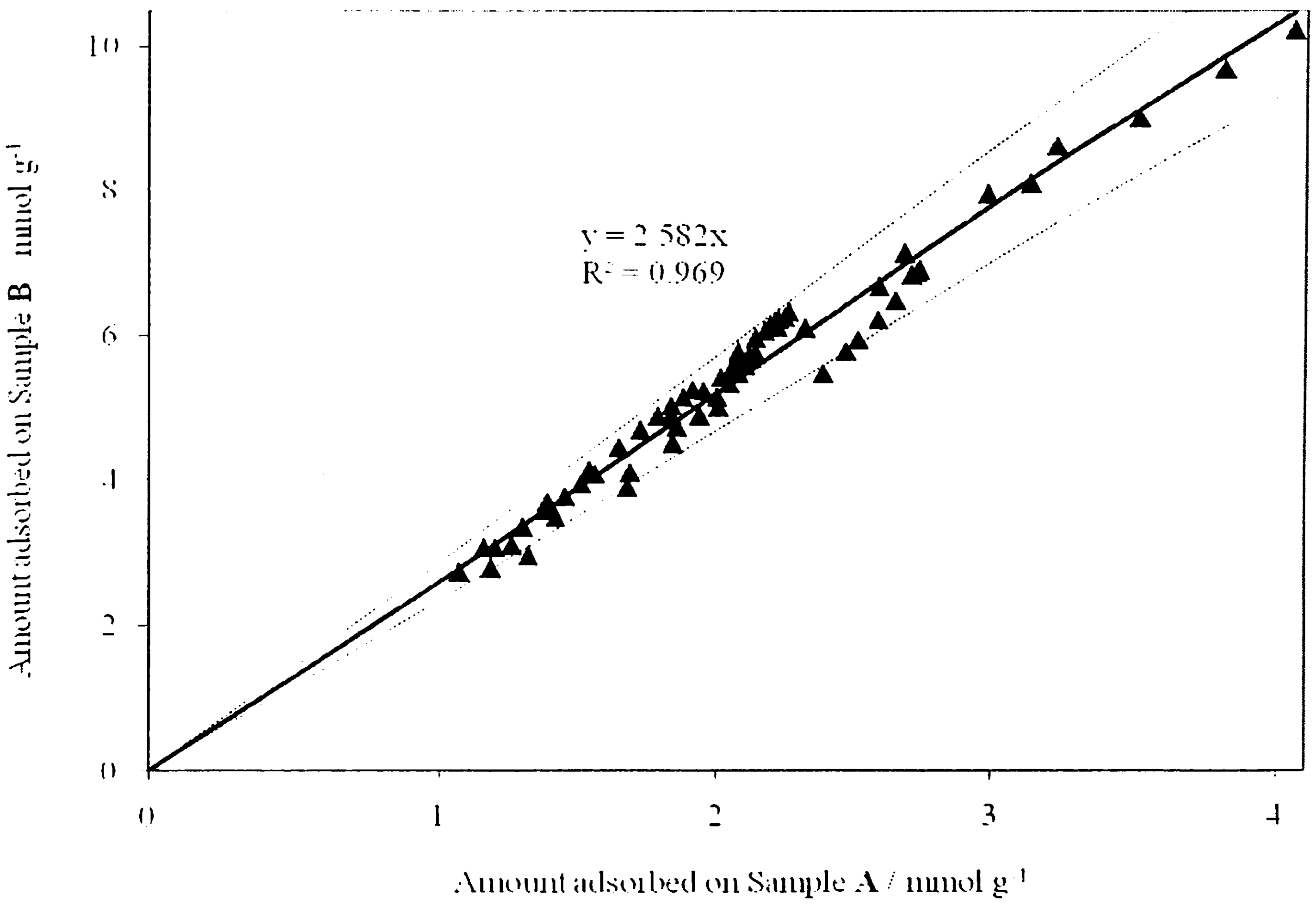

Figure 5.13: Comparison of adsorption capacities of samples **A** and **B** for various gases in high loading region. Abscissa is calculated amount adsorbed on Sample **A** at a given temperature and pressure. Ordinate is for adsorption on Sample **B** at the same temperature and pressure. Solid Line is best fit straight line through origin, with equation as shown; broken lines are 10% envelopes around the best fit line.

As shown in Fig. 5.12, in the low loading region (ca. <1.1 mmol g^{-1} adsorbed on **A**) a scaling factor of 2.04 can be used to relate the adsorption isotherms of all gases on the two samples **A** and **B** with in the 10% error envelope. At the limit of zero pressure the scaling factor will be same as ratio of Henry constants which varies from 1.8 to 2.0 for most gases. In the high loading region (Fig. 5.13) the best fit straight line gives a scaling factor of about 2.58; the 10% error envelopes enclose all the data.

As the loading increases lateral interactions also increase; the increase in lateral interactions will probably be more significant in materials having larger pore volume (Sample **B** in this case). This results in a greater increase in loading with pressure for adsorbent i.e. for Sample **B**; in effect the scaling factor increases with loading.

As highlighted by these results, one needs to be careful when comparing experimental data between different samples or results between experiments and simulations. Simulations are usually performed over pure adsorbent material, which is generally considered free of impurities and other defects. Using a single scaling factor value to account for these differences in the synthesized samples, may not give a complete match in the isotherms. This may also be one of the reasons for significant deviation observed between experiment and simulation results at high pressure although they agree with one another in the low pressure region **[37, 80]**.

5.2.2.3 Enthalpy of Adsorption on Cu-BTC (sample **B**)

Enthalpy of adsorption at zero loading was calculated using the model parameters for various gases. The relation for $-\Delta h_{ads,0}$ can be obtained by taking limit to isosteric heats Eq. 3.49 and 3.50 at zero pressure. For a Langmuir model it is same as that of Eq. 3.49 but for virial model this equation reduces to

$$\Delta h_{ads,0} = \lim_{P \to 0} \Delta h_{ads} = \beta_1 \tag{5.2}$$

Fig. 5.14 shows the enthalpy of adsorption at zero loading versus polarizability of the adsorbate molecules. Since N_2, O_2 and Ar have almost identical values, only Ar is shown in the plot.

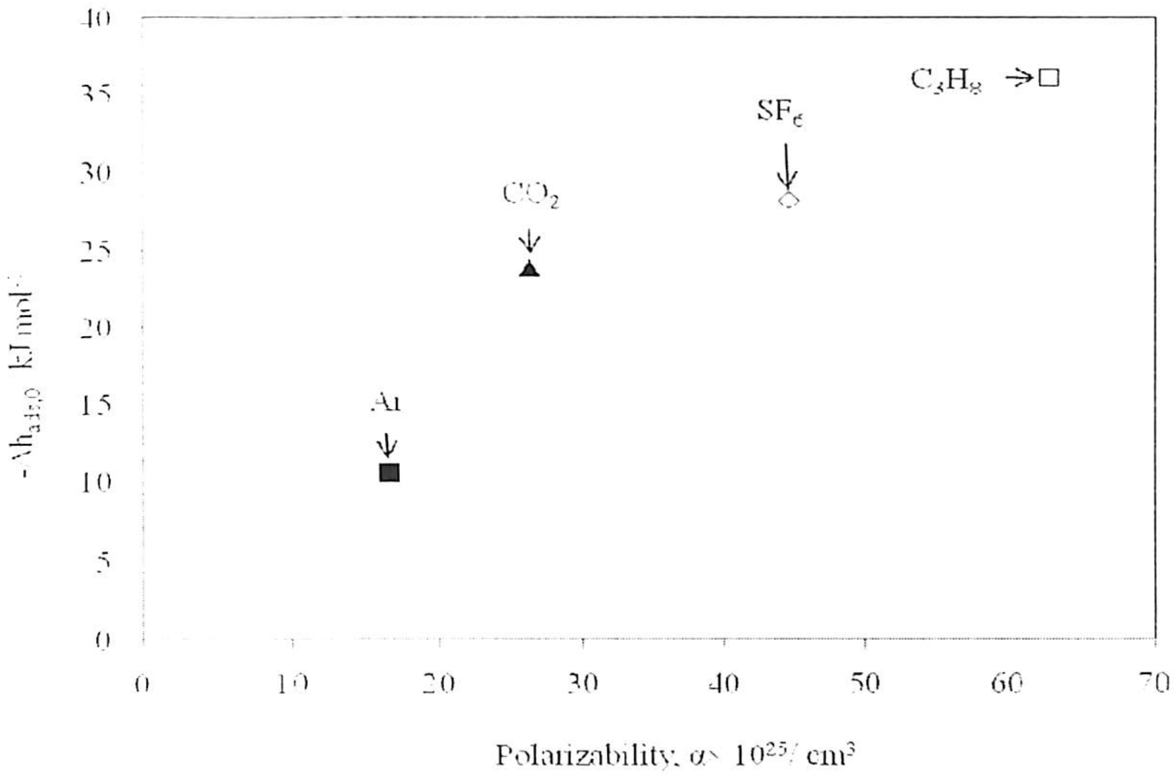

Figure 5.14: Enthalpy at zero loading vs. polarizability on Cu-BTC (sample **B**)

It is very clear from Fig. 5.14 that the limiting enthalpy of adsorption value for most gases varies between 11 to 35 kJ mol^{-1}. The limiting enthalpy of adsorption is a strong function of polarizability and increases linearly with polarizability for Ar, SF_6 and C_3H_8. The only notable exception is observed for CO_2. A higher value for CO_2 is probably due to its high quadrupole moment.

5.3 Gas Adsorption Properties of Cr-BDC Framework (or MIL-101)

This section deals with measurement and modeling of gas adsorption properties on MIL-101 (Cr-BDC) framework. In the first section, characterization of the framework is presented followed by adsorption equilibrium measurements in the subsequent section.

5.3.1 Characterization

5.3.1.1 Thermogravimetric Analysis

The weight loss curve for Cr-BDC was plotted from a thermo gravimetric analysis data (Fig. 5.15). Similar to those reported earlier in literature **[75]**, it shows two distinct weight loss steps. The first step, in the range from 298 to 523 K corresponds to the loss of guest water molecules; the second weight loss step (573 to 673 K) is due to the elimination of OH/F groups leading to the decomposition of the framework **[75]**. The true weight of the sample was taken to be the one after the initial weight loss step at about 403 K.

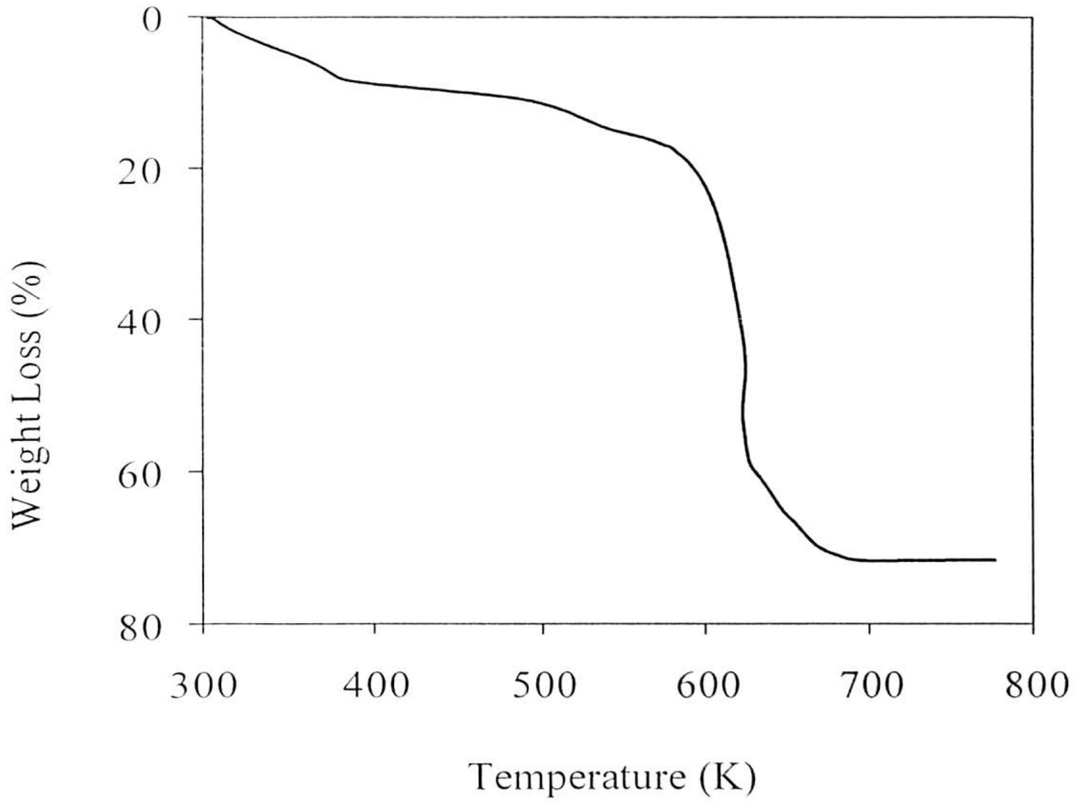

Figure 5.15: Thermogravimetric analysis of Cr-BDC.

5.3.1.2 BET Surface Area Analysis

The N_2 adsorption isotherm plot measured at 77 K is shown in Fig. 5.16. The specific surface area and total pore volume were found to be 2674 m^2 g^{-1} and 1.38 cm^3 g^{-1} respectively. According to IUPAC nomenclature, the isotherm obtained is type IV, characteristic of a mesoporous solid. The point of inflexion shows the formation of a multilayer. The BET surface area and the total pore volume obtained during our synthesis are similar to those reported in other works **[45, 46, 55, 75, 146]**; they are given in table 5.5. The pore size distribution plot is shown in Fig. 5.17. The NLDFT method was used for calculations of pore size distributions from adsorption isotherms in the entire range of micro and mesopores. The plot shows the existence of two maxima centered at pore radii of ca. 1.26 nm and 1.7 nm. The variations between the surface area and pore volume results obtained in this work and that in other works in literature may be attributed to the presence of varying degrees of terephthalic acid which forms during hydrothermal reaction.

Llewellyn et al. [46] showed the importance of post-treatment procedures on the activation of synthesized MIL-101, particularly for CO_2 adsorption. It was shown that difference in activation plays an important role in final surface area and pore volume and consequently affects adsorption characteristics of MIL-101. Our synthesis procedure was similar to that followed by them for synthesis of MIL-101 (sample b) in their work.

Table 5.5: Surface area and pore volume results of different Cr-BDC samples

Researcher	**Surface Area (m^2 g^{-1})**	**Pore Volume (cm^3 g^{-1})**	**Reference**
Férey et al.	4500-5500*	1.5-1.9	75
Llewellyn et al.	2800, 3780, 4230	1.37, 1.74, 2.15	46
Senkovska et al.	2693	1.303	45
Liu et al.	2578	1.250	146
Li et al.	2931	1.450	55
Present Work	2674	1.38	147

* Langmuir surface area

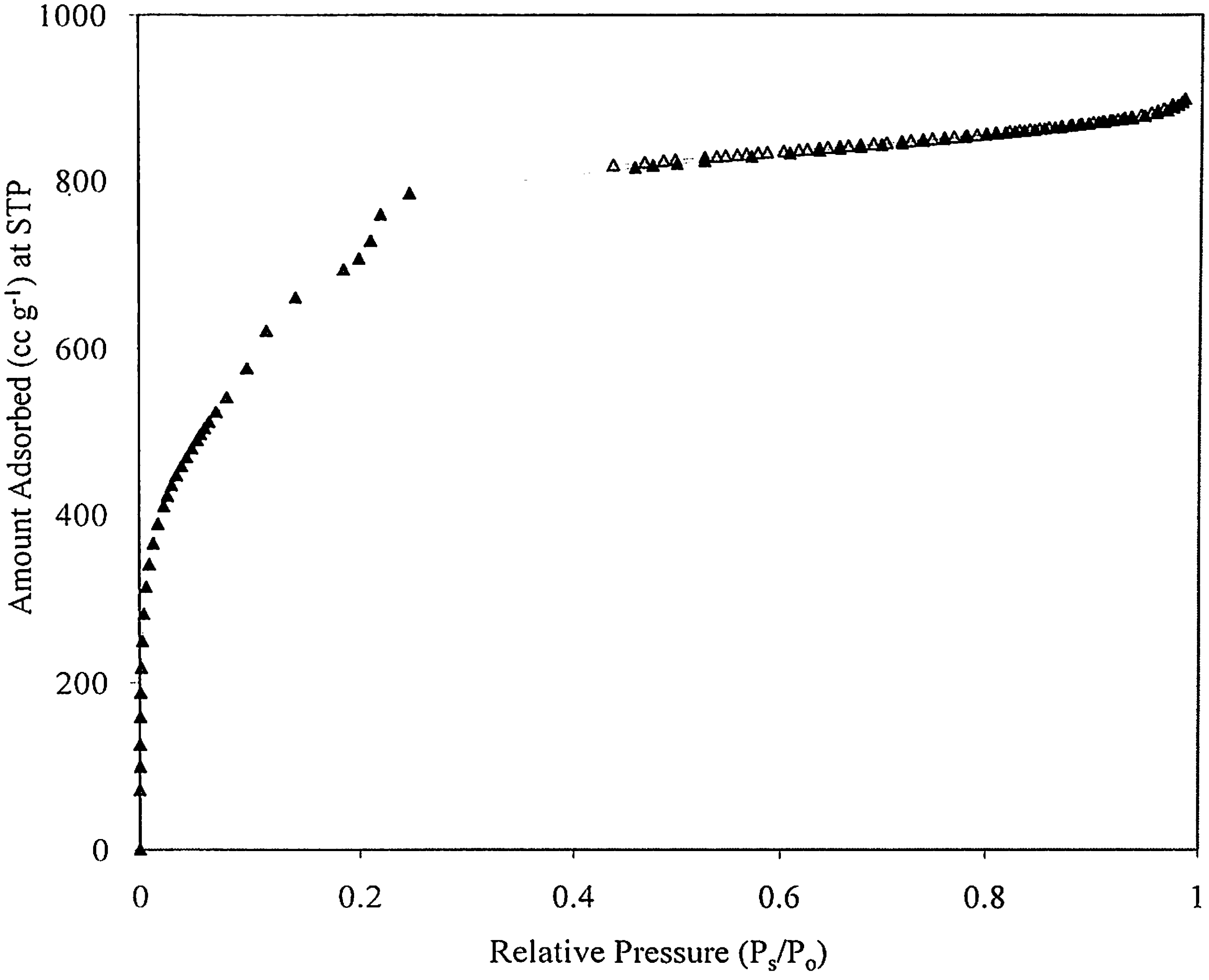

Figure 5.16: N_2 physisorption on Cr-BDC sample at 77 K. Closed triangles denote adsorption step; open triangles denote desorption step.

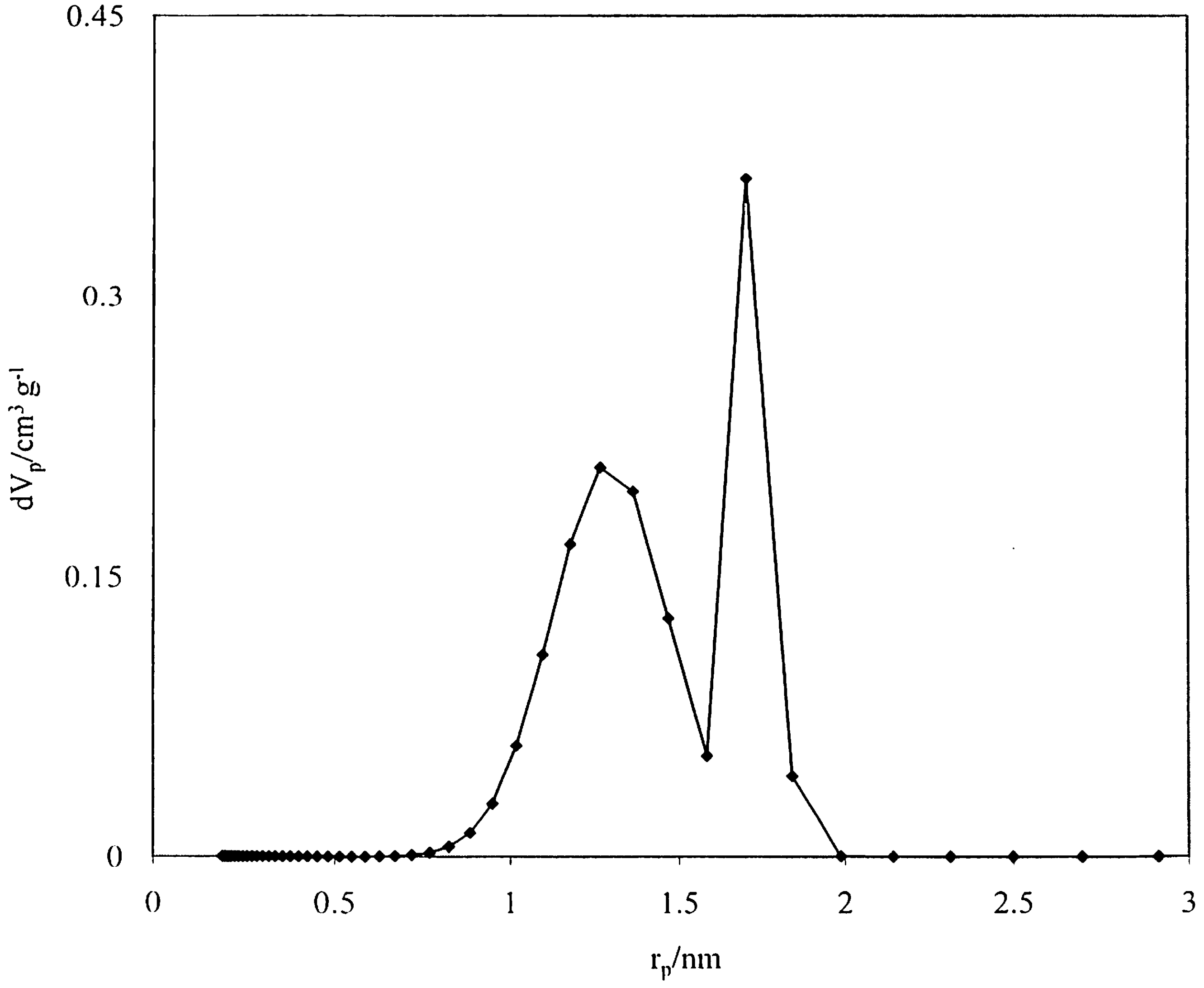

Figure 5.17: Pore size distribution of Cr-BDC from N_2 physisorption at 77 K.

5.3.1.3 SEM and Powder XRD Analysis

The scanning electron microscopy images (Fig. 5.18) shows the morphology of the synthesized material and the crystallized product is octahedral in nature. The bulk of the product looks uniformly distributed with a few exceptions, where we can see large crystals. Powder XRD patterns (Fig. 5.19) further confirms the crystallinity of the synthesized product and the pattern matches with that published literature **[55]**.

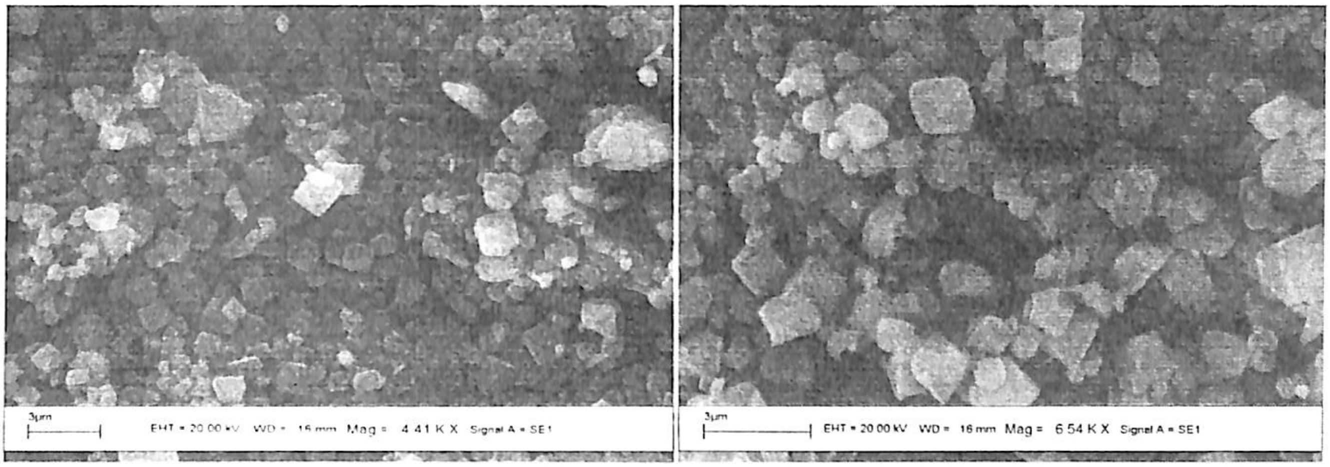

Figure 5.18: Scanning electron microscopy images of Cr-BDC sample at two different magnifications.

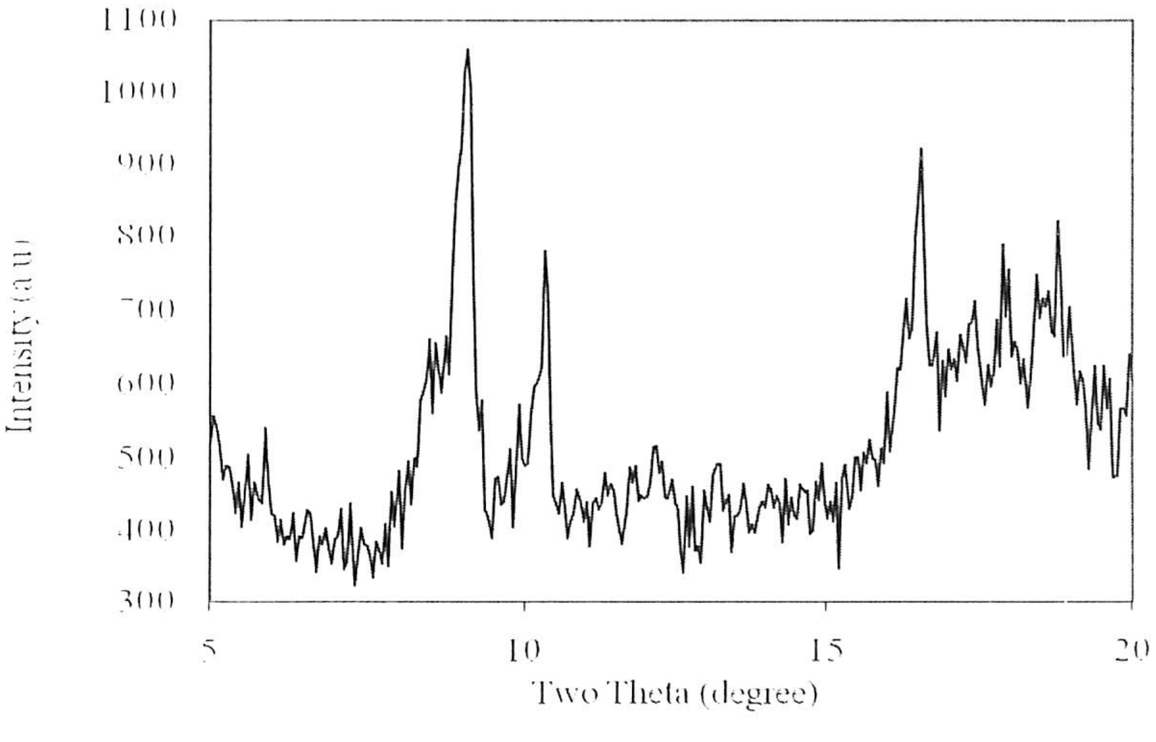

Figure 5.19: Powder XRD pattern of Cr-BDC

5.3.2 Measurement of Adsorption Isotherms on Cr-BDC

Isotherms of several gases (Ar, CH_4, CO_2, C_3H_8 and SF_6) were measured at three different temperatures on Cr-BDC framework.

It is however important to mention that, adsorption experiments on Cu-BTC indicated that N_2, O_2, and Ar loadings are very small and comparable to each other; moreover they exhibit little selectivity for N_2 over O_2. These results prompted us to neglect measurement of N_2 isotherms on Cr-BDC; only Ar isotherms were measured.

Figures 5.20-5.24 show adsorption isotherms for various gases on Cr-BDC. All isotherms are plotted in conventional (N vs. P) domain as well as in virial domain [$\ln(P/N)$ vs. N]. A logarithmic axis was chosen to cover two decades of pressure range and highlight the goodness of fit with the Dual Site Langmuir (DSL) model (as explained later).

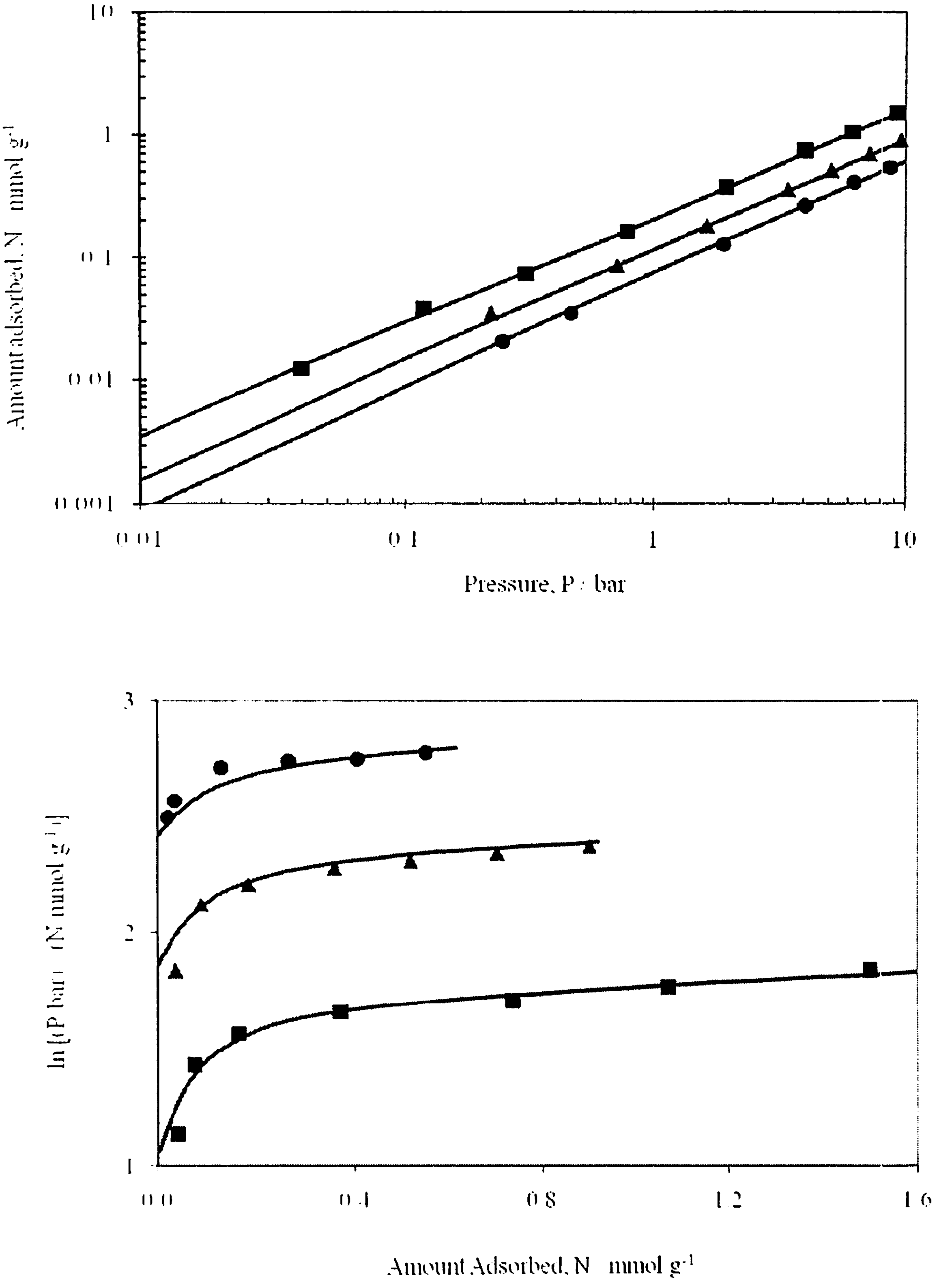

Figure 5.20: Adsorption Isotherms of Argon on Cr-BDC. Points: experimental data; Line: Dual Site Langmuir Model. Squares: 283 K, Triangles: 319 K and Circles: 351 K.

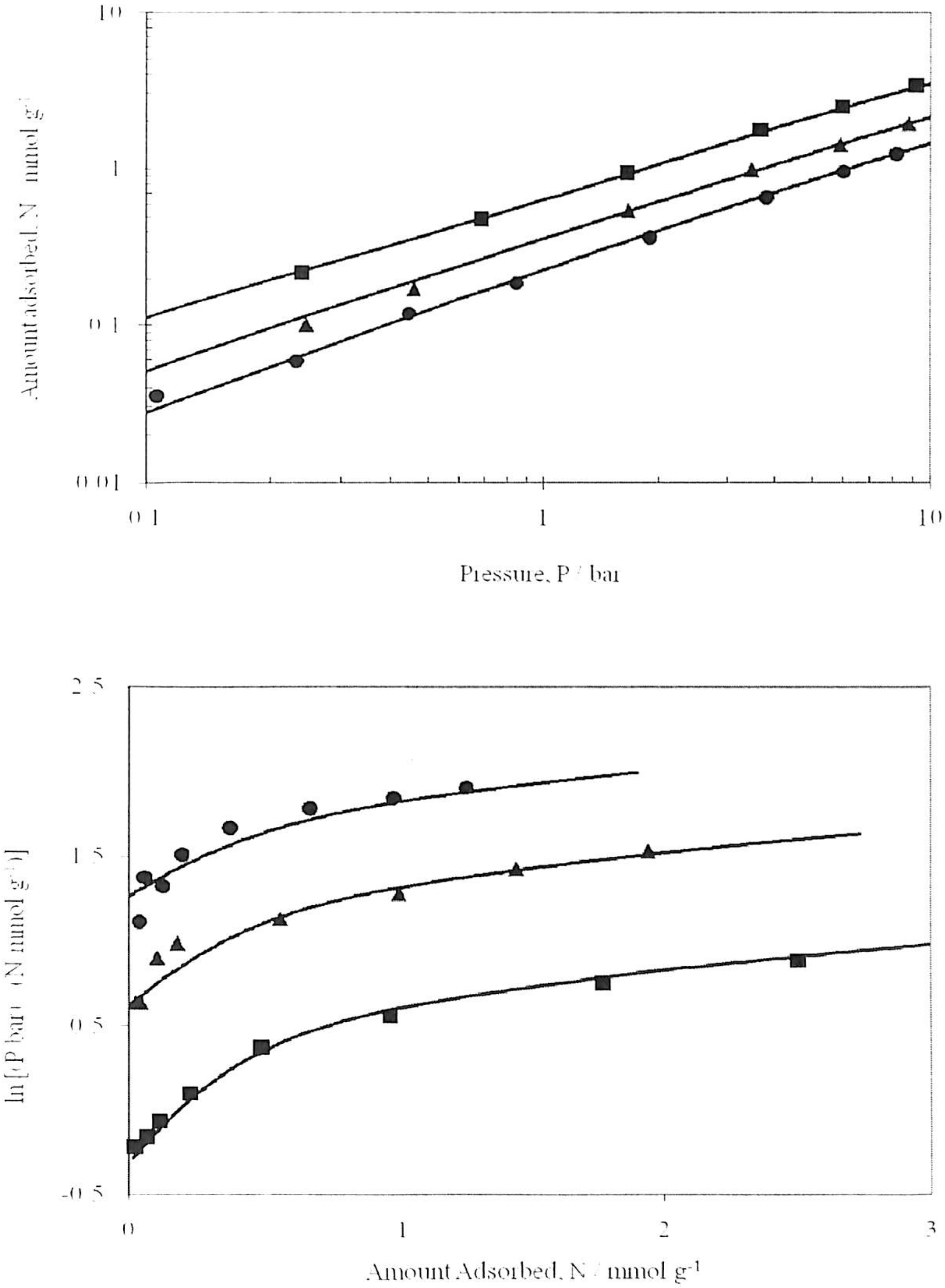

Figure 5.21: Adsorption Isotherms of CH_4 on Cr-BDC. Points: experimental data; Line: Dual Site Langmuir Model. Squares: 283 K, Triangles: 319 K and Circles: 351 K.

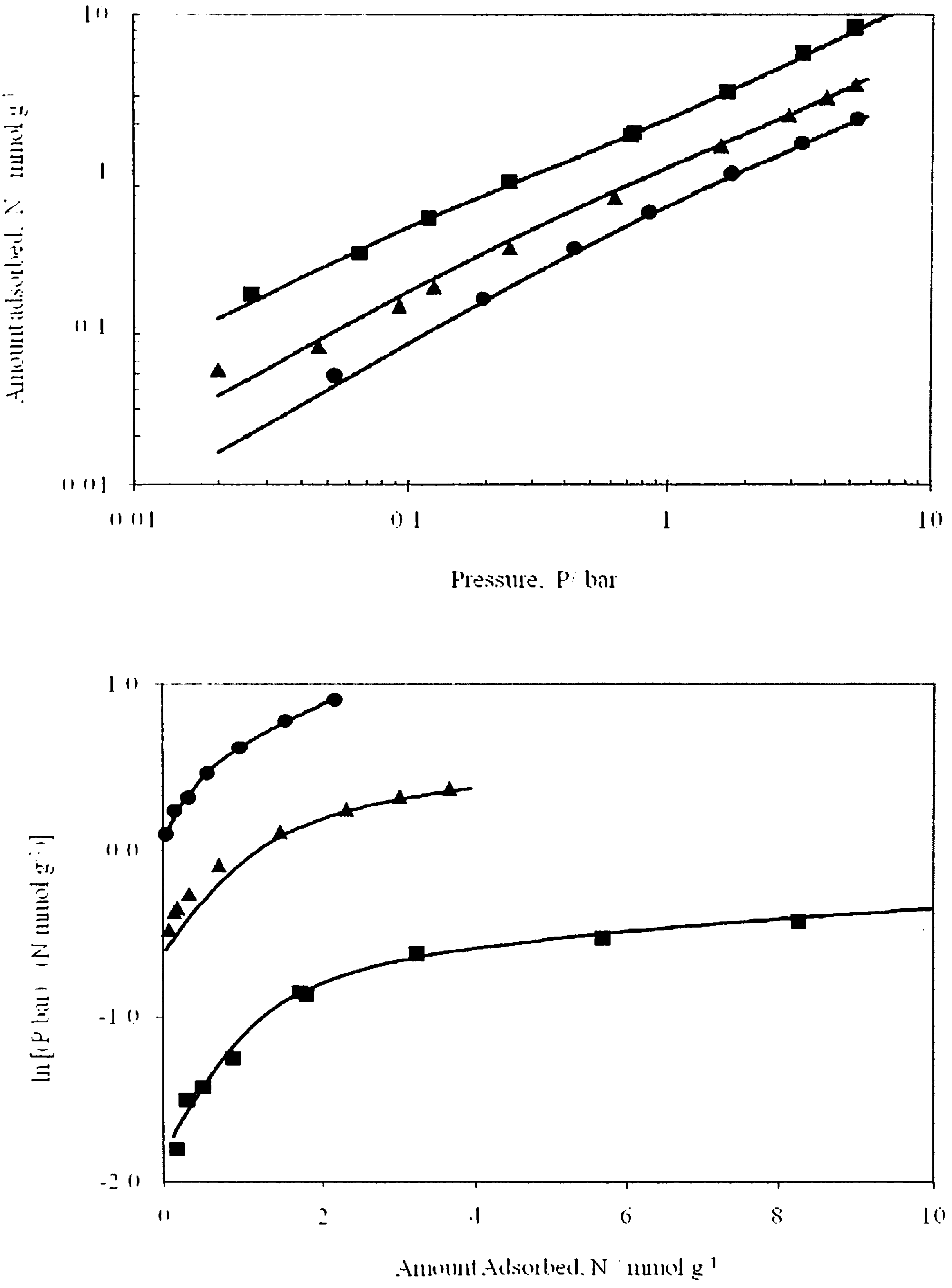

Figure 5.22: Adsorption Isotherms of CO_2 on Cr-BDC. Points: experimental data; Line: Dual Site Langmuir Model. Squares: 283 K, Triangles: 319 K and Circles: 351 K.

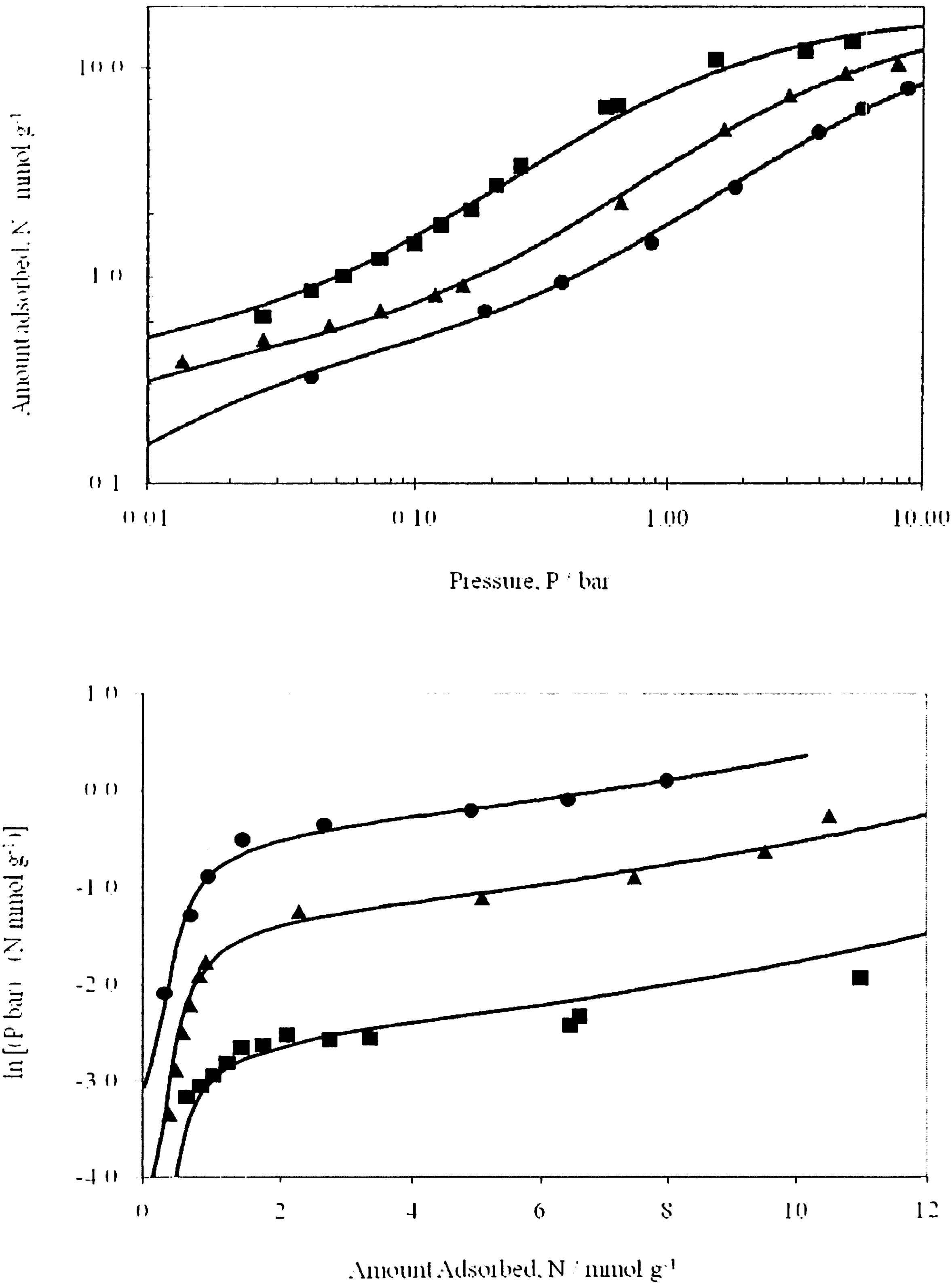

Figure 5.23: Adsorption Isotherms of C_3H_8 on Cr-BDC. Points: experimental data; Line: Dual Site Langmuir Model. Squares: 283 K, Triangles: 319 K and Circles: 351 K.

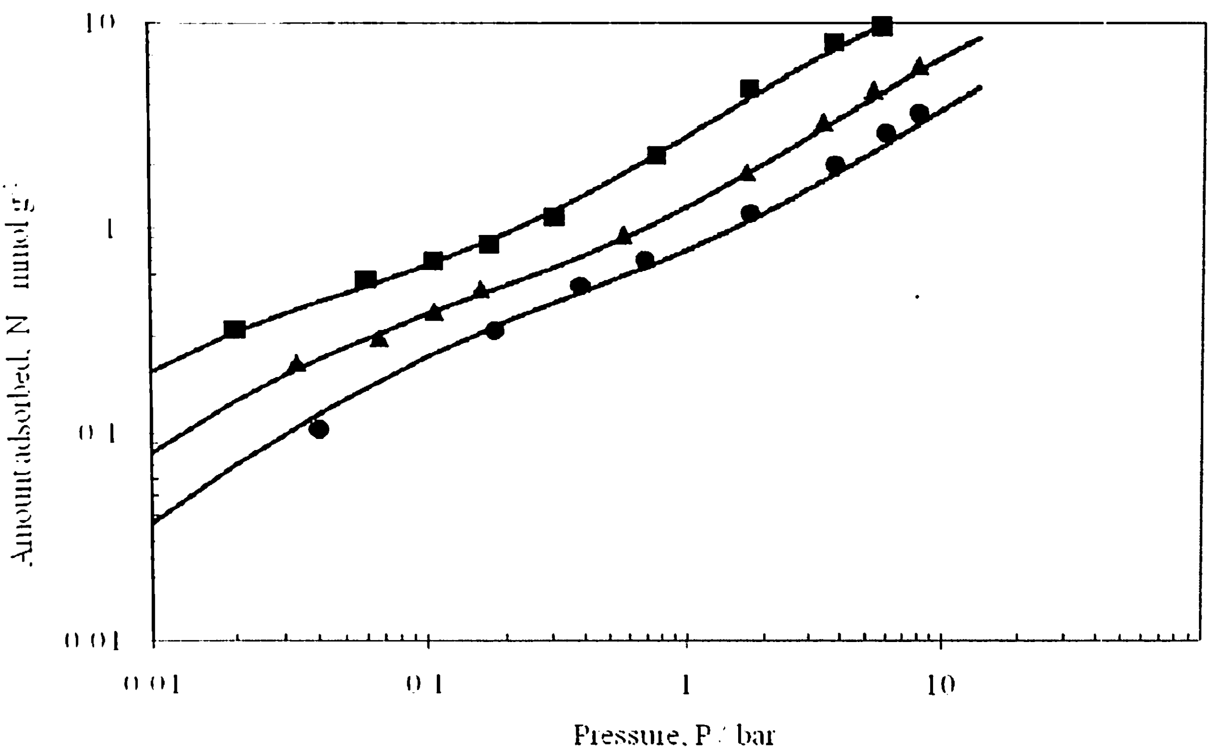

Figure 5.24: Adsorption Isotherm of SF_6 on Cr-BDC. Points: experimental data; Line: Dual Site Langmuir Model. Squares: 283 K, Triangles: 319 K and Circles: 351 K.

The experimental data show that the adsorption capacity increases with the polarizability of the adsorbate. The maximum adsorption capacity was obtained for C_3H_8 (13.4 mmol g^{-1}) at 5.3 bar and 283 K. At the same conditions the adsorption capacities for other gases viz. SF_6, CO_2, CH_4 and Ar are, 9.1, 8.0, 2.2 and 0.9 mmol g^{-1} respectively. The capacities for all these gases on Cr-BDC below 10 bar seem to be lower than that on Cu-BTC at all temperatures. For non-polar gases like Ar and CH_4, the loadings are comparable to that on a purely siliceous zeolite like silicalite under similar conditions **[103, 148]**. The loadings for other gases are higher compared to silicalite **[103]**.

In case of CH_4 the loading at 1 bar and ambient temperature is slightly lower than those on activated carbon, zeolite 5A, 13X while it is better than that on zeolites like NaY, MgY, Al based MOF i.e. MIL-53 and comparable to zeolites CaY, BaY (Table 2.7).

When compared to other adsorbents, loading for CO_2 on Cr-BDC at about 1 bar and ambient temperature is lower than that on zeolites having framework polarity like Na ETS-4, 13X, 5A, H-Mordenite, and activated carbon (Norit R1). Although, Henry's constant for CO_2 adsorption at 318 K for Cu-BTC **[149]** was about 3.14 as compared to 1.86 mmol g^{-1} bar^{-1} on Cr-BDC, at higher pressures exceptional CO_2 capacity of this class of adsorbent were reported by Llewellyn et al. **[46]**. At around 1 bar and ambient temperature, CO_2 loading on this material is better than that on other MOFs like IRMOF-1, MOF-5, ZIF-8 and Al based MIL-53 (Table 2.6).

Both C_3H_8 and SF_6 have no dipole moment; while only C_3H_8 has a quadrupole moment which is three times smaller than that of CO_2. Hence the framework polarity does not play a significant role in adsorption of these gases as in case of CO_2. In fact, the loading of C_3H_8 at about 1 bar and ambient temperature on Cr-BDC is better than that on activated carbon, zeolites like silicalite, NaX and H-Mordenite and comparable to that on Cu-BTC. SF_6 adsorption on Cr-BDC is better at 1 bar and ambient temperature and is more than zeolites like NaX and silicalite but lower than that on BPL carbon (Tables 2.8 and 2.10).

5.3.3 Modeling

A careful review of the literature suggests that there are two major sites for adsorption on these frameworks. In the initial loading region, a strong interaction occurs between the Cr^{3+} metal centers and the adsorbate molecules; however the amount adsorbed on these sites is small, since they may be usually poisoned by coordinated terephthalic acid or by the presence of water molecules **[46, 52, 150]**. A considerable amount adsorbs within the pores through slightly weaker interactions of adsorbate molecules with sites in the super tetrahedra. Earlier observations on enthalpies of adsorption for CO_2 and CH_4, suggest a sharp decline in enthalpy after initial loading [55]. Such a behavior clearly indicates heterogeneity for adsorption on the solid.

Purely from an experimental data analysis perspective, in a virial domain plot such as the one shown in Fig. 5.25, a clear step is visible around a loading of about 2 mmol g^{-1}. This behavior is typical for a heterogeneous adsorbent, which is usually not evident when isotherm is plotted in conventional *N* vs. *P* domain. Such behavior was observed for all the gases studied in this work, indicating that the adsorbent is energetically heterogeneous to adsorption of these gases on Cr-BDC. Moreover, a Langmuir isotherm is not suitable to model the knee observed as shown in the same Fig. 5.25.

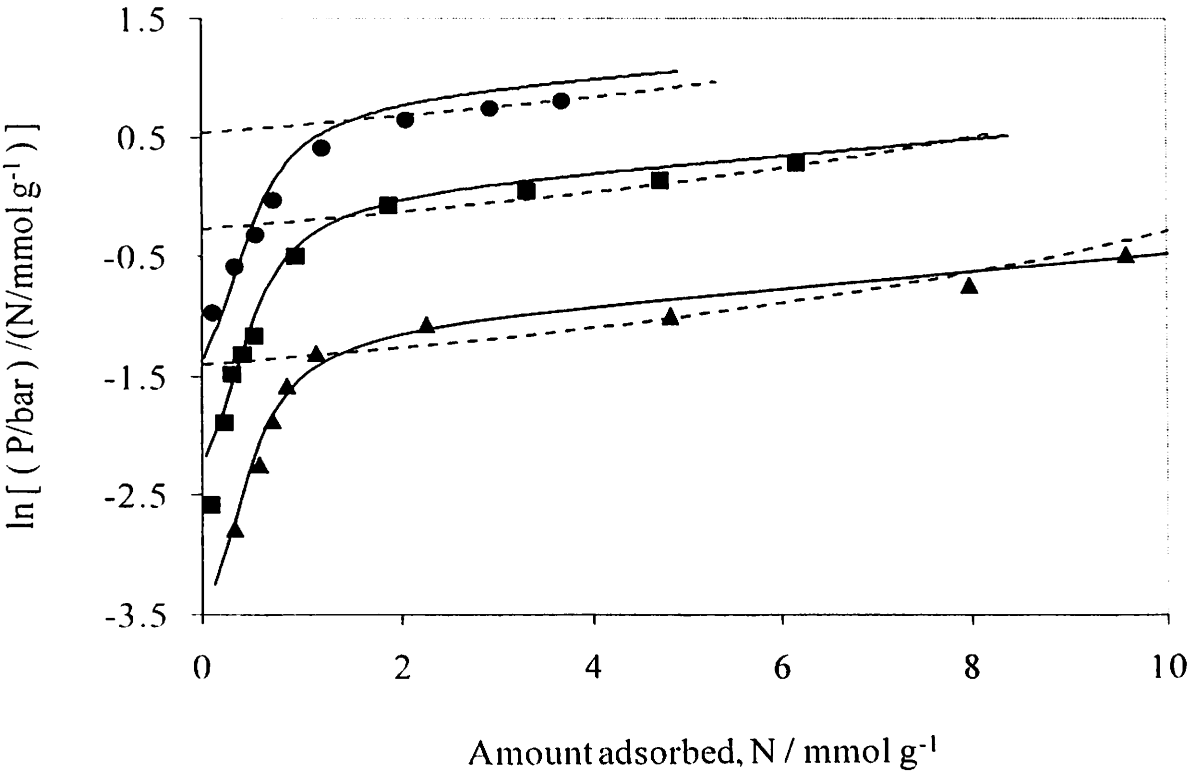

Figure 5.25: Virial domain plot of SF_6 on Cr-BDC. Points: experimental data; Triangles: 283 K, Squares: 319 K and Circles: 351 K. Solid lines are best fits from Dual Site Langmuir model, broken lines are best fits from Langmuir model.

In an attempt to model the adsorption behavior of various adsorbates studied in this work, a Dual Site Langmuir (DSL) model **[116]** was used to account for heterogeneity. The model assumes two distinct sites exist with different energitics for adsorption; any other sites of different energy are lumped into one of these two sites. The DSL model for amount adsorbed is given by Eq. 3.37. The temperature dependency of the parameters is shown in Eq. 3.38 and Eq. 3.39.

All experimental data from the three temperatures was regressed to obtain the parameters for the model individually for each gas. These parameters are given in Table 5.6 where the reference temperature T_0 = 283 K for chosen all gases.

Table 5.6: Dual Site Langmuir isotherm parameters for adsorption on Cr-BDC

Parameters	Gases				
	Ar	CH_4	CO_2	SF_6	C_3H_8
$M^{(1)}$ (mmol g^{-1})	0.031	0.250	0.700	0.460	0.410
Std. Error	0.0174	0.0558	0.249	0.0322	0.0378
t	2.059	4.527	2.821	14.225	10.961
$M^{(2)}$ (mmol g^{-1})	14.3	11.8	58.6	23.1	17.8
Std. Error	13.15	1.195	86.661	7.531	1.211
t	1.09	9.889	0.676	3.072	14.707
$\delta^{(1)}$ (bar^{-1})	4.9	3.5	6.4	66.7	1158.0
Std. Error	2.679	1.407	2.496	9.12	946.38
t	1.832	2.522	2.548	7.312	1.224
$\delta^{(2)}$ (bar^{-1})	0.012	0.038	0.027	0.112	0.683
Std. Error	0.0129	0.0058	0.0451	0.0439	0.0749
t	0.943	6.547	0.596	2.553	9.119
$-\Delta h_{ads}^{(1)}$ (kJ mol^{-1})	21.8	22.2	26.4	26.0	37.9
Std. Error	2.917	3.36	2.172	1.807	10.991
t	7.481	6.6	12.179	14.4	3.45
$-\Delta h_{ads}^{(2)}$ (kJ mol^{-1})	12.9	14.3	19.8	23.0	25.5
Std. Error	0.602	0.241	1.245	2.372	0.718
t	21.478	59.145	15.942	9.676	35.509

Several interesting observations can be made. First, the saturation loading $N_i^{\max}$ on each of the sites is widely different. The sites of Type **1** are roughly one to two orders of magnitude lower than that of sites of Type **2**. This indicates only few active coordinatively unsaturated sites (*cus*) with metal centers are available on this framework. As mentioned earlier, this is probably due to the poisoning of the Lewis acid metal sites by impurities. The saturation loading for each type of site are similar for all adsorbates. A notable exception is carbon dioxide, which is known to have a high loading on Cr-BDC **[46]**; it has higher saturation capacity on both types of sites than any other gas. The parameter $-\Delta h_{ads}^{(i)}$ in the model, which is related to the enthalpy of adsorption, is directly proportional to polarizability. However, for CO_2, which has almost same polarizabilty as that of CH_4, this value is higher because of its quadrupole moment. Detailed analysis of enthalpy of adsorption is presented next.

5.3.4 Calculation of Adsorption Enthalpies

The enthalpy due to adsorption Δh_{ads} can be readily calculated from the DSL model **[116]** using Eq. 3.51. The enthalpy of adsorption at zero coverage, $\Delta h_{ads,0}$ is obtained by taking the limit at zero pressure:

$$\Delta h_{ads,0} = \lim_{P \to 0} \Delta h_{ads} = \frac{\Delta h_{ads}^{(1)} M^{(1)} \delta^{(1)} + \Delta h_{ads}^{(2)} M^{(2)} \delta^{(2)}}{M^{(1)} \delta^{(1)} + M^{(2)} \delta^{(2)}} \tag{5.3}$$

The enthalpy at zero coverage can also be used to describe variation of Henry's constant H with temperature through

$$\beta = \beta_{(0)} e^{-\Delta h_{ads,0}/RT} \tag{5.4}$$

Where $\beta_{(0)}$ is related to entropy of adsorption.

5.3.5 Variation of Adsorption Enthalpy with Loading

The values of Δh_{ads} were plotted as a function of (number of gas molecules adsorbed per metal center) in Fig. 5.26. Clearly, for all adsorbates, $-\Delta h_{ads}$ decreases substantially with loading. This decline is observed between 0.1 and 0.2 molecules adsorbed per metal center, indicating that a fraction of metal centers (sites of Type 1) are available for adsorption of these gases; whereas others may have been poisoned as discussed in earlier works **[46]**. The trend is also evident for an inert gas such as Ar where, $-\Delta h^{1}_{ads}$ decreases from 15 to 12.5 kJ mol^{-1}, suggesting a strong heterogeneity in the adsorbent surface. This enthalpy is comparable to adsorption on zeolites like silicalite, NaX and Na-ZSM-5, which have values between 13 and 18 kJ mol^{-1} **[82, 84]**. The enthalpy of adsorption for CH_4 starts at about 19 kJ mol^{-1} close to those on other MOF materials like MIL-100, MIL-53 **[151]** and falls down to a value of 14.2 kJ mol^{-1} at higher loadings. The heat of adsorption for CO_2 is slightly lower than the one obtained by Llewellyn et al. **[46]**, but the trend is similar to their observations on similarly activated MIL-101 materials (material indicated as MIL 101^{b} in their article). The heats of adsorption for SF_6 follow a similar trend as that of CO_2, with slightly higher values. C_3H_8 however sees a sharp drop in enthalpy at low loadings more than other gases. This indicates a strong interaction between C_3H_8 molecules and the metals sites; this is also evident from DSL parameter $-\Delta h^{1}_{ads}$, which is higher for C_3H_8 compared to those of other gases.

On zeolites like NaX, Na-ZSM-5 and silicalite the values of enthalpies of adsorption are higher than those on MIL-101. The $-\Delta h_{ads}$ / kJ mol^{-1} values on zeolite materials range between 19 and 27 for CH_4, 27 and 49 for CO_2, 29 and 42 for SF_6, and 38 and 50 for C_3H_8 **[82, 84, 103]**. Thus, for the gases considered in this study, the enthalpies of adsorption in most cases are lower as compared to even a purely siliceous zeolite like silicalite. This represents that these gases only have a moderate interaction with the framework of Cr-BDC.

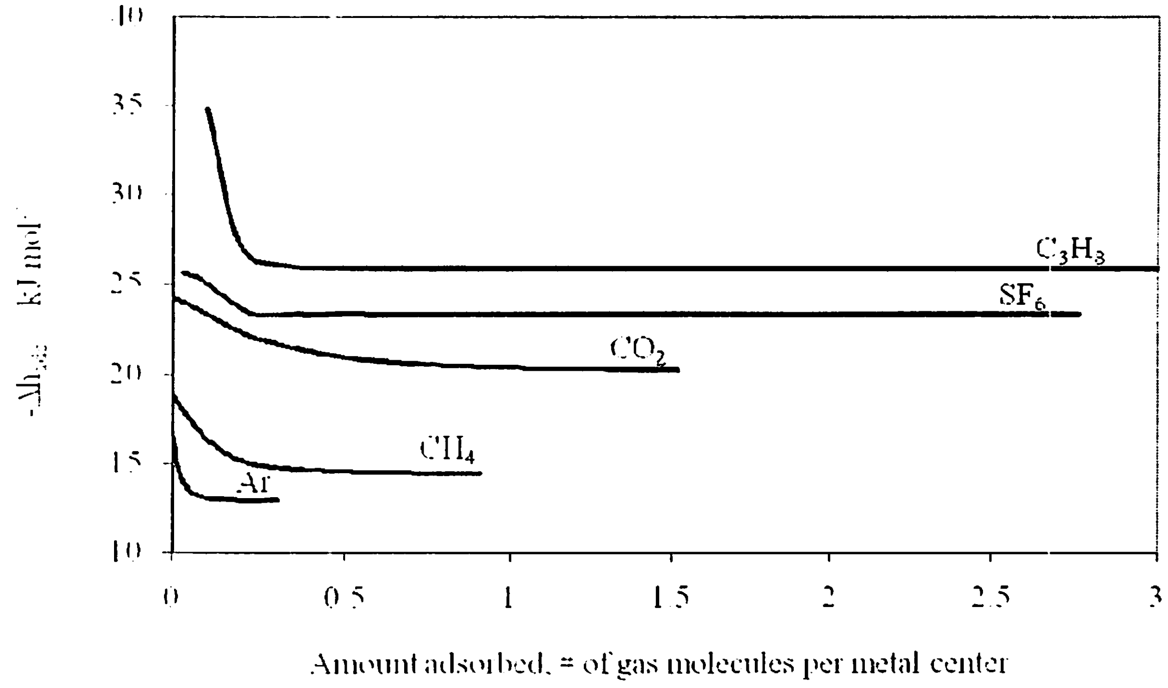

Figure 5.26: Enthalpy of adsorption for various gases on Cr-BDC.

5.3.6 Enthalpy at Zero Coverage

The equations for finding limiting isosteric heat of adsorption at zero coverage are given in Eq. 5.2. The limiting enthalpy of adsorption $-\Delta h_{ads,0}$ shows a linear relationship with polarizability of the adsorbate as shown in Fig. 5.27. This behavior is similar to those observed on zeolitic materials like silicalite **[103]**. The deviation from the trend for CO_2 is probably due to its high quadrupole moment.

Since entropic contributions for adsorption, indicated by the term β_0 in Eq. 5.3 for most of the gases are similar, one can also expect Henry's constant to be directly proportional to polarizability. Fig. 5.28 shows calculated values of Henry's constant at 318 K (via Eq. 5.3) plotted against polarizability of the gas. A linear relation as before is clearly evident, with the exception of CO_2. Plots such as these should be useful to predict behavior of other adsorbates on MOF materials from already available data.

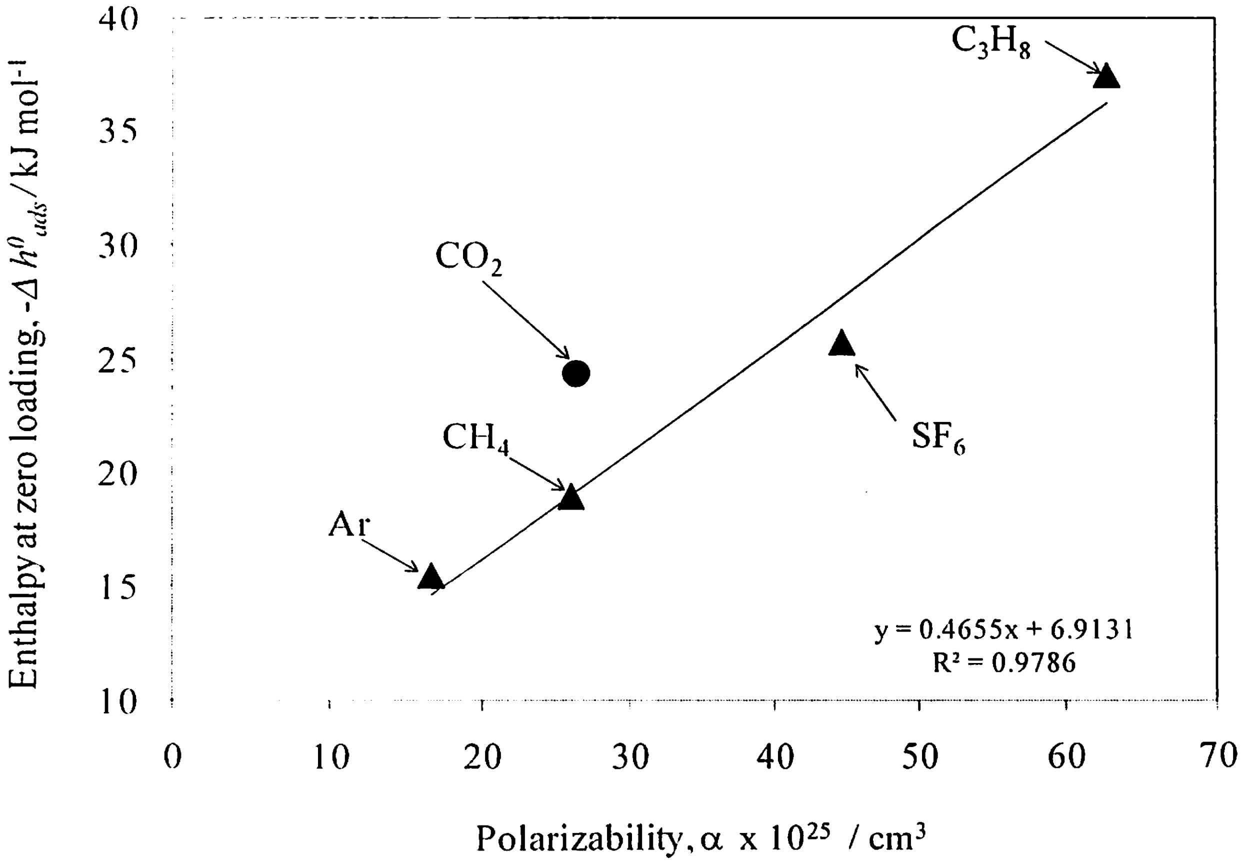

Figure 5.27: Variation of enthalpy at zero coverage with polarizability of adsorbate. Straight line fit excludes CO_2.

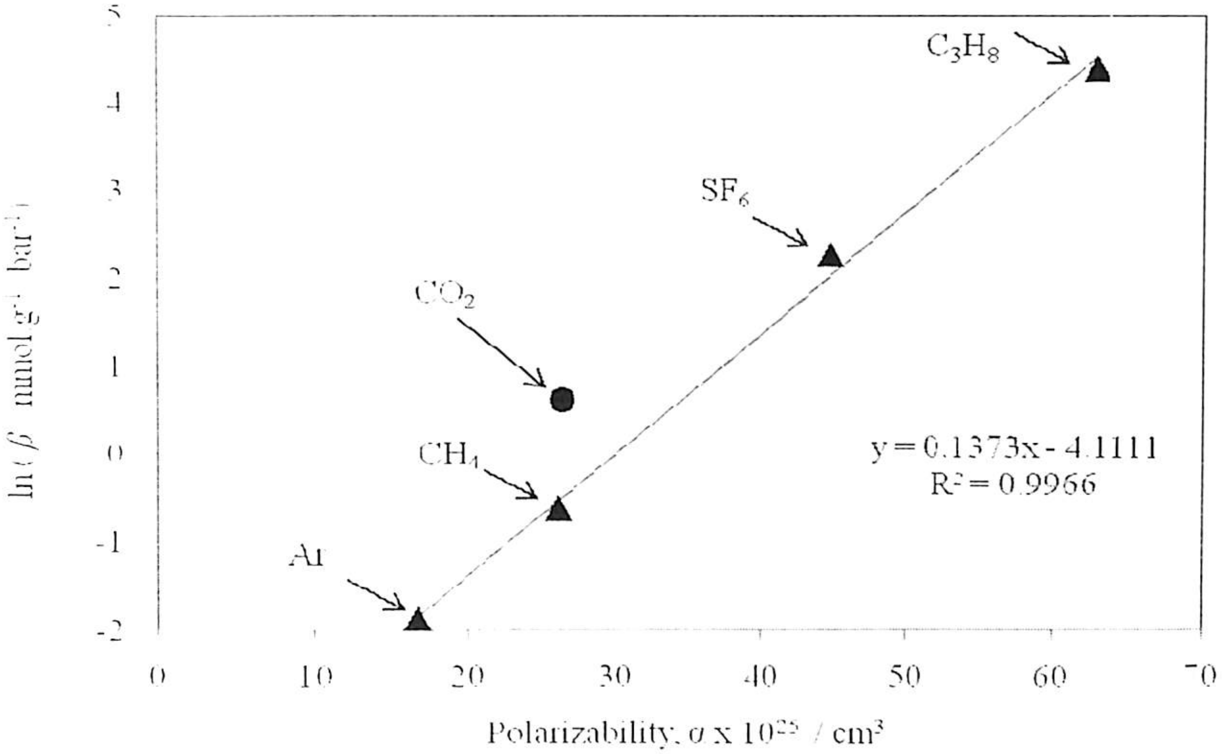

Figure 5.28: Variation of Henry's law constant at 319 K with polarizability of the adsorbate. Straight line fit excludes CO_2.

5.4 Comparative Study of CH_4, CO_2 and CO Adsorption on Cu-BTC and Cr-BDC Metal Organic Frameworks

In this section we present a comparative study of gas adsorption of CH_4, CO_2 and CO on the two frameworks viz. Cu-BTC and Cr-BDC. The rationale behind this choice of adsorbates was because of their industrial importance. Separation of CO_2/CH_4 mixture is very crucial not only for natural gas processing but also important for CH_4 transportation where presence of CO_2 causes severe corrosion to the pipelines. High pressure CH_4 has been a subject of study for adsorbed natural gas (ANG) storage; with a suitable adsorbent it may well replace the more common mode of compressed natural gas (CNG) storage in automobiles. CO_2 adsorption and storage is being widely investigated due to its environmental impact. Separation of CO from mixtures containing CH_4 and/or CO_2 are important since such mixtures are found in a variety of industrial off gases, steam reforming, coal gasification, due to partial oxidation of hydrocarbons etc. Additionally, only limited data was available in literature for CO adsorption on MOFs and high pressure experimental data is unavailable to the best of our knowledge. Wang et al. **[39]** carried out CO adsorption study on Cu-BTC at 295 K and up to 1 bar pressure and compared the results with CO_2, C_2H_4 and CH_4 whereas more recently Karra et al. **[152]** studied the effect of open metal sites of Cu-BTC on adsorption of polar (CO) and non-polar (CH_4) molecules using Grand Canonical Monte Carlo (GCMC) simulations.

Apart from the above mentioned industrial relevance, from a purely fundamental perspective these adsorbates would make an interesting study since CO has a dipole, CO_2 has a quadrupole and CH_4 is non-polar. The effect of electrostatic interactions of adsorbates and their interactions with the two frameworks can be studied. Details of operational ranges for various experiments are given in table 4.2.

5.4.1 Isotherms

Figures from 5.29 to 5.31 show the isotherms for CH_4, CO_2 and CO on Cu-BTC; the isotherms on Cr-BDC are given in Figs. 5.32 through 5.34. Fugacity is used for bulk gas phase to account for it non-ideal nature, which will be significant for the pressures studied. Details of EoS used for fugacity calculations are given in section 3.7.7. The isotherm plots for all three gases are drawn in conventional [N *vs.* f] as well as virial domain [$\ln(f/N)$ *vs.* N]. Even at pressures as high as 50 bar and 295 K, the loading for methane on both Cu-BTC and Cr-BDC is higher than those on activated carbons (BPL, Norit), purely siliceous zeolite like silicalite and even on polar zeolites like 13X, 5A, NaY and MgY. The results for Cu-BTC also compare well and are close to those reported earlier in literature [Table 2.7]. However, for MIL-101, the value are about 10-15% lower than those reported by Llewellyn et al. [46] on their sample MIL-101^b.

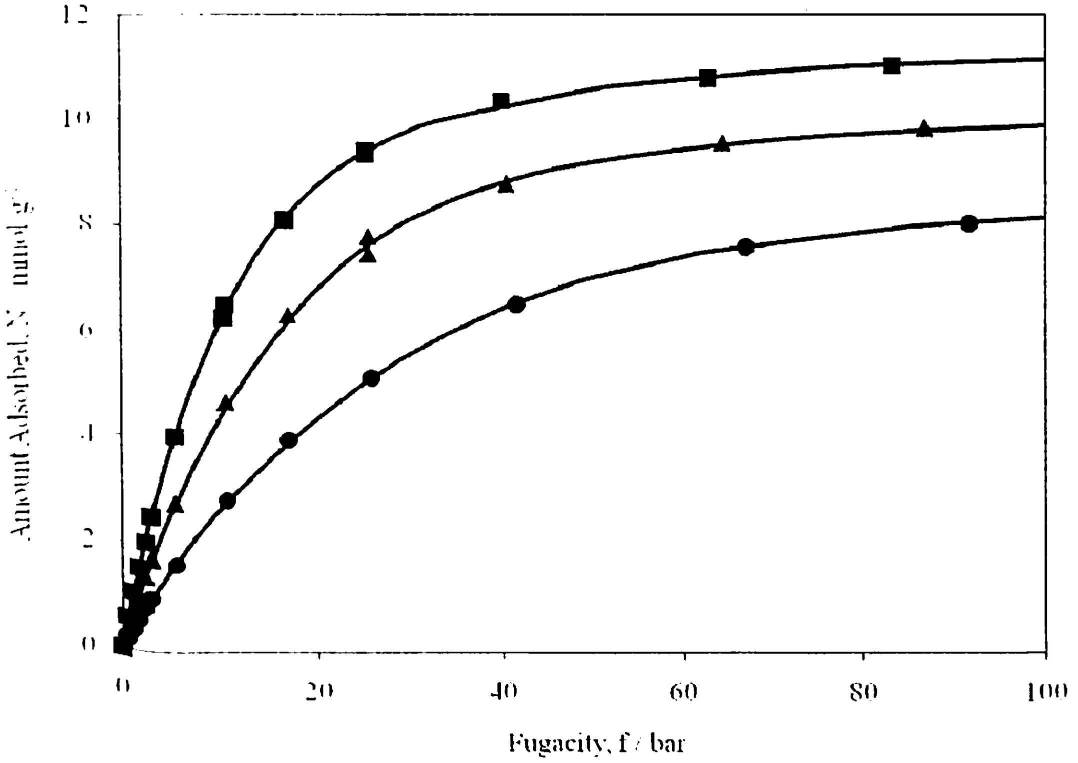

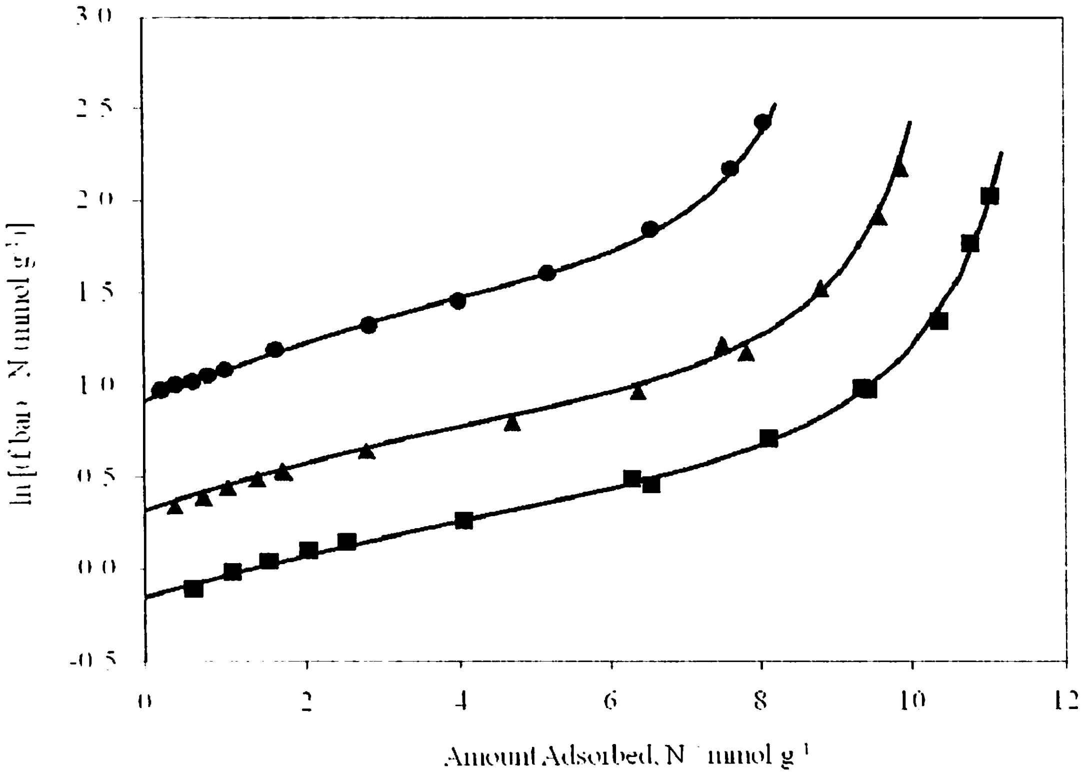

Figure 5.29: Adsorption isotherms for CH_4 on Cu-BTC. Symbols: Experimental points. Lines: Virial-Langmuir model fits. Squares: 295 K, Triangles: 318 K, Circles: 353 K.

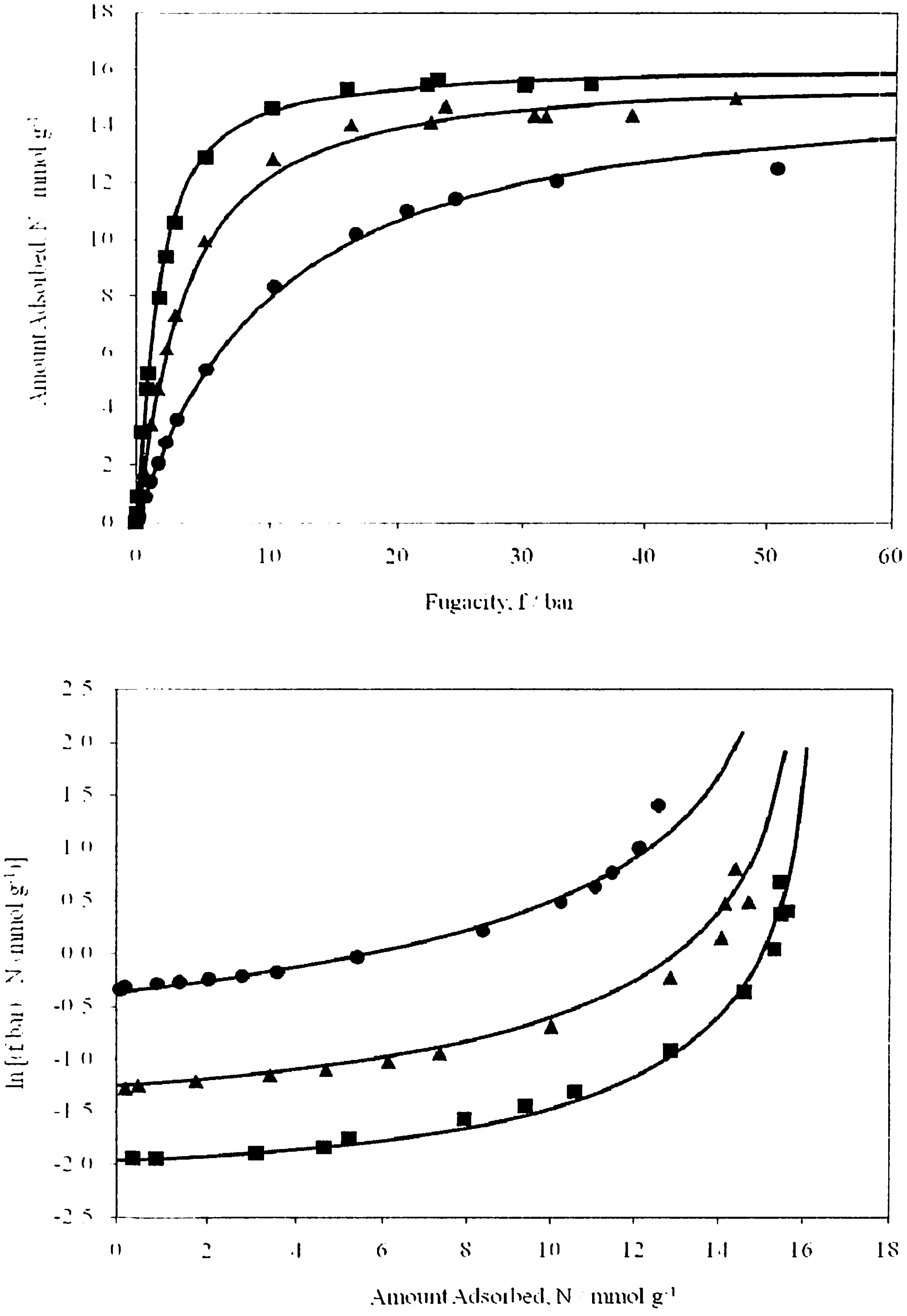

Figure 5.30: High pressure adsorption isotherms for CO_2 on Cu-BTC. Symbols: Experimental points, Lines: Virial-Langmuir model fits. Squares: 295 K, Triangles: 318 K, Circles: 353 K.

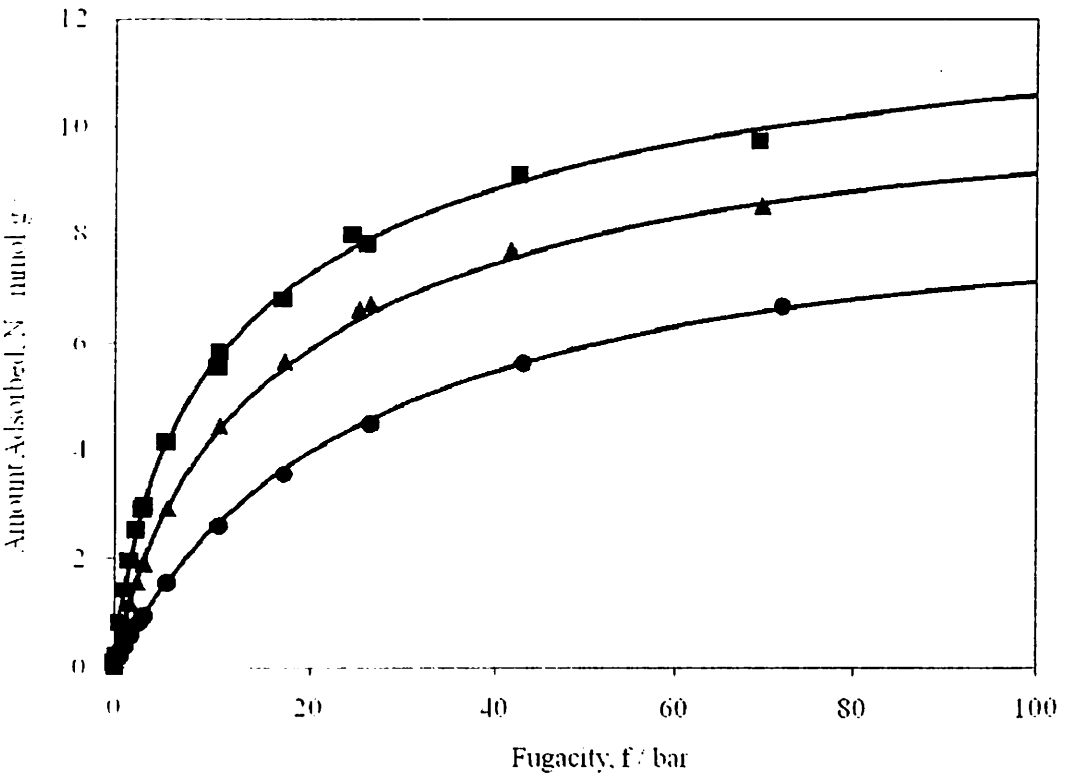

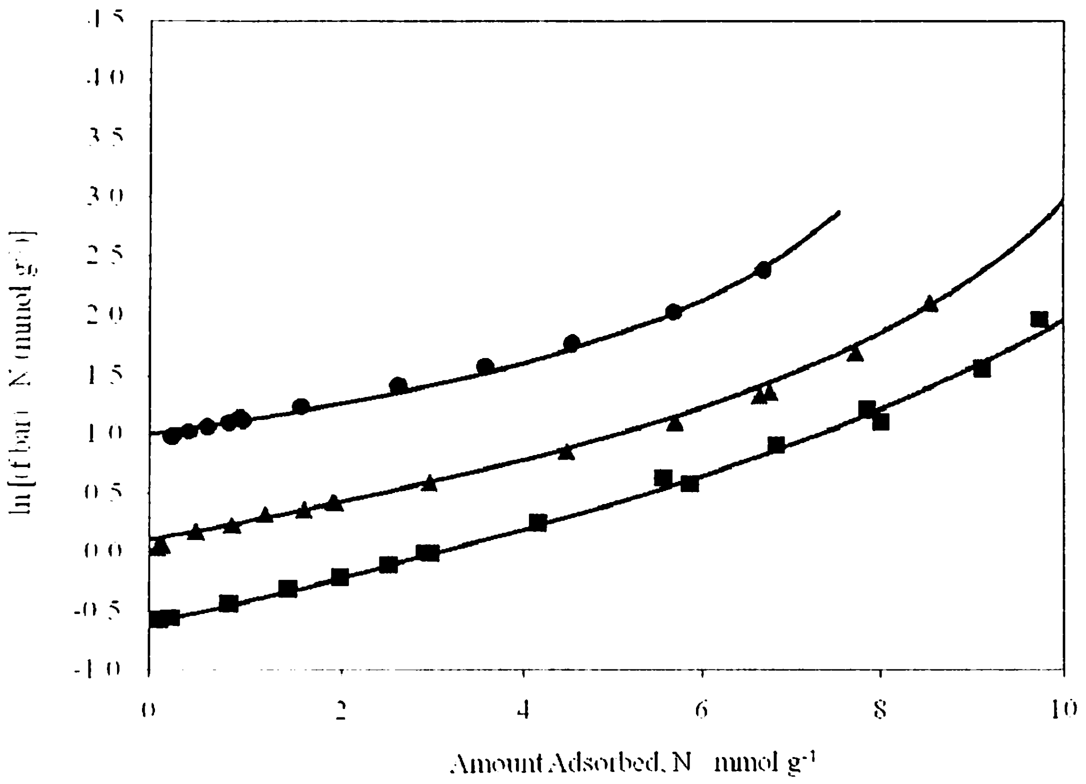

Figure 5.31: High pressure adsorption isotherms for CO on Cu-BTC. Symbols: Experimental points. Lines: Virial-Langmuir model fits. Squares: 295 K. Triangles: 318 K. Circles: 353 K.

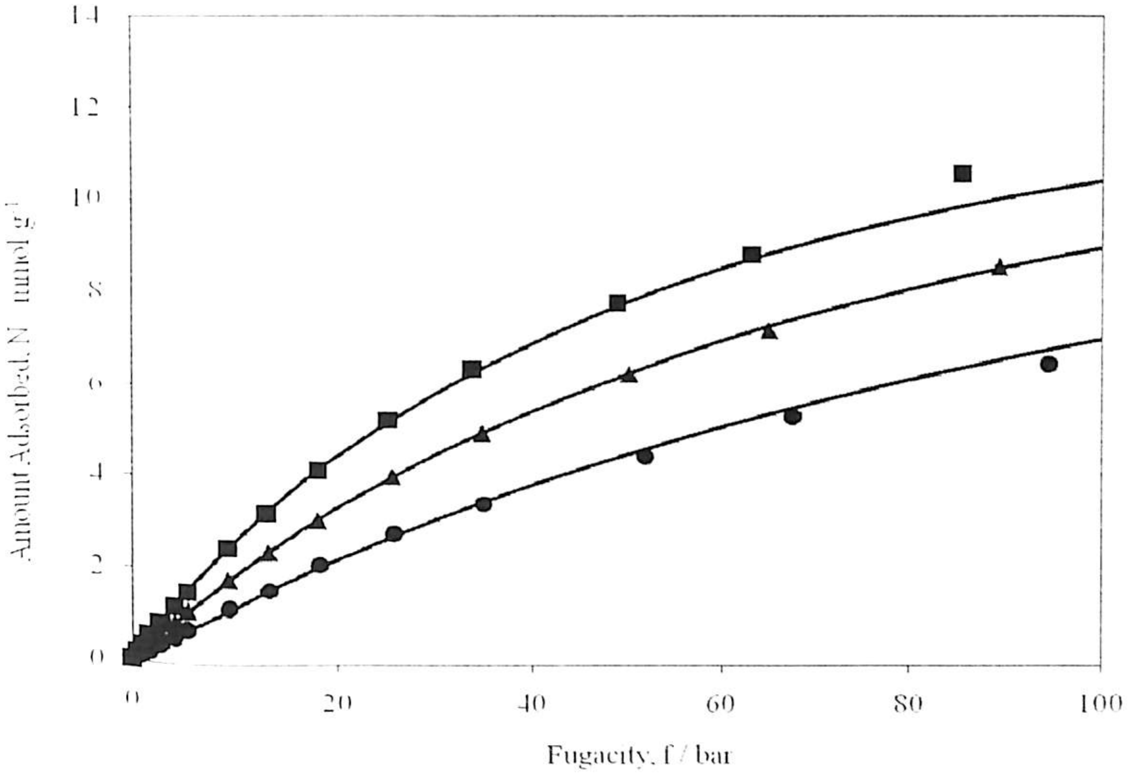

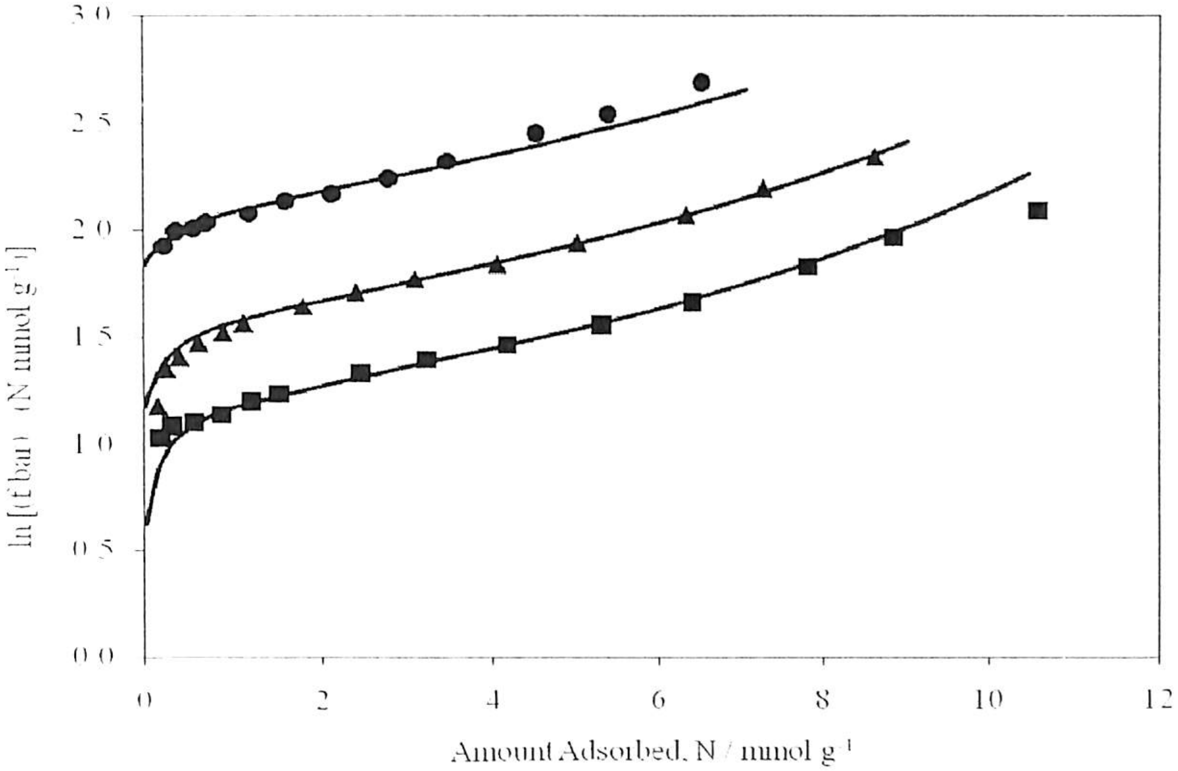

Figure 5.32: Adsorption isotherms for CH_4 on Cr-BDC. Symbols: Experimental points. Lines: Dual Site Langmuir model fits. Squares: 295 K, Triangles: 318 K, Circles: 353 K.

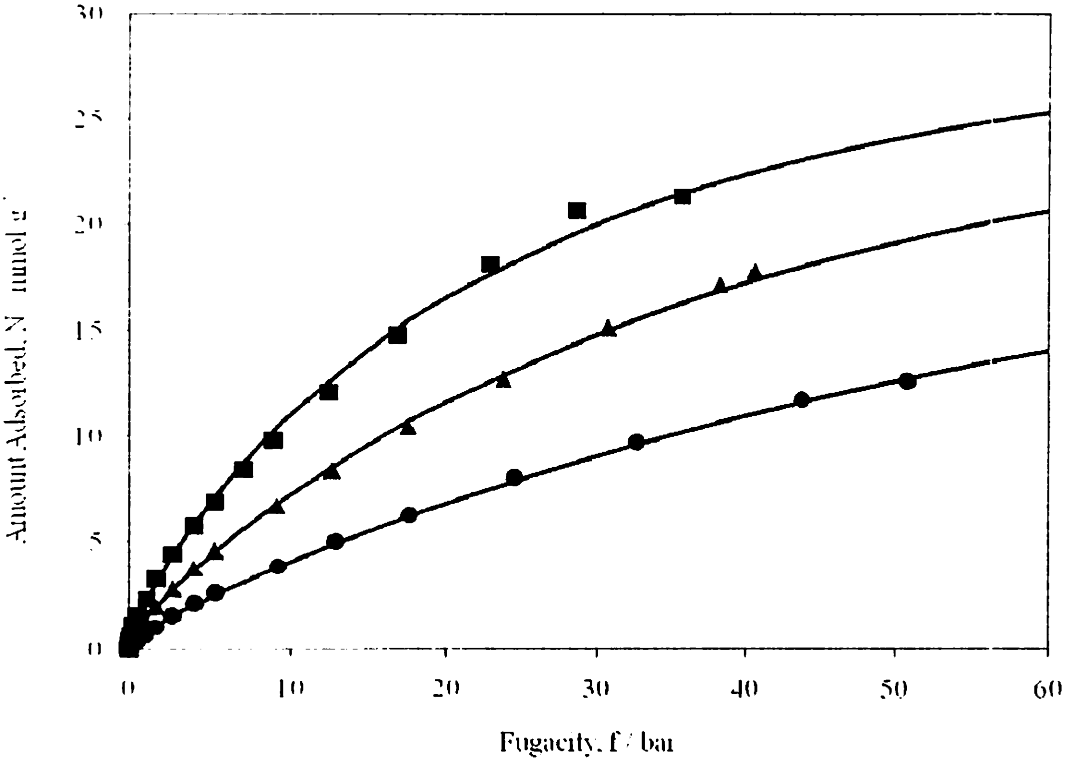

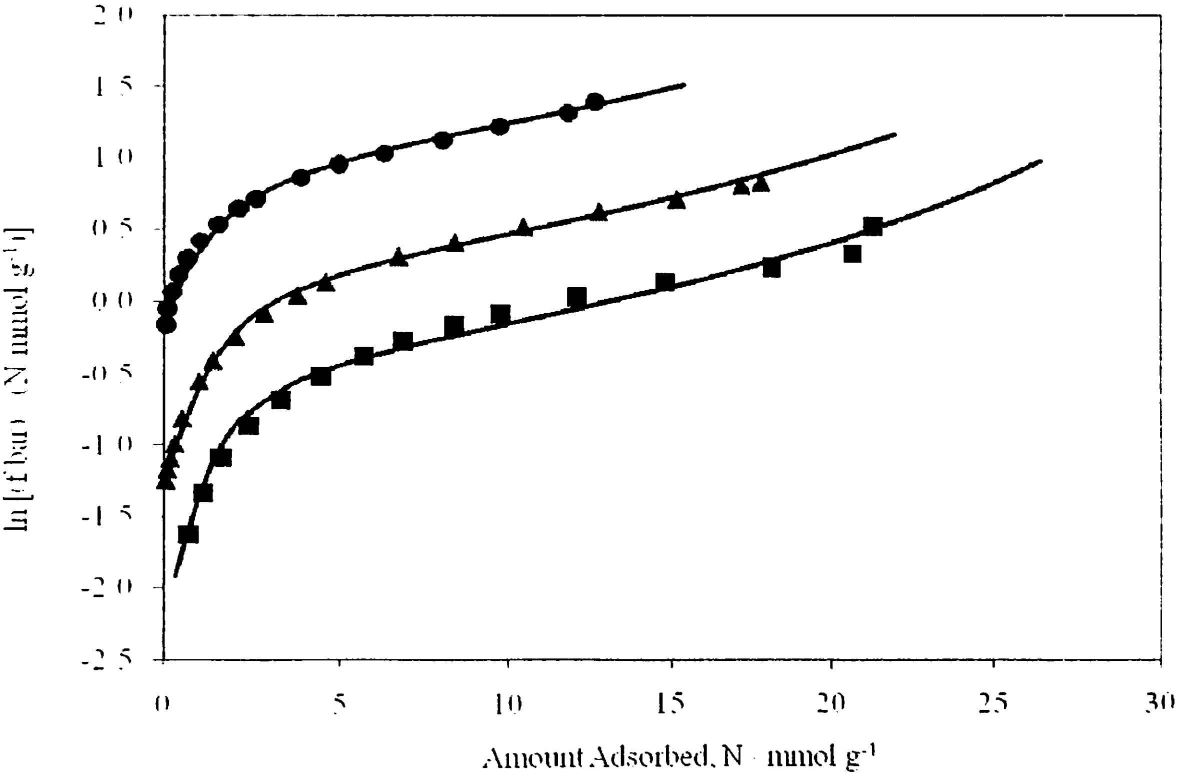

Figure 5.33: High pressure adsorption isotherms for CO_2 on Cr-BDC. Symbols: Experimental points. Lines: Dual Site Langmuir model fits. Squares: 295 K, Triangles: 318 K. Circles: 353 K.

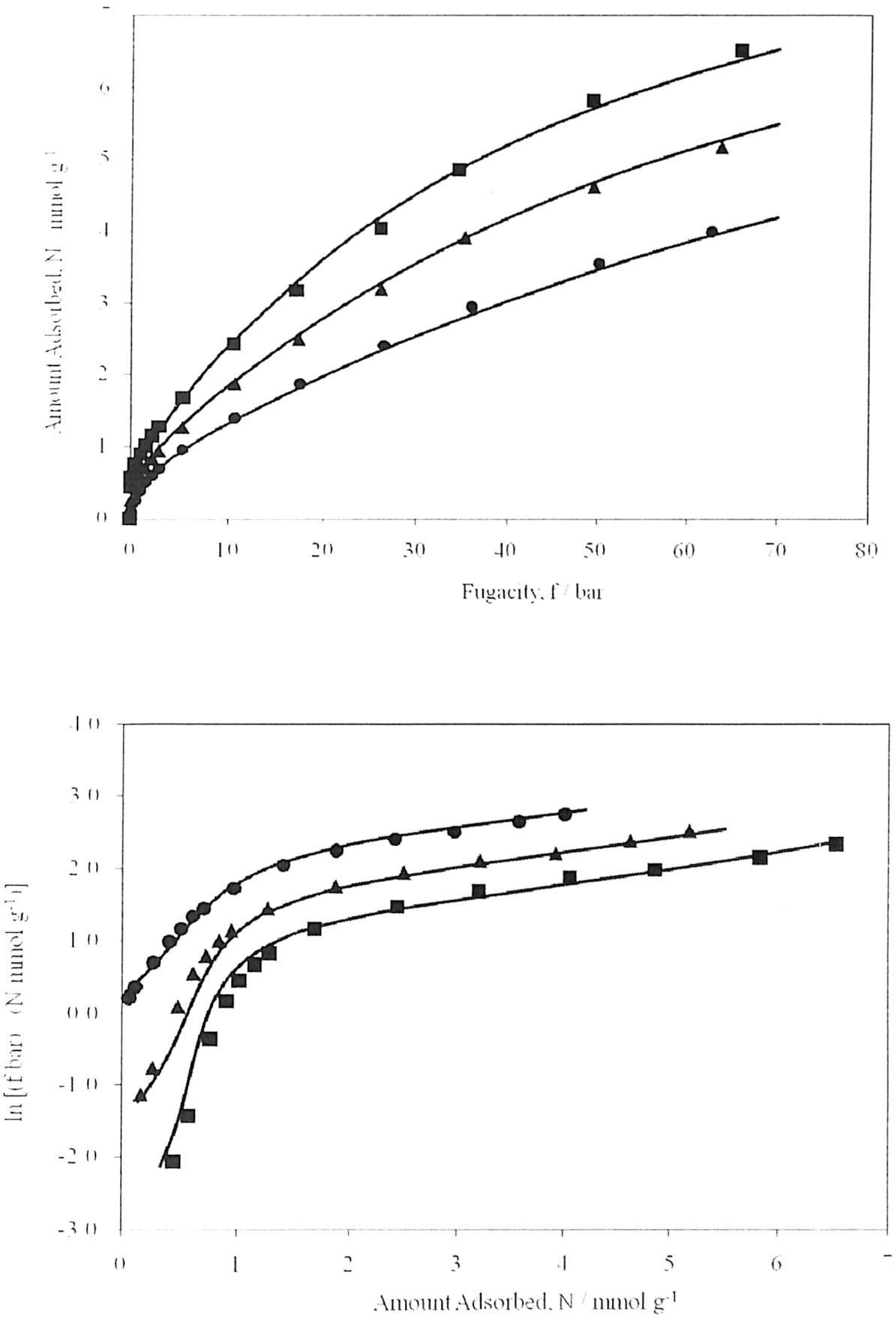

Figure 5.34: High pressure adsorption isotherms for CO on Cr-BDC. Symbols: Experimental points. Lines: Dual Site Langmuir model fits. Squares: 295 K, Triangles: 318 K, Circles: 353 K.

As discussed earlier in section 5.4.1, the loading on both samples is higher than those on benchmark zeolites like 13X at around ambient temperature. This trend holds even at higher pressures. CO_2 loading on MIL-101 measured in this work, was about 15-35 % lower than that reported on MIL-101 samples (a, b and c) by Llewellyn et al. **[46]**.

CO adsorption on Cr-BDC at about ambient temperature, is better than that on purely siliceous zeolite (7 bar), and comparable to that on polar zeolite like 5A (10 bar). As discussed later, CO adsorption on Cu-BTC is better than that on Cr-BDC, above atmospheric pressures. CO loading on Cu-BTC measured in this work is slightly better than that reported earlier by Wang et al. [39] for their sample b at 295 K; while they measured 0.8 mmol g^{-1} of loading (1 bar), loading on our sample **C** was 1.4 mmol g^{-1} at 1.04 bar.

Finally, Fig. 5.35 compares our results with GCMC simulations of Karra et al. **[152]** on Cu-BTC in conventional domain for both CO and CH_4. A good agreement was observed between the two results.

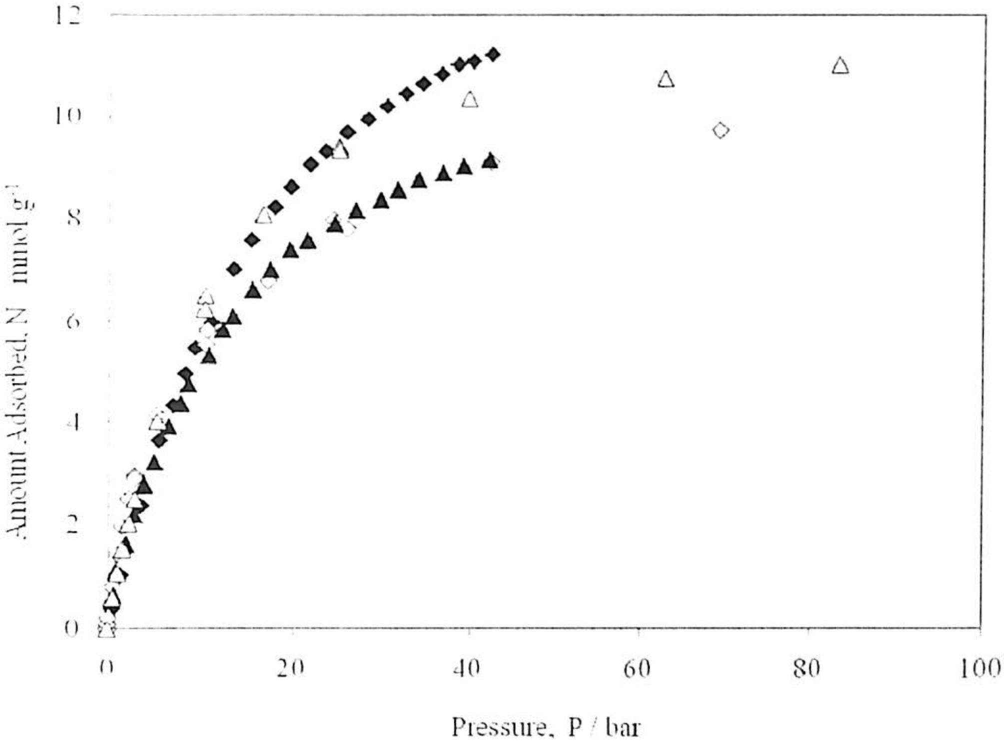

Figure 5.35: Comparison of adsorption of CO and CH_4 on Cu-BTC with reported GCMC simulation **[152]**. Closed symbols represent simulation data and open symbols are for experimental data; CO (diamonds) and CH_4 (triangles).

5.4.2 Modeling

Although CO_2 isotherm on Cu-BTC could be successfully modelled as earlier using a virial model (Fig 5.8), in the high pressure region it shows a type I behaviour approaching a saturation loading. Virial-Langmuir type model is often helpful to model behaviour in such systems; here it was used to model adsorption of CH_4, CO_2 and CO on Cu-BTC framework. The parameters and their fit statistics are given in Table 5.7.

Table 5.7: Virial-Langmuir model fit parameters for CH_4, CO_2 and CO adsorption on Cu-BTC (sample **C**)

Parameters	**Gases**		
	CH_4	**CO_2**	**CO**
k_0	6.388	7.4805	8.8938
Std. Error	0.1566	0.5386	0.155
t	40.808	13.89	57.3944
k_1 (K)	-1931.21	-2774.01	-2810.01
Std. Error	51.1207	175.0123	49.6356
t	-37.7775	-15.8504	-56.6127
b_0 ($mmol^{-1}$ g)	0.239	0.454	-0.1315
Std. Error	0.0917	0.2054	0.1045
t	2.6061	2.2105	-1.2585
b_1 ($mmol^{-1}$ g K)	-59.2719	-157.539	77.2437
Std. Error	29.1514	64.4278	32.4973
t	-2.0332	-2.4452	2.3769
c_0 ($mmol^{-2}$ g^2)	-0.0679	-0.0687	-0.0861
Std. Error	0.0132	0.016	0.0163
t	-5.1609	-4.2964	-5.2849
c_1 ($mmol^{-2}$ g^2 K)	17.1723	21.7839	23.3877
Std. Error	4.0285	4.8774	4.882
t	4.2627	4.4663	4.7906
$M_{(0)}$ (mmol g^{-1})	-4.0299	-8.2865	-8.9845
Std. Error	0.5902	1.5093	1.0292
t	-6.8286	-5.4902	-8.7299
$M_{(1)}$ (mmol g^{-1} K)	4635	7642.651	6003.125
Std. Error	180.2009	492.5321	338.8235
t	25.7213	15.5171	17.7176

The results for CO_2 adsorption on Cu-BTC reported here are slightly higher than those reported earlier for sample **B** (section 5.2.2.1). The Cu-BTC sample used in this study (sample **C**) was prepared following the same procedure as in case of sample **B**; however, the resultant surface area was slightly higher (1663 m^2 g^{-1}) which could have contributed to improvement of loading for CO_2. Hence the parameters and Henry's constant for CO_2 adsorption are different from those given earlier (Table 5.3).

In case of adsorption on Cr-BDC as discussed earlier, the virial domain plot has a knee in the low loading region for all the three gases; it gives a clear indication of existence of strong heterogeneity on the adsorbent. However, for non-polar molecule like CH_4 this effect is obviously less pronounced whereas for CO which has a strong dipole moment it is strongest. A dual site Langmuir model, Eq. 3.37 was used to model the behaviour for all the three gases; the results of parameters and their statistics from the modeling procedure are given in table 5.8.

Reference temperature T_0 = 283 K was chosen for all gases.

Table 5.8: Dual Site Langmuir model fit parameters for CH_4, CO_2 and CO adsorption on Cr-BDC

Parameters	**Gases**		
	CH_4	**CO**	**CO_2**
$M^{(1)}$ (mmol g^{-1})	0.0716	0.6082	0.9744
Std. Error	0.0256	0.0283	0.0576
t	2.7939	21.492	16.928
$M^{(2)}$ (mmol g^{-1})	15.6817	9.6156	34.044
Std. Error	0.894	0.9337	1.4
t	17.54	10.2985	24.303
$\delta^{(1)}$ (bar^{-1})	6.479	66.198	14.0436
Std. Error	2.6729	12.506	1.507
t	2.424	5.2934	9.315
$\delta^{(2)}$ (bar^{-1})	0.0248	0.0296	0.0607
Std. Error	0.0024	0.005	0.0042
t	10.568	5.888	14.3249
$-\Delta h_{ads}^{(1)}$ (kJ mol^{-1})	30.555	48.158	34.668
Std. Error	3739.08	2089.57	1065.609
t	-8.171	-23.046	-32.5336
$-\Delta h_{ads}^{(2)}$ (kJ mol^{-1})	13.45	14.84	20.794
Std. Error	510.694	944.45	359.5
t	-26.337	15.713	57.838

5.4.3 Enthalpy of Adsorption

The enthalpy of adsorption for various gases was calculated using procedure given in Table 3.1. The enthalpy in the low loading region for both frameworks is given in Fig. 5.36. Clearly for all gases the enthalpy of adsorption at low loading is higher on Cr-BDC than that on Cu-BTC. Cr-BDC has co-ordinatively unsaturated metal centers and the difference between enthalpies of these three gases are due to differences in interaction of the adsorbates with these metal centers. In fact, due to this reason, CO which has lowest polarizability of all the three gases shows highest value of adsorption enthalpy due to its dipole moment. While such centers are also present in case of Cu-BTC framework **[100]**, they are either not open and may be hindered due to presence of left over solvent molecules from the synthesis procedure. This results in more modest difference in adsorption enthalpies between the three gases on Cu-BTC.

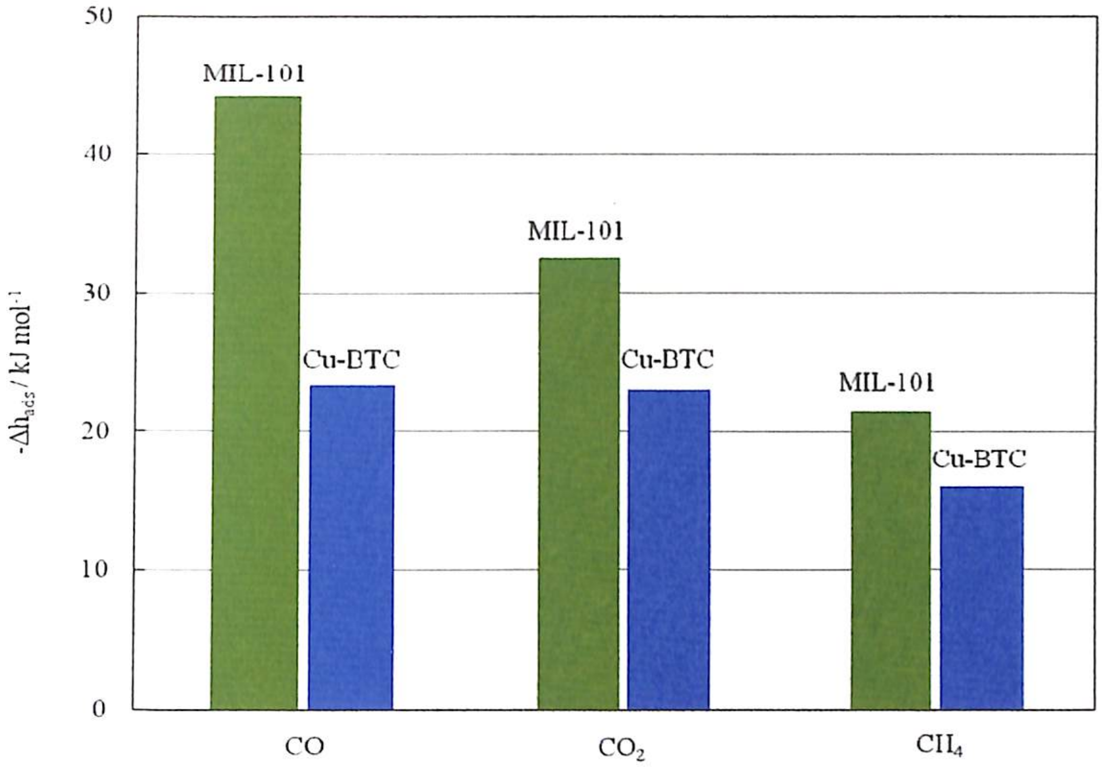

Figure 5.36: Comparison of enthalpy of adsorption of CH_4, CO_2 and CO on Cu-BTC (sample C) and Cr-BDC in low loading

Fig. 5.37 shows variation of enthalpy of adsorption for CH_4, CO_2 and CO on Cu-BTC at 295 K. The enthalpy of adsorption obtained for CO_2 matches with the earlier reports of Wang et al. **[39]** (-25 kJ mol^{-1}) at high loading, although they reported a value of about 35 kJ mol^{-1} at zero loading. While CH_4 and CO_2 only show modest variation in enthalpy with loading; CO on the other hand shows a considerable decrease in enthalpy of adsorption from about -23.4 kJ mol^{-1} at zero loading to about -17.4 kJ mol^{-1} at a loading of ca. 6 mmol g^{-1}. Although electrostatic interactions dominate the low loading region, as these sites are progressively filled up, the enthalpy of adsorption drops down sharply. At higher loadings, the enthalpy of adsorption are directly related to the polarizability of the gas and decrease in the order $CO_2 < CH_4 < CO$.

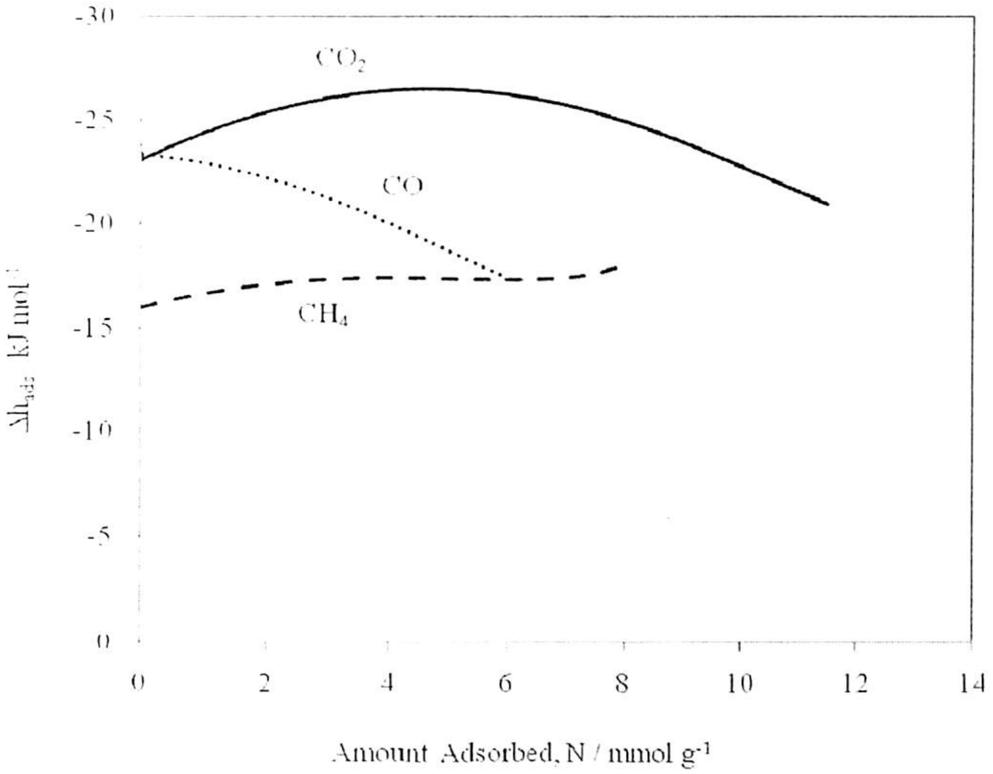

Figure 5.37: Variation of enthalpy of adsorption with loading on Cu-BTC (sample **C**) at 295 K

In case of Cr-BDC more open metal sites are available than that of Cu-BTC **[46]**. This tends to pronounce the effect as observed above for Cu-BTC. In fact, due to availability of enough unsaturated metal sites on the framework all gases exhibit "visible" heterogeneity. However, at a loading of about 1.2 mmol g^{-1} this value drops to about -15.1, -13.7 and -24.2 kJ mol^{-1} for CO, CH_4 and CO_2 respectively [Fig. 5.38].

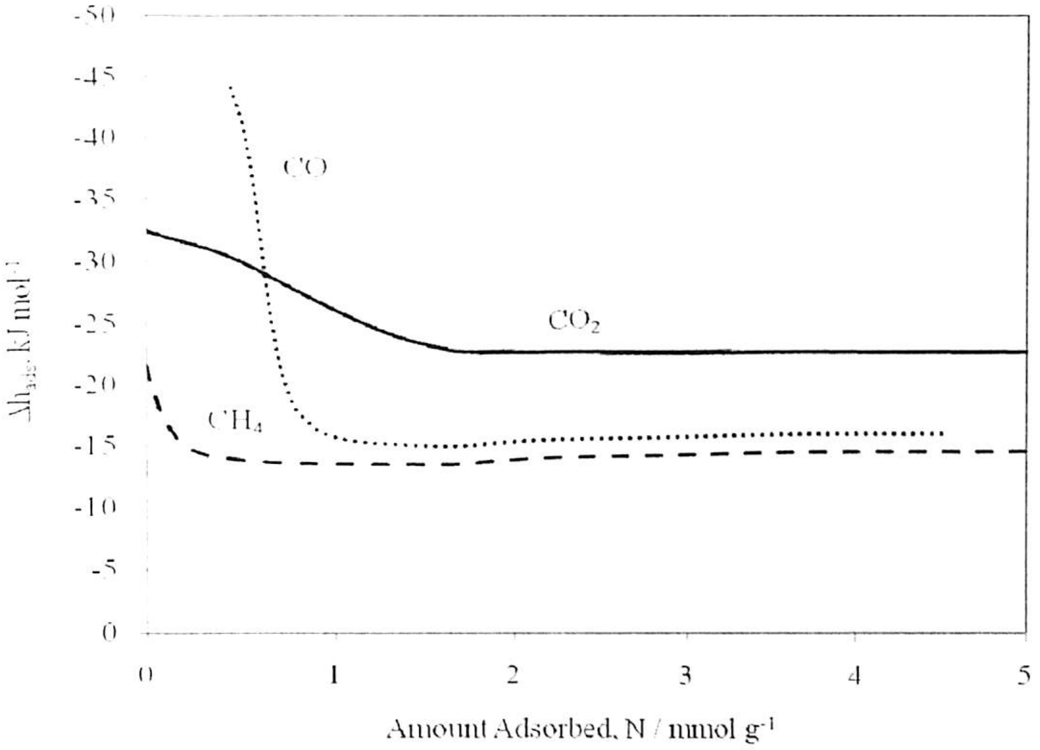

Figure 5.38: Variation of enthalpy of adsorption with loading on Cr-BDC at 295 K

5.4.4 Effect of Adsorbate Polarity on Adsorption Characteristics

Fig. 5.39 shows a plot of Henry's constant against temperature for the three gases on both frameworks. Several interesting features can be observed.

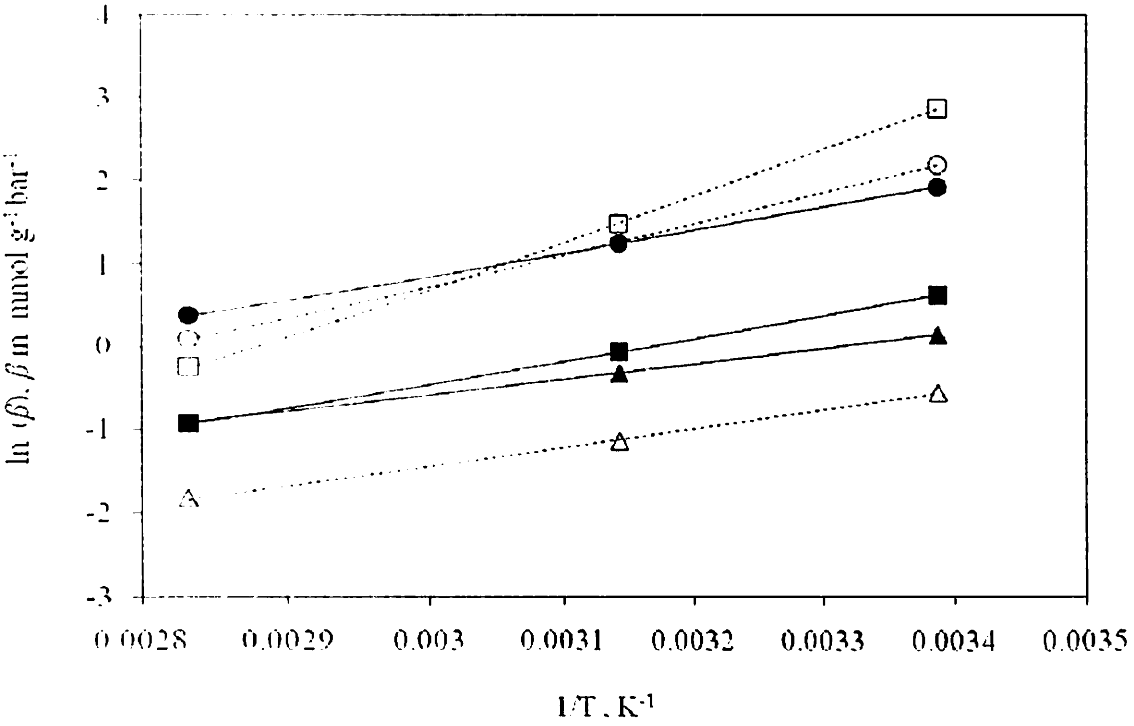

Figure 5.39: Variation of Henry constant with temperature for CO, CO_2 and CH_4 on Cu-BTC and Cr-BDC. Circles (CO_2), Triangles (CH_4), Squares (CO); Open symbols Cr-BDC, Closed symbols Cu-BTC. Lines are drawn as a guide to the eye. Note that temperature scale is increasing from right to left.

[a] At all temperatures β for CH_4 is more on Cu-BTC than on Cr-BDC indicating that the van der Waals interactions are stronger with Cu-BTC framework.

[b] CO on the other hand shows a larger β on Cr-BDC indicating that initial loading in this framework is strongly influenced by electrostatic interactions (with the available *cus* sites) as described earlier. However, the difference between the β values of the two frameworks decreases with temperature, since the electrostatic interactions are inversely proportional to temperature.

[c] CO_2 has a quadrupole moment only; its electrostatic interactions are not as strong as that of CO. Hence it has a higher β on Cr-BDC at low temperature but at higher temperatures these electrostatic interactions become weaker and dispersion interactions dominate. Thus its β value at 353 K on Cu-BTC is larger than that on Cr-BDC.

[d] For the same reason as above.

[i] Although β value of CO at 295 K on Cr-BDC is larger than that of CO_2, the trend reverses at 353 K since polarizability of CO_2 (which determines the dominating van der Waals interactions at higher temperature) is larger.

[ii] The difference between β values of CH_4 and CO decrease with temperature even on Cu-BTC framework. At low temperature electrostatic interactions of CO contribute to somewhat higher value of β ; as temperature increases electrostatic interactions become weaker and the difference in β value between CO and CH_4 at 353 K is almost negligible.

Figs 5.40 through 5.47 show comparison of isotherms for the three gases between the two frameworks at 295 K. These figures show the effect of electrostatic and dispersion interactions in the two frameworks.

[a] First, for methane as discussed earlier in Fig. 5.39, Henry constant on Cu-BTC is larger at 295 K indicating that adsorption capacity of Cu-BTC is larger near the zero pressure limit; this trend continues even in the high pressure region at fugacity as high as 80 bar (Fig. 5.40). However, the difference between the adsorption capacities of the two frameworks at high loading is smaller. While the adsorption on Cu-BTC seems to approach saturation that

on Cr-BDC does not: this is to be expected since Cr-BDC has a large open porous structure with a unit cell volume of 702.000 Å^3 and its measured pore volume from N_2 experiments was 1.38 cm^3 g^{-1}. Cu-BTC or HKUST-1 on the other hand has much smaller pore volume (ca. ~ 0.75 cm^3 g^{-1}).

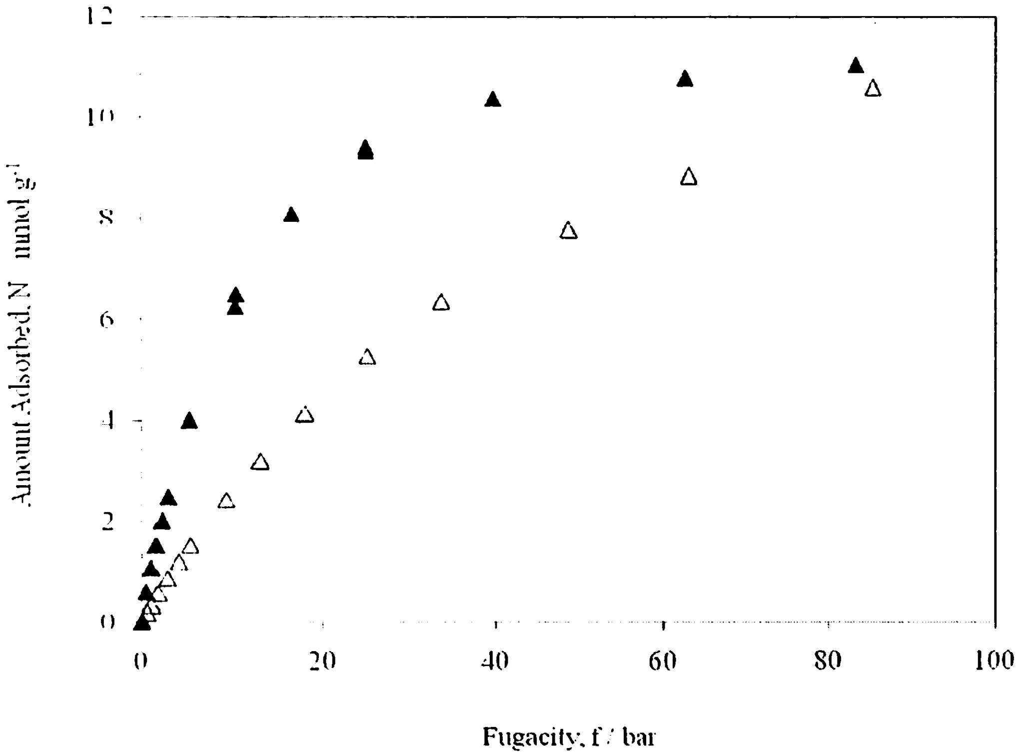

Figure 5.40: CH_4 adsorption on Cu-BTC (closed symbols) and Cr-BDC (open symbols) at 295 K.

[b] In case of CO, the low loading region, the Henry's constant indicated (Fig. 5.39) that the capacity on Cr-BDC is higher due to electrostatic interactions. However, as the *cus* metal centers are occupied, the contribution of strong electrostatic interactions decreases. Since the dispersion interactions (as indicated by β values earlier) are stronger with the Cu-BTC framework than on Cr-BDC framework, the 295 K isotherms of CO on Cu-BTC and Cr-BDC

cross each other at about a loading of 0.75 mmol g^{-1}. Thereafter, loading of CO on Cu-BTC is greater (Fig. 5.41). However, even at 70 bar the loading of CO compared to CH_4 is smaller on Cu-BTC framework and do not seem to approach a "clear" plateau indicating saturation; this may be due to the smaller polarizability of CO (Fig. 5.42).

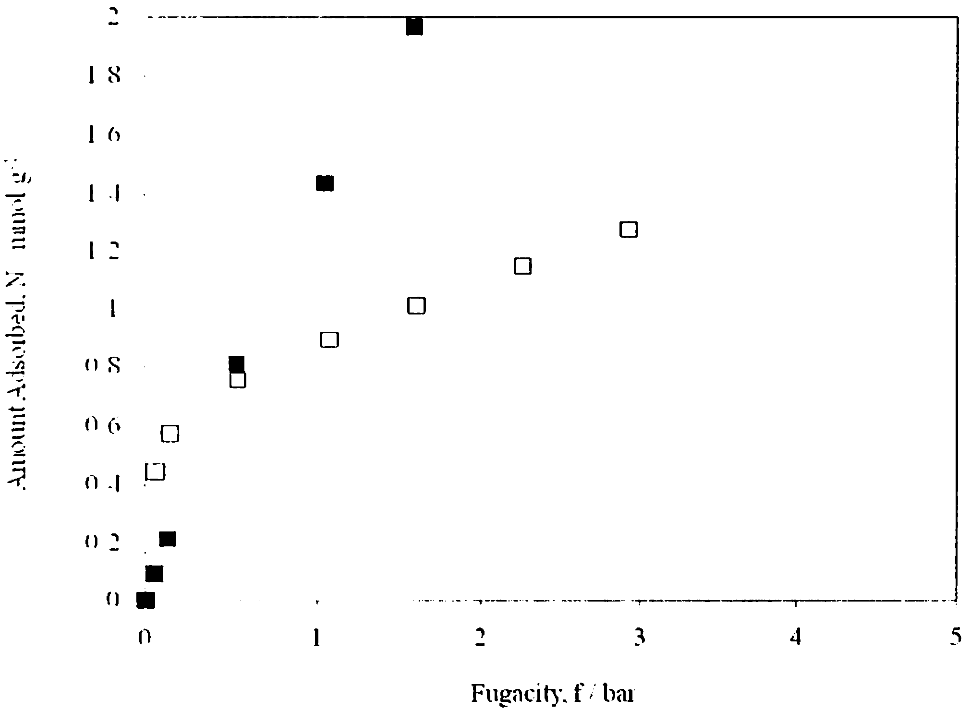

Figure 5.41: CO adsorption on Cu-BTC (closed symbols) and Cr-BDC (open symbols) at 295 K in the low pressure region.

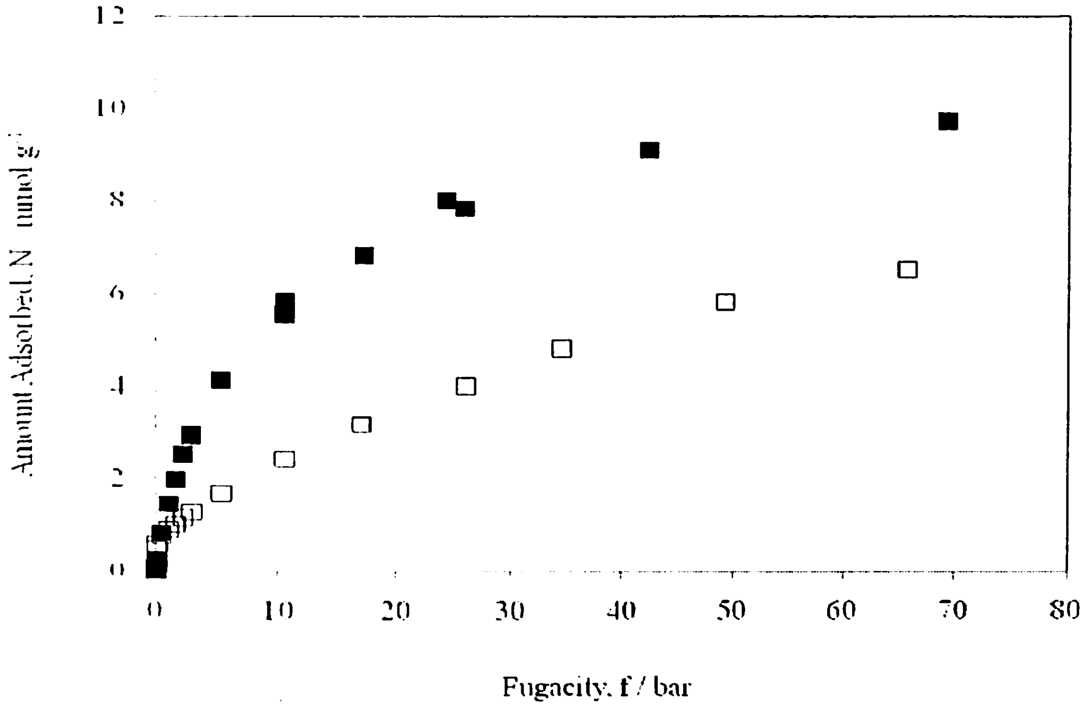

Figure 5.42: CO adsorption on Cu-BTC (closed symbols) and Cr-BDC (open symbols) at 295 K in the high pressure region.

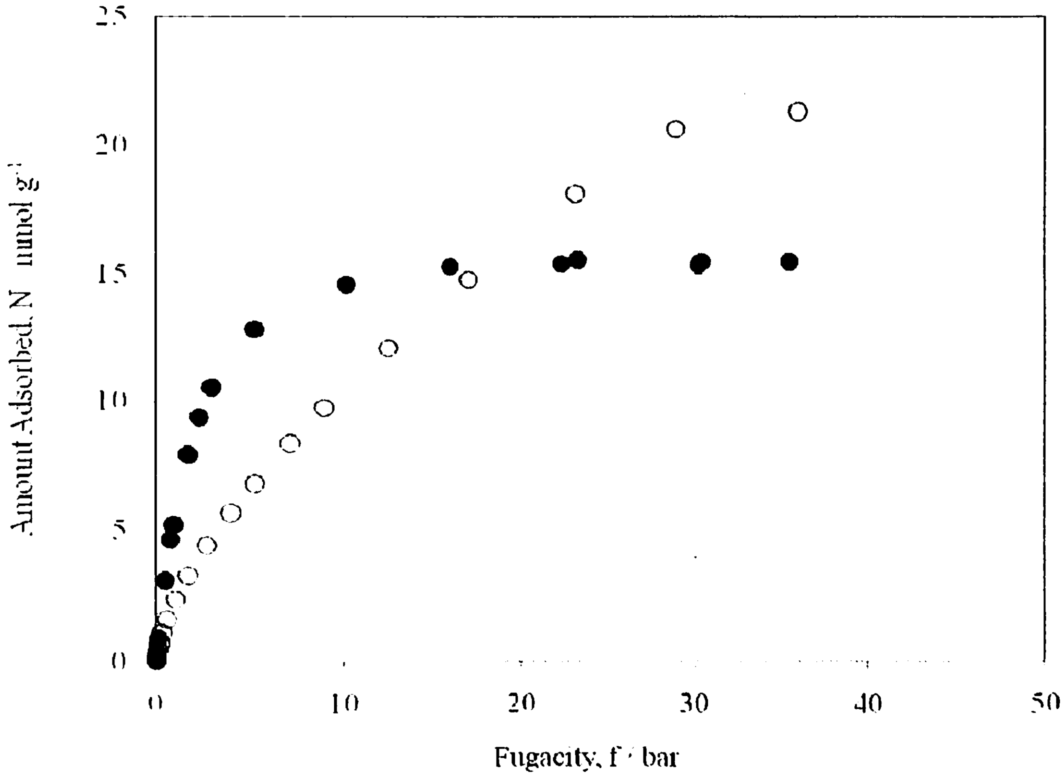

Figure 5.43: CO_2 adsorption on Cu-BTC (closed symbols) and Cr-BDC (open symbols) at 295 K.

[c] In case of CO_2 the behaviour in the low loading region is similar to that of CO (Fig. 5.43). Henry constant value on Cr-BDC is higher due to its quadrupole moment. However as *cus* centers are occupied in the Cr-BDC framework, the contribution of electrostatic interactions decreases; this results in crossing of isotherms at a loading of ca. 0.35 mmol g^{-1}. Thereafter, at the same condition, loading on Cu-BTC is larger than that of Cr-BDC until about 16 bar. The loading on Cu-BTC seems to approach saturation (as in case of CH_4) at this pressure. However, due to availability of large pore volume in Cr-BDC loading on Cr-BDC does not approach saturation and keeps increasing. In fact, at a fugacity of 36 bar loadings on Cr-BDC and Cu-BTC frameworks are 21.3 and 15.5 mmol g^{-1} respectively.

Fig. 5.44 compares isotherms of the three gases on Cu-BTC framework in virial domain. Throughout the experimental data range adsorption of CO_2 on the framework is higher. However, between CO and CH_4, as discussed earlier the Henry's constant for CO is higher at 295 K than that on CH_4 due to its dipole moment; however as sites with which electrostatic interactions can occur are progressively filled up, the higher polarizability of methane dictates the behaviour of the isotherm. Hence, the isotherms for CO and CH_4 cross each other. However, influence of electrostatic interactions at higher temperature is weaker and this effect is not seen at 353 K (Fig. 5.45).

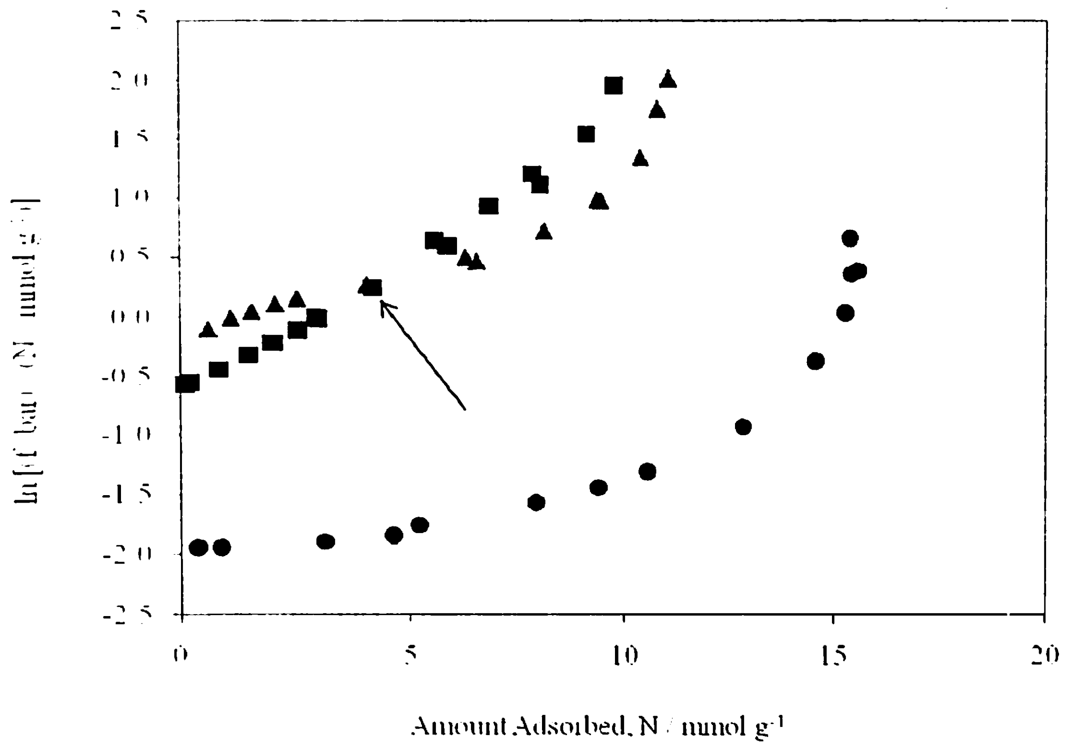

Figure 5.44: Comparison of adsorption isotherms of CO_2 (circle), CO (squares) and CH_4 (triangles) on Cu-BTC framework at 295 K (virial domain plot).

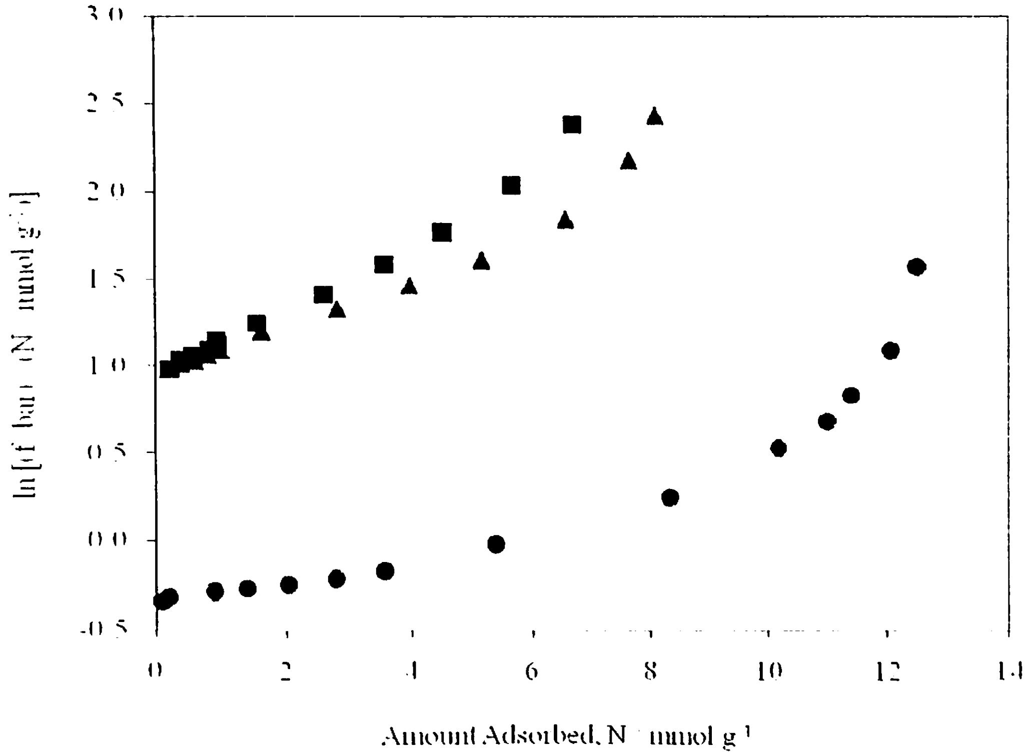

Figure 5.45: Comparison of adsorption isotherms of CO_2 (circle), CO (squares) and CH_4 (triangles) on Cu-BTC framework at 353 K (virial domain plot).

This effect was also observed in case of Cr-BDC framework (Fig. 5.46). Since the electrostatic interactions with the Cr-BDC framework are stronger as discussed earlier, CO has largest Henry constant value at all three temperatures. Thus, a crossover of isotherms at 295 K can be observed between CO and CO_2 in addition to CO and CH_4. The difference between the Henry's constants decreases as temperature increases to 353 K; however, the electrostatic interactions of CO with the framework are still strong enough to have a high value of β even at this temperature compared to other gases. Thus, unlike in case of Cu-BTC, crossover of isotherms between CO and CO_2 as well as CO and CH_4 was observed even at 353 K (Fig. 5.47).

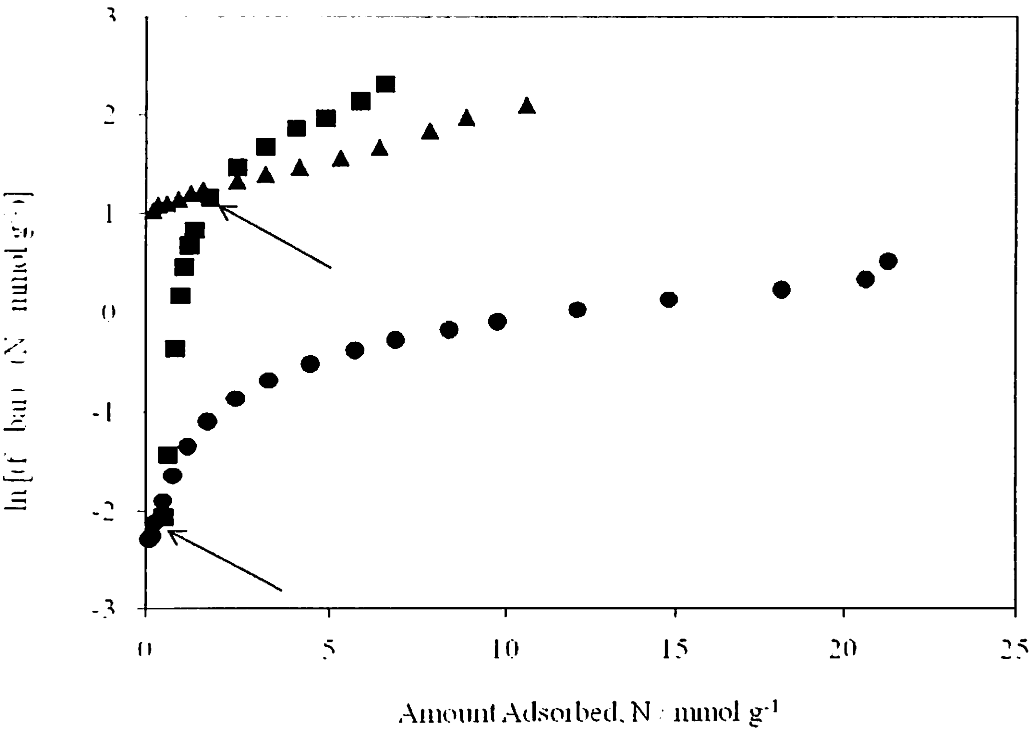

Figure 5.46: Comparison of adsorption isotherms of CO_2 (circle), CO (squares) and CH_4 (triangles) on Cr-BDC framework at 295 K (virial domain plot).

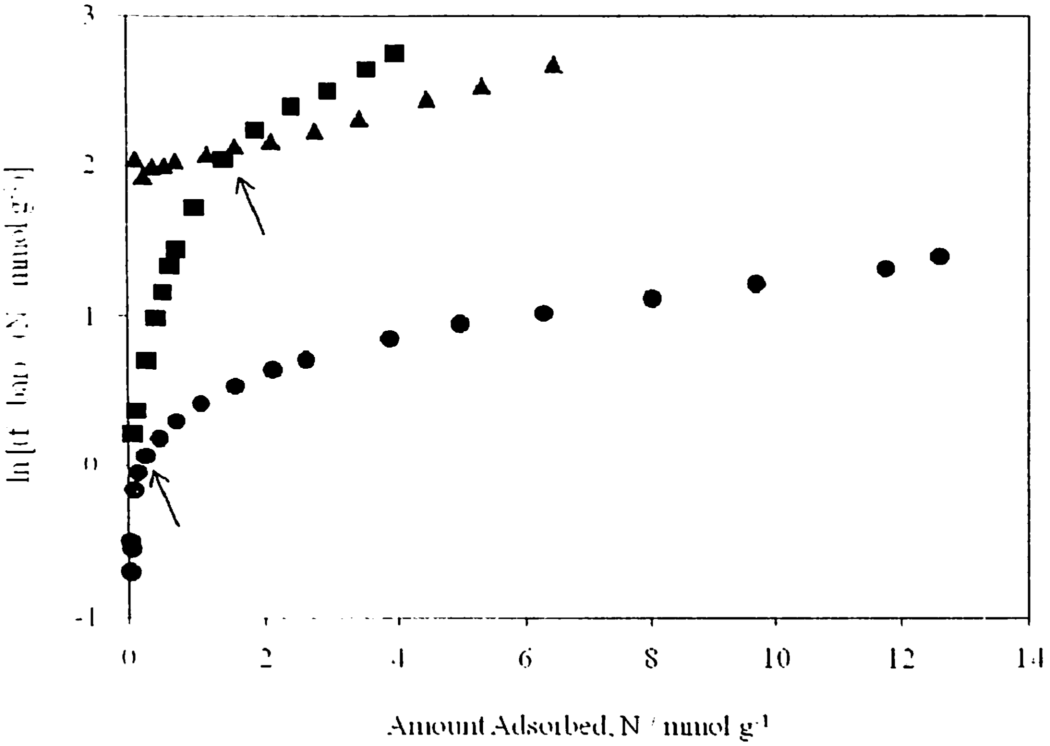

Figure 5.47: Comparison of adsorption isotherms of CO_2 (circle), CO (squares) and CH_4 (triangles) on Cr-BDC framework at 353 K (virial domain plot).

5.5 Binary Adsorption of CO_2+CH_4 Mixture on Cu-BTC Using Gas Chromatography

This section presents results, modeling and analysis of binary adsorption equilibrium using infinite dilution gas chromatography experiments. CO_2+CH_4 mixture on Cu-BTC is taken as a representative system. The main aim of this work was to demonstrate that a simple and easy technique combined with appropriate thermodynamic analysis can effectively characterize binary adsorption equilibria on metal organic frameworks. Such a tool will be of immense use in characterizing behaviour of several gas mixtures on several potential MOFs.

5.5.1 Measurement of Slope of Partial Isotherms at Infinite Dilution

The net retention time of sample gas (gas 2) and slopes of its partial isotherms at infinite dilution in carrier gas was calculated as discussed earlier in section 4.4.3.3. These measurements are reported in Table 5.9. The mass of "clean" adsorbent i.e. Cu-BTC (sample **C**) used in these measurements was 89.4 mg.

Table 5.9: GC measurements

Carrier	Sample	Inert	Fugacity (bar)	RT sample (mmol)	RT inert (mmol)	RT net (mmol)	dn_i / df_i (mmol g^{-1} bar^{-1})
CH_4	CO_2	He	0.0	0.000	0.000	0.000	5.056
			1.0	0.908	0.487	0.421	4.722
			2.2	1.602	0.767	0.834	4.305
			3.3	2.274	1.047	1.227	4.183
			5.4	3.515	1.547	1.968	4.059
			7.2	4.415	1.956	2.459	3.845
			9.8	6.097	2.674	3.423	3.923
CO_2	CH_4	He	0.0	0.000	0.000	0.000	0.977
			1.0	0.574	0.513	0.061	0.690
			1.9	0.916	0.838	0.078	0.456
			3.3	1.336	1.222	0.114	0.384
			5.3	1.897	1.768	0.129	0.274
			7.7	2.620	2.426	0.194	0.282
			9.6	3.319	3.092	0.227	0.266

In case of gas chromatographic experiments, slope of adsorption isotherm is directly related to net retention Eq. 4.13, which is the difference between retention of the sample gas and that of the inert (helium). It is necessary to ensure high accuracy in measurement of retentions (of both carrier and inert) which in turn is related directly to carrier gas flow rate measurements. The variation of retention of an inert gas with density of the carrier gas needs to be linear as shown in Fig. 5.48. Since an inert gas used (helium) is non-adsorbing, its retention is a measure of amount of gas present in the bulk gas phase of the column at the carrier gas conditions (temperature and pressure). Linearity of the plot in Fig. 5.48 (irrespective of the carrier gas) indicate consistency of the flow rate measurements.

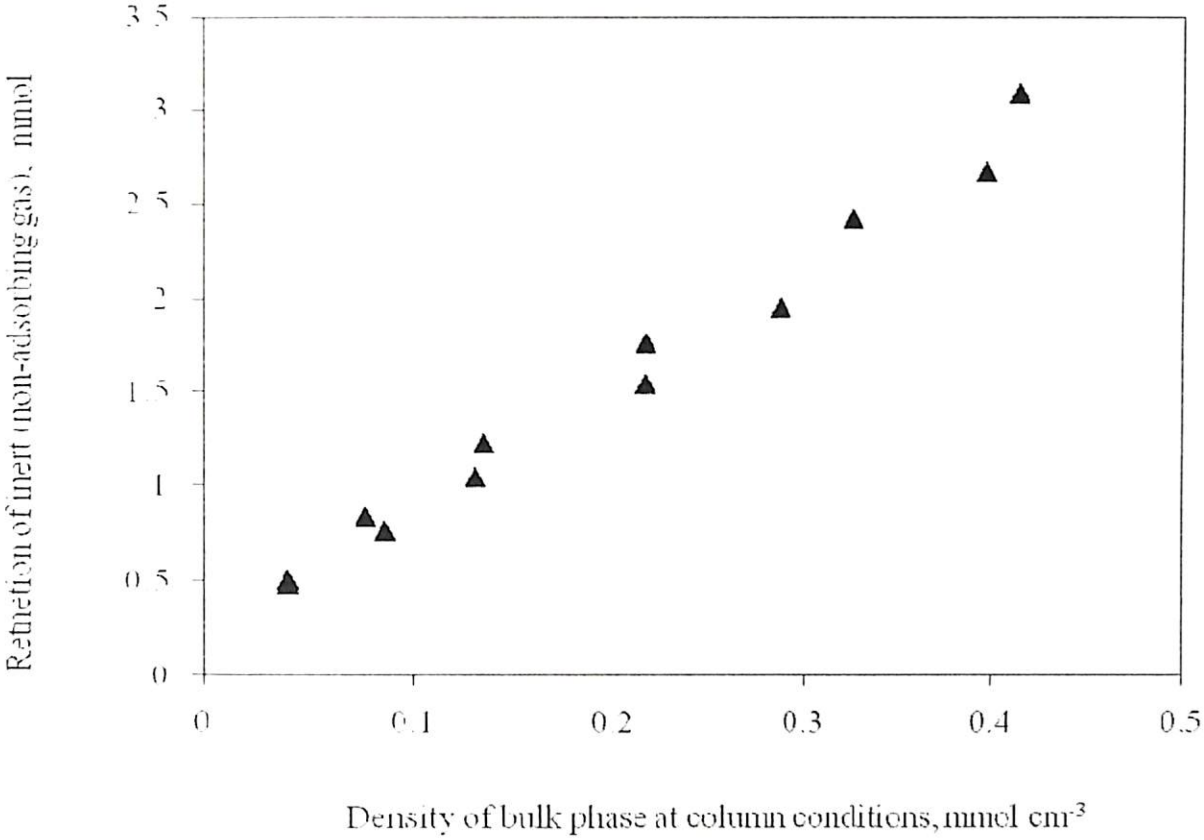

Figure 5.48: Variation of retention time of inert (helium) with bulk gas density

Finally, in a GC technique it is very important to ensure that the flow rate of the carrier gas is not too high and sufficient time is allowed for equilibration of the sample gas with the solid adsorbent packed in the column; a small flow rate on the other hand disperses the peak and increases measurement time. It was ensured that such problems did not arise in these experiments, by performing a few trial runs initially at different pressures and observing the effect of flow rate on peak properties and retention.

5.5.2 Modeling of Infinite Dilution GC Results

As discussed, the EoS approach highlighted in Section 3.7.7 yields the following expression (Eq. 5.5) for species 1 in a binary mixture

$$\ln \frac{\hat{f}_1^g}{\beta_1 N_1} = \left(1 - \frac{M_{mix}}{M_1}\right) + \left(1 - \frac{M_{mix}}{N} + \frac{M_{mix}^2}{NM_1}\right) \ln\left(\frac{M_{mix}}{M_{mix} - N}\right) + N_1 b_1 + N_2 b_{12} + N_1^2 c_{111} + 2N_1 N_2 c_{112} + N_2^2 c_{122}$$

(5.5)

At infinite dilution limit of species 1, both the partial amount adsorbed for 1 (N_1) and adsorbate mole-fraction x_1 approach zero.

Following mixing rule given in Eq. 3.57,

$$\lim_{x_1 \to 0} M_{mix} = M_2 \tag{5.6}$$

Similarly, the total amount adsorbed is essentially amount adsorbed for species 2 as a pure component at temperature and pressure of the column.

$$\lim_{x_1 \to 0} N = N_2^0 \tag{5.7}$$

The superscript "0" indicates that it is a pure component standard state at temperature and pressure of the column.

Eq.5.5 then reduces to

$$\ln \frac{dN_1 / d\hat{f}_1^g}{\beta_1} + 1 - \frac{M_2}{M_1} + \ln\left(\frac{M_2}{M_2 - N_2^0}\right)\left(1 - \frac{M_2}{N_2^0} - \frac{M_2^2}{M_1 N_2^0}\right) = -N_2^0 b_{12} - \left(N_2^0\right)^2 c_{122} \tag{5.8}$$

Similarly at infinite dilution of species 2 in carrier gas 1,

$$\ln \frac{dN_2 / d\hat{f}_2^g}{\beta_2} + 1 - \frac{M_1}{M_2} + \ln\left(\frac{M_1}{M_1 - N_1^0}\right)\left(1 - \frac{M_1}{N_1^0} - \frac{M_1^2}{M_2 N_1^0}\right) = -N_1^0 b_{12} - \left(N_1^0\right)^2 c_{112} \tag{5.9}$$

While the first terms on LHS of equations 5.8 and 5.9 can be obtained from infinite dilution gas chromatographic experiments (Table 5.9), other terms on LHS can be calculated from pure component adsorption data [using Virial-Langmuir parameters listed in Table 5.7]. The only unknowns are the cross virial coefficients on RHS: b_{12}, c_{112}, and c_{122}. The infinite dilution data obtained from GC experiments can be regressed to obtain these cross virial parameters. These parameters can be used for calculation of adsorption from binary gas mixture at finite compositions, as shown later.

The regression was performed to fit LHS to quadratic function of amount adsorbed for carrier gas with the constraint that limit of the slope for both Eqs. 5.8 and 5.9 is same. The results of the regression along with values are given in Table 5.10 and goodness of fit is shown in Fig. 5.49. For sake of comparison, the predictions using IAST approach (section 3.6) are also shown in this figure. Obviously, these results indicate that IAST also predicts infinite dilution behaviour of the system with reasonable accuracy. As pressure approaches zero, irrespective of the composition (even at infinite dilution) the slope of isotherm is equal to Henry's constant. Hence, both in case of experimental data as well as model estimates, ordinate approaches unity at the zero pressure limit.

Table 5.10: Cross virial coefficients for CO_2+CH_4 adsorption on Cu-BTC

	Coefficients	Std. Error	*t*-statistics
b_{12}	0.0248	0.0169	1.4668
c_{112}	-0.0142	0.0041	-3.4553
c_{122}	-0.0062	0.0016	-3.8947

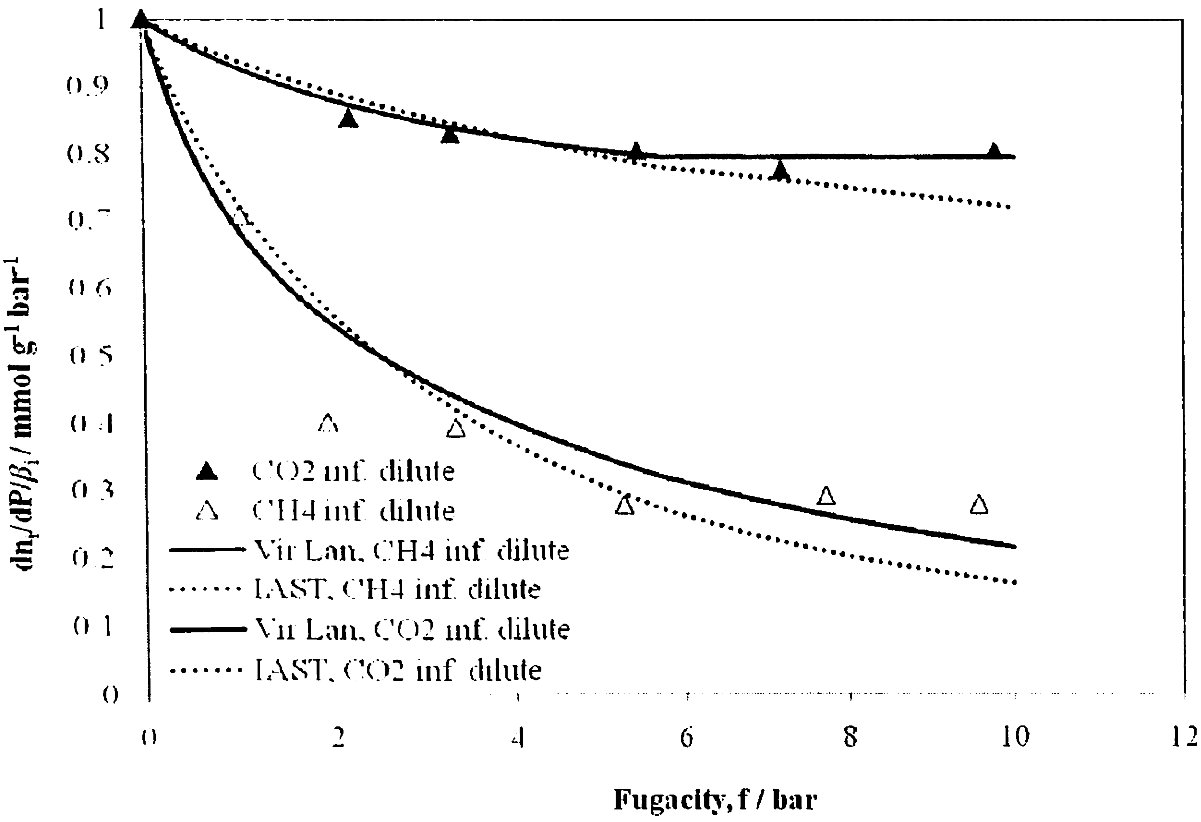

Figure 5.49: Variation of slope of partial isotherm at infinite dilution with fugacity for CO_2+CH_4 mixture on Cu-BTC at 305 K

5.5.3 Estimation of Adsorption Isotherms of CO_2+CH_4 binary mixture

One of the aims of performing GC experiments is to estimate binary adsorption characteristics of a gas mixture using consistent thermodynamic model; instead of purely predictive nature of IAST, we wanted to obtain model parameters from quick but dependable experiments in binary domain. Towards this goal, cross virial coefficients of binary mixture of CO_2 and CH_4 were obtained as discussed in the previous section. Once these cross virial coefficients are available estimate for binary adsorption can be performed using Eq. 3.64. The IAST predictions for this binary mixture were obtained using Virial-Langmuir model for pure gas adsorption. Details of mathematical procedure are given in Appendix C.

Figures 5.50 through 5.55 compare the results for various cases to IAST predictions. As in case of infinite dilution results, only slight difference could be observed between the isotherm estimates of Virial-Langmuir model for the mixture used in this work and the IAST model. In fact IAST was used by several works in literature earlier for estimation of binary adsorption properties of gas mixtures on this type of frameworks. The selectivity values predicted by Viral-Langmuir model varied between 5.7 and 7.2. This selectivity for CO_2/CH_4 mixture thus shows promise for effective separation using Cu-BTC.

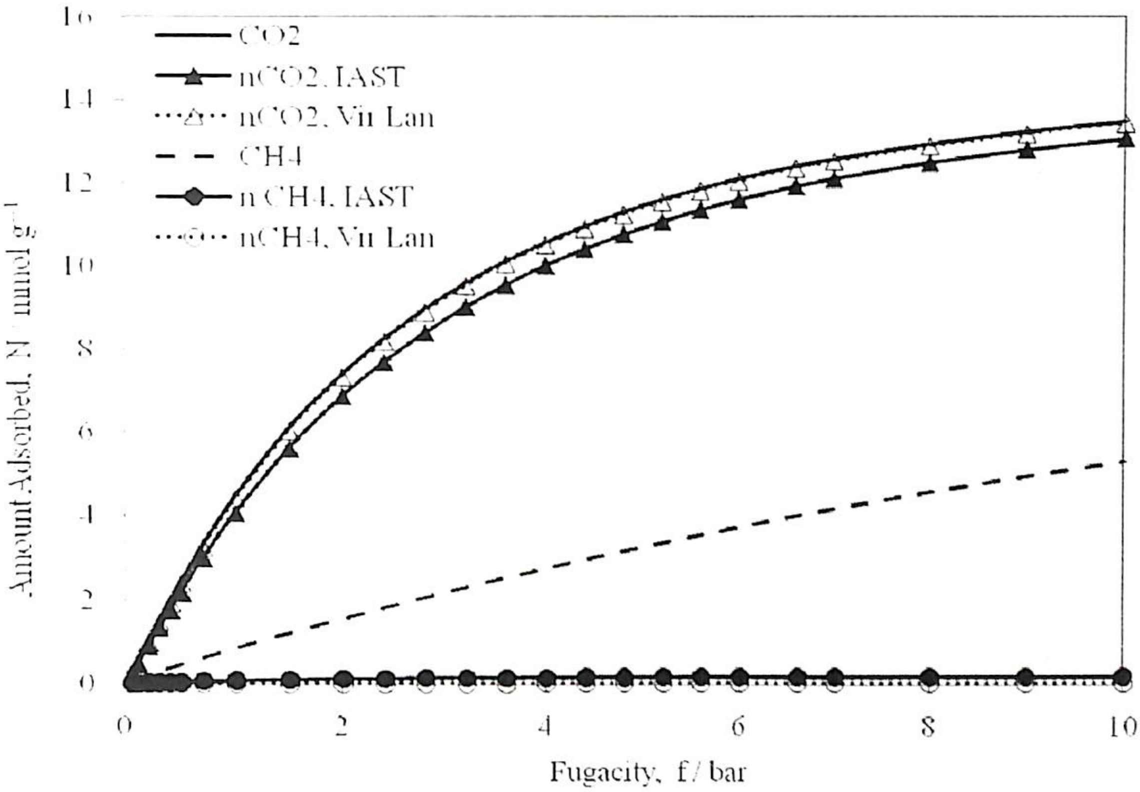

Figure 5.50: Variation of amount adsorbed from CO_2+CH_4 mixture at 305 K, $yCH_4 = 0.1$

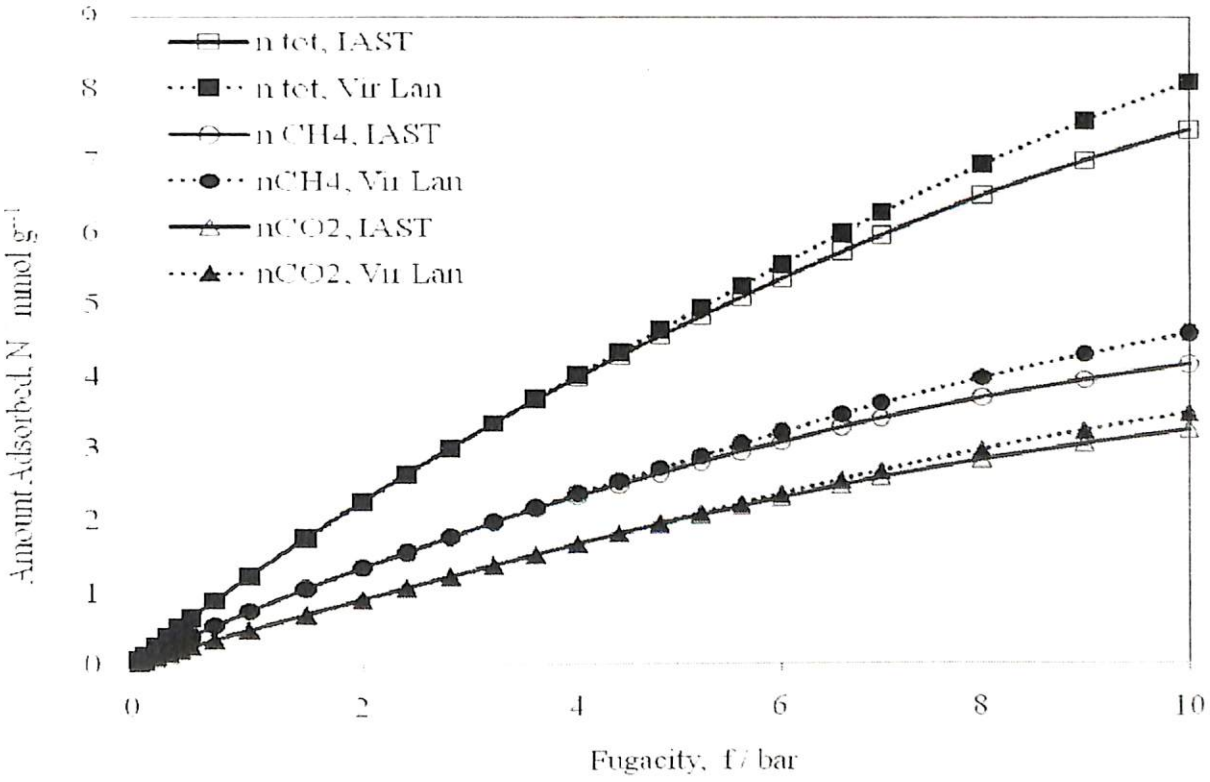

Figure 5.51: Variation of amount adsorbed from CO_2+CH_4 mixture at 305 K, $yCH_4 = 0.9$

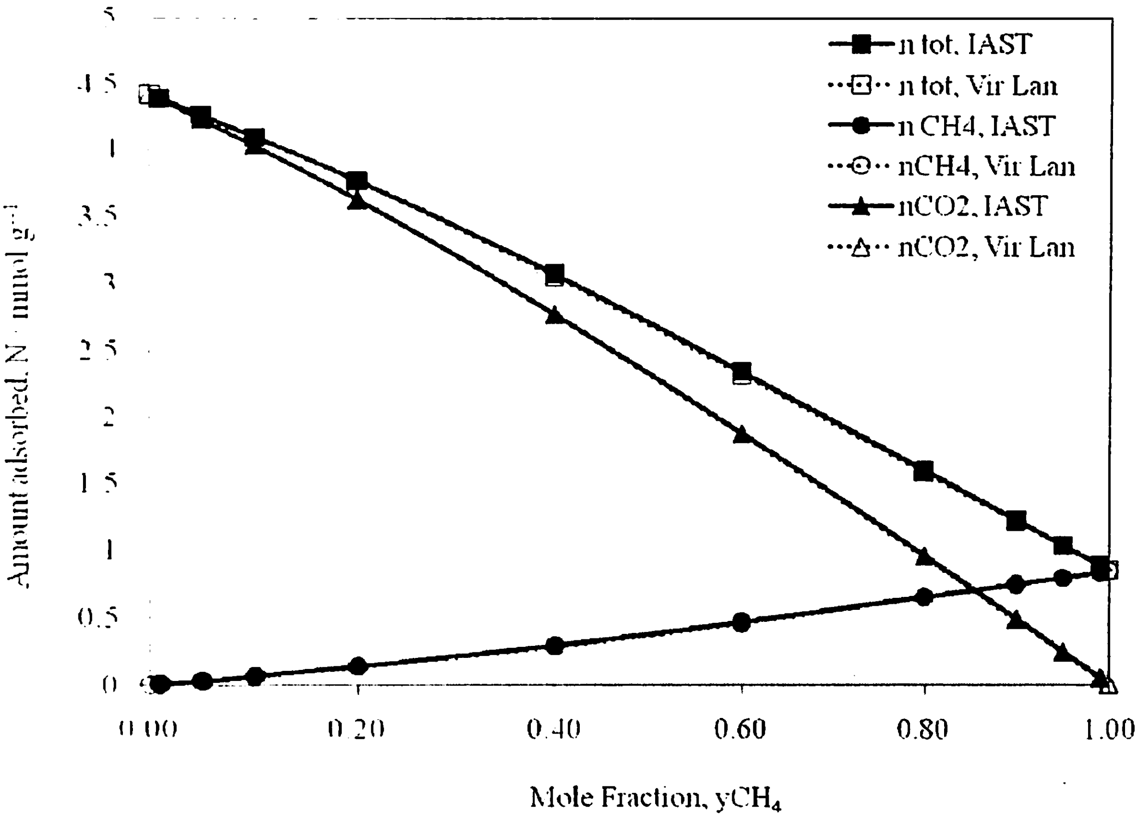

Figure 5.52: Variation of amount adsorbed from CO_2+CH_4 mixture at 305 K, P = 1 bar

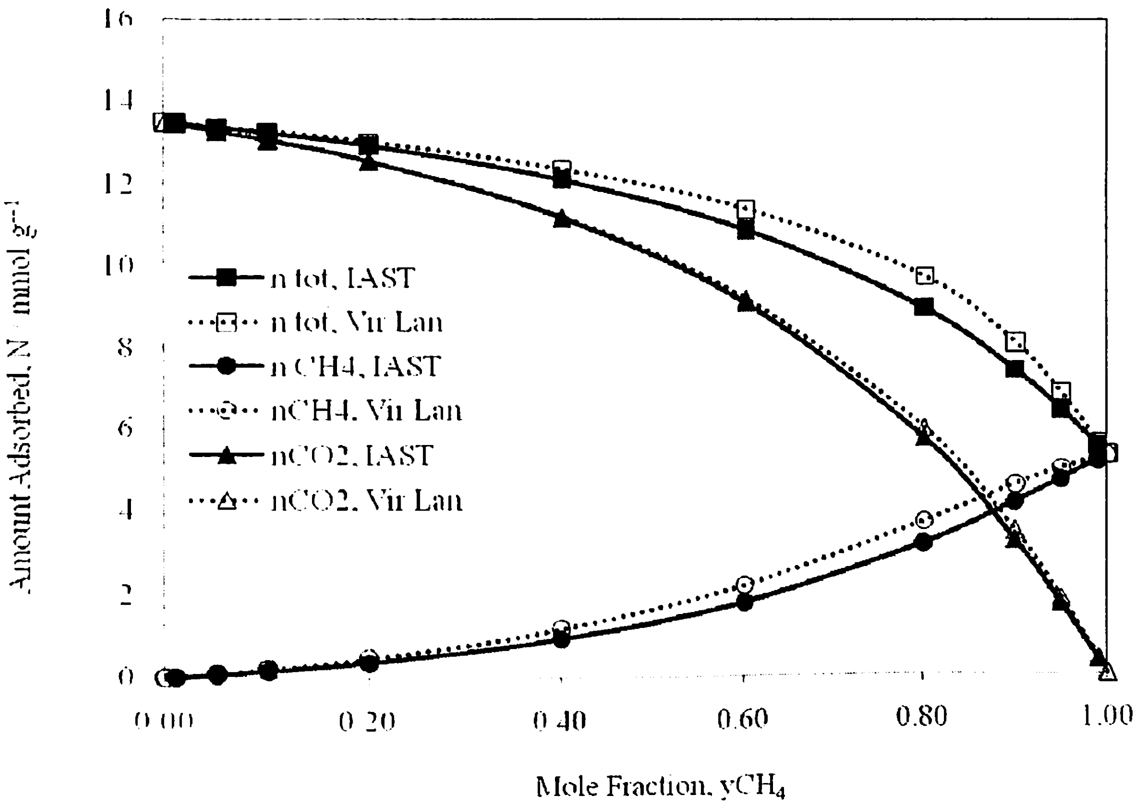

Figure 5.53: Variation of amount adsorbed from CO_2+CH_4 mixture at 305 K, P = 10 bar

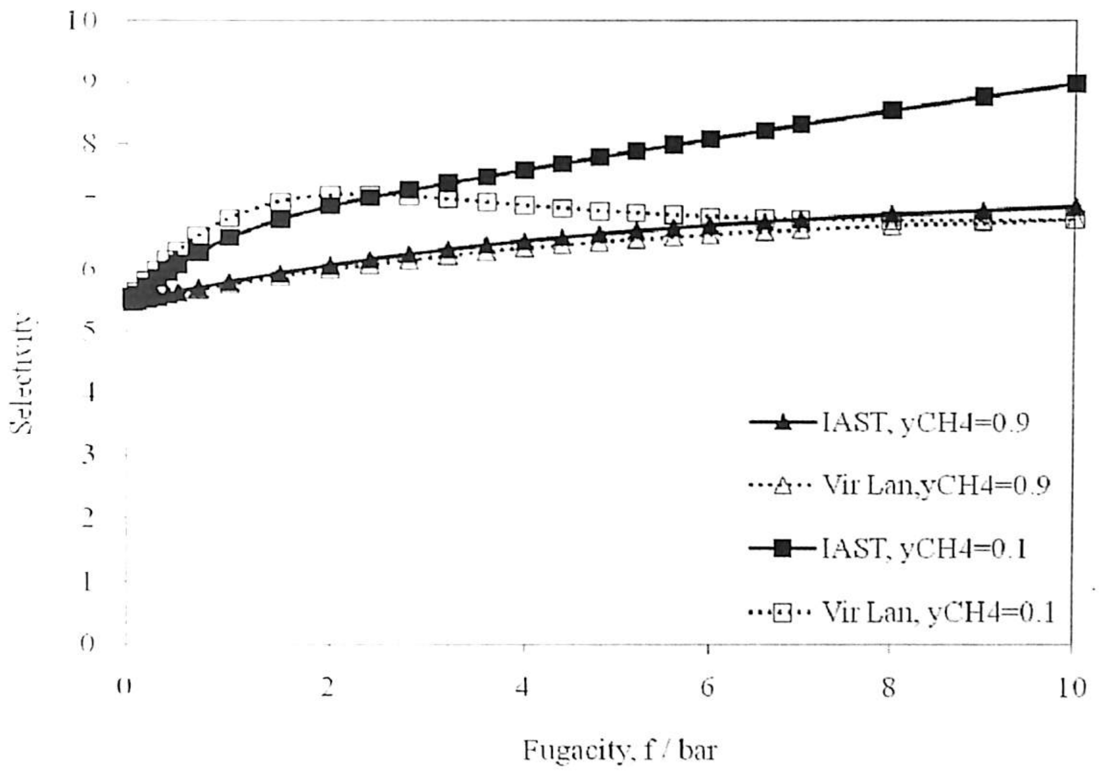

Figure 5.54: Variation of selectivity of CO_2+CH_4 mixture with pressure at 305 K

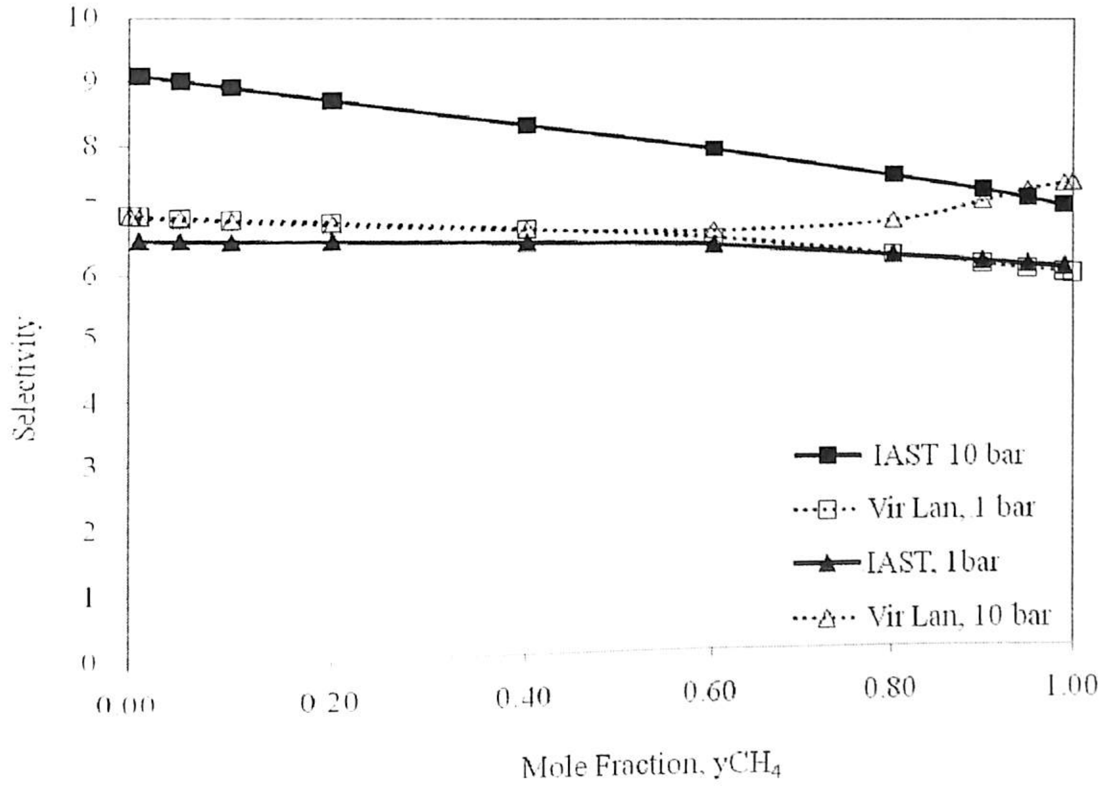

Figure 5.55: Variation of selectivity of CO_2+CH_4 mixture with mole fraction at 305 K

CHAPTER 6

Conclusions and Future Scope

6.1 Conclusions

It was the intention of this study to systematically investigate metal organic frameworks for their adsorption characteristics. Several probe molecules important from fundamental and industrial point of view were used for characterizing the adsorption properties of Cu-BTC and Cr-BDC metal organic frameworks.

Two different metal organic frameworks viz. Cu-BTC (or, HKUST-1) and Cr-BDC (or, MIL-101) were successfully synthesized. The surface area for three different batches of Cu-BTC viz. sample **A**, **B** and **C** were found to be approximately 857, 1482 and 1663 m^2 g^{-1} respectively. On the other hand MIL-101 had a surface area of ca. 2674 m^2 g^{-1}. These values were comparable with the available data from literature.. Synthesis conditions and post-synthesis treatment are critical in determining sample properties of metal organic frameworks.

Pure gas adsorption isotherms for eight different gases viz. Ar, N_2, O_2, CO_2, CH_4, CO, C_3H_8 and SF_6 were measured gravimetrically using a magnetic suspension balance (Rubotherm) in a series of experiments on these adsorbents. Additionally, a fast technique was successfully devised for measuring binary or mixed isotherms using a gas chromatograph. Binary gas adsorption study of industrially relevant mixture of CO_2+CH_4 was successfully carried out on Cu-BTC (sample **C**).

The following are the key findings reported in this work

1) The adsorption study from 0-10 bar on two different samples of Cu-BTC (sample **A** and **B**) were successfully carried out at 295 and 318 K. Cu-BTC showed little selectivity towards N_2, O_2 and Ar; the slightly higher loading for N_2 was probably due to its quadrupole moment. The loading of Ar on Cu-BTC (sample **B**) was found more than zeolites like silicalite, 5A, NaX, Na-ZSM-5 and NaETS-4; whereas the loading was comparable to activated carbon. N_2 adsorption on Cu-BTC (sample **B**) was found less than that on 5A, NaX and activated carbon. When compared with adsorption on inert zeolites like silicalite, ZSM-5 etc. the N_2 loading on sample **B** was found to be more, meaning polar zeolites enhance adsorption because of Nitrogen's high quadrupole value. O_2 loading on Cu-BTC (sample **B**) was found more than 5A, NaX and silicalite and comparable to activated carbon.
2) The maximum loading (about ca. 10 mmol g^{-1}) was obtained for CO_2 within the measurement range on Cu-BTC (sample **B**). This loading was comparable to various literature values on Cu-BTC with similar surface areas. Under similar experimental conditions CO_2 loading on Cu-BTC (sample **B**) was found more than that on zeolites like 13X, 5A, silicalite, H-ZSM-5, NaETS-4, H-Mordenite; carbonaceous material like activated carbon and MOFs' like IRMOF-1, IRMOF-3, MOF-5, MOF-177, MIL-47, MIL-100, ZIF-8.
3) The loading of SF_6 and C_3H_8 on sample **B** (Cu-BTC) was found much higher than conventional zeolites and activated carbon.
4) Virial isotherm model was used for isotherms of N_2, O_2, Ar and CO_2, whereas isotherms for C_3H_8 and SF_6 follow Langmuir model. The Henry constants for the gases increase in the order $C_3H_8 > SF_6 > CO_2 > N_2 > Ar > O_2$.

5) The limiting enthalpy of adsorption ($-\Delta h_{ads,0}$) for all the gases studied on Cu-BTC (sample **B**) varied between 11-35 kJ mol^{-1}. Ar, N_2 and O_2 were found to have almost identical value i.e. ~11 kJ mol^{-1}. The limiting enthalpy of adsorption is a strong function of polarizability and increased linearly with polarizability for Ar, SF_6 and C_3H_8. The only notable exception was observed for CO_2; because of its high quadrupole moment.

6) The adsorption properties of the two solids (samples **A** and **B**) were compared to one another. The scaling factor required for comparing the capacities in the two samples changes with loading. In the zero pressure limit it will be equal to the ratio of Henry constants; in most cases the ratio of Henry's constants was slightly higher than the ratio of specific surface areas. A common scaling factor for all gases (and at both temperatures) was determined, to compare isotherm results between the two samples. In the low loading region the value of scaling factor was about 2.04; this value increases to about 2.58 in the high loading region.

7) Gases like Ar, CH_4, CO_2, SF_6 and C_3H_8 were used as probes and their adsorption isotherms on Cr-BDC were measured at three widely different temperatures: 283, 319 and 351 K and pressures ranging between 0-10 bar. The results compare well with previously available data for CO_2 and CH_4 adsorption in cited articles. For all gases considered in the study the adsorption capacity on Cr-BDC at about 5 bar was found to be same (Ar and CH_4) or better (CO_2, C_3H_8, SF_6) than that on purely siliceous zeolite like silicalite. Within the experimental pressure range, it had a better capacity for CO_2 and CH_4 as compared to Al based MOFs' like MIL-53 and slightly lower capacity than that on Cu-BTC.

8) All adsorption isotherms were successfully modeled by Dual Site Langmuir type isotherm equation. DSL model proves to be particularly useful to model pure gas

adsorption on this class of materials which have two distinct adsorption sites. The limiting enthalpy of adsorption and Henry's constant on this material were directly related to the polarizability of the adsorbates, except for CO_2 which has a high quadrupole moment.

9) The enthalpy of adsorption ($-\Delta h_{ads}$) for all gases decreases with loading initially and then levels off to a constant value indicating a heterogeneity in the solid surface. The values for enthalpy of adsorption were comparable to those on zeolites for Ar. After the initial loading region, they are appreciably lower in Cr-BDC for other gases. As is the case with most other MOFs', MIL -101 seems to have only a moderate enthalpy of adsorption which allows use of milder regeneration conditions. Good capacity for various adsorbates, reasonable thermal stability and moderate adsorbate-adsorbent interactions all indicate that Cr-based MOFs' merit special attention for further study in separation and storage applications.

10) Comparative high pressure (0-100 bar) adsorption study of industrially relevant gases like CH_4, CO_2 and CO was successfully carried out at three different temperatures: 295, 318 and 353 K on Cu-BTC (sample **C**) and Cr-BDC frameworks. At high pressures (ca. 50 bar), the CH_4 loading on Cu-BTC and Cr-BDC was found higher than activated carbon, purely siliceous zeolite like silicalite and polar zeolites like 13X, 5A, NaY and MgY. CO adsorption on Cr-BDC at about ambient temperature was better than that on purely siliceous zeolite and comparable to that on polar zeolite like 5A. CO loading on Cu-BTC (sample **C**) measured in this work was slightly better or comparable to that reported in literature.

11) Virial-Langmuir model best fits the experimental data on Cu-BTC whereas Dual Site Langmuir model explains the adsorption behaviour on Cr-BDC framework which is known to have two distinct sites for adsorption.

12) For all gases the enthalpy of adsorption at low loading was higher on Cr-BDC than that on Cu-BTC since Cr-BDC possess co-ordinatively unsaturated metal centers and the difference between enthalpies of these three gases are due to differences in interaction of the adsorbates with these metal centers. In fact, due to this reason, CO which has lowest polarizability of all the three gases shows highest value of adsorption enthalpy due to its dipole moment.

13) While such centers are also present in case of Cu-BTC framework, they are either not open and may be hindered due to presence of left over solvent molecules from the synthesis procedure. This results in more modest difference in adsorption enthalpies between the three gases on Cu-BTC. On Cu-BTC, at higher loadings, the enthalpy of adsorption are directly related to the polarizability of the gases and decrease in the order $CO_2 < CH_4 < CO$. Presence of more open metal sites tend to pronounce the variation of enthalpy with loading in Cr-BDC as compared to Cu-BTC.

14) At all temperature Henry constant value for CH_4 was found more on Cu-BTC than on Cr-BDC whereas for CO this trend was just the opposite. For CO_2 at low temperature β was more in case of Cr-BDC whereas at high temperature the β value just reverses. Higher β value leads to higher adsorption capacity for CH_4 on Cu-BTC than on Cr-BDC. For CO adsorption, in the low loading region the capacity on Cr-BDC is higher due to electrostatic interactions. However, as the *cus* metal centers are occupied, the contribution of strong electrostatic interactions decreases.

15) Since the dispersion interactions (as indicated by β values) are stronger with the Cu-BTC framework than on Cr-BDC framework, isotherms of CO on Cu-BTC and Cr-BDC cross each other at about a loading of 0.75 mmol g^{-1}. Thereafter loading of CO on Cu-BTC is greater. However, even at 70 bar the loading of CO compared to CH_4 is

smaller on Cu-BTC framework and do not seem to approach a "clear" plateau indicating saturation; this may be due to the smaller polarizability of CO.

16) In case of CO_2 the behaviour in the low loading region is similar to that of CO. Henry constant value on Cr-BDC is higher due to its quadrupole moment. However as *cus* centers are occupied in the Cr-BDC framework, the contribution of electrostatic interactions decreases; this results in crossing of isotherms at a loading of about 0.35 mmol g^{-1}. Thereafter, at the same condition, loading on Cu-BTC is larger than that of Cr-BDC until about 16 bar. The loading on Cu-BTC seems to approach saturation (as in case of CH_4) at this pressure. However, due to availability of large pore volume in Cr-BDC, loading on Cr-BDC does not approach saturation. In fact, at a fugacity of 36 bar, loadings on Cr-BDC and Cu-BTC frameworks are 21.3 and 15.5 mmol g^{-1} respectively.

17) CO_2+CH_4 binary adsorption study was successfully carried out on Cu-BTC (sample C) at 305 K and for pressures up to 10 bar pressure using an infinite dilution gas chromatographic technique coupled with appropriate thermodynamic analysis using Virial-Langmuir model. The calculated cross virial coefficients were used for estimating adsorption isotherms for the mixture. Experimental findings were compared with the IAST predictions on mixed gas adsorption.

18) Based on the infinite dilution GC experiments it was concluded that within 10 bar the adsorption of CO_2+CH_4 mixture on Cu-BTC can be well predicted by IAST. The selectivity value lies between 5.7 and 7.2. This selectivity for CO_2+CH_4 mixture shows promise for effective separation using Cu-BTC.

6.2 Future Scope

Metal organic frameworks seem to be promising for their role in adsorptive separation and gas storage. In this work we have done systematic adsorption study on two metal organic frameworks and indicated a fast alternative technique combined with appropriate thermodynamic analysis for binary gas adsorption measurements. There are several areas which merit attention of scientific community for understanding the adsorption behaviour in the interesting materials.

[A] Synthesis conditions and post-synthesis activation methods are directly related to the physical properties of the metal organic frameworks, most importantly their specific surface area, thermal and chemical stability. The role of various solvents during activation of MOF samples needs to be thoroughly understood to effectively increase their surface area and thermal stability. MOFs` are generally very sensitive to surrounding environment (like moisture and organic vapors) and tend to rapidly degrade unless proper care is not taken. For an adsorbent to be useful at the industrial level needs to be more robust. A thorough study is needed to evaluate and improve their chemical stability.

[B] Experimental data on binary adsorption on MOFs are completely unavailable in literature. Nevertheless design of any adsorptive separation requires this information. A systematic investigation of binary adsorption of relevant gas mixtures on promising MOF materials is necessary to generate some sort of database on numerous MOFs reported.

[C] Only recently experiment and/simulation analysis of MOF materials for processes (PSA/VSA) are reported. Effective application of these materials to industrial processes would require considerable effort devoted to efficient process and/or cycles based on MOF materials.

References Cited

[1] Yang, R. T., *Gas Separation by Adsorption Processes*, Imperial College Press, London (1997), Chapter-1.

[2] Ruthven, D. M. and Sun, M. S., *Principle of Adsorption and Adsorption Processes*, Wiley-Interscience, New York, (1984), Chapter-1.

[3] Guisnet, M. and Gilson, J. P., *Zeolites for Cleaner Technologies*, Imperial College Press, London, (2002), p. 1-2.

[4] Szostak, R., *Molecular Sieves Principles of Synthesis and Identification*, Blackie Academic & Professional, London, (1998), p. 3.

[5] Yang, R. T., *Adsorbents: Fundamentals and Applications*, Wiley-Interscience, New-Jersey, (2003), p. 17-18

[6] Barton, T. J., Bull, L. M., Klemperer, W. G., Loy, D. A., McEnaney, B., Misono, M., Monson, P. A., Pez, G., Scherer, G. W., Vartuli, J. C., and Yaghi, O. M., "Tailored Porous Materials," *Chem. Mater.*, **11**, 2633-2656 (1999).

[7] Ruthven, D. M., Farooq, S. and Knaebel, *Pressure Swing Adsorption*, Wiley-VCH, New York, (1993), p. 12-13.

[8] Talu, O., "Needs, status, techniques and problems with binary gas adsorption experiments,"
Adv. Coll. Inter. Sci., **76-77**, 227-269 (1998).

[9] Yaghi, O. M., O'Keeffe, M., Ockwig, N. W., Chae, H. K., Eddaoudi, M., and Kim, J., "Reticular Synthesis and the design of New Materials," *Nature*, **423**, 705-714 (2003).

[10] Rowsell, J. L. C., and Yaghi, O. M.," Metal–organic frameworks: a new class of porous materials," *Micropor. Mesopor. Mater.*, **73**, 3-14 (2004).

[11] Galet, A., Niel, V., Muñoz, M. C., and Real, J. A., "Synergy between Spin Crossover and Metallophilicity in Triple Interpenetrated 3D Nets with the NbO Structure Type," *J. Am. Chem. Soc.*, **125**, 14224-14225 (2003).

[12] Ma, B. Q., Sun, H. L., and Gao, S., "The Design and Synthesis of a non-centric Diamond- like Network Based NH_4^+ Ion," *Chem. Coummn.*, 2164-2165 (2003).

[13] Lo, S. M- F., Chui, S. S- Y., Shek, L. Y., Lin, Z., Zhang, X. X., Wen, G., and Williams, I.D., "Solvothermal Synthesis of a Stable Coordination Polymer with Copper-I-Copper-II Dimer Units: [Cu4{1,4-C6H4(COO)2}3(4,4¢-bipy)2]*n*," *J. Am. Chem. Soc.*, **122**, 6293-6294 (2000).

[14] Luo, J., Hong, M., Wang, R., Cao, R., Han, L., Yuan, D., Lin, Z., and Zhou, Y., "A Novel Bilayer Cobalt(II)-Organic Framework with Nanoscale Channels Accommodating Large Organic Molecules," *Inorg. Chem.*, **42**, 4486-4488 (2003).

[15] Barthelet, K., Marrot, J., Riou, D., and Férey, G., "A Breathing Hybrid Organic-Inorganic Solid with Very Large Pores and High Magnetic Characteristics," *Angew. Chem. Int. Ed.*, **41**, 281-284 (2002).

[16] Bu, X. H., Tong, M. L., Chang, H. C., Kitagawa, S., and Batten, S. R., "A Neutral 3D Copper Coordination Polymer Showing 1D Open Channels and the First Interpenetrating NbO-Type Network," *Angew. Chem. Int. Ed.*, **43**, 192-195 (2004).

[17] Hong, J., "[Zn_2(BTDA)(bpy)(H_2O)].0.5bpy: a new three-dimensional metal-organic framework constructed from flexible and rigid mixed ligands," *J. Mol. Struct.*, **752**, 166-169 (2005).

[18] Dunbar, K. R., and Heintz, R. A., "Chemistry of Transition Metal Cyanide Compounds: Modern Perspectives," *Prog. Inorg. Chem.*, **45**, 283-391 (1997).

[19] Gramaccioli, C. M., "The crystal structure of zinc glutamate dehydrate," *Acta Cryst.*, **21**, 600-605 (1966).

[20] Okada, K., Kay, M.I., Cromer, D.T., and Almodovar, I., "Crystal Structure by Neutron Diffraction and the Antiferroelectric phase Transition in Copper Formate Tetrahydrate," *J. Chem. Phys.*, **44**, 1648-1653 (1966).

[21] Jarvis, J. A. J., "The crystal structure of a complex of cupric chloride and 1:2:4-triazole," *Acta Cryst.*, **15**, 964-966 (1962).

[22] Sterling, C., "Crystal Structure of Weddellite," *Science*, **146**, 518-519 (1964).

[23] Robl, C., "Water Clustering in the Zeolite-like Channel Structure of $Na_2Zn[C_6H_2(COO)_4].9H_2O$," *Mater. Res. Bull.*, **27**, 99-107 (1992)

[24] Davis, M. E.,"Ordered Porous Materials for Emerging Applications," *Nature*, **417**, 813-821 (2002).

[25] Mueller, U., Schubert, M., Teich, F., Puetter, H., Schierle-Arndt, K., and Pastré, J.,"Metal-organic Frameworks-Prospective Industrial Applications," *J. Mater. Chem.*, **16**, 626-636 (2006).

[26] Li, H., Eddaoudi, M., O'Keeffe, M., and Yaghi, O. M.,"Design and Synthesis of an Exceptionally Stable and Highly Porous Metal-organic Framework," *Nature*, **402**, 276-279 (1999).

[27] Eddaoudi, M., Moler, D. B., Li, H., Chen, B., Reineke, T. M., O'Keeffe, M., and Yaghi, O. M.,"Modular Chemistry: Secondary Building Units as a Basis for the design of Highly Porous Metal-Organic Carboxylate Frameworks," *Acc. Chem. Res.*, **34**, 319-330 (2001).

[28] Ma, S., Eckert, J., Forster, P. M., Woong Yoon, J., Hwang, Y. K., Chang, J.-S., Collier, C. D., Parise, J. B., and Zhou, H.-C., "Further Investigation of the Effect of Framework Catenation on Hydrogen Uptake in Metal-Organic Frameworks," *J. Am. Chem. Soc.*, **130**, 15896-15902(2008)

[29] Sarkisov, L., Düren, T., and Snurr, R.Q., "Molecular modeling of adsorption in novel nanoporous metal-organic materials," *Mol. Phys.*, **102**, 211-221 (2004)

[30] Skoulidas, A. I., and Sholl, D. S.,"Self-diffusion and transport diffusion of light gases in metal-organic framework materials assessed using molecular dynamics simulation," *J. Phys. Chem. B*, **109**, 15760-15768 (2005).

[31] Düren, T., and Snurr, R.Q., "Assessment of Isoreticular Metal-Organic Frameworks for Adsorption Separations: A Molecular Simulation Study of Methane/*n*-Butane Mixtures," *J. Phys. Chem. B*, **108**, 15703-15708 (2004).

[32] Kawakami, T., Takamizawa, S., Kitagawa, Y., Maruta, T., Mori, W., and Yamaguchi, K.," Theoretical studies of spin arrangement of adsorbed organic radicals in metal-organic nanoporous cavity," *Polyhedron*, **20**, 1197-1206 (2001).

[33] Eddaoudi, M., Li, H., and Yaghi, O. M.," Highly Porous and Stable Metal-Organic Frameworks: Structure, Design and Sorption Properties," *J. Am. Chem. Soc.*, **122**, 1391-1397 (2000).

[34] Huang, L., Wang, H., Chen, J., Wang, Z., Sun, J., Zhao, D., and Yan, Y.,"Synthesis, Morphology Control, and Properties of Porous Metal-Organic Coordination Polymers," *Micropor. Mesopor. Mater.*, **58**, 105-114 (2003).

[35] Liu, B., and Smit, B.,"Comparative Molecular Simulation Study of CO_2/N_2 and CH_4/N_2 Separation in Zeolites and Metal-Organic Frameworks," *Langmuir*, **25**, 5918-5926 (2009).

[36] Keskin, S., and Sholl, D. S.," Screening Metal-Organic Framework Materials for Membrane-based Methane/Carbon Dioxide Separations," *J. Phys. Chem. C*, **111**, 14055-14059 (2007).

[37] Krungleviciute, V., Lask, K., Heroux, L., Migone, A. D., Lee, J. -Y., Li, J., and Skoulidas, A.," Argon Adsorption on Cu_3(Benzene-1,3,5-tricarboxylate)$_2$(H_2O)$_3$ Metal-Organic Framework," *Langmuir*, **23**, 3106-3109 (2007).

[38] Vishnyakov, A., Ravikovitch, P. I., Neimark, A. V., Bülow, M., Wang, Q. M.,"Nanopore structure and sorption properties of Cu-BTC metal-organic framework," *Nano Lett.*, **3**, 713-718 (2003).

[39] Wang, Q.M., Shen, D., Bülow, M., Lau, M. L., Deng, S., Fitch, F. R., Lemcoff, N. O., Semanscin, J.,"Metallo-organic molecular sieve for gas separation and purification," *Micropor. Mesopor. Mater.*, **55**, 217-230 (2002).

[40] Wang, S., Yang, Q., and Zhong, C.,"Adsorption and separation of binary mixtures in a metal-organic framework Cu-BTC: A computational study," *Sep. Purf. Tech.*, **60**, 30-35 (2008).

[41] Yang, Q., Xue, C., Zhong, C., and Chen, J. –F.,"Molecular Simulation of Separation of CO_2 from Flue Gases in Cu-BTC Metal-Organic Framework," *AIChE J.*, **53**, 2832-2840 (2007).

[42] Eddaoudi, M., Kim, J., Rosi, N., Vodak, D., Wachter, J., O'Keeffe, M., Yaghi, O. M.," Systematic Design of Pore Size and Functionality in Isoreticular MOFs and Their Application in Methane Storage," *Science*, **295**, 469-472 (2002).

[43] Bourrelly, S., Llewellyn, P. L., Serre, C., Millange, F., Loiseau, T., and Férey, G., "Different Adsorption Behaviors of Methane and Carbon Dioxide in the Isotypic Nanoporous Metal Terephthalates MIL-53 and MIL-47," *J. Am. Chem. Soc.*, **127**, 13519-13521 (2005).

[44] Millward, A. R., and Yaghi, O. M.," Metal-Organic Frameworks with Exceptionally High Capacity for Storage of Carbon Dioxide at Room Temperature," *J. Am. Chem. Soc.*, **127**, 17998-17999 (2005).

[45] Senkovska, I. and Kaskel, S.," High pressure methane adsorption in the metal-organic frameworks $Cu_3(btc)_2$, $Zn_2(bdc)_2dabco$, and $Cr_3F(H_2O)_2O(bdc)_3$," *Micropor. Mesopor. Mater.*, **112**, 108-115 (2008).

[46] Llewellyn, P.L., Bourrelly, S., Serre, C., Vimont, A., Daturi, M., Hamon, L., Weireld, G. D., Chang, J. -S., Hong, D. -Y., Hwang, Y. K., Jhung, S. H., Férey, G., "High Uptakes of CO_2 and CH_4 in Mesoporous Metal-Organic Frameworks MIL-100 and MIL-101," *Langmuir*, **24**, 7245-7250 (2008).

[47] Rosi, N. L., Eckert, J., Eddaoudi, M., Vodak, D. T., Kim, J., O'Keeffe, M., and Yaghi, O. M.," Hydrogen Storage in Microporous Metal-Organic Frameworks," *Science*, **300**, 1127-1129 (2003).

[48] Rowsell, J. L. C., Millward, A. R., Park, K. S., and Yaghi, O. M.," Hydrogen Sorption in Functionalized Metal-Organic Frameworks," *J. Am. Chem. Soc.*, **126**, 5666-5667 (2004).

[49] Wong-Foy, A. G., Matzger, A. J., and Yaghi, O. M., "Exceptional H_2 Saturation Uptake in Microporous Metal-Organic Frameworks," *J. Am. Chem. Soc.*, **128**, 3494-3495 (2006).

[50] Pan, L., Sander, M. B., Huang, X., Li, J., Smith, M., Bittner, E., Bockrath, B., and Karl Johnson, J.," Microporous Metal Organic Materials: Promising Candidates as Sorbents for Hydrogen Storage," *J. Am. Chem. Soc.*, **126**, 1308-1309 (2004).

[51] Férey, G., Latroche, M., Serre, C., Millange, F., Loiseau, T., and Percheron-Guégan, A., "Hydrogen adsorption in the nanoporous metal-benzenedicarboxylate M(OH)(O_2C–C_6H_4–CO_2) (M = Al^{3+}, Cr^{3+}), MIL-53," *Chem. Commun.*, 2976-2977 (2003).

[52] Latroche, M., Surblé S., Serre, C., Mellot-Draznieks, C., Llewellyn, P. L., Lee, J. H, Chang, J. S., Jhung, S. H., and Férey, G., "Hydrogen Storage in the Giant-Pore Metal-Organic Frameworks MIL-100 and MIL-101," *Angew. Chem. Int. Ed.*, **45**, 8227-8231 (2006).

[53] Li, Y., and Yang, R. T.," Significantly Enhanced Hydrogen Storage in Metal-Organic Frameworks via Spillover," *J. Am. Chem. Soc.*, **128**, 726-727 (2006).

[54] Li, Y., and Yang, R. T., "Hydrogen Storage in Metal-Organic Frameworks by Bridged Hydrogen Spillover," *J. Am. Chem. Soc.*, **128**, 8136-8137 (2006).

[55] Li, Y., and Yang, R.T., "Hydrogen Storage in Metal-Organic and Covalent-Organic Frameworks by Spillover," *AIChE J.*, **54**, 269-279 (2008).

[56] Panella, B., Hirscher, M., Putter, H., and Muller, U.," Hydrogen Adsorption in Metal–Organic Frameworks: Cu-MOFs and Zn-MOFs Compared," *Adv. Funct. Mater.*, **16**, 520-524 (2006).

[57] Llabres i Xamena, F. X., Abad, A., Corma, A., and Garcia, H.,"MOFs as catalysts: Activity, reusability and shape-selectivity of a Pd-containing MOF," *J. Catal.*, **250**, 294-298 (2007).

[58] Schlichte, K., Kratzke, T., and Kaskel, S.,"Improved synthesis, thermal stability and catalytic properties of the metal-organic framework compound $Cu_3(BTC)_2$," *Micropor. Mesopor. Mater.*, **73**, 81-88 (2004).

[59] Gomez-Lor, B., Gutierrez-Puebla, E., Iglesias, M., Monge, M. A., Ruiz-Valero, C., and Snejko, N.," Novel 2D and 3D Indium Metal-Organic Frameworks: Topology and Catalytic Properties," *Chem. Mater.*, **17**, 2568-2573 (2005).

[60] Yamada, Y. M. A., Maeda, Y., and Uozumi, Y., "Novel 3D Coordination Palladium-Network Complex: A Recyclable Catalyst for Suzuki-Miyaura Reaction," *Org. Lett.*, **8**, 4259-4262 (2006).

[61] Janiak, C., "Engineering coordination polymers towards applications," *Dalton Trans.*, 2781-2804 (2003).

[62] Cho, S. -H., Ma, B., Nguyen, S. T., Hupp, J. T., and Albrecht-Schmitt, T. E., "A metal–organic framework material that functions as an enantioselective catalyst for olefin epoxidation," *Chem. Commun.*, 2563-2565 (2006).

[63] Szeto, K. C., Prestipino, C., Lamberti, C., Zecchina, A., Bordiga, S., Bjørgen, M., Tilset, M., and Lillerud, K. P., "Characterization of a New Porous Pt-Containing Metal-Organic Framework Containing Potentially Catalytically Active Sites: Local Electronic Structure at the Metal Centers," *Chem. Mater.*, **19**, 211-220 (2007).

[64] Prestipino, C., Regli, L., Vitillo, J. G., Bonino, F., Damin, A., Lamberti, C., Zecchina, A., Solari, P. L., Kongshaug, K. O., and Bordiga, S., "Local Structure of Framework Cu(II) in HKUST-1 Metallorganic Framework: Spectroscopic Characterization upon Activation and Interaction with Adsorbates," *Chem. Mater.*, **18**, 1337-1346 (2006).

[65] Szeto, K. C., Lillerud, K. P., Tilset, M., Bjørgen, M., Prestipino, C., Zecchina, A., Lamberti, C., and Bordiga, S., "A Thermally Stable Pt/Y-Based Metal-Organic Framework: Exploring the Accessibility of the Metal Centers with Spectroscopic Methods Using H_2O, CH_3OH, and CH_3CN as Probes," *J. Phys. Chem. B*, **110**, 21509-21520 (2006).

[66] Alaerts, L., Séguin, E., Poelman, H., Thibault-Starzyk, F., Jacobs, P.A., and De Vos, D.E., "Probing the Lewis Acidity and Catalytic Activity of the Metal-Organic Framework $[Cu_3(btc)_2]$ (BTC=Benzene-1,3,5-tricarboxylate)," *Chem. Eur. J.*, **12**, 7353-7363 (2006).

[67] Kitagawa, S., Kitaura, R., and Noro, S.I.,"Functional Porous Coordination Polymers," *Angew. Chem. Int. Ed.*, **43**, 2334-2375 (2004).

[68] Hagrman, P. J., Hagrman, D., and Zubieta, J.,"Organic-Inorganic Hybrid Materials: From Simple Coordination Polymers to Organodiamine-Templated Molybdenum Oxides, " *Angew. Chem. Int. Ed.*, **38**, 2638-2684 (1999).

[69] Blake, A. J., Champness, N. R., Hubberstey, P., Li, W. S., Withersby, M. A., and Schröder, M.," Inorganic crystal engineering using self-assembly of tailored building-blocks," *Coordin. Chem. Rev.*, **183**, 117-138 (1999).

[70] Moulton, B., and Zaworotko, M. J.,"From Molecules to Crystal Engineering: Supramolecular Isomerism and Polymorphism in Network Solids, " *Chem. Rev.*, **101**, 1629-1658 (2001).

[71] Rao, C. N. R., Natarajan, S., and Vaidhyanathan, R.,"Metal Carboxylates with Open Architectures, " *Angew. Chem. Int. Ed.*, **43**, 1466-1496 (2004).

[72] Xiao, B., Wheatley, P. S., Zhao, X., Fletcher, A. J., Fox, S., Rossi, A. G., Megson, I. L., Bordiga, S., Regli, L., Mark Thomas, K., and Morris, R. E.," High-Capacity Hydrogen and Nitric Oxide Adsorption and Storage in a Metal-Organic Framework," *J. Am. Chem. Soc.*, **129**, 1203-1209 (2007).

[73] Rowsell, J. L. C., and Yaghi, O. M.," Strategies for Hydrogen Storage in Metal-Organic Frameworks," *Angew. Chem. Int. Ed.*, **44**, 4670-4679 (2005).

[74] Chui, S. S.-Y., Lo, S. M.-F., Charmant, J. P. H., Orpen, A. G., and Williams, I. D.,"A Chemically Functionalizable Nanoporous material $[Cu_3(TMA)_2(H_2O)_3]_n$," *Science*, **283**, 1148-1150 (1999).

[75] Férey, G., Mellot-Draznieks, C., Serre, C., Millange, F., Dutour, J., Surblé S., and Margiolaki, I., "A Chromium Terephthalate-Based Solid with Unusually Large Pore Volumes and Surface Area," *Science*, **309**, 2040-2042 (2005).

[76] Lebedev, O. I., Millange, F., Serre, C., Van Tendeloo, G., and Férey, G.," First Direct Imaging of Giant Pores of the Metal-Organic Framework MIL-101," *Chem. Mater.*, **17**, 6525-6527 (2005).

[77] Vermesse, J., Vidal, D., and Malbrunot, P., "Gas Adsorption on Zeolites at High Pressure," *Langmuir*, **12**, 4190-4196 (1996).

[78] Salem, M.M.K., Braeuer, P., Szombathely, M.V., Heuchel, M., Harting, P., Quitzsch, K., and Jaroniec, M., "Thermodynamics of High-Pressure Adsorption of Argon, Nitrogen, and Methane on Microporous adsorbents," *Langmuir*, **14**, 3376-3389 (1998).

[79] Belmabkhout, Y., De Weireld, G., and Frère, M., "High-Pressure Adsorption Isotherms of N_2, CH_4, O_2, and Ar on Different Carbonaceous Adsorbents," *J. Chem. Engg. Data,* **49**, 1379-1391 (2004).

[80] Liu, J., Culp, J.T., Natesakhawat, S., Bockrath, B.C., Zande, B., Sankar, S.G., Garberoglio, G., and Karl Johnson, J., "Experimental and Theoretical Studies of Gas Adsorption in $Cu_3(BTC)_2$: An Effective Activation Procedure," *J. Phys. Chem. C.*, **111**, 9305-9313 (2007).

[81] Pillai, R.S., Peter, S.A., and Jasra, R.V., "Adsorption of carbon dioxide, methane, nitrogen, oxygen and argon in NaETS-4," *Micropor. Mesopor. Mater.*, **113**, 268-276 (2008).

[82] Dunne, J.A., Rao, M., Sircar, S., Gorte, R.J., and Myers, A. L.," Calorimetric Heats of Adsorption and Adsorption Isotherms. 2. O_2, N_2, Ar, CO_2, CH_4, C_2H_6, and SF_6 on NaX, H-ZSM-5, and Na-ZSM-5 Zeolites," *Langmuir*, **12**, 5896-5904 (1996).

[83] Myers, A.L., "Characterization of nanopores by standard enthalpy and entropy of adsorption of probe molecules," Colloids and Surfaces A, **241**, 9-14 (2004).

[84] Golden, T. C., and Sircar, S., "Gas Adsorption on Silicalite," *J. Coll. Inter. Sci.*, 162, 182-188 (1994).

[85] Dunne, J.A., Mariwala, R., Rao, M., Sircar, S., Gorte, R.J., and Myers A.L., "Calorimetric Heats of Adsorption and adsorption Isotherms. 1. O_2, N_2, Ar, CO_2, CH_4, C_2H_6, and SF_6 on Silicalite," *Langmuir*, **12**, 5888-5895 (1996).

[86] Liang, Z., Marshall, M., and Chaffee, A.L., "CO_2 Adsorption-Based Separation by Metal Organic framework (Cu-BTC) versus Zeolite (13X)," *Energy & Fuels*, **23**, 2785-2789 (2009).

[87] Van de Voorde, M., Verelst, H., and Baron, G.V., "Measurement of O_2-N_2 Binary Sorption on 5A Zeolite by Isotope Tracer and Perturbation Chromatography," *J. Porous Materials*, **2**, 51-57 (1995).

[88] Talu, O., Li, J., Kumar, R., Mathias, P.M., Moyer, J.D., Jr, and Schork, J.M., "Measurement and analysis of oxygen/nitrogen/5A-zeolite adsorption equilibria for air separation," *Gas. Sep. Purif.*, **10**, 149-159 (1996).

[89] Frère, M.G., and De Weireld, G.F., "High-Pressure and High-Temperature Excess Adsorption Isotherms of N_2, CH_4, and C_3H_8 on Activated Carbon," *J. Chem. Engg. Data,* **47**, 823-829 (2002).

[90] Dreisbach, F., Staudt, R., and Keller, J.U., "High Pressure Adsorption Data of Methane, Nitrogen, Carbon Dioxide and their Binary and Ternary Mixtures on Activated carbon," *Adsorption*, **5**, 215-227 (1999).

[91] Shen, D., and Bülow, M., "Comparison of Experimental Techniques for Measuring Isosteric Heat of Adsorption," *Adsorption*, **6**, 275-286 (2000).

[92] García-Pérez, E., Gascón, J., Morales-Flórez, V., Castillo, J.M., Kapteijn, F., and Calero, S., "Identification of Adsorption sites in Cu-BTC by Experimentation and Molecular Simulation," *Langmuir*, 25, 1725-1731 (2009).

[93] Farrusseng, D., Daniel, C., Gaudillere, C., Ravon, U., Schuurman, Y., Mirodatos, C., Dubbeldam, D., Frost, H., and Snurr, R.Q., "Heats of Adsorption for Seven Gases in Three Metal-Organic Frameworks: Systematic Comparison of Experiment and Simulation," *Langmuir*, **25**, 7383-7388 (2009).

[94] Li, Y., and Yang, R.T., "Gas Adsorption and storage in Metal-Organic Framework MOF-177," *Langmuir*, **23**, 12937-12944 (2007).

[95] Li, P., and Tezel, F.H.,"Pure and Binary Adsorption Equilibria of Carbon Dioxide and Nitrogen on Silicalite, " *J. Chem. Engg. Data,* **53**, 2479-2487 (2008).

[96] Li, P., and Tezel, F.H., "Pure and Binary Adsorption of Methane and Nitrogen by Silicalite," *J. Chem. Engg. Data,* **54**, 8-15 (2009).

[97] Pakseresht, S., Kazemeini, M., and Akbarnejad, M.M., "Equilibrium isotherms for CO, CO_2, CH_4 and C_2H_4 on the 5A molecular sieve by a simple volumetric apparatus," *Sep. Purf. Tech.*, **28**, 53-60 (2002).

[98] Staudt, R., Herbst, A., Beutekamp S., and Harting, P., "Adsorption of Pure Gases and Mixtures on Porous Solids up to High Pressures," *Adsorption*, **11**, 379-384 (2005).

[99] Talu, O., and Zwiebel, I., "Multicomponent Adsorption Equilibria of Nonideal Mixtures", *AIChE J.*, **32**, 1263-1276 (1986).

[100] Yazaydin, A.O., Snurr, R.Q., Park, T.-H., Koh, K., Liu, J., LeVan, M.D., Benin, A.I., Jakubczak, P., Lanuza, M., Galloway, D.B., Low, J.J., and Willis, R.R., "Screening of Metal-Organic Frameworks for Carbon Dioxide Capture from Flue Gas Using a Combined Experimental and Modeling Approach," *J. Am. Chem. Soc.*, **131**, 18198-18199 (2009).

[101] Zhao, Z., Li, Z., and Lin, Y.S., "Adsorption and Diffusion of Carbon Dioxide on Metal-Organic Framework (MOF-5)," *Ind. Eng. Chem. Res.*, **48**, 10015-10020 (2009).

[102] Siperstein, F.R., and Myers, A.L., "Mixed-Gas Adsorption," *AIChE J.*, 47, 1141-1159 (2001).

[103] Sun, M. S., Shah, D. B., Xu, H. H., and Talu, O., "Adsorption Equilibria of C_1 to C_4 Alkanes, CO_2, and SF_6 on Silicalite," *J. Phys. Chem. B*, **102**, 1466-1473 (1998).

[104] Talu, O., Zhang, S.-Y., and Hayhurst, D.T., "Effect of Cations on Methane Adsorption by NaY, MgY, CaY, SrY, and BaY Zeolites," *J. Phys. Chem.*, **97**, 12894-12898 (1993).

[105] Garberoglio, G., Skoulidas, A.I., and Karl Johnson, J., "Adsorption of Gases in Metal Organic Materials: Comparison of Simulations and Experiments," *J. Phys. Chem. B*, **109**, 13094-13103 (2005).

[106] Wang, S., "Comparative Molecular Simulation Study of Methane adsorption in Metal-Organic frameworks," *Energy & Fuels*, **21**, 953-956 (2007).

[107] Yun, J.-H., Duren, T., Keil, F.J., and Seaton, N.A., "Adsorption of Methane, Ethane, and Their Binary Mixtures on MCM-41: Experimental Evaluation of Methods for the Prediction of Adsorption equilibrium," *Langmuir*, **18**, 2693-2701 (2002).

[108] Cao, D.V., and Sircar, S., "Heat of adsorption of Pure Sulfur Hexafluoride on Micro-Mesoporous Adsorbents," *Adsorption*, **7**, 73-80 (2001).

[109] Van Ness, H. C., "Adsorption of gases on solids," *I & EC Fundamentals*, **8**, 464-473 (1969).

[110] Steele, W. A., *The interaction of gases with solid surfaces*, Pergamon press, New York, (1974).

[111] Smith, J. M. and Van Ness H. C., *Introduction to Chemical Engineering Thermodynamics*, Fourth Edition, McGraw-Hill, New York, (1987).

[112] Myers, A. L., and Prausnitz, J. M., "Thermodynamics of Mixed Gas Adsorption," *AIChE J.*, **11**,121-127 (1965).

[113] Talu, O., *Thermodynamics of multicomponent gas adsorption equilibria of non-ideal mixtures*, PhD Dissertation, Arizona State University (1984).

[114] Hoory, S. E., and Prausnitz, J. M., "Monolayer adsorption of gas mixtures on homogeneous and heterogeneous solids", *Chem. Eng. Sci.*, **22**, 1025-1033 (1967).

[115] Do, D. D., *Adsorption Analysis: Equilibria and Kinetics*, Imperial College Press, London, 1998.

[116] Mathias, P. M., Kumar, R., Moyer, J. D., Schork, J. J. M., Srinivasan, S. R., Auvil, S. R., and Talu, O., "Correlation of Multicomponent Gas Adsorption by the Dual-Site Langmuir Model. Application to Nitrogen/Oxygen Adsorption on 5A-Zeolite," *Ind. Eng. Chem. Res.*, 35, 2477-2483 (1996).

[117] Ross, S., and Olivier, J. P., *On physical adsorption*, Buttersworth, Washington D.C., (1964).

[118] Ustinov, E. A., Do, D. D., Herbst, A., Staudt, R., and Harting, P., "Modeling of Gas Adsorption equilibrium over a Wide Range of pressure: A Thermodynamic Approach Based on Equation of State," *J. Coll. Inter. Sci.*, **250**, 49-62 (2002).

[119] Haydel J.J., and Kobayashi, R., "Adsorption Equilibria in the Methane-Propane-Silica Gel System at High Pressures," *I&EC Fundamentals*, **6**, 546-554 (1967).

[120] Taqvi, S.M., and LeVan, D.M., "Virial Description of Two-Component Adsorption on Homogeneous and Heterogeneous Surfaces", *Ind. Eng. Chem. Res.*, **36**, 2197-2206 (1997).

[121] Appel, W.S., LeVan, D.M., and Finn, J.E., "Nonideal Adsorption Equilibria Described by Pure Component Isotherms and Virial Mixture Coeffcients", *Ind. Eng. Chem. Res.*, **37**, 4774-4782 (1998).

[122] Yaghi, O. M., Li, G., and Li, H., "Selective binding and removal of guests in a microporous metal-organic framework," *Nature*, 378, 703-706 (1995).

[123] Rowsell, J. L. C., and Yaghi, O. M., "Effects of Functionalization, Catenation, and Variation of the Metal Oxide and Organic Linking Units on the Low-Pressure Hydrogen

Adsorption Properties of Metal-Organic Frameworks," *J. Am. Chem. Soc.*, **128**, 1304-1315 (2006).

[124] Dreisbach, F., Reza Seif A.H., and Loesch, H.W., "Gravimetric Measurement of Adsorption Equilibria of Gas Mixture CO/H_2 with a Magnetic Suspension Balance", *Chem. Eng. Technol.*, **25**, 1060-1065 (2002).

[125] http://dippr.byu.edu/student.asp

[126] NIST Chemistry web book [http://webbook.nist.gov/chemistry/]

[127] Conder, J.R., and Young C.L., *Physicochemical Measurement by Gas Chromatography*, John Wiley and Sons, 1979.

[128] Stalkup, F.I., and Kobayashi, R., "High-Pressure Phase Equilibrium Studies by Gas-Liquid Partition Chromatography", *AIChE J.*, **9**, 121-127 (1963).

[129] Schneider, P., and Smith, J.M. "Adsorption Rate Constants from Chromatography", *AIChE J.*, **14**, 762-771 (1968).

[130] Van der Vlist, E., and Van der Meijden, J., "Determination of adsorption isotherms of the components of binary gas mixtures by gas chromatography", *Journal Of Chromatography*, **79**, 1-13 (1973).

[131] Shah, D.B., and Ruthven, D.M., "Measurement of Zeolitic Diffusivities and Equilibrium Isotherms by Chromatography", *AIChE J.*, **23**, 804-809 (1977).

[132] Ruthven, D.M., and Kumar, R., "An Experimental Study of Single-Component and Binary Adsorption Equilibria by a Chromatographic Method", *Ind. Eng. Chem. Fund.*, **19**, 27-32 (1980).

[133] Hyun, S.H., and Danner, R.P., "Gas Adsorption Isotherms by Use of Perturbation Chromatography", *Ind. Eng. Chem. Fundam.*, **24**, 95-101 (1985).

[134] Tezel, F.H., Tezel, H.O., and Ruthven, D.M, "Determination of Pure and Binary isotherms for Nitrogen and Krypton," *J. of Colloid and Interface Science*, **149(1)**, 197-207 (1992).

[135] Triebe, R.W., and Tezel, F.H., "Adsorption of nitrogen and carbon monoxide on clintopolite: determination and prediction of pure and binary isotherms," *The Canadian Journal of Chemical Engineering*, **73**, 717-724 (1995).

[136] Mason, G., Buffahm, Bryan, A., "Gas Adsorption Isotherms from Composition and flow-rate Transient times in Chromatographic Columns II. Effect of Pressure Changes," *Proc. R. Soc. Lond. A* , **452**, 1287-1300 (1996).

[137] Gilmer, H.B., and Kobayashi, R., "The study of Gas-Solid Equilibrium at High Pressures by Gas Chromatography: Part I. Ethane, Propane, n-Butane at Essentially Infinite Dilutions in the Methane-Silica Gel System", *AIChE J.*, **10(6)**, 797-803 (1964).

[138] Gilmer, H.B., and Kobayashi, R., "The study of Multicomponent Gas-Solid Equilibrium at High Pressures by Gas Chromatography: Part II. Generalization of the Theory and Application to the Methane-Propane-Silica Gel System", *AIChE J.*, **11**, 702-705 (1965).

[139] Hyun, S.H., and Danner, R.P., "Determination of gas adsorption equilibria by the concentration pulse technique", *AIChE Symp. Ser.*, **34**, 1861-1877 (1982).

[140] Jonsson, J.A., *Chromatographic Theory and principles*, **38**, Marcel Dekker Inc., (1987).

[141] Heslop, M.J., Buffham, B.A., and Mason,G., "A Test of the Polynomial-Fitting Method of Determining Binary-Gas-Mixture Adsorption Equilibria", *Ind. Eng. Chem. Res.*, **35**, 1456-1466 (1996).

[142] Harlick, P.J.E., and Tezel, F.H., "A Novel Solution Method for Interpreting Binary Adsorption Isotherms from Concentration Pulse Chromatography Data", *Adsorption*, **6**, 293-309 (2000).

[143] Hafizovic, J., Bjorgen, M., Olsbye, U., Dietzel, P. D. C., Bordiga, S., Prestipino, C., Lamberti, C., Lillerud, K. P., "The Inconsistency in Adsorption Properties and Powder XRD Data of MOF-5 Is Rationalized by Framework Interpenetration and the Presence of Organic and Inorganic Species in the Nanocavities," *J. Am. Chem. Soc.*, **129**, 3612-3620 (2007).

[144] Lamia, N., Jorge, M., Granato, M.A., Almeida Paz, F.A., Chevreau, H., and Rodrigues, A.E., "Adsorption of propane, propylene and isobutane on a metal-organic framework: Molecular simulation and experiment," *Chem. Engg. Sci.*, **64**, 3246-3259 (2009).

[145] Yazaydin, A.O., Benin, A.I., Faheem, S.A., Jakubczak, P., Low, J.J., Willis, R.R., and Snurr, R.Q., "Enhanced CO_2 Adsorption in Metal-Organic Frameworks via Occupation of Open-Metal Sites by Coordinated Water Molecules," *Chem. Mater.*, **21**, 1425-1430 (2009).

[146] Liu, Y.-Y.; Zeng, J.-L.; Zhang, J.; Xu, F.; Sun, L.-X.," Improved hydrogen storage in the modified metal-organic frameworks by hydrogen spillover effect," *Int. J. Hydrogen Energy*, **32**, 4005-4010 (2007).

[147] Chowdhury, P., Bikkina, C., and Gumma, S.,"Gas Adsorption Properties of the Chromium-Based Metal Organic Framework MIL-101, " *J. Phys. Chem. C*, **113**, 6616-6621 (2009).

[148] Sircar, S., "Role of adsorbent heterogeneity on mixed gas adsorption," *Ind. Eng. Chem. Res.*, 30, 1032-1039 (1991).

[149] Chowdhury, P., Bikkina, C., Meister, D., Dreisbach, F., and Gumma, S., "Comparison of adsorption isotherms on Cu-BTC metal organic frameworks synthesized from different routes," *Micropor. Mesopor. Mater.*, **117**, 406-413 (2009).

[150] Vimont, A., Goupil, J.-M., Lavalley, J.-C., Daturi, M., Surblé, S., Serre, C., Millange, F., Férey, G., and Audebrand, N., "Investigation of Acid Sites in a Zeotypic Giant Pores Chromium(III) Carboxylate,"*J. Am. Chem. Soc.*, **128**, 3218-3227 (2005).

[151] Finsy, V., Ma, L., Alaerts, L., De Vos, D.E., Baron, G.V., Denayer, J. F. M., "Separation of CO_2/CH_4 mixtures with the MIL-53(Al) metal–organic framework," *Micropor. Mesopor. Mater.*, **120**, 221-227 (2009).

[152] Karra, J. R., and Walton, K. S.," Effect of Open Metal Sites on Adsorption of Polar and Nonpolar Molecules in Metal-Organic Framework Cu-BTC, " *Langmuir*, 24, 8620-8626 (2008).

APPENDIX A

Spreading Pressure Relations for Pure Gas Isotherm Models

The spreading pressure is a thermodynamic variable which cannot be measured directly. Nevertheless it is an important variable in solution thermodynamic approach. Multi-component models like IAST require relations for spreading pressure of pure gas adsorption.

In case of pure gas adsorption, spreading pressure can be readily calculated using, Eq. (3.24)

$$\psi = \frac{\pi A}{RT} = \int_0^P \frac{N}{P} dP \tag{A.1}$$

Langmuir Model

The Langmuir isotherm in Eq. (3.35) can be rewritten as

$$\frac{N}{P} = \frac{M\beta}{M + \beta P} \tag{A.2}$$

From Eqs. (A.1) and (A.2) it follows,

$$\Psi = \int_0^P \frac{M\beta}{M + \beta P} dP = M \ln\left(M + \beta P\right) \tag{A.3}$$

Dual-Site Langmuir Model

The dual site Langmuir model given by eq. (3.37) is

$$N = \frac{M^{(1)}\delta^{(1)}P}{1 + \delta^{(1)}P} + \frac{M^{(2)}\delta^{(2)}P}{1 + \delta^{(2)}P} \tag{A.4}$$

$$\Psi = \int_0^P \left(\frac{M^{(1)}\delta^{(1)}}{1 + \delta^{(1)}P} + \frac{M^{(2)}\delta^{(2)}}{1 + \delta^{(2)}P} \right) dP = M^{(1)} \ln\left(1 + \delta^{(1)}P\right) + M^{(2)} \ln\left(1 + \delta^{(2)}P\right) \tag{A.5}$$

Virial Model

The virial isotherm in Eq. (3.41) can be rewritten as

$$\ln\left(P\right) = \ln(N) + k + bN + cN^2$$

$$\Rightarrow \frac{d\ln\left(P\right)}{dN} = \frac{1}{N} + b + 2cN \tag{A.6}$$

Finally,

$$\Psi = \int_0^P \frac{N}{P}\,dP = \int_0^P N\,d\left(\ln(P)\right) = \int_0^N N\frac{d\left(\ln(P)\right)}{dN}dN \tag{A.7}$$

From Eqs. (A.6) and (A.7) it follows

$$\Psi = \int_0^N N\left(\frac{1}{N} + b + 2cN\right)dN = N + \frac{1}{2}bN^2 + \frac{2}{3}cN^3 \tag{A.8}$$

Virial Langmuir Model

The following equation can be readily obtained from Virial Langmuir model given in Eq. (3.46).

$$\ln\left(P\right) = \ln(N) - \ln(\beta) + \ln(M) - \ln(M - N) + bN + cN^2$$

$$\Rightarrow \frac{d\left(\ln(P)\right)}{dN} = \frac{1}{N} + \frac{1}{M - N} + b + 2cN \tag{A.9}$$

From Eqs. (A.7) and (A.9) it follows

$$\Psi = \int_0^N N\left(\frac{1}{N} + b + 2cN\right)dN = \frac{1}{2}bN^2 + \frac{2}{3}cN^3 - M\ln\left(\frac{M-N}{M}\right) \tag{A.10}$$

APPENDIX B

Enthalpy of Adsorption for Various Models

The enthalpy of adsorption, using various isotherm models is calculated via Eq. (3.48).

Langmuir Model

In case of Langmuir model, the saturation loading is independent of temperature and the temperature dependency of Henry's constant is given by Eq. (3.36).

$$\beta = \beta_{(0)} e^{-\beta_{(1)}/T} \tag{3.36}$$

With this temperature dependency the Langmuir model in Eq. (3.35) reduces to

$$N = \frac{M\beta P}{M + \beta P} \Rightarrow \frac{1}{N} = \frac{1}{\beta P} + \frac{1}{M} \Rightarrow \ln(M) + \ln(\beta) + \ln(P) - \ln(N) = 0 \tag{B.1}$$

Differentiating Eq. (B.1) w.r.t. *1/T* at constant *N*

$$\frac{\partial \ln(\beta)}{\partial(1/T)} + \frac{\partial \ln(P)}{\partial(1/T)} = 0 \tag{B.2}$$

From Eqs. (3.36), (3.48) and (B.2)

$$\Delta h_{ads} = -R\frac{\partial \ln(P)}{\partial(1/T)} = \beta_{(1)} R \tag{B.3}$$

Dual-Site Langmuir Model

The dual site Langmuir model given by eq. (3.37) is

$$N = \frac{M^{(1)}\delta^{(1)}P}{1+\delta^{(1)}P} + \frac{M^{(2)}\delta^{(2)}P}{1+\delta^{(2)}P} \tag{B.4}$$

The affinity parameters are temperature dependent;

$$\delta^{(i)} = \delta^{(i)}_{(0)} \exp\left(\frac{-\Delta h^{(i)}_{ads}}{R}\left[\frac{1}{T} - \frac{1}{T_0}\right]\right) \tag{B.5}$$

$$\frac{\partial \delta^{(i)}}{\partial(1/T)} = \delta^{(i)}_{(0)} \exp\left(\frac{-\Delta h^{(i)}_{ads}}{R}\left[\frac{1}{T} - \frac{1}{T_0}\right]\right)\left(\frac{-\Delta h^{(i)}_{ads}}{R}\right) = \frac{-\Delta h^{(i)}_{ads}}{R}\delta^{(i)} \tag{B.6}$$

Differentiate (B.4) w.r.t. *1/T* at constant *N* and use (B.6) to get

$$\frac{\Delta h_{ads}}{R} = \frac{\Delta h^{(1)}_{ads} M^{(1)}\delta^{(1)}\left(1+\delta^{(2)}P\right)^2 + \Delta h^{(2)}_{ads} M^{(2)}\delta^{(2)}\left(1+\delta^{(1)}P\right)^2}{M^{(1)}\delta^{(1)}\left(1+\delta^{(2)}P\right)^2 + M^{(2)}\delta^{(2)}\left(1+\delta^{(1)}P\right)^2} \tag{B.7}$$

Virial Model

The enthalpy of adsorption is obtained directly by differentiating Eq. (3.41); the necessary temperature dependency of the coefficients is given by Eq. (3.42).

$$\frac{\Delta h_{ads}}{R} = -\left(\beta_{(1)} + b_{(1)}N + c_{(1)}N^2\right) \tag{B.8}$$

Virial-Langmuir Model

The following equation can be readily obtained from Virial Langmuir model given in Eq. (3.46).

$$\ln(P) = \ln(N) - \ln(\beta) + \ln(M) - \ln(M - N) + bN + cN^2 \tag{B.9}$$

The enthalpy of adsorption can be obtained by differentiating this relation, w.r.t *1/T* at constant *N*; the necessary temperature dependency of the coefficients is given by Eqs. (3.36), (3.43), (3.44) and (3.47).

$$\frac{\Delta h_{ads}}{R} = -\left(\beta_1 + b_1 N + c_1 N^2 + \frac{M_{(1)}}{M} - \frac{M_{(1)}}{M - N}\right) \tag{B.10}$$

APPENDIX C

Derivations for Mixed Gas Adsorption

In this section, appropriate derivations for adsorption of a gas mixture based on both Virial and Virial –Langmuir models will be presented, using an EoS approach. Eq. (3.54) relates the fugacity of species i in a gas mixture, $\hat{f}_i^{g}$ to the adsorbed phase properties viz. compressibility factor Z, area A and amount adsorbed N_i.

$$\ln \frac{\hat{f}_i^{g}}{N_i} = -\ln(\beta_i) + \int_A^{\infty} \left(\left. \frac{\partial(N.Z)}{\partial N_i} \right|_{T,A,N_{j\neq i}} - 1 \right) \frac{dA}{A} \tag{C.1}$$

Where β_i, N_i is the Henry constant and partial amount adsorbed (for species i) respectively.

Virial Formalism

The Virial isotherm model can be readily obtained, using Eq. (C.1) in conjunction with a Virial EoS in 2-dimensions.

$$Z = \frac{\pi a}{RT} = 1 + \frac{b'_{mix}}{a} + \frac{c'_{mix}}{a^2} \tag{C.2}$$

where, a is molar surface area i.e. A/N. b'_{mix} and c'_{mix} are the virial coeffients for the mixture. Mixing rules analogous to bulk phase are used to define their dependency on composition.

$$\begin{aligned} b'_{mix} &= \sum_i \sum_j x_i . x_j . b'_{ij} \\ c'_{mix} &= \sum_i \sum_j \sum_k x_i . x_j . x_k c'_{ijk} \end{aligned} \tag{C.3}$$

where b'_{ij} and c'_{ijk} represent the cross virial coefficients.

Rewriting eq. (C.2) in terms of A and differentiating w.r.t N_i

$$\begin{aligned} \frac{\partial(NZ)}{\partial N_i} &= 1 + \frac{1}{A} \frac{\partial(Nb'_{mix})}{\partial N_i} + \frac{1}{A^2} \frac{\partial(N^2 c'_{mix})}{\partial N_i} \\ \Rightarrow \frac{\partial(NZ)}{\partial N_i} - 1 &= \frac{2N}{A} \sum_j x_j b'_{ij} + \frac{3N^2}{A^2} \sum_k \sum_j x_j x_k c'_{ijk} \end{aligned} \tag{C.4}$$

(C.4) can be used to relate fugacity of bulk phase to adsorbed phase properties via Eq. (C.1).

$$\ln \frac{\hat{f}_i^g}{N_i} = -\ln(\beta_i) + \int_A^{\infty} \left(\frac{2N}{A} \sum_j x_j b_{ij}' + \frac{3N^2}{A^2} \sum_k \sum_j x_j x_k c_{ijk}' \right) \frac{dA}{A}$$

$$\Rightarrow \ln \frac{\hat{f}_i^g}{N_i} = -\ln(\beta_i) + \frac{2N}{A} \sum_j x_j b_{ij}' + \frac{3N^2}{2A^2} \sum_k \sum_j x_j x_k c_{ijk}' \tag{C.5}$$

The second and third virial coefficients in the above equation can be modified to include the factors $2/A$ and $3/2A^2$ respectively, to yield

$$\Rightarrow \ln \frac{\hat{f}_i^g}{N_i} = -\ln(\beta_i) + N \sum_j x_j b_{ij} + N^2 \sum_k \sum_j x_j x_k c_{ijk} \tag{C.6}$$

Where

$$b_{ij} = \frac{2}{A} b_{ij}' \quad \text{and} \quad c_{ij} = \frac{3}{2A^2} c_{ij}' \tag{C.7}$$

For a pure gas, Eq. (C.6) reduces to the more familiar form as given by Eq. (3.41).

Virial-Langmuir Formalism

This formalism can be developed by adding a Langmurian term to the 2D virial EoS to account for saturation at high loadings. The 2D EoS in Eq. (C.2) is replaced by

$$Z = \frac{M_{mix}}{N} \ln \left(\frac{M_{mix}}{M_{mix} - N} \right) + \frac{b_{mix}'}{a} + \frac{c_{mix}'}{a^2} \tag{C.8}$$

where M_{mix} is the saturation loading for the mixture in mol/kg (or mmol/g). M_{mix} is however related to the surface area of the adsorbent, via

$$M_{mix} = M_{mix}' A \tag{C.9}$$

where M_{mix}' is saturation loading of the material in mol/m^2 and is independent of the area of the adsorbent, A.

In addition to mixing rules for the virial coefficients, an additional mixing rule is needed for the saturation loading of the mixture M_{mix}. We use the mixing rule proposed by Siperstein et al. [102]

$$\frac{1}{M_{mix}} = \sum_i \frac{x_i}{M_i} \qquad \Rightarrow \frac{1}{M'_{mix}A} = \sum_i \frac{x_i}{M'_i A} \tag{C.10}$$

where the pure species saturation loadings are related through

$$M_j = M'_j A \tag{C.11}$$

From Eq. (C.8)

$$\frac{1}{A}\left(\frac{\partial(NZ)}{\partial N_i} - 1\right) = \frac{1}{A}\left(\frac{\partial(\varepsilon)}{\partial N_i} - 1\right) + \frac{1}{A^2}\frac{\partial(Nb'_{mix})}{\partial N_i} + \frac{1}{A^3}\frac{\partial(N^2 c'_{mix})}{\partial N_i} \tag{C.12}$$

Where

$$\varepsilon = M_{mix} \ln\left(\frac{M_{mix}}{M_{mix} - N}\right) \tag{C.13}$$

In order to evaluate Eq. (A.12) we first try to evaluate expression for $\frac{\partial\left(M_{mix}\right)}{\partial N_i}$ followed by $\frac{\partial(\varepsilon)}{\partial N_i}$.

From Eq. (C.10)

$$\frac{1}{M_{mix}} = \frac{1}{N}\sum_j \frac{N_j}{M_j} = \frac{1}{N}\sum_{j \neq i} \frac{N_j}{M_j} + \frac{1}{N}\frac{N_i}{M_i}$$

$$\Rightarrow \frac{\partial\left(1/M_{mix}\right)}{\partial N_i} = -\frac{1}{N^2}\sum_{j \neq i}\frac{N_j}{M_j} - \frac{1}{N^2}\frac{N_i}{M_i} + \frac{1}{NM_i} = -\frac{1}{NM_{mix}} + \frac{1}{NM_i}$$

$$\Rightarrow \frac{\partial M_{mix}}{\partial N_i} = \frac{M_{mix}}{N} - \frac{M_{mix}^2}{NM_i} \tag{C.14}$$

From Eqs. (C.9) and (C.14)

$$\Rightarrow \iota = \frac{1}{A}\frac{\partial M_{mix}}{\partial N_i} = \frac{M'_{mix}}{N} - \frac{M'^{2}_{mix}}{NM'_{i}} \tag{C.15}$$

Note that, ι is independent of area A.

From Eq. (C.13)

$$\frac{\partial \varepsilon}{\partial N_i} = \left| \begin{aligned} & \ln\left(\frac{M_{mix}}{M_{mix}-N}\right)\frac{\partial M_{mix}}{\partial N_i} \\ & + \frac{1}{M_{mix}-N}\left(\left(M_{mix}-N\right)\frac{\partial M_{mix}}{\partial N_i} - M_{mix}\left(\frac{\partial M_{mix}}{\partial N_i}-1\right)\right) \end{aligned} \right. \tag{C.16}$$

$$= \ln\left(\frac{M_{mix}}{M_{mix}-N}\right)\frac{\partial M_{mix}}{\partial N_i} - \frac{N}{M_{mix}-N}\frac{\partial M_{mix}}{\partial N_i} + \frac{M_{mix}}{M_{mix}-N}$$

$$= \ln\left(\frac{M_{mix}}{M_{mix}-N}\right)\iota A - \frac{N}{M_{mix}-N}\iota A + \frac{M_{mix}}{M_{mix}-N}$$

Before integrating w.r.t. A we have to make saturation loading independent of surface area A, by using Eq. (C.9).

$$\Rightarrow \frac{1}{A}\frac{\partial \varepsilon}{\partial N_i} = \ln\left(\frac{AM'_{mix}}{AM'_{mix}-N}\right)\iota - \frac{N}{AM'_{mix}-N}\iota + \frac{AM'_{mix}}{A\left(AM'_{mix}-N\right)} \tag{C.17}$$

$$\Rightarrow \int \frac{1}{A}\left(\frac{\partial \varepsilon}{\partial N_i}-1\right)dA = \iota A\ln\left(\frac{AM'_{mix}}{AM'_{mix}-N}\right) + \ln\left(\frac{AM'_{mix}-N}{A}\right) - \frac{\iota N}{M'_{mix}}\ln(N)$$

$$\Rightarrow \int_A^\infty \frac{1}{A}\left(\frac{\partial \varepsilon}{\partial N_i}-1\right)dA = \left| \begin{aligned} &= \lim_{A\to\infty}\left(\iota A\ln\left(\frac{AM'_{mix}}{AM'_{mix}-N}\right) + \ln\left(\frac{AM'_{mix}-N}{A}\right)\right) \\ & -\left(\iota A\ln\left(\frac{AM'_{mix}}{AM'_{mix}-N}\right) + \ln\left(\frac{AM'_{mix}-N}{A}\right)\right) \end{aligned} \right.$$

$$\begin{aligned} \Rightarrow \int_A^\infty \frac{1}{A}\left(\frac{\partial \varepsilon}{\partial N_i}-1\right)dA &= \frac{\iota N}{M'_{mix}} + \ln(M'_{mix}) - \left(\iota A\ln\left(\frac{AM'_{mix}}{AM'_{mix}-N}\right) + \ln\left(\frac{AM'_{mix}-N}{A}\right)\right) \\ &= \frac{\iota N}{M'_{mix}} - \iota A\ln\left(\frac{AM'_{mix}}{AM'_{mix}-N}\right) - \ln\left(\frac{AM'_{mix}-N}{AM'_{mix}}\right) \\ &= \frac{\iota N}{M'_{mix}} + (1-\iota A)\ln\left(\frac{AM'_{mix}}{AM'_{mix}-N}\right) \end{aligned} \tag{C.18}$$

Putting Eqs. (C.9), (C.14) and (C.15) into (C.18) to get

$$\Rightarrow \int_{A}^{\infty} \frac{1}{A}\left(\frac{\partial \varepsilon}{\partial N_i} - 1\right) dA = \left(1 - \frac{M_{mix}}{M_i}\right) + \left(1 - \frac{M_{mix}}{N} + \frac{M_{mix}^2}{NM_i}\right) \ln\left(\frac{M_{mix}}{M_{mix} - N}\right) \qquad \text{(C.19)}$$

To relate fugacity to adsorbed phase properties via Eq. (C.1) for virial Langmuir formalism, in addition to Eq. (C.18) the integrals involving $b_{mix}^{'}$ and $c_{mix}^{'}$ need to be solved. For these integrals, an approach similar to that of virial formalism can be used. This manipulation finally yields

$$\ln \frac{\hat{f}_i^{\,g}}{\beta_i N_i} = \left(1 - \frac{M_{mix}}{M_i}\right) + \left(1 - \frac{M_{mix}}{N} + \frac{M_{mix}^2}{NM_i}\right) \ln\left(\frac{M_{mix}}{M_{mix} - N}\right) + N\sum_j x_j b_{ij} + N^2 \sum_k \sum_j x_j x_k c_{ijk} \qquad \text{(C.20)}$$

For case of a pure gas, Eq. (C.20) reduces to the more familiar form, given in Eq. (3.46).

APPENDIX D

IAST Calculation Procedure Using Virial-Langmuir Pure Gas Isotherm Model

The IAST predictions for CO_2+CH_4 binary mixture adsorption on Cu-BTC, at finite composition presented in section 5.5.3 were performed using the following procedure. This discussion here is based on extension of general outline given in section 3.6.

Phase Equilibrium Relations:

$$x_1 P_1^0 = y_1 P \tag{D.1}$$

$$x_2 P_2^0 = y_2 P \tag{D.2}$$

Pure Gas Isotherms (Eq. 3.46):

The following relations are based on virial Langmuir model given by Eq. (3.46) at the standard state

$$\ln\left(\frac{P_1^0 \beta_1}{N_1^0}\right) = \ln\left(\frac{M_1}{M_1 - N_1^0}\right) + b_1 N_1^0 + c_1 N_1^{0^2} \tag{D.3}$$

$$\ln\left(\frac{P_2^0 \beta_2}{N_2^0}\right) = \ln\left(\frac{M_2}{M_2 - N_2^0}\right) + b_2 N_2^0 + c_2 N_2^{0^2} \tag{D.4}$$

Spreading Pressure (Eq. A.10):

$$\Psi = \frac{1}{2} b_1 N_1^{0^2} + \frac{2}{3} c_1^0 N_1^{0^3} - M_1 \ln\left(\frac{M_1 - N_1^0}{M_1}\right) \tag{D.5}$$

$$\Psi = \frac{1}{2} b_2 N_2^{0^2} + \frac{2}{3} c_2^0 N_2^{0^3} - M_2 \ln\left(\frac{M_2 - N_2^0}{M_2}\right) \tag{D.6}$$

$$x_1 + x_2 = 1 \tag{D.7}$$

$$\frac{1}{N} = \frac{x_1}{N_1^0} + \frac{x_2}{N_2^0} \tag{D.8}$$

The above 8 equations (D.1) through (D.8) are solved to yield solution to the 8 unknowns *viz.* bulk phase pressures at standard state (P_i^0), amounts adsorbed at standard state (N_i^0), mole fractions of the adsorbed phase (x_i), total amount adsorbed for the mixture and the spreading pressure of the either component at their standard states (as well as the mixture, ψ).

APPENDIX E

ISOTHERM DATA ON Cu-BTC (or, HKUST-1) SAMPLES

(A & B)

Table A. 1: N_2 adsorption isotherm data on Cu-BTC samples (**A & B**) at 295 and 318 K

Adsorbent	Gas	Temperature *T* / K	Pressure *P* / bar	Amount Adsorbed *N* / mmol g^{-1}
Cu-BTC (Sample **A**)	N_2	295	1.24	0.178
			1.96	0.272
			1.98	0.273
			2.65	0.355
			3.38	0.438
			3.97	0.501
			4.51	0.558
			5.06	0.612
			5.82	0.686
			6.53	0.750
			7.11	0.800
			7.84	0.862
			8.04	0.880
			8.16	0.889
			8.59	0.921
			9.61	0.998
		318	1.91	0.205
			2.64	0.274
			3.57	0.346
			3.63	0.358
			4.44	0.418
			4.63	0.439
			5.69	0.521
			6.40	0.575
			7.79	0.672
			8.37	0.700
			8.39	0.708
			9.57	0.794

Adsorbent	Gas	Temperature T / K	Pressure P / bar	Amount Adsorbed N / mmol g^{-1}
Cu-BTC (Sample **B**)	N_2	295	0.61	0.188
			1.41	0.413
			2.38	0.671
			3.24	0.885
			4.05	1.076
			4.92	1.271
			6.09	1.509
			7.11	1.711
			8.26	1.928
			9.10	2.073
		318	0.49	0.107
			1.38	0.285
			2.60	0.513
			3.83	0.732
			4.90	0.912
			5.97	1.082
			7.18	1.264
			8.02	1.388
			9.32	1.575
			9.78	1.631

Table A.11: O_2 adsorption isotherm data on Cu-BTC samples (**A & B**) at 295 and 318 K

Adsorbent	Gas	Temperature T / K	Pressure P / bar	Amount Adsorbed N / mmol g^{-1}
Cu-BTC (Sample A)	O_2	295	1.31	0.176
			2.22	0.290
			3.20	0.401
			3.12	0.394
			4.18	0.508
			5.26	0.617
			6.16	0.700
			6.86	0.767
			7.93	0.860
			8.90	0.940
			9.23	0.970
		318	1.58	0.170
			2.30	0.237
			7.56	0.650
			8.47	0.709
			8.75	0.737
			9.07	0.748

Adsorbent	Gas	Temperature T / K	Pressure P / bar	Amount Adsorbed N / mmol g^{-1}
Cu-BTC (Sample **B**)	O_2	295	1.63	0.437
			2.56	0.659
			3.51	0.874
			4.63	1.111
			5.70	1.327
			6.95	1.565
			7.95	1.751
			9.18	1.960
			9.77	2.065
		318	0.73	0.136
			1.45	0.270
			2.47	0.445
			3.47	0.613
			4.45	0.770
			5.51	0.936
			6.55	1.089
			7.46	1.221
			8.44	1.357
			9.42	1.490

Table A.III: Ar adsorption isotherm data on Cu-BTC samples (**A** & **B**) at 295 and 318 K

Adsorbent	Gas	Temperature T / K	Pressure P / bar	Amount Adsorbed N / mmol g^{-1}
Cu-BTC (Sample **A**)	Ar	295	1.22	0.174
			2.24	0.304
			3.27	0.423
			4.24	0.529
			5.23	0.632
			6.20	0.726
			7.10	0.809
			8.00	0.889
			9.01	0.974
			9.51	1.019
		318	1.11	0.118
			1.97	0.202
			2.90	0.287
			3.86	0.368
			4.77	0.444
			5.82	0.526
			6.89	0.610
			8.26	0.710
			9.44	0.794

Adsorbent	Gas	Temperature T / K	Pressure P / bar	Amount Adsorbed N / mmol g^{-1}
Cu-BTC (Sample B)	Ar	295	0.61	0.170
			1.58	0.427
			2.64	0.687
			3.63	0.915
			4.73	1.154
			5.58	1.334
			6.56	1.530
			7.56	1.724
			8.48	1.894
			8.95	1.982
			9.94	2.152
		318	1.45	0.283
			2.50	0.470
			3.40	0.627
			4.18	0.758
			5.15	0.916
			6.28	1.091
			7.68	1.301
			8.56	1.430
			10.17	1.655

Table A.IV: CO_2 adsorption isotherm data on Cu-BTC samples (**A** & **B**) at 295 and 318 K

Adsorbent	Gas	Temperature T / K	Pressure P / bar	Amount Adsorbed N / mmol g^{-1}
Cu-BTC (Sample **A**)	CO_2	295	0.09	0.172
			0.23	0.462
			0.44	0.855
			0.68	1.228
			1.19	1.890
			3.41	3.364
			5.59	3.936
			5.81	3.999
		318	0.06	0.103
			0.2	0.316
			0.75	0.898
			1.28	1.381
			1.37	1.455
			1.64	1.635
			2.28	2.004
			3.04	2.314
			3.91	2.656
			4.72	2.886
			5.55	3.079
			5.68	3.108

Adsorbent	Gas	Temperature T / K	Pressure P / bar	Amount Adsorbed N / mmol g^{-1}
Cu-BTC (Sample **B**)	CO_2	295	0.01	0.010
			0.03	0.095
			0.07	0.218
			0.11	0.434
			0.53	2.220
			1.33	5.069
			3.51	8.617
			4.98	9.724
			5.79	10.102
		318	0.22	0.688
			0.44	1.283
			0.58	1.667
			0.90	2.459
			1.96	4.624
			3.42	6.497
			4.89	7.760
			5.83	8.421

Table A.V: C_3H_8 adsorption isotherm data on Cu-BTC samples (**A & B**) at 295 and 318 K

Adsorbent	Gas	Temperature *T* / K	Pressure *P* / bar	Amount Adsorbed *N* / mmol g^{-1}
Cu-BTC (Sample A)	C_3H_8	295	1.07	2.340
			2.21	2.460
			3.13	2.515
			4.09	2.559
			5.05	2.599
			6.00	2.638
			6.95	2.683
		318	0.02	0.487
			0.04	0.776
			0.07	1.073
			0.13	1.486
			0.53	1.940
			0.75	2.018
			1.11	2.105
			4.10	2.377
			7.24	2.522

Adsorbent	Gas	Temperature T / K	Pressure P / bar	Amount Adsorbed N / mmol g^{-1}
Cu-BTC (Sample **B**)	C_3H_8	295	0.01	0.842
			0.04	2.579
			0.05	3.910
			0.12	5.129
			0.30	6.049
			0.63	6.383
			1.37	6.644
			2.32	6.783
			3.19	6.846
			4.29	6.891
			5.68	6.916
			6.87	6.916
			7.82	6.917
			8.19	6.922
		318	0.01	0.288
			0.02	0.612
			0.04	1.166
			0.06	1.744
			0.11	3.223
			0.35	4.997
			0.61	5.405
			1.18	5.745
			4.32	6.235
			7.22	6.324

Table A.VI: SF_6 adsorption isotherm data on Cu-BTC samples (**A & B**) at 295 and 318 K

Adsorbent	Gas	Temperature T / K	Pressure P / bar	Amount Adsorbed N / mmol g^{-1}
Cu-BTC (Sample **A**)	SF_6	295	0.03	0.371
			0.09	0.671
			0.15	1.050
			0.72	1.795
			1.67	1.975
			3.09	2.103
			5.40	2.227
			8.12	2.335
		318	0.11	0.368
			0.07	0.280
			0.22	0.687
			0.53	1.370
			1.68	1.772
			5.70	2.042
			8.09	2.137

Adsorbent	Gas	Temperature T / K	Pressure P / bar	Amount Adsorbed N / mmol g^{-1}
Cu-BTC (Sample **B**)	SF_6	295	0.02	0.091
			0.03	0.344
			0.05	0.692
			0.09	1.334
			0.18	3.236
			0.42	4.817
			0.73	5.159
			1.42	5.521
			4.06	5.849
			7.22	5.948
		318	0.03	0.268
			0.06	0.465
			0.17	1.344
			1.30	4.790
			3.64	5.308
			5.31	5.486
			7.76	5.615

APPENDIX F

ISOTHERM DATA ON Cr-BDC (or, MIL-101) SAMPLE

(0-10 bar)

Table B.1: Ar adsorption isotherm data on Cr-BDC sample at 283, 319 and 351 K

Adsorbent	Gas	Temperature T / K	Pressure P / bar	Amount Adsorbed N / mmol g^{-1}
Cr-BDC	Ar	283	0.04	0.012
			0.12	0.039
			0.31	0.073
			0.78	0.162
			1.95	0.369
			4.06	0.733
			6.27	1.070
			9.36	1.501
		319	0.22	0.035
			0.71	0.085
			1.64	0.181
			3.47	0.358
			5.14	0.514
			7.24	0.699
			9.59	0.897
		351	0.25	0.020
			0.46	0.035
			1.92	0.128
			4.07	0.263
			6.28	0.404
			8.77	0.548

Table B.11: CH_4 adsorption isotherm data on Cr-BDC sample at 283, 319 and 351 K

Adsorbent	Gas	Temperature T / K	Pressure P / bar	Amount Adsorbed N / mmol g^{-1}
Cr-BDC	CH_4	283	0.02	0.025
			0.05	0.063
			0.10	0.108
			0.24	0.218
			0.69	0.475
			1.65	0.949
			3.71	1.763
			5.99	2.513
			9.21	3.407
		319	0.05	0.025
			0.08	0.042
			0.25	0.100
			0.46	0.171
			1.67	0.540
			3.51	0.983
			5.92	1.424
			8.82	1.933
		351	0.11	0.035
			0.23	0.059
			0.45	0.119
			0.85	0.187
			1.91	0.362
			3.84	0.652
			6.03	0.961
			8.28	1.233

Table B.III: CO_2 adsorption isotherm data on Cr-BDC sample at 283, 319 and 351 K

Adsorbent	Gas	Temperature *T* / K	Pressure *P* / bar	Amount Adsorbed *N* / mmol g^{-1}
Cr-BDC	CO_2	283	0.03	0.161
			0.07	0.300
			0.12	0.498
			0.25	0.863
			0.74	1.786
			1.70	3.218
			3.27	5.676
			5.15	8.257
		319	0.02	0.053
			0.05	0.076
			0.09	0.136
			0.13	0.181
			0.25	0.322
			0.63	0.687
			1.61	1.456
			2.92	2.310
			4.07	2.997
			5.19	3.640
		351	0.05	0.049
			0.19	0.153
			0.44	0.322
			0.86	0.543
			1.78	0.962
			3.29	1.520
			5.27	2.160

Table B.IV: C_3H_8 adsorption isotherm data on Cr-BDC sample at 283, 319 and 351 K

Adsorbent	Gas	Temperature T / K	Pressure P / bar	Amount Adsorbed N / mmol g^{-1}
Cr-BDC	C_3H_8	283	0.01	0.193
			0.03	0.639
			0.04	0.849
			0.05	1.013
			0.07	1.226
			0.10	1.432
			0.13	1.754
			0.17	2.092
			0.21	2.726
			0.26	3.354
			0.57	6.460
			0.64	6.592
			1.56	11.007
			3.52	12.055
			5.37	13.408
		319	0.01	0.383
			0.03	0.486
			0.05	0.575
			0.07	0.678
			0.12	0.811
			0.15	0.907
			0.65	2.269
			1.68	5.068
			3.03	7.452
			5.02	9.516
			8.01	10.513
		351	0.04	0.323
			0.19	0.682
			0.38	0.937
			0.86	1.450
			1.85	2.650
			3.94	4.880
			5.87	6.414
			8.76	7.959

Table B.V: SF_6 adsorption isotherm data on Cr-BDC sample at 283, 319 and 351 K

Adsorbent	Gas	Temperature T / K	Pressure P / bar	Amount Adsorbed N / mmol g^{-1}
Cr-BDC	SF_6	283	0.02	0.324
			0.06	0.567
			0.11	0.695
			0.17	0.840
			0.31	1.131
			0.77	2.249
			1.78	4.806
			3.79	7.980
			5.88	9.596
			8.19	10.021
		319	0.03	0.223
			0.07	0.294
			0.11	0.397
			0.16	0.508
			0.57	0.931
			1.72	1.855
			3.44	3.288
			5.41	4.692
			8.15	6.141
		351	0.04	0.105
			0.18	0.322
			0.39	0.529
			0.69	0.705
			1.78	1.182
			3.85	2.036
			6.05	2.898
			8.19	3.651

APPENDIX G

ISOTHERM DATA ON Cu-BTC (or, HKUST-1) SAMPLE C

(High Pressure)

Table C.I: CO adsorption isotherm data on Cu-BTC sample (**C**) at 295, 318 and 353 K

Adsorbent	Gas	Temperature T / K	Pressure P / bar	Amount Adsorbed N / mmol g^{-1}
Cu-BTC (sample C)	CO	295	0.05	0.090
			0.12	0.213
			0.52	0.809
			1.04	1.434
			1.59	1.967
			2.26	2.509
			2.92	2.963
			5.29	4.147
			10.66	5.844
			17.34	6.807
			26.29	7.824
			24.64	7.998
			43.24	9.101
			71.32	9.746
		318	0.07	0.068
			0.13	0.121
			0.55	0.467
			1.06	0.840
			1.62	1.175
			2.27	1.580
			2.91	1.912
			5.32	2.934
			10.65	4.459
			17.34	5.667
			25.25	6.613
			26.48	6.730
			42.01	7.702
			70.74	8.528
		353	0.60	0.225
			1.08	0.386
			1.66	0.575
			2.45	0.816
			2.93	0.952
			5.37	1.543
			10.66	2.597
			17.33	3.555
			26.37	4.485
			43.02	5.632
			71.82	6.652

Table C.II: CO_2 adsorption isotherm data on Cu-BTC sample (**C**) at 295, 318 and 353 K

Adsorbent	Gas	Temperature T / K	Pressure P / bar	Amount Adsorbed N / mmol g^{-1}
Cu-BTC (sample C)	CO_2	295	0.05	0.354
			0.12	0.867
			0.47	3.095
			0.74	4.634
			0.91	5.203
			1.68	7.912
			2.26	9.366
			2.93	10.550
			5.27	12.836
			10.67	14.580
			17.30	15.290
			26.38	15.598
			36.24	15.414
			44.47	15.485
		318	0.05	0.182
			0.13	0.469
			0.52	1.733
			1.07	3.387
			1.57	4.663
			2.22	6.110
			2.90	7.317
			5.11	9.960
			10.64	12.810
			17.35	14.032
			24.90	14.112
			26.38	14.677
			35.66	14.354
			36.89	14.352
			46.92	14.378
			60.35	14.969

Contd...

Adsorbent	Gas	Temperature *T* / K	Pressure *P* / bar	Amount Adsorbed *N* / mmol g^{-1}
Cu-BTC (sample **C**)	CO_2	353	0.06	0.079
			0.14	0.185
			0.67	0.887
			1.07	1.386
			1.59	2.019
			2.25	2.768
			3.00	3.547
			5.26	5.382
			10.65	8.311
			17.35	10.173
			21.95	10.986
			26.43	11.396
			36.17	12.043
			59.99	12.496

Table C.III: CH_4 adsorption isotherm data on Cu-BTC sample (**C**) at 295, 318 and 353 K

Adsorbent	Gas	Temperature T / K	Pressure P / bar	Amount Adsorbed N / mmol g^{-1}
Cu-BTC (sample C)	CH_4	295	0.54	0.594
			1.06	1.072
			1.59	1.523
			2.26	2.023
			2.93	2.502
			5.33	4.036
			10.64	6.531
			17.21	8.102
			26.30	9.435
			43.17	10.378
			71.75	10.785
			100.48	11.044
		318	0.53	0.375
			1.06	0.721
			1.59	1.024
			2.27	1.390
			2.91	1.713
			5.28	2.768
			10.48	4.677
			16.87	6.347
			25.33	7.803
			25.33	7.479
			40.29	8.793
			64.41	9.577
			86.88	9.860
		353	0.55	0.207
			1.07	0.391
			1.66	0.594
			2.27	0.787
			2.95	0.989
			5.38	1.621
			10.68	2.806
			17.35	3.972
			26.37	5.140
			43.17	6.528
			71.68	7.596
			100.84	8.041

APPENDIX H

ISOTHERM DATA ON Cr-BDC (or, MIL-101)

(High Pressure)

Table D.1: CO adsorption isotherm data on Cr-BDC sample at 295, 318 and 353 K

Adsorbent	Gas	Temperature T / K	Pressure P / bar	Amount Adsorbed N / mmol g^{-1}
Cr-BDC	CO	295	0.06	0.442
			0.14	0.573
			0.53	0.753
			1.07	0.893
			1.60	1.011
			2.26	1.145
			2.93	1.274
			5.35	1.677
			10.61	2.427
			17.17	3.178
			26.37	4.032
			35.05	4.843
			50.42	5.821
			67.67	6.520
		318	0.05	0.160
			0.12	0.262
			0.53	0.476
			1.06	0.607
			1.59	0.718
			2.27	0.831
			2.93	0.938
			5.33	1.257
			10.70	1.865
			17.35	2.487
			26.26	3.191
			35.52	3.900
			50.02	4.604
			64.53	5.162

Contd...

Adsorbent	Gas	Temperature T / K	Pressure P / bar	Amount Adsorbed N / mmol g^{-1}
Cr-BDC	CO	353	0.06	0.051
			0.15	0.107
			0.53	0.259
			1.06	0.396
			1.59	0.499
			2.26	0.598
			2.93	0.694
			5.32	0.956
			10.68	1.393
			17.44	1.869
			26.41	2.404
			35.95	2.951
			50.02	3.550
			62.59	3.986

Table D.II: CO_2 adsorption isotherm data on Cr-BDC sample at 295, 318 and 353 K

Adsorbent	Gas	Temperature T / K	Pressure P / bar	Amount Adsorbed N / mmol g^{-1}
Cr-BDC	CO_2	295	0.01	0.123
			0.02	0.195
			0.06	0.420
			0.13	0.688
			0.29	1.090
			0.54	1.615
			1.01	2.384
			1.68	3.294
			2.69	4.431
			3.98	5.679
			5.31	6.821
			7.31	8.345
			9.36	9.742
			13.29	12.056
			18.57	14.771
			26.25	18.132
			34.29	20.629
			45.26	21.299
		318	0.01	0.030
			0.02	0.068
			0.04	0.117
			0.07	0.200
			0.12	0.315
			0.23	0.527
			0.58	1.005
			0.92	1.385
			1.59	2.008
			2.63	2.833
			3.99	3.765
			5.33	4.574
			9.44	6.698
			13.24	8.366
			18.81	10.428
			26.43	12.730
			35.62	15.138
			46.31	17.146
			49.84	17.758

Contd...

Adsorbent	Gas	Temperature T / K	Pressure P / bar	Amount Adsorbed N / mmol g^{-1}
Cr-BDC	CO_2	353	0.01	0.022
			0.02	0.041
			0.06	0.070
			0.12	0.126
			0.26	0.242
			0.53	0.440
			0.93	0.687
			1.59	1.046
			2.66	1.550
			4.06	2.110
			5.38	2.604
			9.35	3.873
			13.35	4.963
			18.43	6.290
			26.35	8.012
			36.09	9.694
			50.39	11.767
			60.13	12.614

Table D.III: CH_4 adsorption isotherm data on Cr-BDC sample at 295, 318 and 353 K

Adsorbent	Gas	Temperature T / K	Pressure P / bar	Amount Adsorbed N / mmol g^{-1}
Cr-BDC	CH_4	295	0.01	0.007
			0.52	0.187
			0.96	0.323
			1.68	0.557
			2.71	0.862
			4.00	1.194
			5.32	1.521
			9.36	2.437
			13.30	3.209
			18.62	4.139
			26.37	5.280
			36.02	6.369
			53.92	7.793
			72.33	8.844
			103.73	10.583
		318	0.51	0.156
			0.95	0.246
			1.63	0.398
			2.68	0.614
			4.05	0.877
			5.36	1.110
			9.32	1.773
			13.38	2.373
			18.46	3.063
			26.41	4.030
			36.60	4.978
			54.14	6.291
			72.11	7.226
			103.95	8.587

Contd...

Adsorbent	Gas	Temperature *T* / K	Pressure *P* / bar	Amount Adsorbed *N* / mmol g^{-1}
Cr-BDC	CH_4	353	0.17	0.027
			0.25	0.043
			0.53	0.088
			0.94	0.122
			1.61	0.233
			2.70	0.368
			4.02	0.542
			5.36	0.701
			9.35	1.163
			13.35	1.570
			18.65	2.105
			26.39	2.760
			36.17	3.437
			54.57	4.473
			72.26	5.337
			104.24	6.469

Research Publications

International Journals

[1] Pradip Chowdhury, Chaitanya Bikkina, Dirk Meister, Frieder Dreisbach, and Sasidhar Gumma, "Comparison of adsorption isotherms on Cu-BTC metal organic frameworks synthesized from different routes," **Microporous and Mesoporous Materials,** 117 (2009) 406-413.

[2] Pradip Chowdhury, Chaitanya Bikkina, and Sasidhar Gumma, "Gas adsorption properties of the Chromium- based Metal Organic Framework MIL-101," **Journal of Physical Chemistry C,** 113 (2009) 6616-6621.

Conference Proceedings

[1] Pradip Chowdhury, Chaitanya Bikkina, Frieder Dreisbach, Dirk Meister, and Sasidhar Gumma, "Adsorption of Gases on Cu-BTC and Cr-BDC Frameworks," Adsorbent Materials II, **AIChE Annual Meeting 2008, Philadelphia, USA.**

[2] Pradip Chowdhury, Mannava Ashok, Chaitanya Bikkina, and Sasidhar Gumma, "Novel adsorbents as a medium for CO_2 capture," **National Conference on Carbon dioxide Capture and Sequestration-Challenges for Engineers**, GCET, Anand, Gujarat.